

Surface chemistry of tailored ceria nanoparticles:  
Interaction with CO and H<sub>2</sub>O

Shilpa Agarwal

**Surface chemistry of tailored ceria nanoparticles:**  
*Interaction with CO and H<sub>2</sub>O*

**Shilpa Agarwal**

Graduation committee:

Prof. dr. ir. J. W. M. Hilgenkamp, chairman	University of Twente, NL
Prof. dr. ir. L. Lefferts, promoter	University of Twente, NL
Dr. B. L. Mojet, co-promoter	University of Twente, NL
Prof. dr. ir. J. E. ten Elshof	University of Twente, NL
Prof. dr. G. Mul	University of Twente, NL
Prof. dr. ir. E. J. M. Hensen	Technical University Eindhoven, NL
Prof. dr. ir. B. M. Weckhuysen	Utrecht University, NL
Prof. A. K. Datye	University of New Mexico, USA

The research described in this thesis was carried out at the *Catalytic Processes and Materials* (CPM) group of the University of Twente, The Netherlands. I acknowledge financial support for this research from ADEM, A green Deal in Energy Materials of the Ministry of Economic Affairs of The Netherlands ([www.adem-innovationlab.nl](http://www.adem-innovationlab.nl))

**Cover design:** Shilpa Agarwal

**Cover painting:** Shilpa Agarwal (supervised by Daniela Flores Magón)

**Motivation:** I spent many days/weeks/months looking at spectra during the past four years so it was clear that the cover image needed to have something like this. Here, the ‘spectrum’ represents the Himalayas. This connects to my roots as well as showing the ups and downs involved in doing a PhD. The shapes represent the fact I was investigating different shaped nanoparticles in my research, hence the inspiration to use the Cubism style.

Publisher: Gildeprint, Enschede, The Netherlands

Copyright © 2014 by Shilpa Agarwal

All rights reserved. No part of this book may be reproduced or transmitted in any form, or by any means, including, but not limited to electronic, mechanical, photocopying, recording, or otherwise, without the prior permission of the author.

ISBN: 978-90-365-3641-7

Author’s email: [shilpa.agarwalicb@gmail.com](mailto:shilpa.agarwalicb@gmail.com)

**SURFACE CHEMISTRY OF TAILORED CERIA  
NANOPARTICLES:  
*INTERACTION WITH CO AND H<sub>2</sub>O***

DISSERTATION

to obtain  
the degree of doctor at the University of Twente,  
on the authority of the rector magnificus,  
Prof. dr. H. Brinksma,  
on account of the decision of the graduation committee,  
to be publicly defended  
on Thursday 3<sup>rd</sup> April 2014 at 12:45

by

**Shilpa Agarwal**

born on 8<sup>th</sup> February 1985  
in Delhi, India

This thesis has been approved by:

**Prof. dr. ir. L. Lefferts** (promoter)

&

**Dr. B. L. Mojet** (co-promoter)

मेरी माँ के लिए  
(Dedicated to my mamma)



*“First they ignore you, then they ridicule you,  
then they fight you, and then you win.”*

– Mahatma Gandhi



# Contents

<b>Summary</b>	<b>1</b>
<b>Samenvatting</b>	<b>5</b>
<b>1 General introduction</b>	<b>9</b>
1.1 Introduction	10
1.2 Cerium oxide (ceria)	10
1.2.1 Structural properties and defect chemistry of ceria	11
1.2.2 Applications	13
1.2.3 Low index surfaces of ceria	19
1.2.4 Ceria nanoshapes	20
1.3 Scope and outline of thesis	25
Bibliography	27
<b>2 Revealing the exposed planes on ceria nanoshapes: The connection to water gas shift reactivity</b>	<b>33</b>
2.1 Introduction	34
2.2 Experimental section	36
2.2.1 Catalyst preparation	36
2.2.2 HRSEM, BET and XRD characterization	37
2.2.3 AC-TEM and STEM measurements	37
2.2.4 FTIR spectroscopy	37
2.2.5 WGS catalytic activity testing	38
2.3 Results and discussion	39
2.3.1 Octahedra	40
2.3.2 Rods	44
2.3.3 Cubes	46
2.3.4 WGS reactivity measurements	47
2.3.5 FTIR spectroscopy	49
2.4 Conclusions	53
Appendix 2	54
Bibliography	58
<b>3 Ceria nanocatalysts: Shape dependent reactivity and formation of hydroxyl groups</b>	<b>61</b>
3.1 Introduction	62
3.2 Experimental section	63
3.2.1 Catalyst preparation	63

3.2.2	TEM, BET and XRD characterization . . . . .	64
3.2.3	Raman and FTIR spectroscopy . . . . .	64
3.3	Results and discussion . . . . .	65
3.3.1	TEM and BET . . . . .	65
3.3.2	XRD and Raman . . . . .	65
3.3.3	FTIR in helium at 200°C . . . . .	68
3.3.4	CO adsorption and reactivity with water . . . . .	70
3.4	General discussion . . . . .	77
3.5	Conclusions . . . . .	80
	Appendix 3 . . . . .	81
	Bibliography . . . . .	82
<b>4</b>	<b>Defect chemistry of ceria nanorods</b>	<b>85</b>
4.1	Introduction . . . . .	86
4.2	Experimental section . . . . .	87
4.2.1	Sample preparation, TEM and BET characterization . . . . .	87
4.2.2	UV Raman spectroscopy . . . . .	88
4.2.3	FTIR spectroscopy . . . . .	89
4.2.4	Experimental sequence . . . . .	89
4.2.5	Data analysis . . . . .	90
4.3	Results and discussion . . . . .	90
4.3.1	<i>In situ</i> Raman and FTIR in helium at room temperature (RT) . . . . .	90
4.3.2	<i>In situ</i> Raman and FTIR in helium at 200°C and 350°C . . . . .	92
4.3.3	<i>In situ</i> Raman at 200°C: CO adsorption and H <sub>2</sub> O reactivity . . . . .	95
4.3.4	<i>In situ</i> Raman at 350°C: CO adsorption and H <sub>2</sub> O reactivity . . . . .	97
4.3.5	<i>In situ</i> FTIR at 200°C: CO adsorption and H <sub>2</sub> O reactivity . . . . .	99
4.3.6	<i>In situ</i> FTIR at 350°C: CO adsorption and H <sub>2</sub> O reactivity . . . . .	100
4.4	General discussion . . . . .	102
4.4.1	Ceria rods defect chemistry at 200°C . . . . .	102
4.4.2	Ceria rods defect chemistry at 350°C . . . . .	103
4.5	Conclusions . . . . .	105
	Appendix 4 . . . . .	107
	Bibliography . . . . .	118
<b>5</b>	<b>Defect chemistry of ceria nanoparticles as a function of exposed planes</b>	<b>121</b>
5.1	Introduction . . . . .	122
5.2	Experimental section . . . . .	124
5.2.1	Sample preparation and initial characterization . . . . .	124
5.2.2	<i>In situ</i> Raman spectroscopy . . . . .	124
5.2.3	<i>In situ</i> FTIR spectroscopy . . . . .	125

5.2.4	Experimental procedure . . . . .	125
5.2.5	Data analysis . . . . .	126
5.3	Results and discussion . . . . .	126
5.3.1	<i>In situ</i> Raman: CO adsorption and reactivity with water . . . . .	129
5.3.2	<i>In situ</i> FTIR: CO and H <sub>2</sub> O adsorption . . . . .	131
5.3.3	<i>In situ</i> FTIR: CO adsorption on Ce <sup>4+</sup> and Ce <sup>3+</sup> . . . . .	134
5.4	General discussion . . . . .	136
5.5	Conclusions . . . . .	140
	Appendix 5 . . . . .	141
	Bibliography . . . . .	151
<b>6</b>	<b>Conclusions and outlook</b>	<b>155</b>
6.1	Conclusions . . . . .	156
6.2	General recommendations . . . . .	159
6.2.1	Wire vs. rod . . . . .	159
6.2.2	Bridged hydroxyls on ceria nanoshapes at 200°C . . . . .	160
6.2.3	Cubes with high surface area . . . . .	160
6.2.4	Role of vacancy clusters in ceria nanoshape catalysis . . . . .	160
6.2.5	Ceria nanoshapes with metal loading . . . . .	161
	Appendix 6 . . . . .	162
	Bibliography . . . . .	163
	<b>Scientific contributions</b>	<b>164</b>
	<b>Acknowledgements</b>	<b>167</b>

## CONTENTS

# Summary

Steam reforming of bio-oil combined with the gasification of coke deposits in the presence of water is a conceptually promising alternative to generate hydrogen gas.  $\text{H}_2\text{O}$  can be activated in the gasification stage to form hydroxyl groups (OH) on oxide-supported (like ceria) metal catalysts, which increases both the  $\text{H}_2$  yield and the catalyst's lifetime. The reactivity for the water dissociation as well as the reactivity of resulting hydroxyl groups can be further improved by altering the shape and size of ceria support. Based on the recent studies, ceria nanoshapes exhibit excellent redox properties and high specific activity/selectivity in comparison to the bulk ceria particles. However, the knowledge related to the surface species actually responsible for enhanced catalytic activity of ceria nanocatalysts so far remain lacking. The work presented in this thesis highlights the fundamental aspects of ceria nanoshapes, with emphasis on the effects of surface planes on overall catalytic performance. The main objectives of this work are to investigate the true exposed facets, as well as to understand the reactivity of hydroxyl species and the role of defects on the ceria nanoshapes.

In the first part of this thesis (chapter 2), definitive information on the nature of the exposed surfaces in these  $\text{CeO}_2$  nanoshapes is provided using aberration-corrected transmission electron microscopy (AC-TEM) and high-angle annular dark field imaging (HAADF). Prior to the present work, discrepancies in literature existed related to the exposed planes on these ceria nanoshapes. For instance, it was the common belief that rods showed enhanced activity due to the exposure of active  $\{110\}$  and  $\{100\}$  planes. These findings were reported prior to the recent advancements in TEM (of AC and HAADF), and thus the results were unclear. Furthermore, our initial FTIR results suggested that ceria rods and octahedra share similarity in terms of exposed planes. This spurred us to re-examine rods with up-to-date TEM equipment. From the AC-TEM results it is apparent that ceria octahedra and rods both expose  $\{111\}$  surfaces, whereas ceria cubes mainly expose  $\{100\}$  surfaces.

Additionally,  $\text{H}_2$ -reduced ceria nanoshapes were examined for water gas shift (WGS) reaction to evaluate the structure-performance relationship. It is observed that the WGS activity normalized with surface area ( $\text{m}^2$ ) was identical for ceria oc-

tahedra and rods, whereas ceria cubes were found to be much more active. Further, to understand the interaction of surface species with CO during WGS catalytic reaction, H<sub>2</sub>-reduced ceria nanoshapes were analyzed using FTIR spectroscopy at 350°C. Similar to WGS results, the FTIR spectra specifically, the hydroxyl (OH) vibration bands and their interaction with CO, for rods and octahedra were observed to be the same. On the other hand, cubes with {100} planes exhibited different relative amount of the surface OH species and their interaction with CO resulted in different spectral features in comparison to rods and octahedra. It is clearly demonstrated in present work that the nature of the exposed surfaces affects the WGS activity as well as interaction of surface sites with CO. Due to the presence of the same {111} exposed planes, ceria rods and octahedra show similar WGS activity, as well as similar interaction of OH species with CO obtained using FTIR spectroscopy. Interestingly, cubes with more active {100} surface planes have different OH bands and interactions with CO, resulting in a higher WGS activity per m<sup>2</sup>.

It is known that the hydroxyl species are the active sites in CeO<sub>2</sub> supported catalytic reactions such as WGS, and steric constraint can lead to different amounts of hydroxyl species on different exposed planes. In the second part of this thesis (chapter 3), the role of different types of active hydroxyl (OH) species on the nanoshapes (wires, octahedra and cubes) and their respective reactivity towards CO and extent of regeneration of OH species with water has been investigated using in situ FTIR spectroscopy at 200°C. All three ceria nanoshapes showed similar OH stretching bands although with different relative intensities. Likewise rods, wires resemble octahedra in the hydroxyl range of FTIR spectra. The bridged hydroxyl species (OH<sup>3641</sup>) on ceria wires and cubes were found to be reactive towards CO, whilst only limited interaction with CO was observed for octahedra. In addition, the formation of hydrogen carbonates was observed only in case of octahedra and the relative amount of defects detected follows the trend: Wires > cubes > octahedra. Based on all these observations, it is suggested that both the presence of defects as well as the shape of ceria nanoparticles influences the interaction of specific hydroxyl groups with CO. Finally, subsequent exposure to water vapor at 200°C showed a clear shape dependent water activation to OH species, resulting in removal of different relative amounts of formates and carbonates formed in either

ambient or CO.

It is well known in the literature that the presence of intrinsic defects, as well as the ease of formation of defects during the reaction, strongly influences the ceria-catalyzed reactions. To understand the involvement of defects in ceria rods during the formation of specific formate and carbonate surface species at 200 and 350°C is investigated using a combination of *in situ* Raman and FTIR spectroscopies (chapter 4). It was observed at 200°C that the majority of formates and carbonates formed in CO do not form vacancies in the ceria lattice, whilst at 350°C formation of both formates and carbonates (mono/bi-dentate) result in the creation of vacancies. In addition, formation of stable polydentate carbonates was observed at 350°C. These polydentate carbonates were stable in water vapor as well as not forming vacancies in the ceria lattice. It must be noted that based on temperature the Raman signatures of the defect peaks arising in CO were very similar. However, their chemical origin seems to be different since at 350°C the addition of H<sub>2</sub>O is needed to remove the vacancies, while at 200°C the majority disappeared already in He flowed immediately after CO flow. In the present work, it is also proposed that apart from the reported defects, such as anion Frenkel pair and oxygen vacancies, other CO-induced defects, e.g., vacancy clusters, interstitial and Schottky disorder might also form in the ceria lattice. Further theoretical studies are highly recommended for specific defect identification and corresponding peak assignment in the Raman spectra.

Finally, in the last part of the thesis, the defect chemistry of reduced ceria nano-shapes during the interaction with CO and H<sub>2</sub>O is extensively discussed as a function of exposed plane (chapter 5). The defect chemistries of both rods and octahedra (with {111} plane) as a function of gas environment were similar. Specifically, the CO-induced defects for rods and octahedra were found to be the same, while the defect formation in CO (i.e., the {100} plane) for cubes was fundamentally different. For instance, in cubes the oxygen vacancy ( $O_{vac}$ ) defects were formed in CO at the expense of existing anion Frenkel pair defects ( $I_D$ ), whereas in case of other two nanoshapes both defects ( $O_{vac}$  and  $I_D$ ) were formed irrespective of existing  $I_D$  defects. These Raman findings are further supported by FTIR results that confirm that H<sub>2</sub>-pretreated rods and octahedra can be further reduced in CO, simultaneously creating bare cerium ions and forming new defects ( $O_{vac}$  and  $I_D$ ).

## SUMMARY

In contrast to rods and octahedra, H<sub>2</sub>-pretreated cubes are not further reducible in CO and hence undergo structural/vacancy rearrangement to further react with CO. These observations confirm that the defect chemistry on ceria nanoshapes is directly dependent on the surface terminations.

From this work it is clear that the ceria cubes show higher catalytic activity (per m<sup>2</sup>) than rods and octahedra. This is attributed to the different exposed planes, which give rise to different defect-formation mechanisms, different relative amount and reactivity of hydroxyl species.

# Samenvatting

Steam reforming van bio-olie in combinatie met de vergassing van cokesafzettingen in aanwezigheid van water is een conceptueel veelbelovend alternatief om waterstofgas te produceren.  $\text{H}_2\text{O}$  kan in de vergassingsstap worden geactiveerd om hydroxylgroepen (OH) te vormen op oxide-gedragen (zoals bv. ceriumoxide) metaal katalysatoren, wat zowel de  $\text{H}_2$  opbrengst als de levensduur van de katalysator verhoogt. De reactiviteit van het ontleden van water en de reactiviteit van de resulterende hydroxylgroepen kunnen verder worden verbeterd door de vorm en grootte van de ceriumoxide drager te veranderen. Gebaseerd op recent onderzoek laten ceriumoxide nanokristallen excellente redox eigenschappen en zeer specifieke activiteit/selectiviteit zien in vergelijking met bulk ceriumoxide deeltjes. Echter, de kennis van de oppervlakte groep die verantwoordelijk is voor de verbeterde katalytische activiteit van de ceriumoxide nanokatalysatoren is tot op heden zeer beperkt. Het werk dat in deze thesis wordt gepresenteerd belicht de fundamentele aspecten van ceriumoxidenanokristallen, met een sterke nadruk op de rol van het oppervlak. De hoofddoelstellingen van dit werk zijn het onderzoeken van de werkelijk blootgestelde facetten, alsmede het begrijpen van de reactiviteit van verschillende hydroxylgroepen en de rol van defecten op de ceriumoxide nanokristallen.

In het eerste deel van deze thesis (hoofdstuk 2), wordt relevante informatie over de aard van de blootgestelde oppervlakken in deze  $\text{CeO}_2$  nanovormen verkregen, gebruikmakend van aberratie gecorrigeerde transmission electron microscopy (AC-TEM) en high-angle annular dark field imaging (HAADF). Voor het huidige werk bestonden er tegenstrijdigheden in de literatuur met betrekking tot de blootgestelde oppervlakken van deze ceriumoxide nanokristallen. Er werd bijvoorbeeld in het algemeen aangenomen dat staven een verhoogde activiteit laten zien ten gevolge van de blootstelling van de actieve  $\{110\}$  en  $\{100\}$  oppervlakken. Deze bevindingen werden gerapporteerd vr de huidige ontwikkelingen in TEM (van AC en HAADF), en dus waren de resultaten onduidelijk. Bovendien suggereerden onze initiele FTIR resultaten dat ceriumoxide staven en octahedra overeenkomsten laten zien met betrekking tot de blootgestelde oppervlakken. Dit spoorde ons aan om de staven opnieuw te onderzoeken met up-to-date TEM apparatuur. Uit de AC-

TEM resultaten blijkt dat ceriumoxide octahedra en staven beide getermineerd zijn met  $\{111\}$  oppervlakken, terwijl de ceriumoxide kubussen vooral een  $\{100\}$  terminatie hebben.

Bovendien werden  $H_2$ -gereduceerde ceriumoxide nanokristallen onderzocht op de water gas shift (WGS) reactie, om de structuur-prestatie relatie te evalueren. We vonden dat de WGS activiteit, wanneer genormaliseerd per oppervlakte-eenheid ( $m^2$ ), identiek was voor ceriumoxide octahedra en staven, terwijl ceriumoxide kubussen veel actiever bleken te zijn. Verder werden  $H_2$ -gereduceerde ceriumoxide nanokristallen geanalyseerd, met FTIR spectroscopie bij  $350^\circ C$ , om de interactie van verschillende oppervlakken met CO tijdens de WGS katalytische reactie te begrijpen. Net als de WGS resultaten, bleek uit de observaties van de FTIR spectra, dat hydroxyl (OH) vibratiebanden en hun interactie met CO, van zowel staven als octahedra er precies hetzelfde uitzien. Aan de andere kant vertoonden kubussen getermineerd met  $\{100\}$  vlakken een andere relatieve hoeveelheid van de oppervlakte OH soort en de interacties met CO resulteerden in andere spectrale kenmerken in vergelijking met staven en octahedra. In het huidige onderzoek wordt duidelijk aangetoond dat de aard van de blootgestelde oppervlakken zowel de WGS activiteit alsook de interactie van de oppervlakteplaatsen met CO beïnvloedt. Vanwege de aanwezigheid van dezelfde  $\{111\}$  blootgestelde oppervlakken laten ceriumoxide staven en octahedra een vergelijkbare WGS activiteit zien, evenals een vergelijkbare interactie van OH soorten met CO, zoals gemeten met FTIR spectroscopie. Interessant is dat kubussen met meer actieve  $\{100\}$  oppervlakken andere OH banden en interacties met CO hebben, wat resulteert in een hogere WGS activiteit per  $m^2$ .

Het is bekend dat de hydroxyl soorten de actieve plaatsen zijn in  $CeO_2$  gedragen katalytische reacties zoals WGS en sterische hindering kan leiden tot verschillende hoeveelheden hydroxyl groepen op verschillende blootgestelde oppervlakken. In het tweede deel van deze thesis (hoofdstuk 3), wordt de rol van verschillende types actieve hydroxyl (OH) groepen op de nanokristallen (draden, octahedra en kubussen) en hun respectievelijke reactiviteit voor CO en omvang van regeneratie van OH groepen met water bestudeerd, waarbij FTIR spectroscopie wordt gebruikt bij  $200^\circ C$ . Alle drie de ceriumoxide nanokristallen lieten gelijksoortige OH stretching banden zien, maar wel met verschillende relatieve intensiteiten.

Op dezelfde manier lijken staven en draden op octahedra in het hydroxylgebied van FTIR spectra. De brughydroxyl groep ( $\text{OH}^{3641}$ ) op ceriumoxide draden en kubussen werden reactief bevonden voor CO, terwijl alleen een gelimiteerde interactie met CO werd geobserveerd voor octahedra. Bovendien werd de formatie van waterstofcarbonaten alleen gevonden voor octahedra. De relatieve hoeveelheid gedetecteerde defecten volgt de trend: draden > kubussen > octahedra. Gebaseerd op deze observaties wordt voorgesteld dat zowel de aanwezigheid van defecten als de vorm van ceriumoxide nanodeeltjes invloed hebben op de interactie van specifieke hydroxylgroepen met CO. Tenslotte laat daaropvolgende blootstelling aan waterdamp bij 200°C een duidelijke vorm van afhankelijke wateractivatie met betrekking tot de OH groepen zien, wat resulteert in de verwijdering van verschillende relatieve hoeveelheden van formaten en carbonaten die gevormd worden in omgevings of CO atmosfeer.

Het is algemeen bekend dat de aanwezigheid van intrinsieke defecten, evenals het gemak waarmee defecten vormen tijdens de reactie, een sterke invloed heeft op ceriumoxide gekatalyseerde reacties. Om dit te begrijpen, wordt de betrokkenheid van defecten in ceriumoxide staven bij de formatie van specifieke formaten en carbonaat oppervlakken bij 200°C en 350°C bestudeerd middels een combinatie van *in situ* Raman en FTIR spectroscopieën (hoofdstuk 4). Bij 200°C werd geobserveerd dat de meerderheid van de formaten en carbonaten die gevormd worden in CO, geen vacatures vormen in het ceriumoxide rooster, terwijl bij 350°C de formatie van zowel formaten als carbonaten (mono/bidentate) resulteren in de productie van vacatures. Daarnaast werd de formatie van stabiele polydentaatcarbonaten gevonden bij 350°C. Deze polydentaatcarbonaten waren stabiel in waterdamp en vormden geen vacatures in het ceriumoxide rooster. Hierbij moet worden opgemerkt dat, gebaseerd op de temperatuur, de Raman signaturen van de pieken van de defecten die verschenen in CO zeer vergelijkbaar waren. Echter hun chemische oorsprong lijkt verschillend omdat bij 350°C de toevoeging van  $\text{H}_2\text{O}$  nodig is om de vacatures te verwijderen, terwijl bij 200°C de meerderheid al verdwenen is in de He flow die meteen na de CO productie wordt toegevoerd. In het huidige werk wordt ook voorgesteld dat behalve de gerapporteerde defecten, zoals anion Frenkel paar en zuurstof vacatures, andere CO-geïnduceerde defecten, i.e. vacature clusters, interstitiële en Schottky wanorde ook gevormd zouden kunnen worden in het

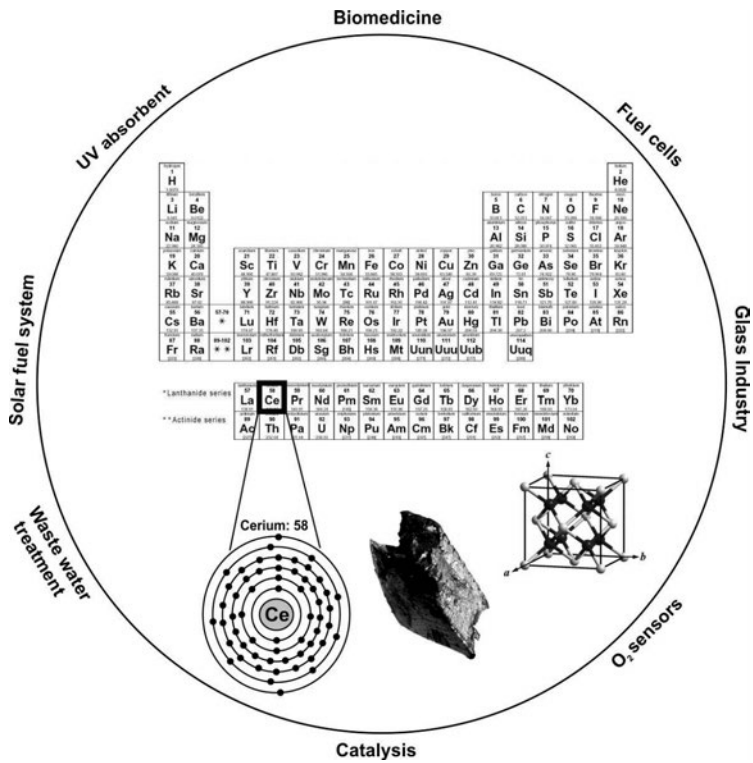
ceriumoxide rooster. Verdere theoretische studies worden ten sterkste aangeraden voor de identificatie van specifieke defecten en de bijbehorende piek toekenningen in Raman spectra.

Ten slotte, in het laatste deel van de thesis, wordt de defectchemie van gereduceerde ceriumoxide nanokristallen tijdens de interactie met CO en H<sub>2</sub>O uitgebreid besproken als functie van de blootgestelde oppervlakken (hoofdstuk 5). De defectchemie van zowel staven als octahedra (met {111} vlakken) als functie van de gasomgeving waren vergelijkbaar. In het bijzonder de CO geïnduceerde defecten voor staven en octahedra zijn zeer vergelijkbaar, terwijl de defectformatie in CO (i.e. de {100} vlakken) voor kubussen fundamenteel anders was. Bijvoorbeeld de zuurstofvacature ( $O_{vac}$ ) in kubussen wordt gevormd in CO ten koste van bestaande anion Frenkel paar defecten ( $I_D$ ), terwijl in het geval van de andere twee nanokristallen beide defecten ( $O_{vac}$  en  $I_D$ ) werden gevormd, ongeacht de bestaande  $I_D$  defecten. Deze Raman bevindingen worden verder ondersteund door FTIR resultaten die bevestigen dat H<sub>2</sub>-behandelde staven en octahedra verder kunnen worden gereduceerd in CO omgeving, waarbij gelijktijdig onbedekte ceriumionen en nieuwe defecten ( $O_{vac}$  en  $I_D$ ) ontstaan. In tegenstelling tot staven en octahedra, zijn H<sub>2</sub>-behandelde kubussen niet verder reduceerbaar in CO en daarom ondergaan deze structurele/vacature herschikking om verder te reageren met CO. Deze observaties bevestigen dat defectchemie op ceriumoxide nanokristallen direct afhankelijk is van de oppervlakte terminatie.

Uit dit onderzoek blijkt duidelijk dat ceriumoxide kubussen een hogere katalytische activiteit (per m<sup>2</sup>) hebben dan staven en octahedra. Dit wordt toegeschreven aan de verschillende blootgestelde oppervlakken, welke leiden tot verschillende defectformatie mechanismes, verschillende relatieve hoeveelheid en reactiviteit van hydroxylgroepen.

# 1

## General introduction



## Abstract

*This introductory chapter gives an overview of the structure, properties and applicability of cerium oxide. Emphasis is put on the recent technological advancements to synthesize these materials into nanoshapes. The knowledge reported so far related to ceria nanoshapes is discussed. At the end of the chapter the scope of this thesis is presented.*

## 1.1 Introduction

Chemical processes form an integral part of our modern lifestyles - from manufacturing pharmaceuticals and processed food, cleaning polluted air/water, making paper and plastic materials, refining metal and fuel for transport purposes, etc. The chemical industry is one of the largest industrial sectors of the global economy.[1] 90% of all commercially produced chemical products benefit from a catalytic material that is responsible for enhancing the reaction rate and selectively generating the desired product.[2]

Metal oxide catalysts with high catalytic activity and relatively low costs are heavily exploited for the production of renewable energy, remediation of environmental pollutants and synthesis of chemicals.[3–5] The role of oxides in the field of catalysis has evolved from being simple inert catalyst supports to engineered catalysts with distinct shapes and compositions tailored for achieving optimum selectivity and activity in a chemical reaction.[5–7]

## 1.2 Cerium oxide (ceria)

Rare-earth oxides have been widely used as structural and electronic promoters to improve activity, selectivity and thermal stability of catalysts.[4] Cerium is the most abundant rare-earth metal in the Earth's crust (approx. 66.5 ppm) and is more abundant than copper, cobalt and lithium.[8] The main sources of cerium are the light rare earth element (LREE) minerals such as, bastnäsite, allanite, cerite and monazite.[9, 10] Cerium oxide (commonly known as ceria,  $\text{CeO}_2$ ) is one of the most significant and applied rare earth oxides in industrial catalysis.[8, 11]

## 1.2. CERIUM OXIDE (CERIA)

### 1.2.1 Structural properties and defect chemistry of ceria

Cerium oxide ( $\text{CeO}_2$ ) has a cubic fluorite structure with space group  $\text{Fm}\bar{3}\text{m}$  and a cell parameter of  $5.41 \text{ \AA}$  at room temperature.[12] The  $\text{CeO}_2$  structure (figure 1.1) consists of a cubic close-packed array with each cerium ion (white circles) coordinated by eight oxygen ions (grey circles), and, vice versa, each oxygen ion is surrounded by four cerium ions in a crystal unit.[13]

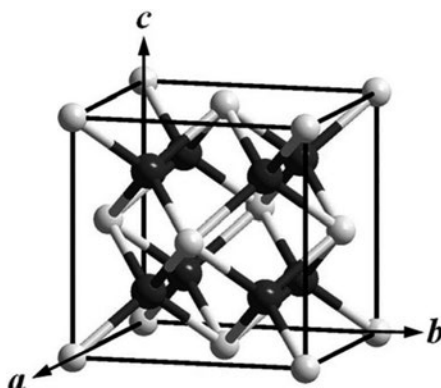


**Figure 1.1:** Fluorite structure of ceria. Oxygen ions are the dark grey circles and cerium ions are the white circles.[14]

The importance of  $\text{CeO}_2$  originates from its unique redox properties and high oxygen storage capacity (OSC), allowing to switch between  $\text{Ce}^{4+}$  and  $\text{Ce}^{3+}$  in a stable fluorite structure. In other words,  $\text{CeO}_2$  can undergo substantial oxygen stoichiometric changes in response to change in temperature, oxygen pressure, electric field and presence of dopants, without undergoing a change in the fluorite crystal structure.[15–22] The transport of oxygen in the ceria lattice results in the creation of intrinsic point defects.[12] These point defects can be created either by thermal disorder or by interaction with the surrounding atmosphere. The predominant defects observed in reduced ceria are anion Frenkel pairs and anion vacancies (figure 1.2).[12, 23]

In the *anion Frenkel* type defect, an oxygen ion is displaced from its lattice position to an interstitial position, hence creating a vacancy at its original position and a defect at the interstitial site.[23–25] In general, the formation of these defects does not influence the overall charge and stoichiometry of the lattice. The defect

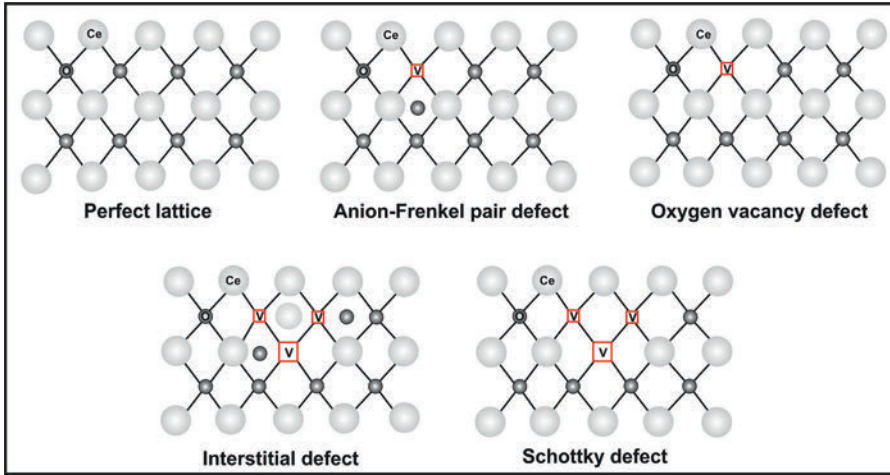


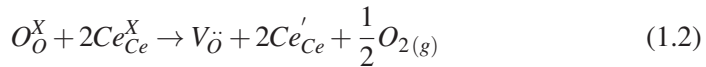
**Figure 1.2:** Possible types of point defects in the  $\text{CeO}_2$  lattice. Key: Oxygen - dark grey circles; cerium - white circles; vacant sites - red squares with “V”.

type is illustrated using the Kröger and Vink defect notation as



where,  $O_O^X$  and  $O_i''$  represent oxygen ions in the lattice and interstitial positions respectively and  $V_O$  indicates an oxygen vacancy created at a lattice site.

In the *oxygen vacancy* defect, an oxygen ion is removed from one of the lattice positions, hence creating a vacant site. [26–28] In order to maintain the charge balance in the lattice, two Ce(IV) ions reduce to Ce(III) ions. The defect formation is represented by the following equation:

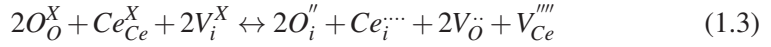


$Ce_{Ce}^X$  indicates a cerium ion in its lattice position and  $Ce'_{Ce}$  denotes the reduction of cerium from Ce(IV) to Ce(III).

In the past years, several studies based on energy calculations have also suggested the presence of additional defects in the ceria lattice, such as interstitial and Schottky disorder.[12, 24, 25] An *interstitial defect* is the displacement of both a

## 1.2. CERIUM OXIDE (CERIA)

cerium and two oxygen ions to form interstitial sites, e.g.



In the above equation,  $O_i''$  and  $Ce_i'''$  indicate oxygen and cerium ions in their respective interstitial sites and  $V_i^X$  and  $V_{Ce}'''$  represent the vacant interstitial site and vacant site created at the cerium lattice position, respectively.

Finally, in the case of *Schottky disorder*, vacant sites are created by the removal of both the cations and anions from their lattice sites, whilst maintaining stoichiometry.[12, 25] The following equation illustrates the defect:



Due to the unique oxygen transport properties and ability to accommodate large concentration of defects, ceria is an attractive material for processes that require a constant supply of oxygen in a reducing environment.

### 1.2.2 Applications

Because of its exceptional oxygen transport and defect creation properties, ceria finds use in a wide range of applications, such as:

#### **Solid oxide fuel cells (SOFC)**

Fuel cells are well recognized as a sustainable technology to convert chemical energy directly into electricity, with higher efficiencies than conventional thermal engines.[29] SOFC are a class of fuel cells characterized by the use of a solid oxide material as the electrolyte. The oxygen ions move from cathode to anode, thereby undergoing an electrochemical reaction with  $H_2$  at the anode (figure 1.3). Ceria is added to many SOFC anode formulations due to their higher oxygen ion conductivity and lower cost.[30]

#### **Solar fuel system**

For the production of syngas ( $H_2$  and  $CO$ ), the key components in the Fischer-Tropsch synthesis of transportation fuels, the solar fuel system is gaining recogni-

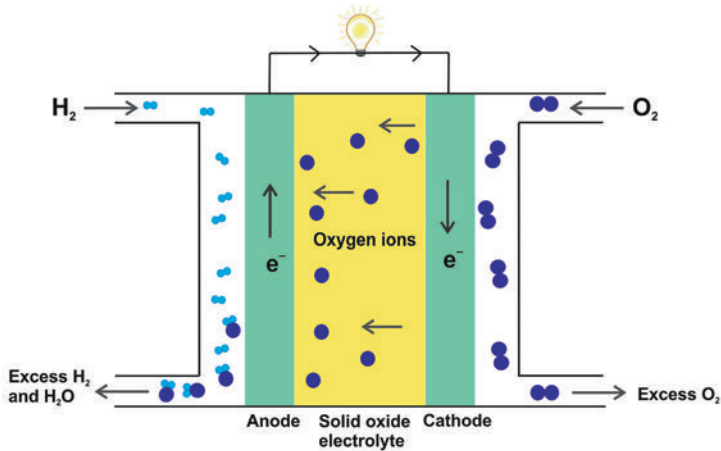


**Figure 1.3:** Schematic drawing of a solid oxide fuel cell.

tion. Syngas can be obtained by splitting  $\text{H}_2\text{O}$  and  $\text{CO}_2$  via solar-driven thermochemical cycles using metal oxide redox reactions. Due to the reduction/oxidation properties, rapid oxygen diffusion kinetics, morphological stability and high catalytic activity, ceria-based materials have emerged as a potential candidate for solar fuel systems.[31, 32] See figure 1.4 for the conceptual ceria based solar system.

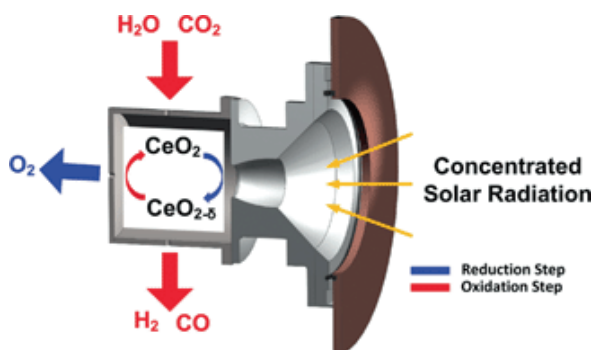


**Figure 1.4:** Schematic of the two-step ceria based solar fuel system.[33]

## 1.2. CERIUM OXIDE (CERIA)

### Biomedicine

The ability of ceria to switch between  $Ce^{4+}$  and  $Ce^{3+}$  is easily comparable to that of biological antioxidants, hence making ceria attractive for biological applications. [34–36] Interestingly, brain cell cultures have shown enhanced lifespan on introduction of ceria nanoparticles in their environment by reversibly binding with free radical oxygen species (ROS). The ROS are identified as a component in medical diseases, including atherosclerosis, arthritis and neurodegenerative disorders such as Parkinson's and Alzheimer's.[37]

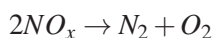
### Catalysis

Because of its distinctive redox properties, ceria can greatly enhance the catalytic activities for a number of important reactions when it is used as a support for transition metals.[38–41] Some of the key example include:

#### *Three-way catalysts (TWC)*

To limit harmful emissions, three-way catalysts are incorporated in petrol and diesel engines. The catalyst uses a ceramic or metallic substrate coated with metal oxides with combinations of precious metals like platinum, palladium and rhodium.[39, 42] A three-way catalytic converter has three simultaneous functions:

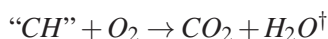
1. Reduction of nitrogen oxides into elemental nitrogen and oxygen.



2. Oxidation of carbon monoxide to carbon dioxide.



3. Oxidation of hydrocarbons into carbon dioxide and water.



---

<sup>†</sup>Unbalanced equation

$\text{CeO}_2$  is widely used as a promoter in three-way catalysts for treatment of toxic exhaust gases, to remove soot from exhaust gases.[39] This application is attributed to the high OSC as well as high metal dispersion that can be easily achieved using ceria.

### *Preferential oxidation of CO*

High purity  $\text{H}_2$  gas is essential for fuel cell applications requiring a proton exchange membrane as electrolyte (PEMFC, proton exchange membrane fuel cell). [43–46] In PEMFC, the hydrogen is ionized to a proton, generating an electron at the anode. The proton migrates through the polymer membrane to the cathode and further reacts with  $\text{O}_2$  to form  $\text{H}_2\text{O}$  (figure 1.5).

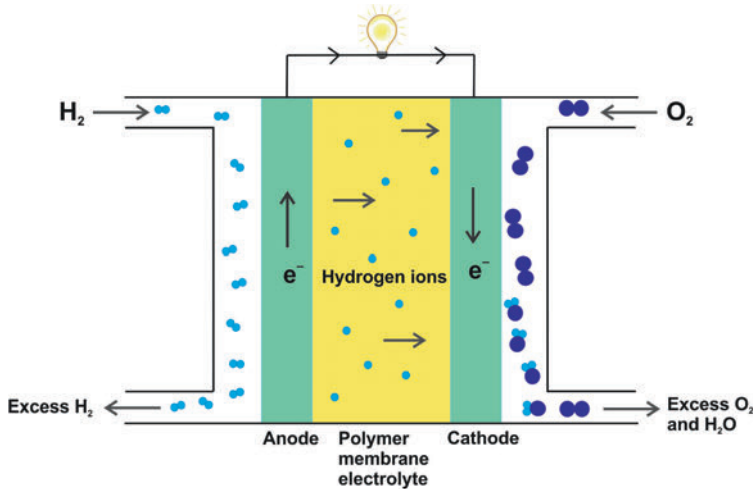


**Figure 1.5:** Schematic drawing of proton exchange membrane fuel cell.

The CO content in the reactant gas (i.e.  $\text{H}_2$ ) must be kept below 100 ppm for proper operation.[46] Industrially, hydrogen can be produced by steam reforming, partial oxidation and auto-thermal reforming of hydrocarbons.[43, 47] However, during these reactions  $\text{CO}_x$  (i.e. CO,  $\text{CO}_2$ ) is also formed as a by-product. Notably, the CO content can be reduced to 0.5 – 1% by the reaction with steam (water gas shift reaction).[48] However, the remaining concentration of CO is still too high for use in PEMFC and should be further lowered ( $< 100$  ppm) by preferentially oxidizing (PROX) CO on a suitable catalyst without excessive consumption of

## 1.2. CERIUM OXIDE (CERIA)

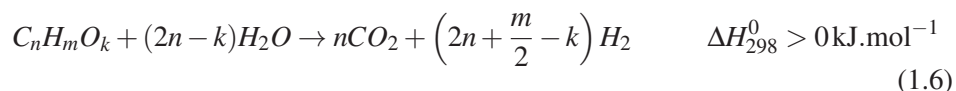
H<sub>2</sub>. [46]



Based on the high activity required to remove CO while maintaining a high CO oxidation selectivity and minimum oxidation of H<sub>2</sub>, desirable PROX catalysts generally comprise of metal (Pt, Rh, Pd, Au, etc.) supported on an oxide (ceria, alumina, silica). [49–51] So far, ceria-supported platinum (Pt), rhodium (Rh) and palladium (Pd) catalysts have been found to have remarkable activity in the low temperature oxidation of CO. [50] This can be attributed to the CeO<sub>2</sub> support that can promote oxidation even under an oxygen-deficient environment due to its high OSC. [45]

### *Steam reforming of bio-oil*

The continuous depletion of fossil fuels has necessitated the search for an efficient and environmentally acceptable way to generate hydrogen (H<sub>2</sub>) from sustainable resources. [52, 53] One of the promising alternatives is to generate hydrogen by steam reforming of bio-oil (obtained via flash pyrolysis of bio-mass), see figure 1.6.



Bio-oil is a complex mixture of oxygenates. Therefore a wide variety of model compounds such as carbon monoxide, methanol, ethanol, acetic acid, etc. are studied for designing and understanding the appropriate catalyst for steam reforming. [54] Transition metal oxides like CeO<sub>2</sub>, ZrO<sub>2</sub>, TiO<sub>2</sub> and mixed oxides with metal loading seem to be good catalyst supports for steam reforming because of their tunable oxidation states which render better stability and enhanced activity. [54–57]

### *Low temperature water gas shift reaction (LT-WGS)*

WGS is a reversible exothermic process to convert CO and H<sub>2</sub>O into H<sub>2</sub> and CO<sub>2</sub>. The WGS reaction is usually coupled with steam reforming of hydrocarbons to

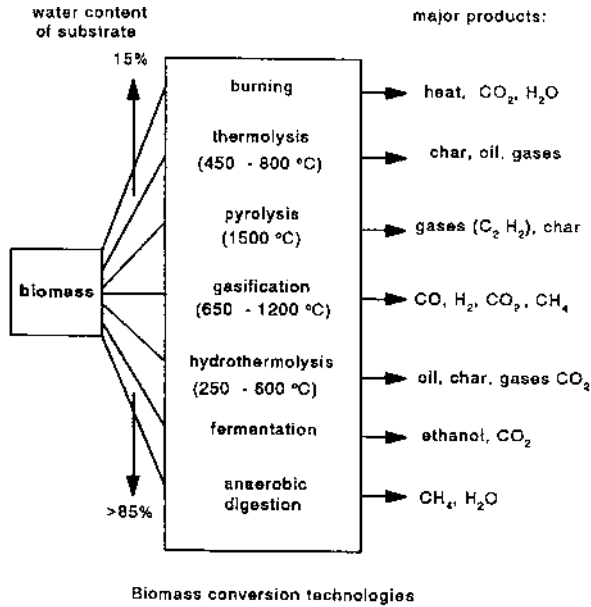
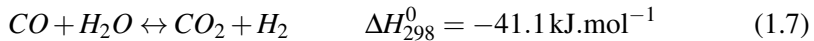


**Figure 1.6:** Schematic showing bio-mass conversion routes.[52]

maximize the  $H_2$  yield and decrease the amount of CO.[58]



The WGS reaction is exothermic, i.e., with an increase in temperature the reaction equilibrium shifts to the left. Therefore, to suppress thermodynamic limitations and attain higher CO conversions, the WGS reaction is carried out in two stages. In the first stage, a high-temperature shift (HTS) is performed at  $300 - 450^\circ\text{C}$ , followed by a low-temperature shift (LTS) reaction operated at  $180 - 230^\circ\text{C}$ . [59] Standard industrial catalysts for HTS and LTS stages are  $\text{Fe}_2\text{O}_3$  promoted with  $\text{Cr}_2\text{O}_3$  and Cu on  $\text{ZnO}/\text{Al}_2\text{O}_3$  respectively. [60–62]

These traditional catalysts are unsuitable for mobile use, such as in PEM fuel cells, since they are pyrophoric (reactive to  $\text{O}_2$ ) and require very careful engine start-up/shut-down procedures. [63] Alternative materials, such as ceria-supported metal catalysts, have received much attention as a new low temperature single step WGS catalyst. [62, 64, 65] It has been suggested, especially for Pt-supported catalysts that ceria support acts as a bi-functional catalyst in which CO is adsorbed

## 1.2. CERIUM OXIDE (CERIA)

on the metal sites and  $\text{H}_2\text{O}$  dissociation (to regenerate hydroxyl groups on ceria support) occurs on the defect sites (oxygen vacancies) leading to higher catalytic activity (figure 1.7).[38, 66]

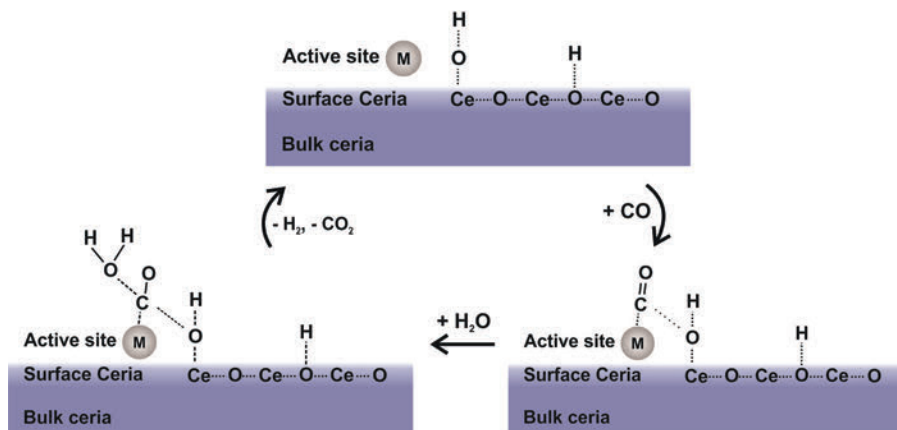


**Figure 1.7:** Low temperature water gas shift reaction pathway on hydroxylated  $\text{CeO}_2$  supported catalyst. “M” illustrates the active site of a metal particle.

### 1.2.3 Low index surfaces of ceria

Ceria particles with fluorite lattice (figure 1.1) preferentially expose the stable (111) planes.[67, 68] However, by reducing the particle size of ceria to nano-dimensions, contributions from the less stable (110) and (100) terminations have been reported.[8, 11, 17] The three index lattice planes on the surface of  $\text{CeO}_2$  nanocrystals are shown in figure 1.8.[3, 69]  $\text{CeO}_2$  (111) has an open structure with O in the top layer followed by an accessible Ce layer, whereas, on the (110) surface, both Ce and O atoms are in the top layer.[13] In the case of the ceria (100) plane, the surface layer is terminated by O and the Ce layer underneath is not accessible, making this surface polar and unstable.[13, 70] Different planes have different numbers of nearest bonded neighbors for Ce and O on the exposed surface. For instance, in the (111) plane Ce is bonded to 7 oxygen, with oxygen bonded to 3 cerium. For the (110) and (100) planes, the Ce:O coordination number on the exposed surface is 6:3 and 6:2 respectively.[3] This leads to the relative stability of the low index ceria surfaces following the trend: (111) > (110) > (100).[69, 71]

The non-polar  $\text{CeO}_2$  (111) surface undergoes little relaxation, whereas the other two planes can undergo significant lattice relaxations.[3, 69, 72] Furthermore, the formation energies of oxygen vacancies on different surface planes of ceria vary, following the order  $(110) < (100) < (111)$ .[73]

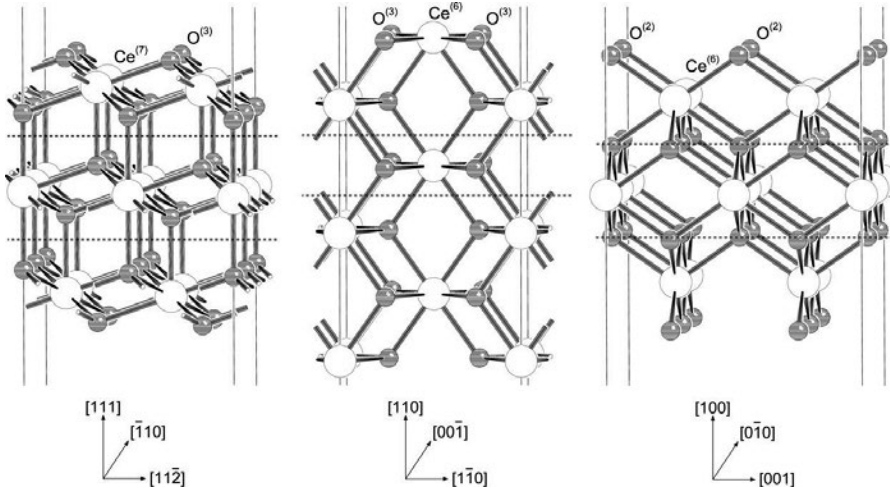


**Figure 1.8:**  $\text{CeO}_2$  (111), (110) and (100) surfaces. White and black circles represent cerium and oxygen ions respectively.[3]

With plane specificity in mind, several fundamental investigations have been performed on epitaxial ceria thin films in ultra high vacuum, such as adsorption of probe molecules like  $\text{CO}$ ,[74]  $\text{H}_2\text{O}$ ,[13, 75] acetone,[76] acetaldehyde,[77] formic acid,[78] etc., and even the WGS reaction.[79] From those studies, it is concluded that the (100) surface is more active in adsorbing and reacting with probe molecules than the (111) surface.[70] Furthermore, (100) planes are more susceptible to surface reconstruction and defect formation to relocate the surface charge in the lattice for attaining stability.[72] Whilst these plane-specific investigations give a glimpse of the fundamental surface-dependent behavior of  $\text{CeO}_2$ , the conditions (ultra high vacuum) are far from real catalytic conditions, so transfer of knowledge to more practical situations is not straightforward.

## 1.2. CERIUM OXIDE (CERIA)

### 1.2.4 Ceria nanoshapes

Based on the above, it can be concluded that ceria particles with low index surface planes and easy defect formation are desirable for catalytic applications. Nanostructured ceria can be synthesized using various approaches, such as precipitation, hydrothermal, sol-gel and surfactant-assisted (figure 1.9).[8, 11, 17, 80] The common cerium precursors used for synthesis include cerium(III) sulfate hydrate  $[\text{Ce}_2(\text{SO}_4)_3 \cdot x\text{H}_2\text{O}]$ , [81] cerium(III) nitrate hexahydrate  $[\text{Ce}(\text{NO}_3)_3 \cdot 6\text{H}_2\text{O}]$ , [82, 83] ammonium cerium nitrate  $[(\text{NH}_4)_2\text{Ce}(\text{NO}_3)_6]$  [84, 85] and cerium chloride ( $\text{CeCl}_3$ ). [86, 87] The new synthetic procedures developed in recent years have allowed synthesizing ceria into desirable nanoshapes with well-defined exposed planes. For instance, ceria nanoparticles usually have an octahedral shape, mainly exposing stable (111) facets.[88] Ceria cubes preferentially expose active (100) planes, whilst ceria rods are thought to expose (100) and (110) surfaces, which are less stable and thus more reactive than the (111) surface.[82, 83, 89] Compared with bulk ceria, these ceria nanoshapes exhibit excellent redox properties and high specific activity/selectivity due to the exposure of active surface planes, as well as having more defects and higher surface to volume ratio.[8, 11, 73]

Already some interesting activity trends have been identified for these ceria nanoshapes. For instance, ceria rods were reported to have the highest catalytic activity towards oxidation of CO (figure 1.10), [83, 89, 90] naphthalene, [91] 1,2-dichloroethane and ethyl acetate, in comparison to other nanoshapes (trend: Rods > cubes > octahedra). [92] This observation was related to the exposed planes on rods as well as surface defects such as vacancy clusters, pits and a high degree of surface roughness. In fact, it has been suggested that the activation and transportation of active oxygen species in ceria rods is greatly enhanced due to the presence of oxygen vacancy clusters. [93] In addition, these vacancy clusters cause exposure of  $\text{Ce}^{3+}$  ions, which provide effective sites for the adsorption of CO, as illustrated in figure 1.11. Hence, the existence of vacancy clusters, along with  $\text{Ce}^{3+}$  sites, positively affects the overall catalytic performance.

Furthermore, ceria cubes with (100) exposed planes have been reported to exhibit excellent reducibility and high OSC. [94] Recently, Désaunay *et al.* investigated hydrogen oxidation on ceria nanoshapes and reported the following reducibility trend: Cube > rod > octahedron, indicating that hydrogen oxidation is

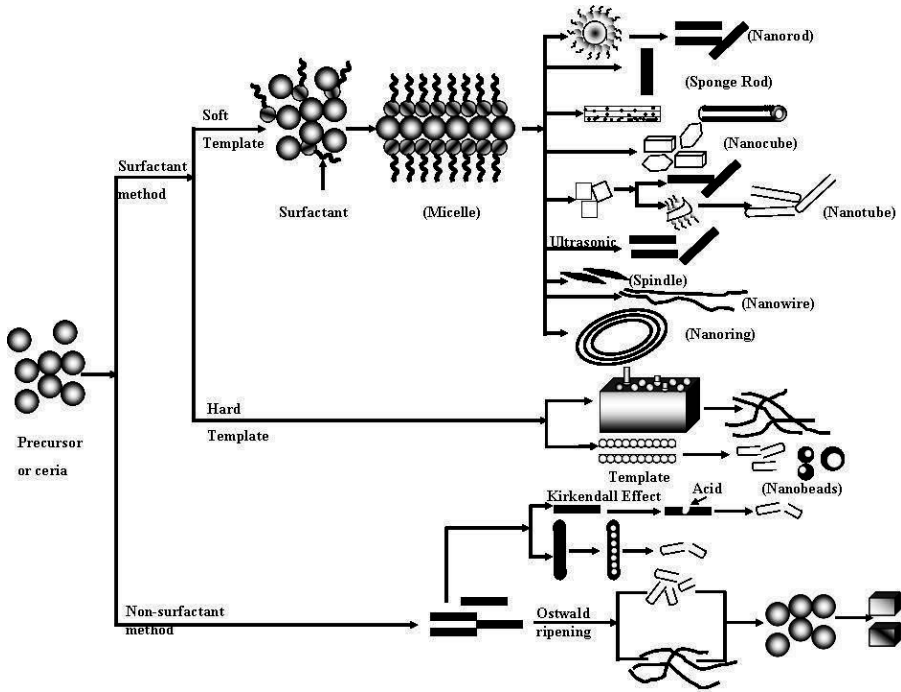


**Figure 1.9:** Synthesis pathways for the formation of CeO<sub>2</sub> in different shapes.[80]

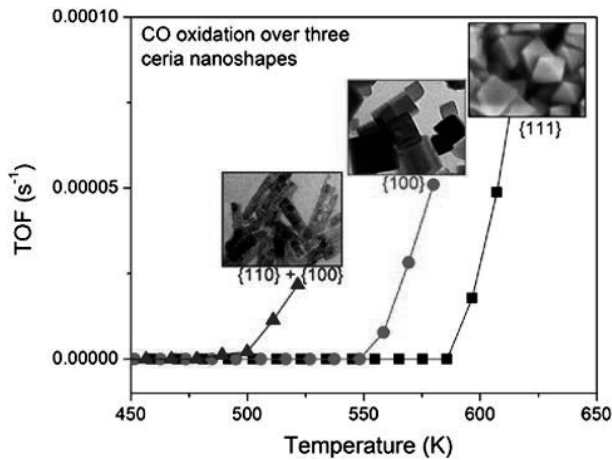


**Figure 1.10:** CO oxidation plots at 400°C on ceria rods, cubes, and octahedra. Insets in plot are TEM images of ceria rods, cubes and SEM image of octahedra.[90]

## 1.2. CERIUM OXIDE (CERIA)

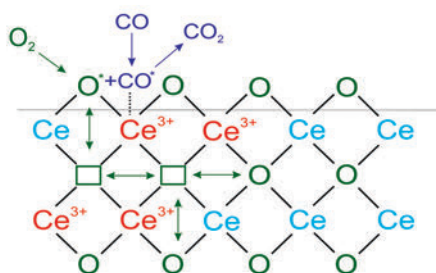


**Figure 1.11:** Catalytic pathway for CO oxidation on CeO<sub>2</sub> rods. Adapted from Reference[93]

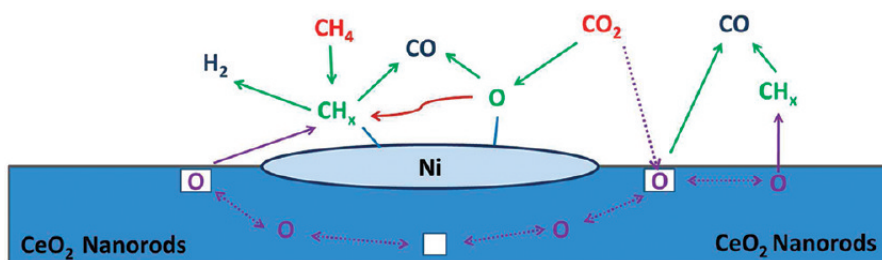


**Figure 1.12:** Catalytic mechanism for CO<sub>2</sub> reforming of methane over Ni-supported CeO<sub>2</sub> rod.[97]

dependent on the structure of the exposed ceria surfaces.[67]

As mentioned in the previous section, reactions such as WGS, CO oxidation, steam reforming, etc., widely use metal particles supported on cerium oxide. The performance of the catalyst is strongly influenced by the particle size, porosity, surface area and exposed planes of the support material.[11] These properties of support material not only influence the dispersion of metal particles but also affect the metal-support interactions. For instance, ceria rods have been found to strongly adhere to highly dispersed gold particles of size < 1 nm, whilst gold particles of size  $\approx$  3 nm have been almost exclusively formed on ceria cubes.[95] Similarly, in the case of the Ag/CeO<sub>2</sub> catalyst, CeO<sub>2</sub> rods have been shown to exhibit stronger Ag-CeO<sub>2</sub> interaction than ceria cubes.[96] Another example includes Ni supported on CeO<sub>2</sub> rods, an excellent catalytic activity and coke resistance has been reported during CO<sub>2</sub> reforming of methane (figure 1.12). The enhanced activity is attributed

to the increased bonding strength between the Ni metal particles with the ceria support, as well as an increase in the presence and transfer of lattice oxygen from the ceria support to metal particles.[97] Similar findings were also reported for Pt and Pd-loaded ceria nanoshapes.[98, 99]

Most of the literature on ceria nanoshapes is mainly dedicated to different synthesis routes followed by catalytic testing.[11, 83, 91–93, 96, 98, 100–102] In fact, it has only been in the last few years that some efforts have been made to understand the structure-performance of these ceria nanoshapes. For example, Wu *et al.* reported that the adsorption of surface dioxygen species varies with the defect sites on these nanocrystals.[73] The stability and reactivity of these oxygen species are also found to vary with the exposed planes on ceria nanoforms.

The adsorption and desorption of methanol was also investigated to probe the nature of surface sites on ceria nanoshapes with well-defined exposed planes.[103] Interestingly, on the surfaces of rods (exposing (110) and (100) planes) and cubes (with (100) planes), three types of methoxy ( $\text{CH}_3\text{O}$ ) species, i.e., on-top (I), bridging (II) and three-coordinate (III) were identified on exposure to methanol at room temperature, whilst exclusively on-top (I) types of methoxy groups were observed on the ceria octahedra surface (with (111) facets, figure 1.13). This difference is attributed to the different Ce/O coordination ratios as well as the number of defect sites on the three nanoshapes. Furthermore, the methoxy species are found to be less stable and hence more reactive on ceria rods, resulting in formation and desorption of  $\text{H}_2$  and CO at lower temperatures ( $< 310^\circ\text{C}$ ) than on cubes and octahedra.

The suggestion that the higher catalytic activity of rods is due to the exposed (100) and (110) planes was originally made in the seminal works of Zhou[83] and Mai.[82] Indeed the synthesis approach within those papers has become the standard recipe for the preparation of rods and cubes.[92, 101, 104–107] Furthermore, the conclusion from those papers that ceria rods have exposed (100) and (110) surfaces and grow along the [110] direction has been significantly relied on during the past eight years for furthering the field.[73, 90, 91, 93, 96, 98, 99, 101, 103, 105, 107–109] However, discrepancies in the literature do exist. More recently, it was suggested that ceria rods can also expose (111) surfaces as well as small amounts of (100) planes.[110–112] In addition, it was proposed that the origin

### 1.3. SCOPE AND OUTLINE OF THESIS

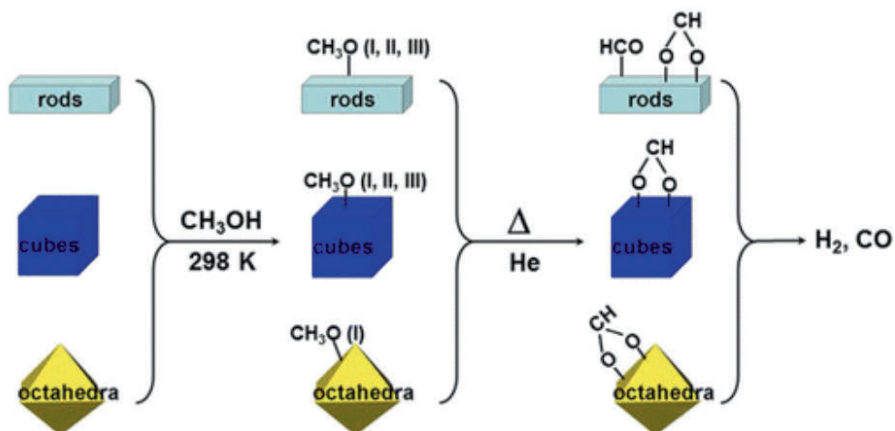


**Figure 1.13:** Schematic overview of adsorption and desorption of methanol on ceria nano-shapes.[103]

of the enhanced reactivity for CO oxidation may not be connected with the surface planes, but rather with the defects seen in these rods, particularly vacancy clusters.[93, 100] Another recent report proposed that the ceria rods are not single crystals but have a kind of complex core-shell structure exposing at least 50% of (110) along with the (111) plane.[67] Likewise, it has been suggested that  $\text{CeO}_2$  cubes exhibiting (100) surfaces may actually be composed of octahedral units, implying thereby that their surfaces are composed of (111) facets.[113] In light of these uncertainties, this thesis focuses on the in-depth characterization of the ceria nanoshapes to understand the true exposed planes and the surface species actually responsible for enhanced activity of nanocatalysts.

### 1.3 Scope and outline of thesis

Steam reforming of bio-oil, including the gasification of coke deposits in the presence of water, is a conceptually promising alternative to generate hydrogen gas. During the gasification,  $\text{H}_2\text{O}$  can be activated via the formation of hydroxyl groups (OH) on oxides like ceria, which increases both the  $\text{H}_2$  yield and the catalyst's lifetime. Further, ceria support can be tailored in different shapes to optimize the reactivity for water dissociation as well as reactivity of resulting hydroxyl groups.

To the best of our knowledge, consistent reports focusing on the characterization of the surface species actually responsible for enhanced catalytic activity of nanocatalysts so far remain lacking. The scope of this thesis is to provide a coherent, systematic and consistent picture of fundamental aspects of ceria nanoshapes, with emphasis on the effects of exposed planes on overall catalytic performance. Focus is on the composition and surface structure of the oxide to determine the reactivity for water dissociation, as well as the reactivity of the resulting hydroxyl species with the model compounds representing coke deposits.

In **chapter 2**, definitive information on the nature of the exposed surfaces in these CeO<sub>2</sub> nanostructures is provided using aberration-corrected high-resolution transmission electron microscopy (AC-TEM). Furthermore, it is clearly demonstrated that the nature of the exposed surface affects the activity in the WGS reaction, as well as the interaction of surface sites with CO.

In **chapter 3**, the role of different types of active hydroxyl (OH) species on the nanoshapes, their respective reactivity towards CO (simple representative probe molecule for oxygenates in coke) and their extent of regeneration of hydroxyl species with water has been investigated using *in situ* FTIR spectroscopy. Emphasis in this work is on a detailed understanding of water activation and reaction into hydroxyl groups.

In **chapter 4**, the involvement of defects in ceria rods for the formation of specific formate and carbonate surface species at 200 and 350°C is investigated using a combination of *in situ* Raman and FTIR spectroscopies. Furthermore, we use CO adsorption and subsequent reaction with water to uncover the role of defects as a function of exposed plane in **chapter 5**. The results in chapter 5 demonstrate a detailed understanding of the roles of defects in ceria nanoshapes (reduced vs. unreduced), with focus on the local defect structure as well as the extent of the reducibility of ceria nanoshapes.

Finally, in **chapter 6**, all the results of the present research are summarized and suggestions for future research are presented.

## Bibliography

- [1] “The European chemical industry in worldwide perspective: Facts and figure 2012” (CEFIC: The European Chemical Industry Council, 2012).
- [2] “Studying the Chemistry as It Happens in Catalytic Reactions” (Pacific Northwest National Laboratory, 2012).
- [3] Ganduglia-Pirovano, M. V., Hofmann, A., and Sauer, J. (2007) *Surf. Sci. Rep.* **62(6)**, 219–270.
- [4] Hussein, G. A. (1996) *J. Anal. Appl. Pyrolysis* **37(2)**, 111–149.
- [5] Idriss, H. and Barteau, M. A. Active sites on oxides: From single crystals to catalysts, in *Advances in Catalysis* chapter Active sites on oxides: From single crystals to catalysts Academic Press USA (2004).
- [6] Zaera, F. (2013) *ChemSusChem* **6(10)**, 1797–1820.
- [7] Zhou, K. and Li, Y. (2012) *Angew. Chem., Int. Ed.* **51(3)**, 602–613.
- [8] Sun, C., Li, H., and Chen, L. (2012) *Energy Environ. Sci.* **5**, 8475–8505.
- [9] “Cerium” (Investor INTEL, 2013); downloaded from <http://reehandbook.com/cerium.html> at 18:13 on 05/01/2014.
- [10] Schermanz, K. Mining, Production, Application And Safety Issues Of Cerium-Based Materials chapter 1, pp. 1–13 World Scientific (2002).
- [11] Zhang, D., Du, X., Shi, L., and Gao, R. (2012) *Dalton Trans.* **41**, 14455–14475.
- [12] Trovarelli, A. Structural Properties And Nonstoichiometric Behavior Of CeO<sub>2</sub> chapter 2, pp. 15–50 World Scientific (2002).
- [13] Mullins, D. R., Albrecht, P. M., and Calaza, F. (2013) *Top. Catal.* **56(15-17)**, 1345–1362.
- [14] Sun, C. and Xue, D. (2013) *Phys. Chem. Chem. Phys.* **15**, 14414–14419.
- [15] Esch, F., Fabris, S., Zhou, L., Montini, T., Africh, C., Fornasiero, P., Comelli, G., and Rosei, R. (2005) *Science* **309(5735)**, 752–755.
- [16] Paier, J., Penschke, C., and Sauer, J. (2013) *Chem. Rev.* **113(6)**, 3949–3985.
- [17] Yuan, Q., Duan, H.-H., Li, L.-L., Sun, L.-D., Zhang, Y.-W., and Yan, C.-H. (2009) *J. Colloid Interface Sci.* **335(2)**, 151–167.
- [18] Gao, P., Kang, Z., Fu, W., Wang, W., Bai, X., and Wang, E. (2010) *J. Am. Chem. Soc.* **132(12)**, 4197–4201.
- [19] Herman, G. S. (1999) *Surf. Sci.* **437(1-2)**, 207–214.
- [20] Nakajima, A., Yoshihara, A., and Ishigame, M. (1994) *Phys. Rev. B* **50**, 13297–13307.
- [21] Sheldon, B. W. and Shenoy, V. B. May 2011 *Phys. Rev. Lett.* **106**, 216104.
- [22] Taniguchi, T., Watanabe, T., Sugiyama, N., Subramani, A. K., Wagata, H., Matsushita, N., and Yoshimura, M. (2009) *J. Phys. Chem. C* **113(46)**, 19789–19793.

- [23] Mamontov, E. and Egami, T. (2000) *J. Phys. Chem. Solids* **61(8)**, 1345–1356.
- [24] Sayle, T. X. T., Molinari, M., Das, S., Bhatta, U. M., Möbus, G., Parker, S. C., Seal, S., and Sayle, D. C. (2013) *Nanoscale* **5**, 6063–6073.
- [25] Walsh, A., Woodley, S. M., Catlow, C. R. A., and Sokol, A. A. (2011) *Solid State Ionics* **184(1)**, 52–56.
- [26] Choudhury, B. and Choudhury, A. (2012) *Mater. Chem. Phys.* **131(3)**, 666–671.
- [27] Land, P. L. (1973) *J. Phys. Chem. Solids* **34(11)**, 1839–1845.
- [28] Sayle, T., Parker, S., and Catlow, C. (1994) *Surf. Sci.* **316(3)**, 329–336.
- [29] Stambouli, A. B. and Traversa, E. (2002) *Renewable Sustainable Energy Rev.* **6(3)**, 295–304.
- [30] Kharton, V. V., Figueiredo, F. M., Navarro, L., Naumovich, E. N., Kovalevsky, A. V., Yaremchenko, A. A., Viskup, A. P., Carneiro, A., Marques, F. M. B., and Frade, J. R. (2001) *J. Mater. Sci.* **36(5)**, 1105–1117.
- [31] Chueh, W. C. and Haile, S. M. (2010) *Philos. Trans. R. Soc., A* **368(1923)**, 3269–3294.
- [32] Chueh, W. C., Falter, C., Abbott, M., Scipio, D., Furler, P., Haile, S. M., and Steinfeld, A. (2010) *Science* **330(6012)**, 1797–1801.
- [33] Furler, P., Scheffe, J. R., and Steinfeld, A. (2012) *Energy Environ. Sci.* **5**, 6098–6103.
- [34] Karakoti, A., Monteiro-Riviere, N., Aggarwal, R., Davis, J., Narayan, R., Self, W., McGinnis, J., and Seal, S. (2008) *JOM* **60(3)**, 33–37.
- [35] Rzigalinski, B. A., Meehan, K., Davis, R. M., Xu, Y., Miles, W. C., and Cohen, C. A. (2006) *Nanomedicine* **1(4)**, 399–412.
- [36] Sahu, T., Singh Bisht, S., Ranjan Das, K., and Kerkar, S. (2013) *Curr. Nanosci.* **9(5)**, 588–593.
- [37] Nowacek, A., Kosloski, L. M., and Gendelman, H. E. (2009) *Nanomedicine* **4(5)**, 3541–3555.
- [38] Azzam, K., Babich, I., Seshan, K., and Lefferts, L. (2007) *J. Catal.* **251(1)**, 153–162.
- [39] Diwell, A., Rajaram, R., Shaw, H., and Truex, T. (1991) The role of ceria in three-way catalysts In A. Crucq, (ed.), *Studies in Surf. Sci. and Catalysis*, volume **71**, pp. 139–152 Elsevier.
- [40] Gorte, R. J. (2010) *AIChE Journal* **56(5)**, 1126–1135.
- [41] Trovarelli, A., de Leitenburg, C., Boaro, M., and Dolcetti, G. (1999) *Catal. Today* **50(2)**, 353–367.
- [42] Kašpar, J., Fornasiero, P., and Hickey, N. (2003) *Catal. Today* **77(4)**, 419–449.
- [43] Choudhary, T. and Goodman, D. (2002) *Catal. Today* **77(1-2)**, 65–78.
- [44] Brown, L. F. (2001) *Int. J. Hydrogen Energy* **26(4)**, 381–397.

- [45] Ghenciu, A. F. (2002) *Curr. Opin. Solid State Mater. Sci.* **6(5)**, 389–399.
- [46] Pozdnyakova, O., Teschner, D., Wootsch, A., Kröhnert, J., Steinhauer, B., Sauer, H., Toth, L., Jentoft, F., Knop-Gericke, A., Paála, Z., and Schlögl, R. (2006) *J. Catal.* **237(1)**, 1–16.
- [47] Trimm, D. L. and Önsan, Z. I. (2001) *Catal. Rev.* **43(1-2)**, 31–84.
- [48] Armor, J. N. (1999) *Appl. Catal., A* **176(2)**, 159–176.
- [49] Bion, N., Epron, F., Moreno, M., Mario, F., and Duprez, D. (2008) *Top. Catal.* **51(1-4)**, 76–88.
- [50] Wootsch, A., Descorme, C., and Duprez, D. (2004) *J. Catal.* **225(2)**, 259–266.
- [51] Chin, S. Y., Alexeev, O. S., and Amiridis, M. D. (2006) *J. Catal.* **243(2)**, 329–339.
- [52] Okkerse, C. and vanBekum, H. (1999) *Green Chem.* **1**, 107–114.
- [53] Trane, R., Dahl, S., Skjøth-Rasmussen, M., and Jensen, A. (2012) *Int. J. Hydrogen Energy* **37(8)**, 6447–6472.
- [54] Güell, B. M., Babich, I., Nichols, K. P., Gardeniers, J. G. E., Lefferts, L., and Seshan, K. (2009) *Appl. Catal., B* **90(1-2)**, 38–44.
- [55] Rioche, C., Kulkarni, S., Meunier, F. C., Breen, J. P., and Burch, R. (2005) *Appl. Catal., B* **61(1-2)**, 130–139.
- [56] Wan, S., Pham, T., Zhang, S., Lobban, L., Resasco, D., and Mallinson, R. (2013) *AIChE Journal* **59(7)**, 2275–2285.
- [57] Snell, R. W. and Shanks, B. H. (2013) *ACS Catal.* **3(4)**, 783–789.
- [58] Newsome, D. S. (1980) *Catal. Rev.* **21(2)**, 275–318.
- [59] Ruettinger, W., Ilinich, O., and Farrauto, R. J. (2003) *J. Power Sources* **118(1-2)**, 61–65.
- [60] Azzam, K., Babich, I., Seshan, K., and Lefferts, L. (2008) *Appl. Catal., B* **80(1-2)**, 129–140.
- [61] Burch, R. (2006) *Phys. Chem. Chem. Phys.* **8**, 5483–5500.
- [62] Gorte, R. and Zhao, S. (2005) *Catal. Today* **104(1)**, 18–24.
- [63] Azzam, K. G. A Further Step toward H<sub>2</sub> in Automobile: Development of an Efficient Bi-Functional Catalyst for Single Stage Water Gas Shift PhD thesis University of Twente, Enschede, The Netherlands may 2008.
- [64] Jacobs, G., Patterson, P. M., Williams, L., Sparks, D., and Davis, B. H. (2004) *Catal. Lett.* **96(1-2)**, 97–105.
- [65] Jacobs, G., Chenu, E., Patterson, P. M., Williams, L., Sparks, D., Thomas, G., and Davis, B. H. (2004) *Appl. Catal., A* **258(2)**, 203–214.
- [66] Azzam, K., Babich, I., Seshan, K., and Lefferts, L. (2007) *J. Catal.* **251(1)**, 163–171.
- [67] Désaunay, T., Bonura, G., Chiodo, V., Freni, S., Couzinié, J.-P., Bourgon, J., Ringuedé, A., Labat, F., Adamo, C., and Cassir, M. (2013) *J. Catal.* **297**, 193–

- 201.
- [68] Wang, R. and Mutinda, S. I. (2011) *Chem. Phys. Lett.* **517(4-6)**, 186–189.
- [69] Yang, Z., Woo, T. K., Baudin, M., and Hermansson, K. (2004) *J. Chem. Phys.* **120(16)**, 7741–7749.
- [70] Albrecht, P. M. and Mullins, D. R. (2013) *Langmuir* **29(14)**, 4559–4567.
- [71] Nolan, M., Grigoleit, S., Sayle, D. C., Parker, S. C., and Watson, G. W. (2005) *Surf. Sci.* **576(1-3)**, 217–229.
- [72] Nörenberg, H. and Harding, J. H. (2001) *Surf. Sci.* **477(1)**, 17–24.
- [73] Wu, Z., Li, M., Howe, J., Meyer, H. M., and Overbury, S. H. (2010) *Langmuir* **26(21)**, 16595–16606.
- [74] Mullins, D. and Overbury, S. (1999) *J. Catal.* **188(2)**, 340–345.
- [75] Molinari, M., Parker, S. C., Sayle, D. C., and Islam, M. S. (2012) *J. Phys. Chem. C* **116(12)**, 7073–7082.
- [76] Senanayake, S. D., Gordon, W. O., Overbury, S. H., and Mullins, D. R. (2009) *J. Phys. Chem. C* **113(15)**, 6208–6214.
- [77] Mullins, D. R. and Albrecht, P. M. (2013) *J. Phys. Chem. C* **117(28)**, 14692–14700.
- [78] Senanayake, S. D. and Mullins, D. R. (2008) *J. Phys. Chem. C* **112(26)**, 9744–9752.
- [79] Rodriguez, J. A., Ma, S., Liu, P., Hrbek, J., Evans, J., and Pérez, M. (2007) *Science* **318(5857)**, 1757–1760.
- [80] Lin, K.-S. and Chowdhury, S. (2010) *Int. J. Mol. Sci.* **11(9)**, 3226–3251.
- [81] Wang, G., Wang, L., Fei, X., Zhou, Y., Sabirianov, R. F., Mei, W. N., and Cheung, C. L. (2013) *Catal. Sci. Technol.* **3**, 2602–2609.
- [82] Mai, H.-X., Sun, L.-D., Zhang, Y.-W., Si, R., Feng, W., Zhang, H.-P., Liu, H.-C., and Yan, C.-H. (2005) *J. Phys. Chem. B* **109(51)**, 24380–24385.
- [83] Zhou, K., Wang, X., Sun, X., Peng, Q., and Li, Y. (2005) *J. Catal.* **229(1)**, 206–212.
- [84] Pahari, S. K., Sutradhar, N., Sinhamahapatra, A., Pal, P., and Panda, A. B. (2011) *New J. Chem.* **35**, 1460–1465.
- [85] Schneider, J. J., Naumann, M., Schäfer, C., Brandner, A., Hofmann, H. J., and Claus, P. (2011) *Beilstein J. Nanotechnol.* **2**, 776–784.
- [86] Bugayeva, N. (2005) *Mater. Res. Soc. Symp. Proc.* **876**, 195–200.
- [87] Wang, W., Howe, J. Y., Li, Y., Qiu, X., Joy, D. C., Paranthaman, M. P., Doktycz, M. J., and Gu, B. (2010) *J. Mater. Chem.* **20**, 7776–7781.
- [88] Wang, Z. L. and Feng, X. (2003) *J. Phys. Chem. B* **107(49)**, 13563–13566.
- [89] Tana, Zhang, M., Li, J., Li, H., Li, Y., and Shen, W. (2009) *Catal. Today* **148(1-2)**, 179–183.
- [90] Wu, Z., Li, M., and Overbury, S. H. (2012) *J. Catal.* **285(1)**, 61–73.
- [91] Torrente-Murciano, L., Gilbank, A., naPuertolas, B., Garcia, T., Solsona, B., and

- Chadwick, D. (2013) *Appl. Catal., B* **132-133**, 116–122.
- [92] Dai, Q., Huang, H., Zhu, Y., Deng, W., Bai, S., Wang, X., and Lu, G. (2012) *Appl. Catal., B* **117-118**, 360–368.
- [93] Liu, X., Zhou, K., Wang, L., Wang, B., and Li, Y. (2009) *J. Am. Chem. Soc.* **131(9)**, 3140–3141.
- [94] Yang, Z., Zhou, K., Liu, X., Tian, Q., Lu, D., and Yang, S. (2007) *Nanotechnology* **18(18)**, 185606.
- [95] Boucher, M. B., Goergen, S., Yi, N., and Flytzani-Stephanopoulos, M. (2011) *Phys. Chem. Chem. Phys.* **13**, 2517–2527.
- [96] Chang, S., Li, M., Hua, Q., Zhang, L., Ma, Y., Ye, B., and Huang, W. (2012) *J. Catal.* **293**, 195–204.
- [97] Du, X., Zhang, D., Shi, L., Gao, R., and Zhang, J. (2012) *J. Phys. Chem. C* **116(18)**, 10009–10016.
- [98] Han, W.-Q., Wen, W., Hanson, J. C., Teng, X., Marinkovic, N., and Rodriguez, J. A. (2009) *J. Phys. Chem. C* **113(52)**, 21949–21955.
- [99] Singhanian, N., Anumol, E. A., Ravishankar, N., and Madras, G. (2013) *Dalton Trans.* **42**, 15343–15354.
- [100] Liu, L., Cao, Y., Sun, W., Yao, Z., Liu, B., Gao, F., and Dong, L. (2011) *Catal. Today* **175(1)**, 48–54.
- [101] Si, R. and Flytzani-Stephanopoulos, M. (2008) *Angew. Chem.* **120(15)**, 2926–2929.
- [102] Snell, R. W., Hakim, S. H., Dumesic, J. A., and Shanks, B. H. (2013) *Appl. Catal., A* **464-465**, 288–295.
- [103] Wu, Z., Li, M., Mullins, D. R., and Overbury, S. H. (2012) *ACS Catal.* **2(11)**, 2224–2234.
- [104] Agarwal, S., Lefferts, L., and Mojet, B. L. (2013) *ChemCatChem* **5(2)**, 479–489.
- [105] Ciftci, A., Ligthart, D. M., Pastorino, P., and Hensen, E. J. (2013) *Appl. Catal., B* **130-131**, 325–335.
- [106] Guan, Y., Ligthart, D. M., Pirgon-Galin, Ö., Pieterse, J. A., Santen, R. A., and Hensen, E. J. (2011) *Top. Catal.* **54(5-7)**, 424–438.
- [107] Yi, G., Yang, H., Li, B., Lin, H., Tanaka, K., and Yuan, Y. (2010) *Catal. Today* **157(1-4)**, 83–88.
- [108] Han, J., Kim, H. J., Yoon, S., and Lee, H. (2011) *J. Mol. Catal. A: Chem.* **335(1-2)**, 82–88.
- [109] Yi, N., Si, R., Saltsburg, H., and Flytzani-Stephanopoulos, M. (2010) *Energy Environ. Sci.* **3**, 83–837.
- [110] Soykal, I. I., Bayram, B., Sohn, H., Gawade, P., Miller, J. T., and Ozkan, U. S. (2012) *Appl. Catal., A* **449(0)**, 47–58.
- [111] Ta, N., Liu, J. J., Chenna, S., Crozier, P. A., Li, Y., Chen, A., and Shen, W. (2012)

*J. Am. Chem. Soc.* **134**(51), 20585–20588.

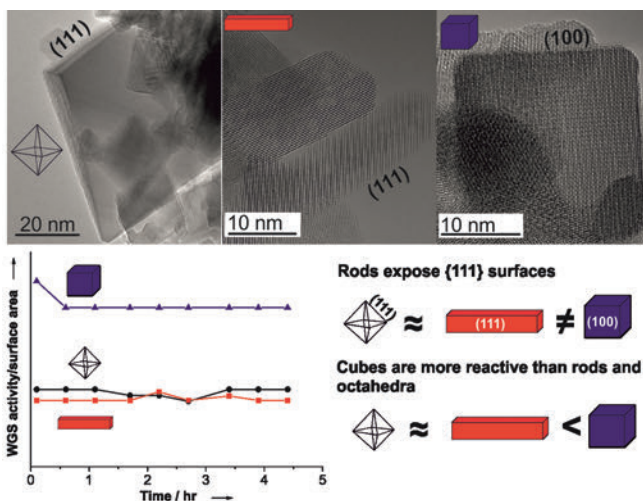
- [112] Wang, S., Zhao, L., Wang, W., Zhao, Y., Zhang, G., Ma, X., and Gong, J. (2013) *Nanoscale* **5**, 5582–5588.
- [113] Asahina, S., Takami, S., Otsuka, T., Adschiri, T., and Terasaki, O. (2011) *Chem-CatChem* **3**(6), 1038–1044.

# 2

## Revealing the exposed planes on ceria nanoshapes: The connection to water gas shift reactivity

### Research question:

What are the true exposed planes of ceria nanoshapes?



*Our starting point was to validate the exposed surface planes as a function of nanoshape, because the exposed planes are one of the key factors affecting the catalytic activity of ceria supports.*

\*Published as: S. Agarwal *et al.*, “Exposed surfaces on shape-controlled ceria nanoparticles revealed through AC-TEM and water gas shift reactivity,” *ChemSusChem* **6**, 1898–1906 (2013)

## Abstract

*Aberration-corrected transmission electron microscopy and high-angle annular dark field imaging were used to investigate the surface structures and internal defects of CeO<sub>2</sub> nanoparticles (octahedra, rods and cubes). Further, their catalytic reactivity in the water gas shift (WGS) reaction and the exposed surface sites by using FTIR spectroscopy were tested. Rods and octahedra expose stable (111) surfaces whereas cubes have primarily (100) facets. Rods also have internal voids and surface steps. The exposed planes are consistent with observed reactivity patterns, and the normalized WGS reactivity of octahedra and rods are similar, but the cubes are more reactive. In situ FTIR spectroscopy showed that rods and octahedra exhibit similar spectra for OH groups and that carbonates and formates form upon exposure to CO, whereas for cubes clear differences were observed. These results provide definitive information on the nature of the exposed surfaces in these CeO<sub>2</sub> nanostructures and their influence on the WGS reactivity.*

## 2.1 Introduction

Ceria (CeO<sub>2</sub>) has been extensively investigated in the field of heterogeneous catalysis both as a catalyst and as a support for noble metals. This is due to its unique redox properties and high oxygen storage capacity (OSC), allowing it to quickly switch oxidation state between Ce<sup>4+</sup> and Ce<sup>3+</sup> in the stable fluorite structure.[1] Because of these redox properties, CeO<sub>2</sub> is used in a wide range of applications such as an ultraviolet (UV) absorber in sun blocks,[2] O<sub>2</sub> sensors,[3, 4] and antioxidant in the field of biomedicine.[5] CeO<sub>2</sub> is commercially used as a catalyst support in applications such as three-way automotive exhaust catalysis (TWC)[6] and as solid electrolytes in low temperature solid oxide fuel cells (SOFC).[7, 8] Further, the oxidation of CO,[9–11] NO,[12] hydrocarbons,[13] the low temperature water gas shift reaction (WGS),[14–16] and steam reforming of bio-oil[17] have been investigated on CeO<sub>2</sub> and CeO<sub>2</sub>-supported catalysts.

In recent years, many studies have reported improved activity of CeO<sub>2</sub> catalysts through synthesis of CeO<sub>2</sub> nanostructures with controlled morphology.[18, 19] The controlled morphology generates well-defined exposed crystallographic planes, which may lead to improved catalytic activity. Synthesis procedures for

## 2.1. INTRODUCTION

these CeO<sub>2</sub> nanocrystals are well developed for generating morphologies such as cubes,[20] rods,[1, 10, 18, 20, 21] wires,[1] tubes,[22, 23] octahedra,[24] spindles,[25] 3D flower-like shapes,[26, 27] and spheres.[21] These materials have also been studied in catalytic reactions. The literature shows that CeO<sub>2</sub> morphology can play an important role in catalytic performance.[1, 11, 18, 21, 23, 26, 27] For instance, CeO<sub>2</sub> cubes were reported to exhibit excellent reducibility and high oxygen storage capacity (OSC) attributed to the presence of (100) planes.[28] CeO<sub>2</sub> rods attracted attention because they provide a high surface area. The rods are thought to expose (100) and (110) surfaces, which are less stable and thus more reactive than the (111) surface.[29] It has also been suggested that the CeO<sub>2</sub> rods have surface defects[9, 30] such as vacancy clusters, pits and a high degree of surface roughness. CeO<sub>2</sub> rods have been reported to exhibit enhanced reactivity for the oxidation of CO,[1, 10, 11] NO,[12] 1,2-dichloroethane, and ethyl acetate.[31]

The morphology of CeO<sub>2</sub> rods was deduced in the work of Zhou[10] and Mai,[20] and the synthesis approach reported by these authors has become the standard recipe for the preparation of CeO<sub>2</sub> rods and cubes.[11, 30–36] Most recent studies rely on the morphology proposed in these early papers, suggesting that CeO<sub>2</sub> rods have exposed (100) and (110) surfaces and grow along the [110] direction.[33, 37–41] However, careful examination of the early studies shows that the limited resolution of TEM in those days made it difficult to obtain clear images of the surface regions. Furthermore, high-angle annular dark field (HAADF) imaging was not used in these studies to provide definitive shape information. More recently, it was suggested that CeO<sub>2</sub> rods can also expose (111) surfaces and it was implied that the origin of the enhanced reactivity for CO oxidation may not be connected with the surface facets but rather with the defects seen in these rods, particularly vacancy structures.[9, 12, 25, 42] Likewise, Asahina *et al.*[43] suggested that CeO<sub>2</sub> cubes exhibiting (100) surfaces may actually be composed of octahedral units, implying thereby that their surfaces are composed of (111) facets. In light of these uncertainties, we decided to investigate the surfaces of CeO<sub>2</sub> by using a combination of TEM technique as well as surface reactivity measurements.

Previous researchers used high-resolution TEM (HRTEM) to identify surface features and the morphology of the nanoparticles. Conventional HRTEM does not allow us to visualize the surfaces very clearly due to image delocalization and

Fresnel fringes. The development of aberration-corrected transmission electron microscopy (AC-TEM) has pushed the resolution below 1 Å, both in TEM and STEM modes.[44, 45] AC-TEM has recently been used to investigate the beam-induced cationic mobility on the surface of CeO<sub>2</sub> nanoparticles.[46, 47] In the present study, we used a double aberration-corrected microscope (JEOL JEM-ARM 200F) equipped with both image and probe correctors. This combination of atomic-scale resolution in TEM and STEM images provides insights into the nature of the surfaces of these CeO<sub>2</sub> nanoshapes. As microscopy is a local technique, we have also included XRD and Brunauer-Emmett-Teller (BET) surface area measurements to provide a better average of the structure and morphology of these powders. To characterize the surface reactivity, we have used the water gas shift (WGS) reaction as a probe reaction. In addition, FTIR spectroscopy of adsorbed CO allows us to obtain mechanistic insight into the surface reactions taking place on the respective CeO<sub>2</sub> nanoshapes. This combination of techniques allows us to present a complete picture of the nature of the surfaces in shape-controlled CeO<sub>2</sub> nanoparticles.

## 2.2 Experimental section

### 2.2.1 Catalyst preparation

All materials used were of analytical purity, obtained from Sigma-Aldrich. CeO<sub>2</sub> rods and cubes were synthesized through the hydrothermal procedure first reported by Mai.[20] Ce(NO<sub>3</sub>)<sub>3</sub>·6H<sub>2</sub>O (2.17 g) and NaOH (24 g) were dissolved in 5 and 35 mL deionized water, respectively. The solutions were mixed and stirred for 30 min. This resulted in the formation of milky slurry, which was then transferred to an autoclave (125 mL) and filled with deionized water up to 80% of the total volume of the autoclave. The solution was subjected to hydrothermal treatment for 24 h at temperatures of 100 (for rods) and 180°C (for cubes). Next, the fresh precipitates (yellow color for rods and white for cubes) were separated by centrifugation, washed with deionized water several times, followed by washing in ethanol and drying at 60°C in air overnight. The reference shape used in this study was the CeO<sub>2</sub> octahedron (99.9% pure), which was obtained from Sigma-Aldrich and had an average particle size smaller than 25 nm. The samples were calcined at

## 2.2. EXPERIMENTAL SECTION

500°C (heating rate 5 K/min) for 4h in synthetic air (flow rate = 50 mL/min) and subsequently cooled down to room temperature in air before use.

### 2.2.2 HRSEM, BET and XRD characterization

The HRSEM and TEM images (after WGS testing) of the CeO<sub>2</sub> nanoshapes were recorded by using Carl Zeiss Merlin and Philips CM300ST-FEG electron microscope (operated at an acceleration voltage of 300kV), respectively. BET surface areas were determined by performing N<sub>2</sub> physisorption using a Micromeritics Tristar instrument. The samples were out-gassed in vacuum at 300°C for 24h prior to analysis.

X-Ray diffraction data were recorded with a Bruker D2 Phaser diffractometer using CuK<sub>α</sub> radiation ( $\lambda = 0.1544$  nm). XRD patterns were measured in reflection geometry in the  $2\theta$  range between 0° and 90°.

### 2.2.3 AC-TEM and STEM measurements

The investigation was performed by using a double-aberration-corrected JEOL ARM200F operated at 200kV accelerating voltage equipped with a Gatan GIF Quantum with dual EELS capability as well as an Oxford XMax 80 EDS (Energy-dispersive X-Ray spectroscopy) detector. The TEM imaging was conducted by using a Gatan Ultrascan USFTXP camera with the STEM imaging performed in both BF and ADF mode. The probe used for STEM imaging had a convergence angle of 17 mrad with a probe current density of approximately 68 pA. The acceptance-angle range used for ADF imaging was 68 – 230 mrad. The nominal probe diameter for STEM imaging was 0.08 nm, and the point resolution for TEM imaging was 0.11 nm. We used the Gatan Digital Micrograph software for analysis of the images and the CrystalMaker software for visualizing the structure of CeO<sub>2</sub> along different crystallographic projections.

### 2.2.4 FTIR spectroscopy

Transmission FTIR measurements were recorded with a Bruker Vector 22 by averaging 128 scans with a spectral resolution of 4 cm<sup>-1</sup> and time intervals of 120s. The background spectrum was recorded by using an empty cell. The FTIR signal

was recorded with MCT (mercury-cadmium-telluride) detector. A self-supporting pellet of about 13 – 15 mg of sample was pressed and added into a homemade stainless steel cell. The samples were pretreated in H<sub>2</sub> flow (20 mL/min) at 450 °C for 1 h (heating rate 5 K/min). After pretreatment, the FTIR cell was cooled to 150 °C in a He flow and then heated to reaction temperature. He was dried by using a Varian Chromopack CP17971 gas clean moisture filter, to trap any moisture in the gases. For CO adsorption experiments, 33 vol% CO (Hoekloos 4.7) in He (Hoekloos 5.0, total flow 20 mL/min) was used. All tubes from the gas panel to the cell were preheated to 200 °C to avoid a sudden temperature drop in the FTIR cell.

Background: Empty cell.

### 2.2.5 WGS catalytic activity testing

WGS catalytic activity measurements were performed in a parallel ten-flow microreactor system. For the H<sub>2</sub>O/He stream, He was introduced into an evaporator mixer unit filled with deionized water, which was connected to a liquid flow controller and mass flow controller (Bronkhorst) to control the H<sub>2</sub>O/He flow. All the tubes from the evaporator unit to the microreactor was heated above 100 °C to avoid condensation in the line. High-purity gases were used in the catalytic experiments [e.g., H<sub>2</sub>, He (5.0) and CO (4.7, from Linde)]. The CO/H<sub>2</sub>O reaction feed ratio used was 1:3 balanced by He, and the total volume flow rate was 200 mL/min, resulting in a gas hourly space velocity (GHSV) of about  $2.4 \times 10^4 \text{ mL}_{\text{gcat}}^{-1} \text{ h}^{-1}$ . The particle size of the samples was between 125 – 250 μm, and the amount of catalyst used was 50 mg diluted with 320 mg of SiC of the same sieve fraction. The reactions were performed at atmospheric pressure and at 350 °C. The catalyst was reduced in H<sub>2</sub> balanced by He flow (H<sub>2</sub>/He = 1:4) at 500 °C for 1 h prior to catalytic measurements. After pretreatment, the reactor system was cooled to 150 °C in He flow and then heated to reaction temperature in a CO/H<sub>2</sub>O/He flow. The effluent stream from the reactor was directed to a Compact GC (Interscience) equipped with Porapak Q (TCD-thermal conductivity detector) and Molecular sieve 5A (TCD) columns for online detection of H<sub>2</sub>, CO, and CO<sub>2</sub> gases.

### 2.3 Results and discussion

CeO<sub>2</sub> rods and cubes were synthesized by using the approach described by Mai *et al.*[20] The BET surface areas of ceria rods, octahedra, and cubes were found to be 80, 58, and 10 m<sup>2</sup>/g, respectively. The samples did not possess microporosity and have average pore sizes larger than 10 nm. The pore volumes of CeO<sub>2</sub> rods, octahedra, and cubes were 0.33, 0.20, and 0.05 cm<sup>3</sup>/g, respectively. The surface area is consistent with the particle sizes observed by SEM and TEM, showing that on average the cubes are significantly larger in size than the other two samples. Figure 2.1 shows the XRD patterns of the three samples. The prominent CeO<sub>2</sub> diffraction peaks are consistent with the expected CeO<sub>2</sub> reflections according to ICDD card 431002.[48] The XRD peaks are broad due to the small size of the CeO<sub>2</sub> crystallites. Although it is difficult to derive average crystallite dimensions from Scherrer analysis for particle shapes that differ from spherical geometry, we have performed this analysis to obtain corroboration of our TEM observations. The sizes derived from the analysis of XRD data were as follows: Rods 29 nm, cubes 58.7 nm, and octahedra 51.2 nm. Our XRD data for CeO<sub>2</sub> nanoshapes are in agreement with the work of Mai *et al.*[20] (recipe we used for synthesis) as well as with the work of Wu *et al.*,[30] Dai *et al.*,[31] Gamarra *et al.*,[49] Torrente-Murciano *et al.*,[50] and Désaunay *et al.*[51] (see data compiled in table A2.1 of the Appendix).

All three samples in figure 2.1 show some degree of asymmetry in the peak profile, as seen from the presence of a shoulder, or second peak on the left of the (311) reflection (see the Appendix, figure A2.1; most prominent for rods).

We assign this shoulder to the existence of a bimodal particle size distribution, with the smaller particles showing a lattice constant that is larger than bulk CeO<sub>2</sub>. The lattice expansion can be caused by the presence of Ce<sup>3+</sup> ions in this ionic lattice as explained by the model presented by Tsunekawa *et al.*[52] A bimodal particle size distribution can be clearly observed in the HRSEM and TEM images and, hence, is consistent with this interpretation. In this sample set, all samples exhibit this bimodal particle size distribution, but we will show below that the particle size does not affect the surface termination of the CeO<sub>2</sub> nanoshapes. To establish the surface structure and morphology, the CeO<sub>2</sub> nanoshapes were analyzed by HRSEM, AC-TEM, and AC-STEM, the latter in bright field (BF) as well

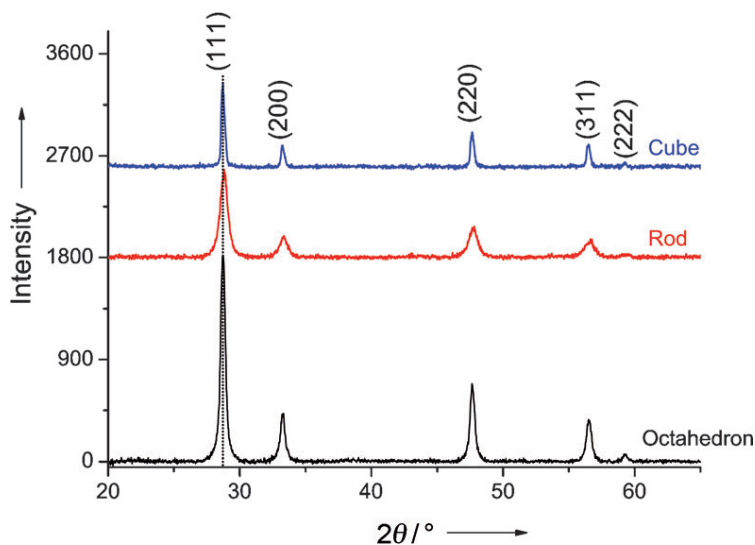


**Figure 2.1:** XRD patterns for controlled-morphology  $\text{CeO}_2$  powders used in this study. The (111) reflection is highlighted with a vertical line and shows that the rods and octahedra samples have very similar lattice constants. The Appendix (figure A2.1) presents an expanded view of the (311) reflection of these samples, showing the asymmetry in peak shape (related to bimodal particle size distribution) more clearly.

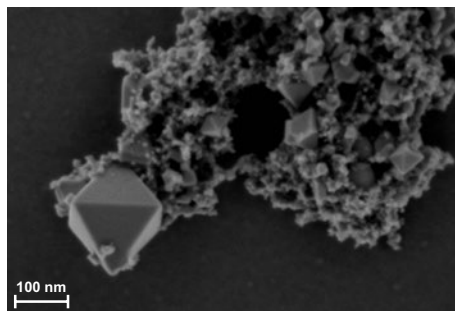
as in dark field (HAADF) imaging modes. We also embedded the rods in epoxy and prepared cross-section samples using an ultramicrotome, which allows us to analyze rods end-on. We next describe the morphology of these samples, followed by the catalytic reactivity and the FTIR spectroscopy of adsorbed species on the surface.

### 2.3.1 Octahedra

Figure 2.2 shows an HRSEM image of  $\text{CeO}_2$  octahedra. Well-defined, faceted octahedra can be clearly seen. In addition, some fine-grained material is observed of which morphology cannot be determined at this magnification. As we show in the images to follow and in the Appendix (figures A2.2 and A2.3), the fine-grained material has a similar morphology and exposed facets as the larger particles and the octahedral shape is the dominant one in this sample.

BF and HAADF STEM images are shown in figure 2.3. The BF image contrast

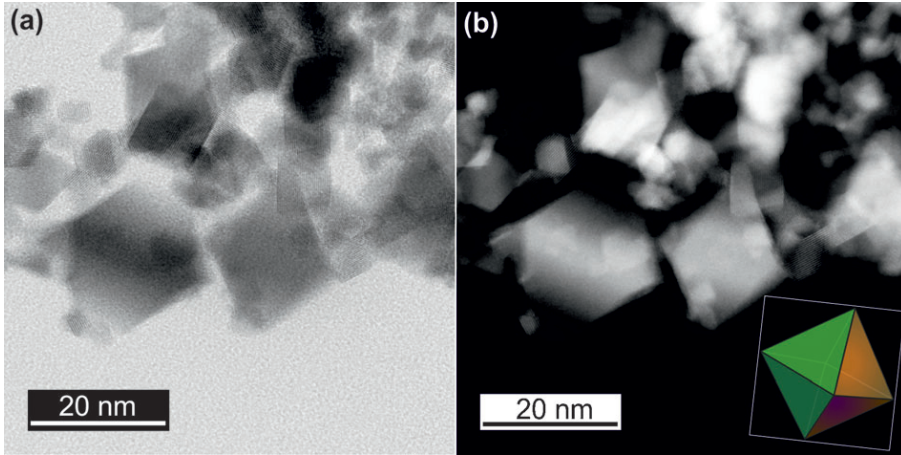
### 2.3. RESULTS AND DISCUSSION



**Figure 2.2:** HRSEM image of the octahedra. Well-defined, faceted octahedra of differing size are present in this sample. This sample shows a distinct bimodal size distribution, with numerous particles that are much smaller than the large octahedra imaged here. This bimodal size distribution gives rise to the asymmetric peaks for the (311) reflection seen in figure A2.1 in the Appendix.

can arise due to diffraction effects, for which the orientation of each particle also matters, whereas the HAADF image is dominated by atomic number and sample thickness. As we are only dealing with  $\text{CeO}_2$ , the differences in contrast in the HAADF images can be directly related to sample thickness and this allows for confirmation of the sample morphology. As shown in the inset, the octahedron is composed of eight  $\{111\}$  surfaces with the top and bottom oriented along the  $[100]$  direction. As seen in the dark field image, the prominent diamond-shaped particles are thicker in the center than at the edges; hence, they are consistent with an octahedron imaged edge-on. In addition to the dominant  $\{111\}$  planes, we also observe that the truncated ends of the octahedra have exposed  $\{100\}$  planes, as shown previously.[24, 53] Finally, the octahedra have four sharp corners in the plane of square symmetry, directed in the  $\langle 110 \rangle$  directions. As illustrated in the model shown in the inset in figure 2.3 and A2.3 in the Appendix, we see sharp corners where a  $\{110\}$  surface should have been present. The fact that we did not see any  $\{110\}$  surface facets and the fact that growth occurs along  $[110]$  direction indicates that the  $\{110\}$  surfaces are not stable.

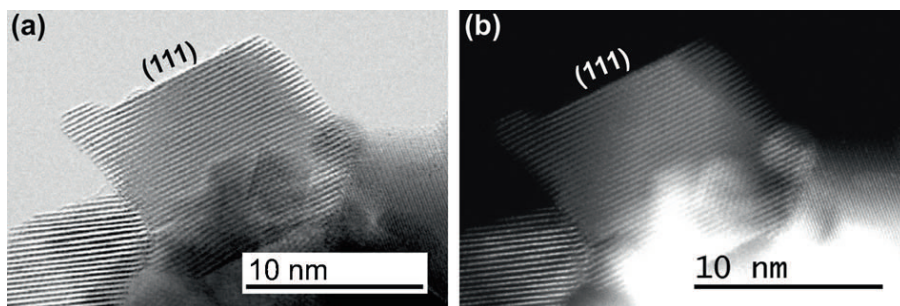
A higher magnification STEM image is shown in figure 2.4. As the beam diameter is about  $0.8 \text{ \AA}$  in this microscope, we can easily resolve the  $\text{CeO}_2$  crystal lattice. The BF image is analogous to an HRTEM image; hence, contrast at these high magnifications comes from phase contrast. On the other hand, the HAADF



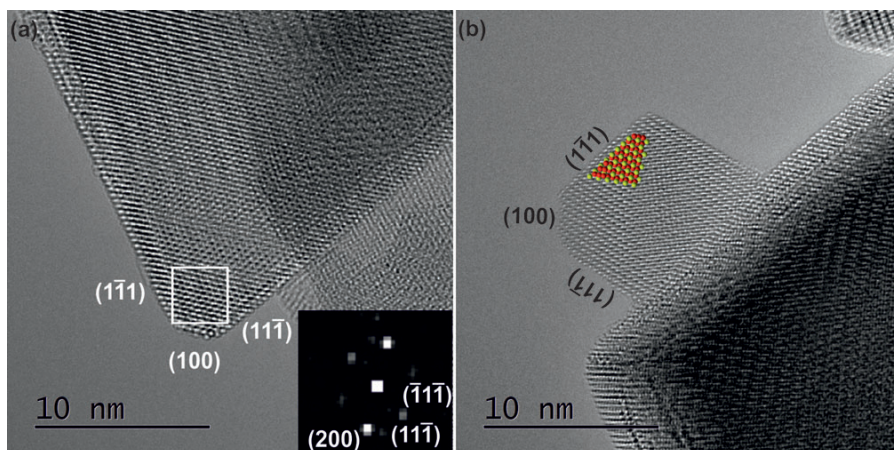
**Figure 2.3:** (a) BF and (b) HAADF STEM images showing the octahedral shapes. The thickness variation leads to the observed contrast change in the HAADF image (right), confirming the octahedral shape, as the center is thicker compared to the top and bottom (as seen from the inset). The smaller particles also expose the same dominant  $\{111\}$  surface, which is seen more clearly in the higher magnification images shown in figures 2.3 and 2.4 and figures A2.2 and A2.3 in the Appendix.

image arises from incoherent scattering at high angles and is dominated by atomic number contrast. The bright lines consequently represent rows of Ce atoms, because O atoms will be almost invisible due to their low atomic number. The complementary BF and HAADF images allow us to see clearly the morphology of the sample and the nature of the surfaces. The particles are randomly oriented; hence, they are not lined up along the low index zone axes, which is why most of them do not show cross fringes. Figure 2.4 shows that the  $\text{CeO}_2$   $\{111\}$  surfaces are smooth and free from any surface steps, defects, or surface reconstruction. A TEM image is a projection of a three-dimensional object. When the particle is large, some degree of surface roughness can arise because the surface is not perfect over large distances. The nature of the surfaces is further confirmed by the AC-TEM images (see figure 2.5), where a large and a small octahedron are shown. The prominent  $\{111\}$  facets show clearly resolved rows of Ce-atom columns with small  $\{100\}$  facets. The inset is a model of the  $\text{CeO}_2$  lattice showing that the AC-TEM image clearly resolves single-atom columns of Ce. Approximately 20 – 25 images were systematically analyzed for exposed crystal planes. Care was taken to ensure

### 2.3. RESULTS AND DISCUSSION



**Figure 2.4:** Higher magnification (a) BF and (b) HAADF STEM images showing the nature of the (111) surface. There is no significant surface roughness evident on these.



**Figure 2.5:** Aberration-corrected TEM images of large (a) and small (b) CeO<sub>2</sub> octahedra. These expose the (111) facets and very small (100) facets. The surface termination is abrupt, and there is no amorphous layer or surface roughness present. The inset in (b) shows the structure of the CeO<sub>2</sub> lattice (Ce atoms: green; O atoms: red) and the agreement between the white dots and the Ce atom columns.

that selected regions did not contain multiple overlapping particles to avoid interference when analyzing the data. Additional images are shown in the Appendix (figures A2.2 and A2.3), showing that even the smallest particles expose {111} facets.

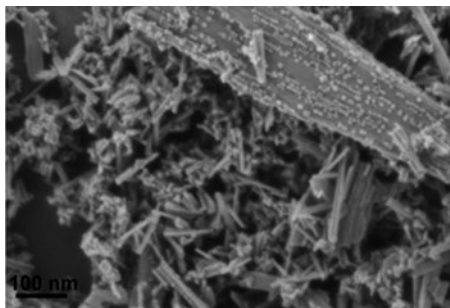


**Figure 2.6:** HRSEM image of the rods. These rods have a high aspect ratio (length/width) exceeding 20.

### 2.3.2 Rods

Figure 2.6 shows a HRSEM image of the rods. This low magnification view reveals that the sample contains a uniform distribution of rods with a width of 5 – 10 nm and a length of about 200 nm, that is, an aspect ratio exceeding 20. The low-magnification view does not show the cross-section of this rod, but it is clear that the primary exposed surface is along the length of the rods and that the ends contribute minimally to the total surface area. In figure 2.7, we show BF and HAADF STEM images from these rods. The insets show fast Fourier transforms (FFTs) that provide information on the periodicities seen in the image. Based on the calibration of the microscope, we can index these spots as  $\{111\}$  planes, implying that the rods expose their  $\{111\}$  surfaces. The BF images also show characteristic regions of low contrast that appear to follow the crystallographic directions. The fact that these regions are dark in the HAADF image indicates less mass in those regions. These features could arise from voids within the structure or from surface steps. Recently, Florea *et al.*, based on electron tomography, have assigned these low-contrast features to internal pores in the CeO<sub>2</sub> rods.[54] As can be seen in figure 2.7a, surface steps are observed along the length of the rods. Therefore, we conclude that these low-contrast features represent voids as well as surface steps in the CeO<sub>2</sub> rods. The shapes of these voids follow the stable surfaces of the CeO<sub>2</sub> structure; hence, these voids are bounded by  $\{111\}$  surfaces.

The CeO<sub>2</sub> rods grow along the  $[110]$  direction. This is confirmed by the lattice fringe images seen in figure 2.8c, where we see  $(220)$  lattice fringes. We recorded

### 2.3. RESULTS AND DISCUSSION

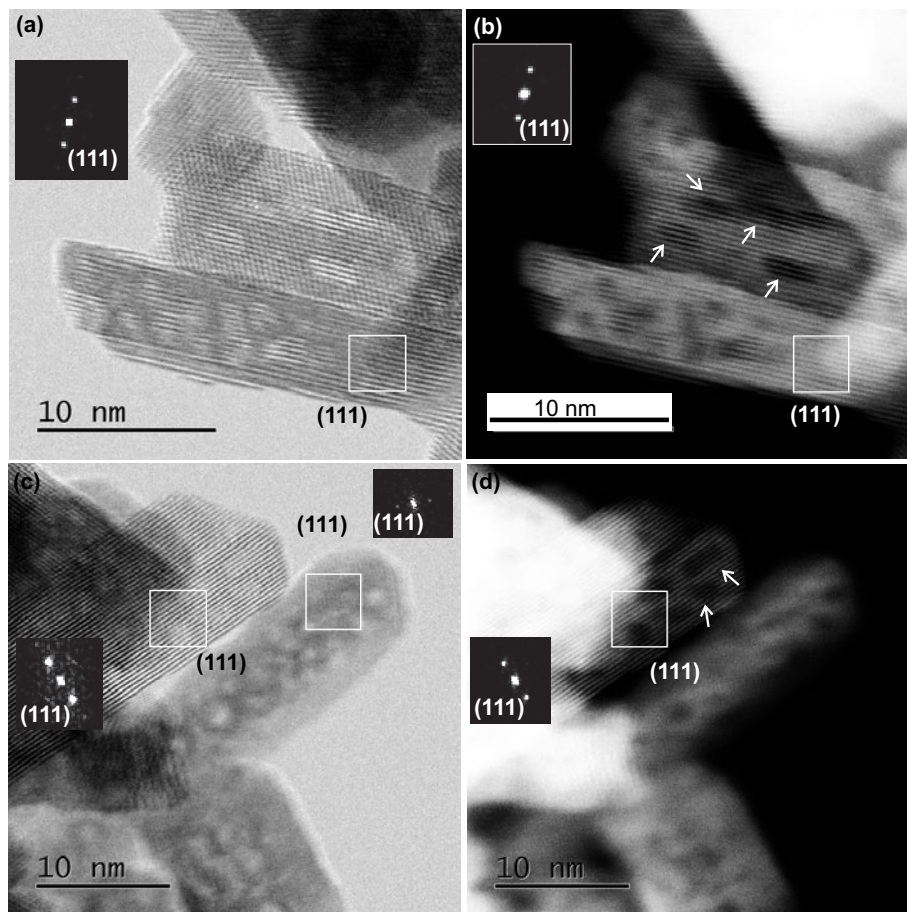


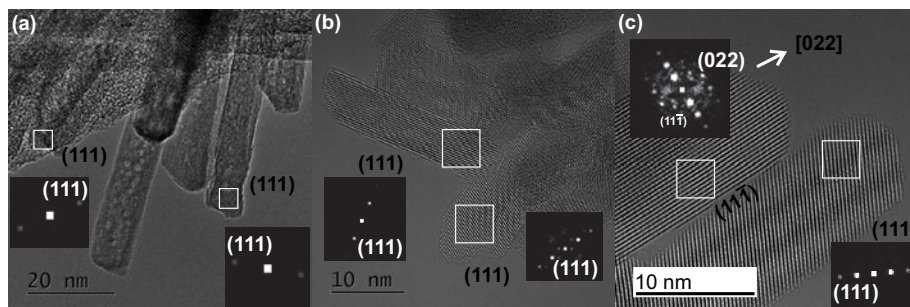
**Figure 2.7:** STEM images of CeO<sub>2</sub> rods. (a, c) BF images, (b, d) HAADF images. The inset in the figures is the FFT that allows indexing of the lattice planes. The rods expose (111) surfaces and have surface steps along the length. Areas of light contrast can be seen in the BF image and these same areas look dark in the HAADF image. The HAADF images confirm that these low-contrast features are voids in the CeO<sub>2</sub> rods that are bounded by (111) surfaces. The contrast variation in the HAADF image suggests a rectangular profile in the cross-section.

numerous other images that confirm the growth direction to be  $[110]$ ; this is consistent with the crystallography proposed in the literature by Mai *et al.*[20] and Zhou *et al.*[10] These authors have further proposed a rectangular cross-section for the rods that would expose  $(110)$  and  $(100)$  surfaces. However, as can be seen in figures 2.7 and 2.8, our results show only  $\{111\}$  surfaces exposed by rods prepared according to Mai's recipe. In all of the images we analyzed, we did not observe a well-defined  $\{110\}$  facet in any of the rods we imaged. To visualize the top and bottom surfaces of these rods, we prepared a cross-section sample by embedding the rods in epoxy and using a microtome to prepare a cross-section. Figure A2.4 shows the microtomed section where the rods are now embedded in epoxy. We reasoned that some of the rods must lie end-on so we could image their cross sections. Based on their aspect ratio ( $> 20$ ), any features with significantly smaller aspect ratios must represent rods. Because the rods are long, we could not achieve lattice resolution in the end-on views because the samples became too thick. We note that there are other proposed models for  $\text{CeO}_2$  rods based on multiply twinned structures;[55] however, because the rods all show contiguous lattice fringes along their length, they cannot be composed of internally twinned units. We also do not observe the diamond-shaped cross sections suggested by Ta *et al.*[42] because the thickness variation seen in our HAADF images does not agree with such a cross-section. Based on our results, we can state that the only prominent well-defined facet visible is the  $\{111\}$  surface, with the other surfaces being irregular and not well-defined.

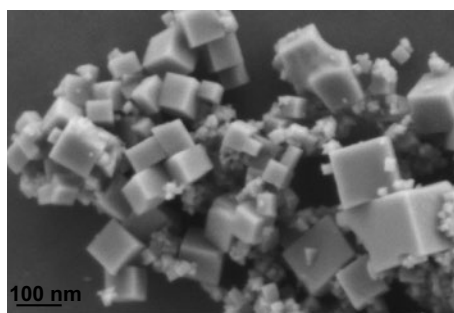
### 2.3.3 Cubes

Figure 2.9 shows a HRSEM image of the cubes. Well-defined cubic crystals range in size from 10 – 100 nm. The image also shows many smaller cubes giving rise to a bimodal particle size distribution, which may explain the the asymmetric peaks seen in the XRD pattern (see figure A2.1). Figure 2.10 shows an image of a cube oriented along the cube edge. It is composed of  $\{100\}$  surfaces, but the corner at which a  $(110)$  surface would be expected is not well-defined. We have included insets showing the atomic arrangement of the  $\text{CeO}_2$  structure indicating that the  $(100)$  surface is not corrugated but perfectly matches what would be expected from a row of Ce atoms. Because the  $(100)$  surface is polar, the charge imbalance can be

## 2.3. RESULTS AND DISCUSSION



**Figure 2.8:** AC-TEM images of CeO<sub>2</sub> rods at two different magnifications [(a) and (b)]. Insets in the figures are FFTs of the boxed region in the images. (c) The lattice fringes confirm that the surfaces are {111} and the growth direction is  $\langle 110 \rangle$ . The other images likewise show only {111} surface facets.



**Figure 2.9:** HRSEM image of cubes.

compensated by incomplete surface termination. As a result, we see incompletely occupied rows of Ce atoms at the surface instead of a fully occupied row of atoms as seen on the {111} surfaces.

### 2.3.4 WGS reactivity measurements

To investigate the catalytic behavior, the samples were tested in the WGS reaction. CeO<sub>2</sub> is known to be an excellent support for noble metals for this reaction.[16] However, there are no reports of WGS reactivity on shape-controlled CeO<sub>2</sub> nanoparticles without added precious metals. Researchers in the past have tested these CeO<sub>2</sub> shapes for the CO/NO oxidation/reduction reaction, which are known to be influenced by the OSC and defects in the CeO<sub>2</sub> surfaces.[9, 12, 30]

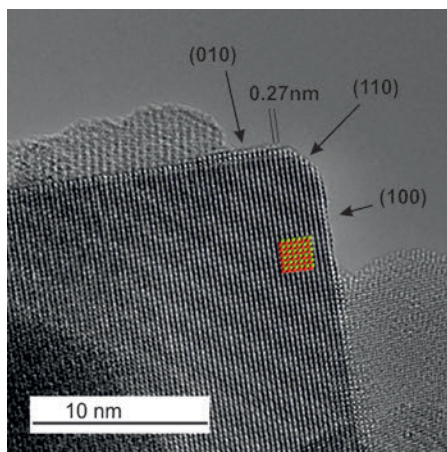


**Figure 2.10:** AC-TEM image of a cube nearly oriented along its cube axis [010]. The (100) surfaces can be clearly seen. They show single-atoms steps but no other form of surface reconstruction [i.e., into (111) facets]. The (110) surface is indicated at the cube corner, but it does not appear to be a well-defined facet. The structure of  $\text{CeO}_2$  along the [010] direction is also included as an inset, to show the agreement with the white atom contrast on the right side of the image. The higher magnification view shows the arrangement of Ce (green) and O atoms (red).

The literature suggests that WGS involves active hydroxyl species (OH) on the  $\text{CeO}_2$  surface.[56–59] We have previously reported that the interaction of OH species with CO depends on the specific  $\text{CeO}_2$  nanoshapes.[32] For this reason, WGS was chosen as a suitable probe reaction for evaluating the role of the  $\text{CeO}_2$  surface on catalytic activity.

WGS catalytic measurements performed at 350°C after hydrogen pretreatment (see the Section 2.2 for pretreatment details) are shown in figure 2.11. The activity of the samples was expressed in mol CO per  $\text{m}^2$  of  $\text{CeO}_2$  to be able to correlate the surface structure with activity. The BET surface areas of  $\text{CeO}_2$  rods, octahedra, and cubes were 80, 58, and  $10 \text{ m}^2/\text{g}$ , respectively. Strikingly, the specific CO conversion rates for octahedra and rods are identical, whereas cubes are twice more active per surface area at 350°C. For cubes, a slight deactivation in the first half hour was observed, but otherwise all three samples show stable conversion over several hours. The  $\text{CeO}_2$  nanoshapes preserved their shapes during reaction, as evident from TEM images of samples after reaction (see the Appendix, figure A2.5).

## 2.3. RESULTS AND DISCUSSION

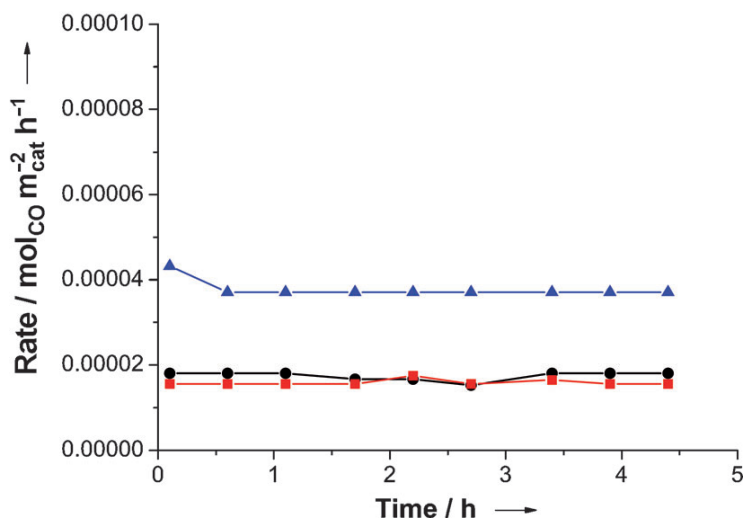


**Figure 2.11:** Rate of CO conversion per m<sup>2</sup> during WGS reaction for rods (red), octahedra (black), and cubes (blue) at 350°C after H<sub>2</sub> pretreatment at 500°C.

The activity trends are consistent with our observations from AC-TEM on the exposed surfaces of the three CeO<sub>2</sub> shapes. The similar specific catalytic activities for rods and octahedra can be explained by the dominance of exposed {111} surfaces. The higher catalytic activity, generally expressed as CO conversion per gram of catalyst, of rods reported in the literature[1, 10, 11] thus may be caused by the high surface area rather than the type of exposed crystal planes. On the other hand, CeO<sub>2</sub> cubes expose the highly active {100} surfaces, which clearly show enhanced specific WGS activity compared to the stable {111} surfaces. It should be recognized that the surface reactivity is not only determined by the exposed planes but also by the sub-surface structure and the nature of defects. These features may also determine reducibility, oxygen-vacancy formation and catalytic activity. The WGS mechanism over CeO<sub>2</sub> nanoshapes and the nature of the reactive surface intermediates is currently under investigation and will be reported in the future.

### 2.3.5 FTIR spectroscopy

To characterize the chemistry of the exposed planes of the reduced CeO<sub>2</sub> nanoshapes in more detail, Fourier transform infrared spectroscopy (FTIR) at 350°C

was performed. The experimental conditions chosen for FTIR were the same as for WGS to gain spectroscopic insight related to the interaction of CeO<sub>2</sub> surfaces with CO/H<sub>2</sub>O molecules during WGS catalytic reaction. The spectra have not been normalized to the surface area because the observed intensity was not only caused by the amount of species present but also by the light scattering properties of these nanoshapes, which are both size and shape dependent.[60]

### **After H<sub>2</sub> reduction, in flowing helium at 350°C**

Transmission FTIR data of the H<sub>2</sub>-reduced (for details see the Experimental Section) CeO<sub>2</sub> nanoshapes in a helium flow at 350°C are displayed in Figure 2.12 (black lines). Figure 2.12a-c shows the range of O-H stretch vibrations between 3800 – 3000 cm<sup>-1</sup>. The three nanoshapes show distinct OH stretching bands, with different intensities depending on the specific shape.

The hydroxyl stretch regions for octahedra and rods look quite similar, showing a strong band at 3639 cm<sup>-1</sup> for bridging hydroxyls, with a shoulder at 3669 cm<sup>-1</sup> arising from single-coordinated hydroxyl species.[61,62] In addition, both samples show multi-bonded and hydrogen bonded OH species between 3600 and 3000 cm<sup>-1</sup>. [32] CeO<sub>2</sub> rods have a significant higher intensity for the multi-bonded hydroxyl species at 3454 cm<sup>-1</sup> than octahedra. The higher amount of bridging OH groups for rods is most likely attributable to the voids and surface roughness observed with AC-TEM (figures 2.7 and 2.8).

The hydroxyl region for cubes (figure 2.12c) looks more complex than those for octahedra and rods. Closer examination reveals that cubes have the same OH bands as rods but with different relative intensities. In addition, three additional pronounced hydroxyl bands at 3738, 3602 and 3253 cm<sup>-1</sup> are observed for cubes.

So far, these specific hydroxyl bands have not been individually assigned in the literature. The different surface termination for CeO<sub>2</sub> {111} and CeO<sub>2</sub> {100} most likely explains why cubes show specific hydroxyl bands more strongly than rods and octahedra. The CeO<sub>2</sub> (111) surface has both Ce and O exposed in the top layer, whereas CeO<sub>2</sub> (100) is either O terminated or Ce terminated (see the Appendix, figure A2.6). These different surface terminations will lead to hydroxyl groups with different stretching frequency. Thus, the FTIR spectra show that rods and octahedra resemble each other in surface termination, as evidenced by the

## 2.3. RESULTS AND DISCUSSION

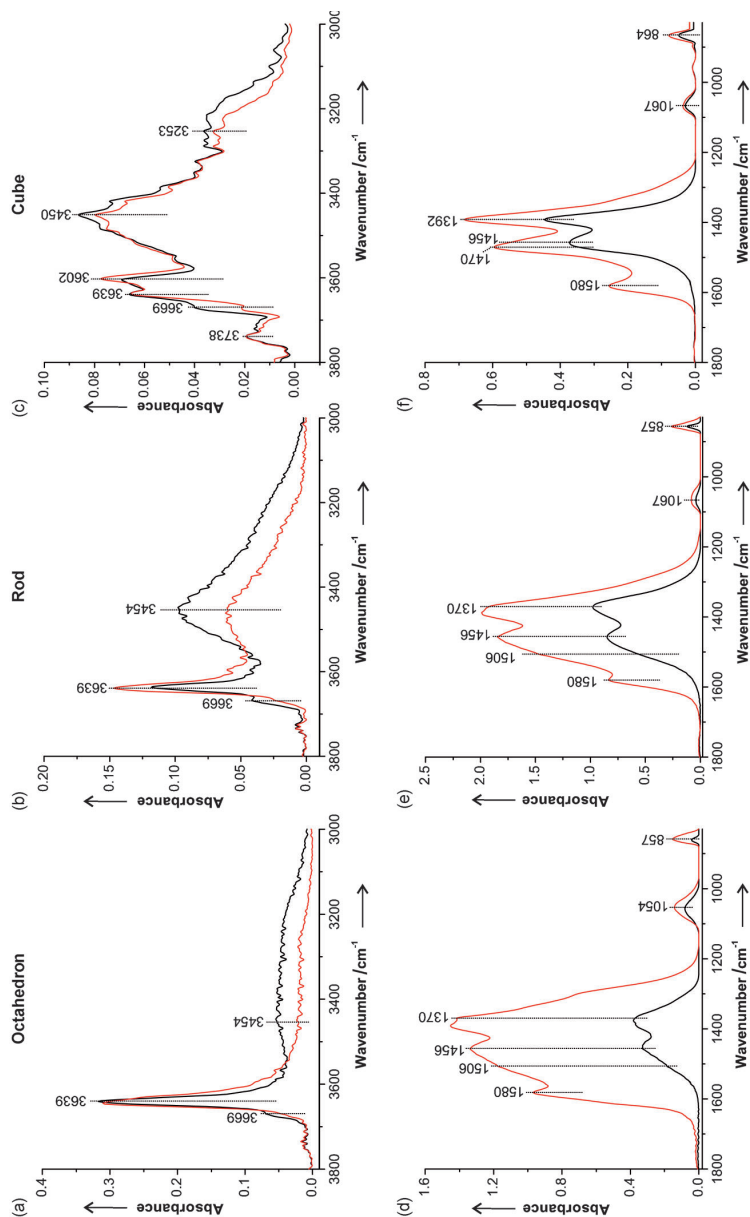


**Figure 2.12:** Baseline corrected *in situ* FTIR spectra at 350°C of  $\text{H}_2$ -reduced  $\text{CeO}_2$  rods, octahedra, and cubes in He flow (black spectrum) followed by 33 vol%  $\text{CO}/\text{He}$  (red spectrum) from (a)-(c) 3800 – 3000  $\text{cm}^{-1}$  (hydroxyl region) and (d)-(f) 1800 – 800  $\text{cm}^{-1}$  (carbonates and formates region).

hydroxyl vibration bands, whereas cubes clearly have a different distribution of the surface OH groups.

Figure 2.12 d-f (black lines) show the stretching and deformation bands of carbonates ( $1800 - 800\text{cm}^{-1}$ ) for octahedra, rod, and cubes.[63] These carbonate species were formed on the fresh  $\text{CeO}_2$  samples due to interaction with atmospheric  $\text{CO}_2$  when exposed to air.[32, 61] Clearly, these carbonates are stable towards the reduction treatment in hydrogen. In comparison to our previous work on fresh  $\text{CeO}_2$  samples at  $200^\circ\text{C}$ , reduced  $\text{CeO}_2$  nanoshapes are cleaner due to the decomposition of some additional carbonates during hydrogen pretreatment at higher temperatures.[32] Although the bands look similar for the three samples, cubes clearly exhibit sharper carbonate bands at slightly different positions (maxima at  $1392$  and  $1456\text{cm}^{-1}$ ) than octahedra and rods ( $1370$  and  $1456\text{cm}^{-1}$ ).

### CO adsorption at $350^\circ\text{C}$

After 30 min in helium flow at  $350^\circ\text{C}$ , the  $\text{CeO}_2$  nanoshapes were exposed to CO and the FTIR spectra after 30 min in CO are shown in figure 2.12 (red lines). Only subtle changes are observed in the OH region upon exposure to CO (figure 2.12a-c). For octahedra and rods, the broad band related to multi-coordinated and hydrogen bonded hydroxyls decreased in intensity. For rods, a slight and increased intensity for bridged OH groups ( $3639\text{cm}^{-1}$ ) can be seen. For cubes, a minor decrease in the hydrogen bonded hydroxyl groups ( $3253\text{cm}^{-1}$ ) was found. All three nanoshapes show a significant decrease in intensity for single-coordinated OH groups at  $3669\text{cm}^{-1}$ .

The interaction of CO with OH groups leads to the formation of adsorbed formate species as evidenced by the band at  $1580\text{cm}^{-1}$  in figure 2.12d-f and C-H stretching bands at  $2846$  and  $2932\text{cm}^{-1}$  (figure A2.7).[16, 64] In addition to formates, carbonates are formed upon exposure of the nanoshapes to CO (figure 2.12d-f). The spectral fingerprint for the carbonates after exposure to CO is very similar for octahedra and rods, with multiple bands between  $1600$  and  $1200\text{cm}^{-1}$ . For  $\text{CeO}_2$  cubes, the two bands initially present increased in intensity. CO adsorption on fresh  $\text{CeO}_2$  shapes at  $200^\circ\text{C}$  followed a similar trend, although exact band positions and shapes were different.[32] The formate and carbonate bands on cubes are relatively narrow compared to the formate and carbonate on

## 2.4. CONCLUSIONS

octahedra and rods. This suggests, in combination with the well-resolved OH vibrations, that the surface adsorption sites on cubes are more distinct than on the other two shapes.

The AC-TEM results in this study show that rods and octahedra expose  $\{111\}$  surface planes that result in similar catalytic WGS activities per  $\text{m}^2$ . In addition, the type of hydroxyl species present and the surface interaction with CO on octahedra and rods are similar, which is consistent with the identical WGS activities per  $\text{m}^2$  (figure 2.11). Cubes consist of the more reactive  $\{100\}$  surface planes, which have different OH bands and interactions with CO, resulting in a higher WGS reactivity per  $\text{m}^2$ .

## 2.4 Conclusions

We used aberration-corrected TEM and HAADF STEM to investigate the morphology of shape-controlled  $\text{CeO}_2$  nanoparticles. Although differently shaped  $\text{CeO}_2$  particles were generated, we found that the WGS activity normalized per  $\text{m}^2$  was identical for  $\text{CeO}_2$  octahedra and rods, whereas  $\text{CeO}_2$  cubes were much more reactive. Likewise, FTIR data of adsorbed CO and OH groups show a similar surface structure and reactivity for rods and octahedra, which were again different from the cubes. A detailed investigation of the  $\text{CeO}_2$  nanoparticles was conducted by AC-TEM and AC-STEM. The exposed surfaces were identified, and the nature of the surfaces examined at atomic resolution. The TEM observations help us explain the reactivity trends, as we found that both  $\text{CeO}_2$  octahedra and rods expose  $\{111\}$  surfaces. On the other hand, the  $\text{CeO}_2$  cubes expose  $\{100\}$  surfaces, which are consistent with their cubic habits. The combination of WGS reactivity and FTIR and TEM measurements help us to reveal the true nature of the exposed surfaces in these  $\text{CeO}_2$  nanoparticles.

## Appendix 2

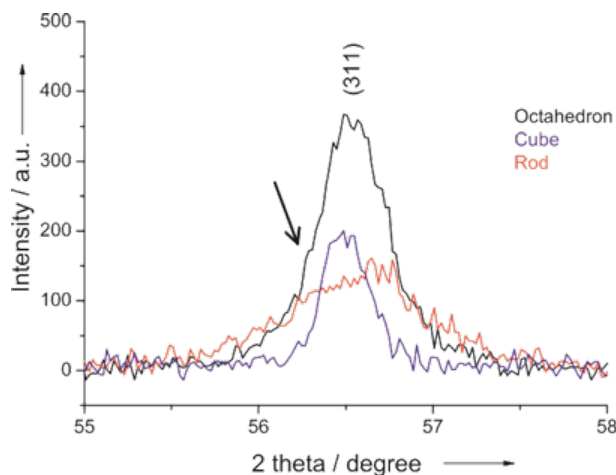


**Figure A2.1:** Expanded view of the (311) reflection in the XRD patterns of the  $\text{CeO}_2$  samples. The peak asymmetry can be clearly seen and the presence of the shoulder on the left (pointed with an arrow) indicates that a portion of the sample has an expanded lattice constant.

**Table A2.1:** Summary of BET surface areas ( $\text{m}^2/\text{g}$ ) and average particle size (nm, calculated using Scherrer analysis) values reported in literature[11, 25, 30, 31, 35–37, 49, 50, 65, 66] for ceria rods and cubes synthesized using the Mai *et al.* recipe[20].

BET ( $\text{m}^2/\text{g}$ )	Rod		Cube		Calcination temperature ( $^\circ\text{C}$ )	Reference
	BET ( $\text{m}^2/\text{g}$ )	Particle size (nm)	BET ( $\text{m}^2/\text{g}$ )	Particle size (nm)		
56		16.4	21	31.2	350	[31]
93		11	29	43	400	[11]
79		11	24	95	400	[30]
93		11	29	43	400	[66]
110		8	24	35	500	[36]
130		10	14	75	500	[35]
76		16	20	46	500	[49]
66.7		-	35.9	-	500	[37]
43		22	11	48	600	[65]
62		-	30	-	600	[25]
74		9.1	13	37.3	-	[50]
<b>Mean = 80</b>	<b>Mean = 13</b>		<b>Mean = 23</b>	<b>Mean = 50</b>		
<b>SD = 25</b>	<b>SD = 5</b>		<b>SD = 8</b>	<b>SD = 21</b>		

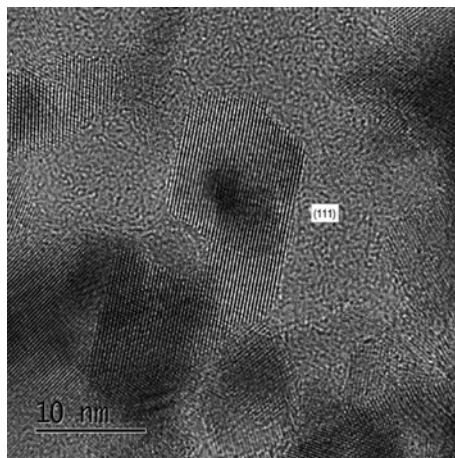


**Figure A2.2:** AC-TEM image of CeO<sub>2</sub> octahedra showing that the smaller particles (~ 1 nm) also expose prominent (111) facets. The shapes are not as well defined as the larger octahedra imaged by HRSEM (figures 2.2 and 2.3). The exposure of two parallel (111) surfaces with the other surfaces being irregular is also a common feature, and it is expected that the rod cross section also has this same characteristic.

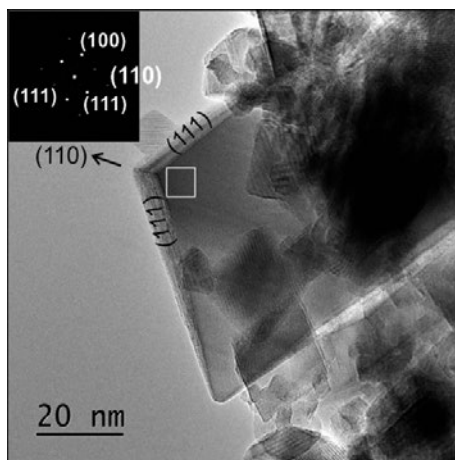


**Figure A2.3:** AC-TEM image shows that the smallest particles as well as the larger ones exhibit well-defined facets with smooth surfaces. These particles all expose prominent (111) surface facets and the (110) facet is missing, and instead we see a sharp corner.

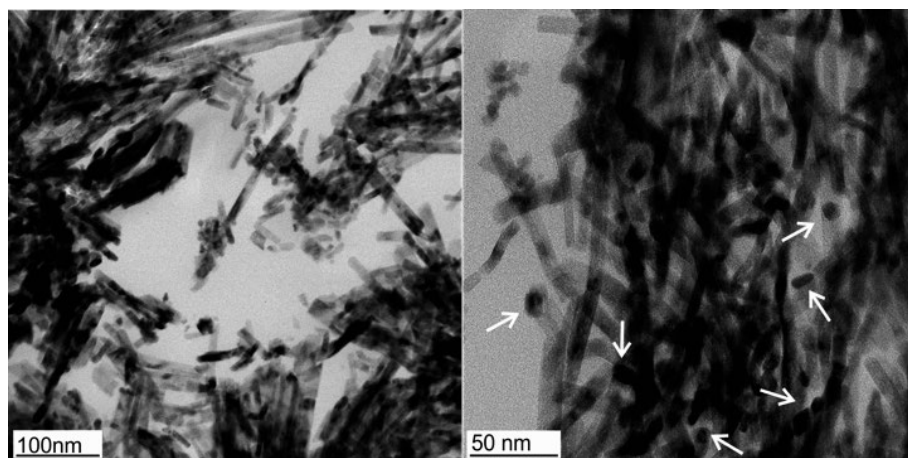


**Figure A2.4:** TEM images of microtomed sections of  $\text{CeO}_2$  rods embedded in epoxy. These sections provide an opportunity to see the rods end-on. The image on the right shows some of the rods end-on (i.e. those with a short aspect ratio), allowing us to image the rods in cross-section. Since the rods are thick when viewed end-on, it is not possible to obtain HRTEM images.

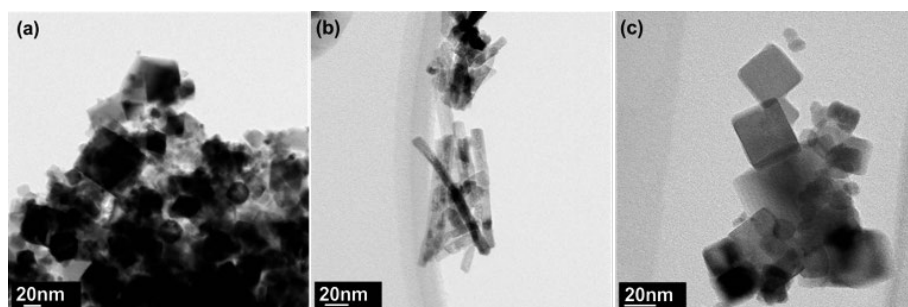


**Figure A2.5:** TEM of ceria (a) octahedra, (b) rods and (c) cubes after water gas shift (WGS) reaction. The ceria nanoshapes retain their morphology after the WGS testing at  $350^\circ\text{C}$ .

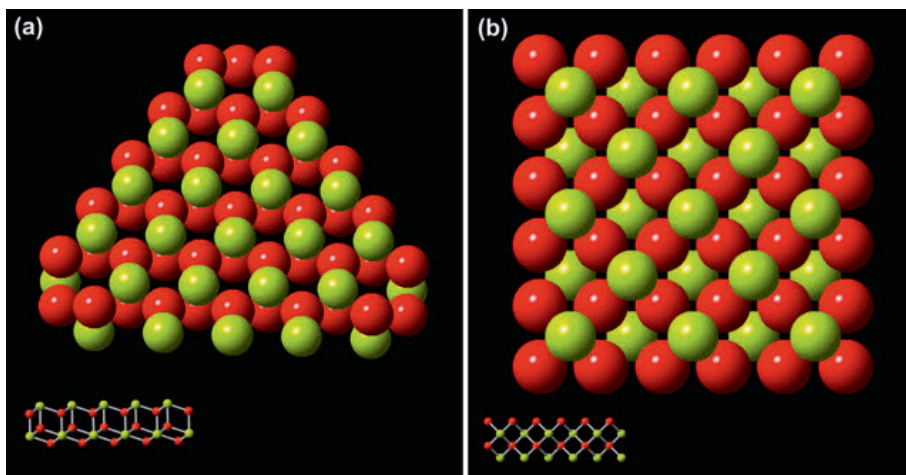


**Figure A2.6:** The lattice models show the arrangement of Ce (green) and O (red) atoms. (a) Top down view of CeO<sub>2</sub> (111). (b) Top down view of CeO<sub>2</sub> (100) surface. Insets show ball and stick models of the side view of (111) and (100) surfaces respectively. The CeO<sub>2</sub> (111) surface has both Ce and O exposed in the top layer, whereas CeO<sub>2</sub> (100) is either O terminated or Ce terminated. These structures were drawn using CrystalMaker software.

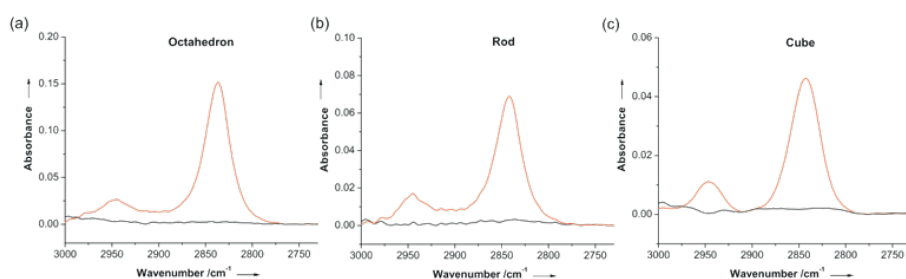


**Figure A2.7:** Baseline corrected *in situ* FTIR spectra at 350°C of H<sub>2</sub> reduced ceria (a) octahedron, (b) rod and (c) cube in He flow (black spectrum) followed by 33 vol% CO/He (red spectrum) from 3000 – 2730 cm<sup>-1</sup> (C-H formate) region.

## Bibliography

- [1] Tana, Zhang, M., Li, J., Li, H., Li, Y., and Shen, W. (2009) *Catal. Today* **148(1-2)**, 179–183.
- [2] de Lima, J. F., Martins, R. F., Neri, C. R., and Serra, O. A. (2009) *Applied Surf. Sci.* **255(22)**, 9006–9009.
- [3] Izu, N., Shin, W., Murayama, N., and Kanzaki, S. (2002) *Sens. Actuators, B* **87(1)**, 95–98.
- [4] Beie, H.-J. and Gnörich, A. (1991) *Sens. Actuators, B* **4(3-4)**, 393–399.
- [5] Karakoti, A., Monteiro-Riviere, N., Aggarwal, R., Davis, J., Narayan, R., Self, W., McGinnis, J., and Seal, S. (2008) *JOM* **60(3)**, 33–37.
- [6] Diwell, A., Rajaram, R., Shaw, H., and Truex, T. (1991) The role of ceria in three-way catalysts In A. Crucq, (ed.), *Studies in Surf. Sci. and Catalysis*, volume **71**, pp. 139–152 Elsevier.
- [7] Xia, C. and Liu, M. (2002) *Solid State Ionics* **152-153**, 423–430.
- [8] Steele, B. (1994) *J. Power Sources* **49(1-3)**, 1–14.
- [9] Liu, X., Zhou, K., Wang, L., Wang, B., and Li, Y. (2009) *J. Am. Chem. Soc.* **131(9)**, 3140–3141.
- [10] Zhou, K., Wang, X., Sun, X., Peng, Q., and Li, Y. (2005) *J. Catal.* **229(1)**, 206–212.
- [11] Wu, Z., Li, M., and Overbury, S. H. (2012) *J. Catal.* **285(1)**, 61–73.
- [12] Liu, L., Cao, Y., Sun, W., Yao, Z., Liu, B., Gao, F., and Dong, L. (2011) *Catal. Today* **175(1)**, 48–54.
- [13] Trovarelli, A., de Leitenburg, C., Boaro, M., and Dolcetti, G. (1999) *Catal. Today* **50(2)**, 353–367.
- [14] Gorte, R. and Zhao, S. (2005) *Catal. Today* **104(1)**, 18–24.
- [15] Gorte, R. J. (2010) *AIChE Journal* **56(5)**, 1126–1135.
- [16] Jacobs, G., Patterson, P. M., Williams, L., Sparks, D., and Davis, B. H. (2004) *Catal. Lett.* **96(1-2)**, 97–105.
- [17] Czernik, S., Evans, R., and French, R. (2007) *Catal. Today* **129(3-4)**, 265–268.
- [18] Zhou, K. and Li, Y. (2012) *Angew. Chem., Int. Ed.* **51(3)**, 602–613.
- [19] Tschöpe, A., Liu, W., Flytzanistephanopoulos, M., and Ying, J. (1995) *J. Catal.* **157(1)**, 42–50.
- [20] Mai, H.-X., Sun, L.-D., Zhang, Y.-W., Si, R., Feng, W., Zhang, H.-P., Liu, H.-C., and Yan, C.-H. (2005) *J. Phys. Chem. B* **109(51)**, 24380–24385.
- [21] Zhang, D., Du, X., Shi, L., and Gao, R. (2012) *Dalton Trans.* **41**, 14455–14475.
- [22] Han, W.-Q., Wu, L., and Zhu, Y. (2005) *J. Am. Chem. Soc.* **127(37)**, 12814–12815.
- [23] Sun, C., Li, H., and Chen, L. (2012) *Energy Environ. Sci.* **5**, 8475–8505.
- [24] Wang, Z. L. and Feng, X. (2003) *J. Phys. Chem. B* **107(49)**, 13563–13566.

- [25] Wang, S., Zhao, L., Wang, W., Zhao, Y., Zhang, G., Ma, X., and Gong, J. (2013) *Nanoscale* **5**, 5582–5588.
- [26] Li, H., Lu, G., Dai, Q., Wang, Y., Guo, Y., and Guo, Y. (2010) *ACS Appl. Mater. Interfaces* **2(3)**, 838–846.
- [27] Zhong, L.-S., Hu, J.-S., Cao, A.-M., Liu, Q., Song, W.-G., and Wan, L.-J. (2007) *Chem. Mater.* **19(7)**, 1648–1655.
- [28] Yang, Z., Zhou, K., Liu, X., Tian, Q., Lu, D., and Yang, S. (2007) *Nanotechnology* **18(18)**, 185606.
- [29] Yang, Z., Woo, T. K., Baudin, M., and Hermansson, K. (2004) *J. Chem. Phys.* **120(16)**, 7741–7749.
- [30] Wu, Z., Li, M., Howe, J., Meyer, H. M., and Overbury, S. H. (2010) *Langmuir* **26(21)**, 16595–16606.
- [31] Dai, Q., Huang, H., Zhu, Y., Deng, W., Bai, S., Wang, X., and Lu, G. (2012) *Appl. Catal., B* **117-118**, 360–368.
- [32] Agarwal, S., Lefferts, L., and Mojet, B. L. (2013) *ChemCatChem* **5(2)**, 479–489.
- [33] Si, R. and Flytzani-Stephanopoulos, M. (2008) *Angew. Chem.* **120(15)**, 2926–2929.
- [34] Yi, G., Yang, H., Li, B., Lin, H., Tanaka, K., and Yuan, Y. (2010) *Catal. Today* **157(1-4)**, 83–88.
- [35] Ciftci, A., Ligthart, D. M., Pastorino, P., and Hensen, E. J. (2013) *Appl. Catal., B* **130-131**, 325–335.
- [36] Guan, Y., Ligthart, D. M., Pirgon-Galin, Ö., Pieterse, J. A., Santen, R. A., and Hensen, E. J. (2011) *Top. Catal.* **54(5-7)**, 424–438.
- [37] Chang, S., Li, M., Hua, Q., Zhang, L., Ma, Y., Ye, B., and Huang, W. (2012) *J. Catal.* **293**, 195–204.
- [38] Han, J., Kim, H. J., Yoon, S., and Lee, H. (2011) *J. Mol. Catal. A: Chem.* **335(1-2)**, 82–88.
- [39] Han, W.-Q., Wen, W., Hanson, J. C., Teng, X., Marinkovic, N., and Rodriguez, J. A. (2009) *J. Phys. Chem. C* **113(52)**, 21949–21955.
- [40] Yi, G., Xu, Z., Guo, G., Tanaka, K., and Yuan, Y. (2009) *Chem. Phys. Lett.* **479(1-3)**, 128–132.
- [41] Yi, N., Si, R., Saltsburg, H., and Flytzani-Stephanopoulos, M. (2010) *Energy Environ. Sci.* **3**, 83–837.
- [42] Ta, N., Liu, J. J., Chenna, S., Crozier, P. A., Li, Y., Chen, A., and Shen, W. (2012) *J. Am. Chem. Soc.* **134(51)**, 20585–20588.
- [43] Asahina, S., Takami, S., Otsuka, T., Adschiri, T., and Terasaki, O. (2011) *ChemCatChem* **3(6)**, 1038–1044.
- [44] Pennycook, S. (2012) *Ultramicroscopy* **123**, 28–37.
- [45] Krivanek, O. L., Chisholm, M. F., Murfitt, M. F., and Dellby, N. (2012) *Ultrami-*

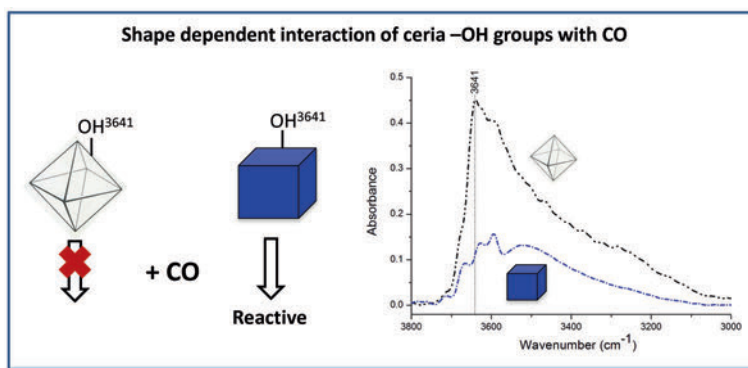
- croscopy* **123**, 90–98.
- [46] Bhatta, U. M., Ross, I. M., Sayle, T. X. T., Sayle, D. C., Parker, S. C., Reid, D., Seal, S., Kumar, A., and Möbus, G. (2012) *ACS Nano* **6(1)**, 421–430.
- [47] Möbus, G., Saghi, Z., Sayle, D. C., Bhatta, U. M., Stringfellow, A., and Sayle, T. X. (2011) *Adv. Funct. Mater.* **21(11)**, 1971–1976.
- [48] JCPDS (2003), vol. PCPDFWIN v. 2.4.
- [49] Gamarra, D., Cámara, A. L., Monte, M., Rasmussen, S., Chinchilla, L., Hungra, A., Munuera, G., Gyorffy, N., Schay, Z., Corberán, V. C., Conesa, J., and Martínez-Arias, A. (2013) *Appl. Catal., B* **130-131**, 224–238.
- [50] Torrente-Murciano, L., Gilbank, A., naPuertolas, B., Garcia, T., Solsona, B., and Chadwick, D. (2013) *Appl. Catal., B* **132-133**, 116–122.
- [51] Désaunay, T., Bonura, G., Chiodo, V., Freni, S., Couzinié, J.-P., Bourgon, J., Ringuedé, A., Labat, F., Adamo, C., and Cassir, M. (2013) *J. Catal.* **297**, 193–201.
- [52] Tsunekawa, S., Ishikawa, K., Li, Z.-Q., Kawazoe, Y., and Kasuya, A. (2000) *Phys. Rev. Lett.* **85**, 3440–3443.
- [53] Tan, J. P. Y., Tan, H. R., Boothroyd, C., Foo, Y. L., He, C. B., and Lin, M. (2011) *J. Phys. Chem. C* **115(9)**, 3544–3551.
- [54] Florea, I., Feral-Martin, C., Majimel, J., Ihiawakrim, D., Hirlimann, C., and Ersen, O. (2013) *Cryst. Growth Des.* **13(3)**, 1110–1121.
- [55] Bugayeva, N. (2005) *Mater. Res. Soc. Symp. Proc.* **876**, 195–200.
- [56] Azzam, K., Babich, I., Seshan, K., and Lefferts, L. (2007) *J. Catal.* **251(1)**, 153–162.
- [57] Azzam, K., Babich, I., Seshan, K., and Lefferts, L. (2007) *J. Catal.* **251(1)**, 163–171.
- [58] Jacobs, G., Chenu, E., Patterson, P. M., Williams, L., Sparks, D., Thomas, G., and Davis, B. H. (2004) *Appl. Catal., A* **258(2)**, 203–214.
- [59] Shido, T. and Iwasawa, Y. (1992) *J. Catal.* **136(2)**, 493–503.
- [60] Yang, P., Wei, H., Huang, H.-L., Baum, B. A., Hu, Y. X., Kattawar, G. W., Mishchenko, M. I., and Fu, Q. (2005) *Appl. Opt.* **44(26)**, 5512–5523.
- [61] Binet, C., Daturi, M., and Lavalley, J.-C. (1999) *Catal. Today* **50(2)**, 207–225.
- [62] Badri, A., Binet, C., and Lavalley, J.-C. (1996) *J. Chem. Soc., Faraday Trans.* **92**, 4669–4673.
- [63] Vayssilov, G. N., Mihaylov, M., Petkov, P. S., Hadjiivanov, K. I., and Neyman, K. M. (2011) *J. Phys. Chem. C* **115(47)**, 23435–23454.
- [64] Binet, C., Jadi, A., and Lavalley, J.-C. (1992) *J. Chim. Phys. Phys. - Chim. Biol.* **89**, 1779–1797.
- [65] Snell, R. W., Hakim, S. H., Dumesic, J. A., and Shanks, B. H. (2013) *Appl. Catal., A* **464-465**, 288–295.
- [66] Wu, Z., Li, M., Mullins, D. R., and Overbury, S. H. (2012) *ACS Catal.* **2(11)**, 2224–2234.

# 3

## Ceria nanocatalysts: Shape dependent reactivity and formation of hydroxyl groups

### Research question:

Are the active hydroxyl species on ceria shape-dependent?



*Now we know which planes are exposed, we turn our attention to the types of hydroxyl species that are present, as a function of nanoshape. This helps identify shape-dependent performance because hydroxyl species are the active sites in ceria-supported catalytic reactions.*

\*Published as: S. Agarwal, L. Lefferts, & B.L. Mojet, "Ceria Nanocatalysts: Shape Dependent Reactivity and Formation of OH," *ChemCatChem* **5**, 479–489 (2013)

## Abstract

*Ceria nanoshapes (octahedra, wires and cubes) were investigated for CO adsorption and subsequent reaction with water. Surprisingly, the reactivity of specific OH groups was explicitly determined by the ceria nanoshape. The nanoshapes showed different levels of carbonates and formates after exposure to CO, the amount of carbonates increasing from octahedra  $\ll$  wires  $<$  cubes. Subsequent reaction with water at 200°C was also found to be shape dependent, resulting in different amounts of recovered OH groups and removed carbonates and formates on the different ceria nanoshapes.*

## 3.1 Introduction

Cerium oxide ( $\text{CeO}_2$ ) is a key component of various commercial catalysts and catalyst supports, used for applications such as three-way automotive exhaust catalysts (TWC), oxygen sensors, solid electrolytes for low temperature solid oxide fuel cells (SOFC), UV block, oxidation of CO and hydrocarbons, and low temperature water gas shift reaction (WGS).[1–12] The unique catalytic behavior of  $\text{CeO}_2$  is a result of its excellent redox property and high oxygen storage capacity (OSC) because it can quickly switch oxidation state between  $\text{Ce}^{4+}$  and  $\text{Ce}^{3+}$  in a stable fluorite structure.[13]

With the development of nanotechnology, successful effort has been made to synthesize ceria nanocrystals with controlled crystallographic planes that show new and improved chemical properties.[13–18] It has been reported that catalytic activity for CO oxidation is greatly enhanced by tuning the dimension and morphology of the  $\text{CeO}_2$ , due to the presence of the highly active (110) and (100) surface planes.[4, 8]

In the 1980s, detailed spectroscopic investigations had already been performed on polycrystalline  $\text{CeO}_2$ . [19, 20] Sakata *et al.* studied the surface species formed when CO and  $\text{CO}_2$  were exposed to polycrystalline  $\text{CeO}_2$ . A few years later, Binet *et al.* extensively studied polycrystalline ceria in oxidized and reduced states, describing the type of surface hydroxyl species and carbon species formed in the presence of CO and  $\text{CO}_2$ . [21–24] More recently, the formation of different types of carbonate, formate (via unstable intermediate, formyl species), and carboxylate

## 3.2. EXPERIMENTAL SECTION

species was theoretically and experimentally identified on hydroxylated polycrystalline  $\text{CeO}_2$  upon exposure of CO and  $\text{CO}_2$ . [25] Recently, an FTIR spectroscopy study reported on the surface species formed when CO was exposed to  $\text{CeO}_2$  nano-shapes. [26]

Furthermore, several fundamental investigations, such as adsorption of probe molecules such as CO,  $\text{H}_2\text{O}$ , acetone, formic acid, etc, and even the water gas shift reaction have been studied on epitaxially grown ceria thin films in ultra high vacuum. [6, 27–31] Although these plane-specific investigations give a glimpse of the fundamental surface-related behavior of  $\text{CeO}_2$ , the conditions of those experiments (ultra high vacuum) are far from real catalytic conditions.

So far, the specific reactivity of hydroxyl groups on the different ceria morphologies has not been studied in-depth. The goal of the present work is to determine the effect of different ceria nanoshapes on their surface composition, emphasizing on the reactivity of the surface hydroxyl species towards CO and subsequent interaction with water.

## 3.2 Experimental section

### 3.2.1 Catalyst preparation

$\text{CeO}_2$ -wires [13] and cubes [16] were synthesized via the hydrothermal procedure reported in the literature. All materials used were of analytical purity, obtained from Sigma-Aldrich. A fixed amount of  $\text{Ce}(\text{NO}_3)_3 \cdot 6\text{H}_2\text{O}$  (2.17 g for cubes and 1.09 g for wires) and NaOH (24 g for cubes and 20 g for wires) were respectively dissolved in 5 mL and 35 mL of deionized water. The solutions were mixed and stirred for 30 min, which resulted in the formation of milky slurry. The resulting liquid was then transferred to an autoclave (125 mL) and filled with deionized water up to 80% of the total volume of autoclave. The solution was subjected to hydrothermal treatment at temperatures of  $100^\circ\text{C}$  (for synthesizing wire) and  $180^\circ\text{C}$  (for synthesizing cubes) for 24 h. After the hydrothermal treatment, fresh white precipitates were separated by centrifugation, washed with deionized water several times to remove any possible ionic residues, followed by washing in ethanol and then drying at  $60^\circ\text{C}$  in air overnight. After drying, the products were yellow powders. The reference shape used in this study was  $\text{CeO}_2$  octahedra (99.9% pure),

which was obtained from Sigma-Aldrich, with an average particle size  $< 25$  nm. The samples were calcined at  $500^{\circ}\text{C}$  (heating rate  $5\text{ K/min}$ ) for 4 h in synthetic air (flow rate =  $50\text{ mL/min}$ ) and subsequently cooled down to room temperature in air before use in this study.

### 3.2.2 TEM, BET and XRD characterization

Transmission electronic microscopy (TEM) images were obtained on a Philips CM300ST-FEG electron microscope operated at an acceleration voltage of  $300\text{ kV}$ . Samples for TEM measurements were ultrasonically dispersed in ethanol and subsequently droplets of the suspension were deposited on a copper grid coated with carbon. The high resolution scanning electron microscope (HRSEM) images of the ceria nanoparticles were recorded on a Carl Zeiss Merlin FE-SEM.

BET surface areas of the samples were determined with nitrogen physisorption using a Micromeritics Tristar instrument. The samples were out-gassed in vacuum at  $300^{\circ}\text{C}$  for 24 h prior to analysis.

X-Ray diffraction patterns were recorded with a Bruker D2 Phaser diffractometer using  $\text{Cu K}\alpha$  radiation,  $\lambda = 0.1544\text{ nm}$ . XRD patterns were measured in reflection geometry in the  $2\theta$  range between  $0^{\circ}$  and  $90^{\circ}$ .

### 3.2.3 Raman and FTIR spectroscopy

Raman measurements were conducted with a SENTERRA instrument equipped with a cooled CCD detector ( $-60^{\circ}\text{C}$ ). The samples were excited with a  $532\text{ nm}$  green laser with  $2\text{ mW}$  of power. Spectra were recorded at room temperature in air from  $150$  to  $3500\text{ cm}^{-1}$ , at a resolution of  $9\text{ cm}^{-1}$ .

Transmission FTIR measurements were recorded by using a Bruker Vector 22 with MCT detector by averaging 128 scans with a spectral resolution of  $4\text{ cm}^{-1}$  and time interval of 120 s. A self-supporting wafer was pressed of about  $\approx 10\text{ mg}$  of sample and placed into a purpose built stainless steel cell. Sample pellets were pre-treated in helium flow ( $20\text{ mL/min}$ ) from room temperature to  $200^{\circ}\text{C}$  (heating rate  $5\text{ K/min}$ ) for 60 min to remove physisorbed water. To avoid moisture in the gases, helium was dried with a Varian Chromopack CP17971 Gas Clean Moisture Filter.  $33\text{ vol}\%$   $\text{CO}$  (Hoekloos 4.7) in He (Hoekloos 5.0, total flow  $20\text{ mL/min}$ ) was used for adsorption experiments.

### 3.3. RESULTS AND DISCUSSION

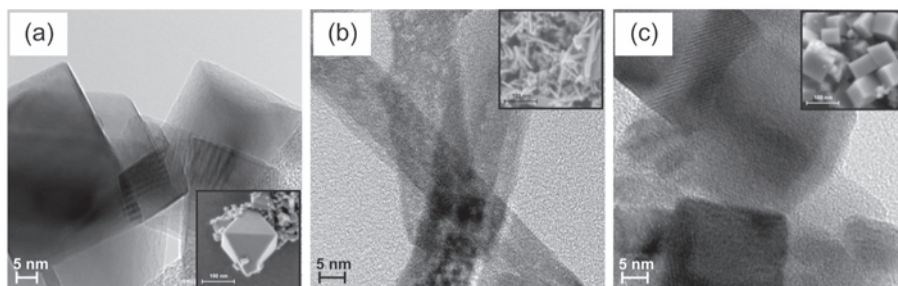


**Figure 3.1:** TEM and HRSEM (inset) images of the CeO<sub>2</sub> octahedra (a), wires (b) and cubes (c).

For the water reactivity experiments, He was flowed through a saturator filled with H<sub>2</sub>O at 5 °C, resulting in water with vapor pressure of 6.8 mmHg. The tubing from the saturator to the cell was heated to 110 °C in order to avoid condensation in the lines.

## 3.3 Results and discussion

### 3.3.1 TEM and BET

TEM and HRSEM images of the ceria nanomaterials after calcination are shown in figure 3.1. In the images the structures of the different shapes are indicated by the solid lines. The ceria samples have octahedral (figure 3.1a), wire (figure 3.1b) and cubic (figure 3.1c) morphologies, which we refer to from now on as octahedra, wires and cubes.

The BET surface areas of wires, octahedra and cubes were respectively 112, 66, and 31 m<sup>2</sup>/g.

### 3.3.2 XRD and Raman

XRD analysis was done at ambient conditions to investigate crystallinity, structure and dominant planes in the ceria nanoshapes. The typical X-ray diffraction patterns for the ceria nanoshapes are shown in figure 3.2. The observed diffraction peaks can all be indexed as face-centered cubic phase CeO<sub>2</sub>.<sup>[32]</sup> The dominant Bragg diffractions at 28.3, 32.9 and 47.1 (2 $\theta$ ) correspond to (111), (200) and (220)

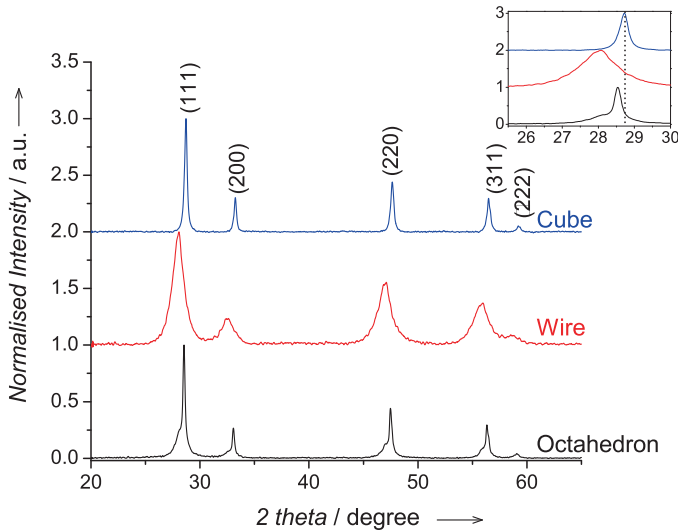


**Figure 3.2:** XRD spectra of the different ceria nanoshapes, normalized to the (111) peaks.

crystal planes, respectively.[32] The three nanoshapes differ in the details of their XRD-patterns. For cubes, the narrowest peaks are observed, while wires exhibit a clear broadening for all reflections. For octahedra, a shoulder can be seen on the left sides of the reflections, which can be attributed to inhomogeneity in the crystal structure. Generally, line broadening in XRD is often attributed to a decrease in particle size in the sample. However, in the present study the different particle shapes cause line broadening because of their different geometries, in agreement with the recent work of Wu *et al.*[32] In addition to the different peak shapes, a shift can be observed for the three samples (see inset figure 3.2). This shift can also be related to the different shapes of the samples, causing specific micro-strain in the ceria lattice.[33, 34]

In addition to XRD, Raman spectra were also taken at room temperature to investigate the ceria lattice vibrations of the different shapes (figure 3.3). For easier comparison, the spectra have been normalized to the main peak at  $465\text{ cm}^{-1}$ . The strong peak at  $465\text{ cm}^{-1}$  is due to the symmetrical stretching mode of  $\text{Ce-O}_8$ , characteristic for the fluorite lattice structure, which is in agreement with the

### 3.3. RESULTS AND DISCUSSION

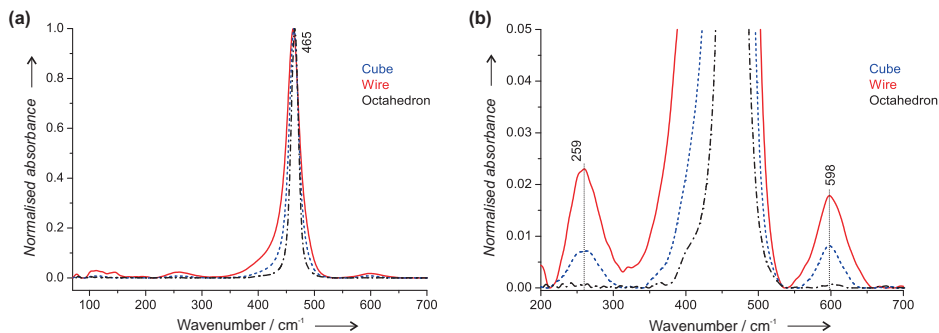


**Figure 3.3:** (a) Raman spectra (532 nm at 2 mW) of ceria cubes (dashed blue), wires (solid red) and octahedra (dash-dotted black) obtained at room temperature in air, normalized to the main peak at  $465\text{ cm}^{-1}$ ; (b) magnification of the wave number range  $200 - 700\text{ cm}^{-1}$ .

XRD-patterns.[35, 36] A clear broadening of the band at  $465\text{ cm}^{-1}$  is observed in the order octahedra < cubes < wires, which, according to literature, is due to inhomogeneous strain broadening associated with the different particle dimensions and phonon confinement.[37] Because of the different geometries of the samples, the line broadening in Raman spectroscopy cannot be directly related primarily to particle sizes of the materials.[38]

A magnification of the smaller peaks between  $200$  and  $700\text{ cm}^{-1}$  can be seen in figure 3.3b. The bands below  $200\text{ cm}^{-1}$  can be attributed to particle scattering. Two additional bands are observed at  $259$  and  $598\text{ cm}^{-1}$ . The peak at  $259\text{ cm}^{-1}$  has been assigned previously to the displacement of oxygen atoms from ideal fluorite lattice positions.[39] The peak at  $598\text{ cm}^{-1}$  indicates the presence of oxygen vacancies in the ceria lattice.[32, 40] The presence of these peaks is a clear indication of local defects and reduced  $\text{Ce}^{3+}$  cations in the cubes and wires. It is clear that different ceria shapes, with other surface planes exposed, have different amounts of defect sites, as has been shown previously.[32, 41] For octahedra (black spectrum in figure 3.3b), no oxygen vacancy or oxygen displacement bands were observed. The relative intensity of both bands increases in the order octahedra < cubes < wires, indicating the highest fraction of oxygen vacancies in ceria wires, consistent with previous studies.[32, 42]

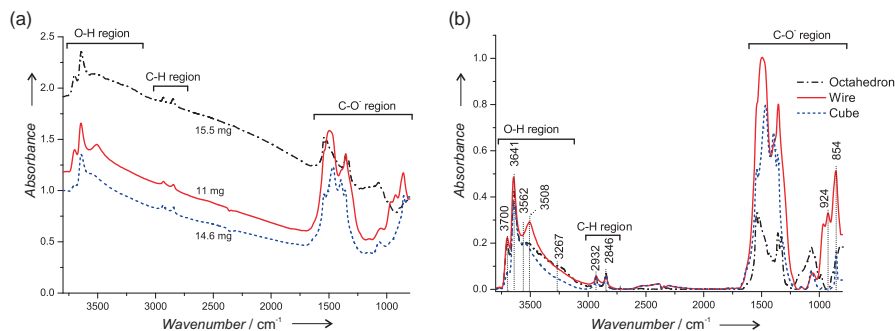


**Figure 3.4:** *In situ* FTIR (a) raw and (b) baseline corrected spectra of ceria cubes (dashed blue), wires (solid red) and octahedra (dash-dotted black spectrum) at 200°C in He flow (after 30 min of flow).

### 3.3.3 FTIR in helium at 200°C

The ceria nanoshapes were characterized with FTIR in helium at 200°C to remove physisorbed water. The transmission FTIR spectra for the different nanoshapes taken with an empty cell as a background are shown in figure 3.4a. The baseline levels of the spectra are not correlated with the amount of sample used to press the pellets. For example, the baseline of 15.5 mg of ceria wires is almost twice in intensity compared to a similar amount of cubes (14.6 mg). In general, the baseline in spectra of solid materials is determined by the light scattering capacity of the solid particles. Thus, in the present case, it can be concluded that the infrared light scattering is largely affected by the particular shape of the ceria particles. Shape specific scattering of infrared light is also known to occur for ice-crystals with different morphologies.[43] In a separate experiment (not shown), we found no linear correlation of peak intensities with sample weight. Thus, the absolute peak intensities cannot be normalized to the amount of sample. Nevertheless, peak ratios found in the respective spectra can be compared to each other.

The baseline corrected spectra for the three samples are given in figure 3.4b. Comparison of the peak positions in the spectra before and after baseline correction showed that the peak maxima shifted to lower frequency with maximal  $2\text{cm}^{-1}$ , which is within the resolution of the spectra. Three distinct sets of peaks can be observed: O-H stretching vibrations between  $3800$  and  $3100\text{cm}^{-1}$ , C-H stretching

### 3.3. RESULTS AND DISCUSSION

between 3000 and 2700 $\text{cm}^{-1}$ ,  $\text{C-O}^-_{x(x=2,3)}$  stretching and deformation between 1700 and 800 $\text{cm}^{-1}$ .

In the O-H stretch range the following bands can be distinguished for the ceria nanoshapes: Isolated hydroxyls (3700 $\text{cm}^{-1}$ ), bridging hydroxyls (3641 $\text{cm}^{-1}$ ), multiple bonded hydroxyls (3550 – 3500 $\text{cm}^{-1}$ ) and hydrogen bridging hydroxyls (broad band 3400 – 3100 $\text{cm}^{-1}$ ).[21, 23] All three nanoshapes show similar O-H stretching bands albeit with different relative intensities. Wires and octahedra resemble each other closely in the whole hydroxyl range, but wires have a distinct peak at 3508 $\text{cm}^{-1}$ , whilst octahedra have a shoulder at 3267 $\text{cm}^{-1}$ . Cubes have a higher ratio of bridged ( $\text{OH}^{3641}$ ) to isolated ( $\text{OH}^{3700}$ ) hydroxyl intensities, accompanied by a shoulder at 3562 $\text{cm}^{-1}$ . This seems to be consistent with the more open structure of the (100) plane terminating cubes.

C-H stretching bands are observed at 2932 and 2846 $\text{cm}^{-1}$  for all samples and can be assigned to formate species.[24, 25] The bands have similar low intensities and peak positions for the three nanoshapes.

In addition, high intensity bands were observed between 1800 and 1250 $\text{cm}^{-1}$ , which can be assigned to C-O stretch vibrations in formate and carbonate species. Clearly these species are stable at 200 $^{\circ}\text{C}$  in He. The different types of carbonate and formate are formed as soon as  $\text{CeO}_2$  is exposed to carbon species, such as atmospheric  $\text{CO}_2$ . [19, 20, 22–25] Clearly wires and cubes have much higher integrated intensity ratios of carbonates to hydroxyl than octahedra. In addition, the spectral shapes between 1200 and 1700 $\text{cm}^{-1}$  are different for the three samples, indicating different relative amounts of formate and carbonate species depending on ceria shape. In general, the peak positions found here are in agreement with those published previously for ceria particles.[24] However, we do not assign specific peaks individually to species at this point, because of the large overlap between them (a more thorough analysis is presented by Vayssilov *et al.*, who give an extensive theoretical and experimental overview of  $\text{CO}_2$  and CO adsorption on ceria surfaces[25]).

Finally, additional peaks are observed between 1250 – 850 $\text{cm}^{-1}$ , which can be assigned to the deformation vibrations of formates and carbonates. Specifically, the band at 854 $\text{cm}^{-1}$  is observed for wires and cubes, due to the presence of multi-bonded carbonates.[25] In addition, wires also show a distinct band at 924 $\text{cm}^{-1}$ ,

which is absent in the other two samples. According to the literature, this peak may be assigned to oxalate types of species.[22]

Clearly, the three ceria nanoshapes show different relative amounts of hydroxyls, carbonates and formates after calcination and treatment in He at 200°C. The differences might arise from the different crystal planes terminating the particles, and the differences in BET surface area. Furthermore, the carbonate species are extremely difficult to remove because high temperatures are needed ( $> 600^\circ\text{C}$ ) at which the nanoparticles start to lose their specific geometries and crystal planes.[23, 26, 32] This study shows that synthesized, calcined ceria nanoshapes already differ in their composition and vibrational spectra before starting adsorption experiments, an observation that has been mentioned but not studied in the literature.[26]

### 3.3.4 CO adsorption and reactivity with water

#### Ceria octahedra

After drying at 200°C in helium (figure 3.5a, dash-dotted black line), CO was adsorbed on the octahedra (figure 3.5a, solid red line). The black spectrum is identical to the spectrum for octahedra in figure 3.4b and is used as a reference. Exposure to CO/He resulted in a variety of changes in the spectrum. The CO induced changes, the [CO-He] difference spectrum is plotted in figure 3.5b. The positive peaks in the difference spectrum correspond to species formed in the presence of CO, whereas the negative peaks correspond to species that disappeared as soon as the sample was exposed to CO. The intensity of peaks known to correspond to formates and carbonates ( $1800 - 1250\text{cm}^{-1}$ ) increased significantly; carbonate formation is further suggested by the appearance of a band at  $854\text{cm}^{-1}$ . The C-H stretch at  $2848\text{cm}^{-1}$  tripled in intensity, confirming formate formation. The band at  $2932\text{cm}^{-1}$  became broader but did not change much in integrated intensity. Finally, in the O-H stretch range, the peak at  $3700\text{cm}^{-1}$  completely disappeared. Looking at the figure 3.5a inset and figure 3.5b, an increase in intensity was observed between  $3641$  and  $3300\text{cm}^{-1}$  resulting in a broad band with a maximum at  $3586\text{cm}^{-1}$ . Bands at these frequencies have been attributed to hydrogen carbonates ( $\text{CO}_2(\text{OH})^-$ ).[23] Evidently, the OH species giving rise to the  $3641\text{cm}^{-1}$  band are not reactive with CO.

The production of carbonates upon CO exposure is in accordance with recently

### 3.3. RESULTS AND DISCUSSION

#### Octahedron

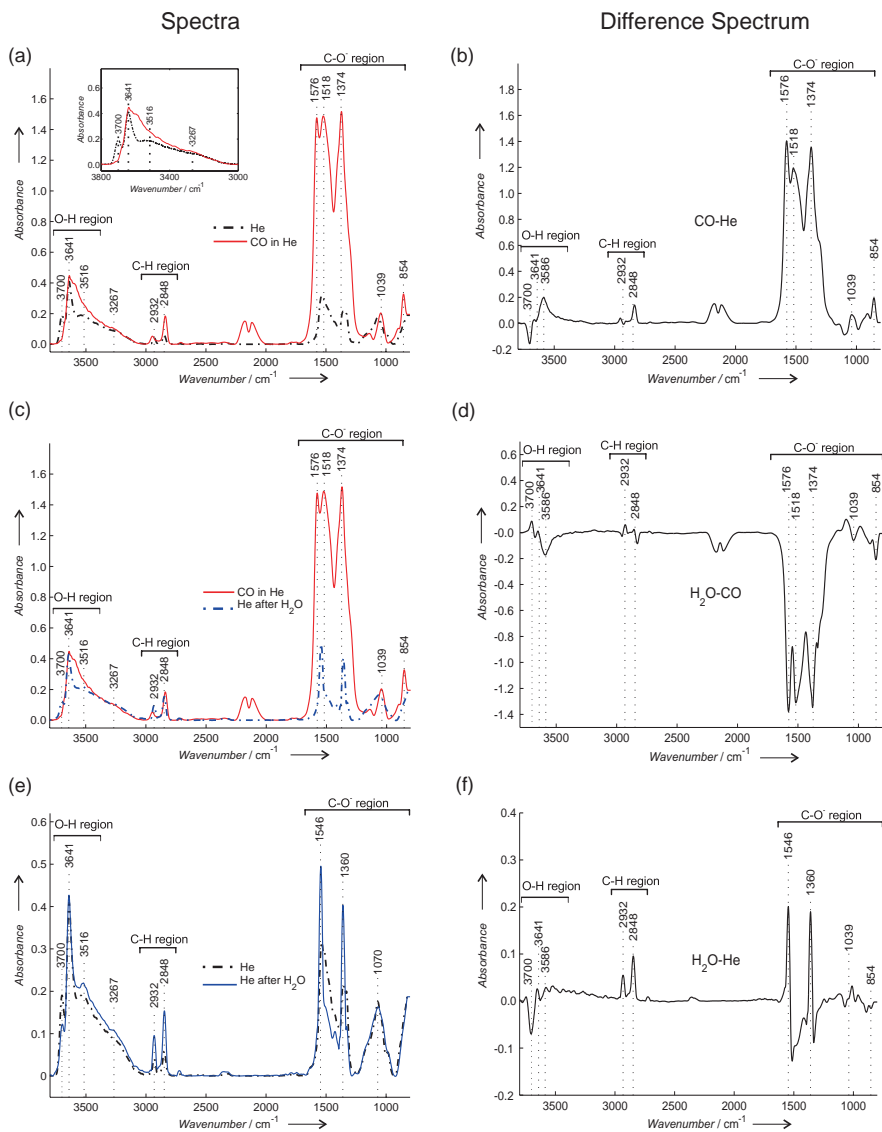


**Figure 3.5:** Baseline corrected *in situ* FTIR spectra at 200°C of ceria octahedra (a) in He flow (black dash-dotted spectrum), followed by 33 vol% CO/He (red solid line); (b) He-subtracted CO spectrum (black solid line); (c) in 33 vol% CO/He (red solid line) followed by He+H<sub>2</sub>O flow (blue dash-dotted spectrum); (d) He/H<sub>2</sub>O subtracted CO spectrum (black solid line); (e) comparison between the regenerated sample with H<sub>2</sub>O/He (blue solid line) and fresh sample in He flow (black dash-dotted line) and (f) corresponding subtraction of He/H<sub>2</sub>O spectrum with He spectrum (black solid line).

published experiments at room temperature.[26] However, the frequencies reported for these species are at significantly higher wavenumber (between  $1616$  and  $1700\text{cm}^{-1}$ ) than the ones we observe in the current study. The formation of formates from the interaction of CO with hydroxyls is in agreement with previous studies on ceria particles.[20, 25, 26, 44] Formate band positions are similar to those reported in the literature, although bands vary in position by  $30\text{cm}^{-1}$ , suggesting that the samples are similar but not identical.[26] Furthermore, the disappearance of the  $3700\text{cm}^{-1}$  band has been assigned to reduction of the  $\text{Ce}^{4+}$  to  $\text{Ce}^{3+}$  upon removing this specific OH species.[23, 25]

After exposure to CO, the cell was flushed with helium to check the stability of the adsorbed species. Approximately 10% of the formed surface species disappeared upon helium flow (see Appendix). Subsequently, the sample was exposed to  $\text{H}_2\text{O}/\text{He}$  at  $200^\circ\text{C}$ , followed by helium to remove physisorbed water. The resulting spectrum is given in figure 3.5c (dash-dotted blue line). In figure 3.5d the accompanying  $[\text{H}_2\text{O}-\text{CO}]$  difference spectrum is shown. Upon water addition, gas phase CO ( $2143\text{cm}^{-1}$ ) and most of the species formed during CO treatment disappeared, as can clearly be seen between  $1800$  and  $1200\text{cm}^{-1}$ . The polycarbonate band at  $854\text{cm}^{-1}$  disappeared, suggesting complete removal of carbonates from the ceria octahedra. The small band at  $2932\text{cm}^{-1}$  increased, whereas the formate C-H stretch at  $2848\text{cm}^{-1}$  slightly decreased, because of water. The integrated intensities of the two bands hardly changed. This indicates that the bands are not likely to originate from a combination of carbonate and formate vibrations as has been suggested in the literature,[23, 25, 45] because almost all carbonates were removed by water. Consequently, we conclude that these bands belong to the stable formate species on the surface, in good agreement with the literature.[44] In addition, the O-H stretch band at  $3700\text{cm}^{-1}$  starts to re-appear upon exposure of water, whereas the band at  $3586\text{cm}^{-1}$  decreases, indicating re-oxidation of the ceria by water.[23]

Finally, the comparison of the spectra of the fresh sample (dash-dotted black line) and the sample after water treatment (solid blue line) can be seen in figure 3.5e and f. The spectra look similar, but the difference spectrum in figure 3.5f does show subtle changes. The band at  $3700\text{cm}^{-1}$  did not fully recover to its original intensity (only 60%) and a slightly increased intensity remained in the hydroxyl

### 3.3. RESULTS AND DISCUSSION

range below  $3641\text{ cm}^{-1}$ . In addition, formate species ( $\approx 40\%$ ) have formed that are stable in  $\text{H}_2\text{O}$  at  $200^\circ\text{C}$  as reflected by the peak at the C-H stretch wave numbers ( $2932$  and  $2848\text{ cm}^{-1}$ ) and the peaks at  $1546$  and  $1360\text{ cm}^{-1}$ . It is likely that the loss of about  $40\%$  isolated hydroxyl species<sup>3700</sup> is a result of their strong interaction with CO to form stable formates at the given temperature. Furthermore, the bands at  $1518 - 1400\text{ cm}^{-1}$  decreased compared to the fresh sample. No change is observed in the band at  $854\text{ cm}^{-1}$ , this suggests the presence of multiple types of carbonate species on the ceria surface. These species have different behavior towards water at  $200^\circ\text{C}$ .

#### **Ceria wires**

The spectra for ceria wires after CO adsorption and as a result of rehydration with  $\text{H}_2\text{O}$  at  $200^\circ\text{C}$  can be seen in figure 3.6. In the difference spectrum (figure 3.6b), the induced changes on adsorption of CO can be seen more specifically. Unlike for the octahedra, two negative OH peaks can be observed for ceria wires at  $3700$  and  $3641\text{ cm}^{-1}$  in figure 3.6a inset, which are caused by the interaction of CO with the active OH species. Owing to this interaction, three more distinct OH bands are now visible that indicate the presence of other types of OH groups after CO adsorption. Furthermore, no hydrogen carbonates ( $3583\text{ cm}^{-1}$ ) were found for ceria wires.

As a result of the interaction between CO and ceria hydroxyls, formates and carbonates were formed on ceria wires, as can be concluded from the C-H stretch bands ( $2932$  and  $2846\text{ cm}^{-1}$ ) and the C-O stretch bands from formates and carbonates between  $1700$  and  $1200\text{ cm}^{-1}$ . Upon exposure to  $\text{H}_2\text{O}$ , these adsorbates decompose and OH groups are partially restored on the catalyst (figure 3.6c and d). Furthermore, the band at  $857\text{ cm}^{-1}$  decreased in intensity on switching from CO to  $\text{H}_2\text{O}$ , indicating the decomposition of carbonates on the surface.

Finally, the comparison is shown of the spectra after regeneration with  $\text{H}_2\text{O}$  (solid blue line) and the fresh sample in He (dash-dotted black line) is shown in figure 3.6e and f. The spectra look similar, but in the difference spectrum of figure 3.6f, subtle changes can be seen. The OH bands at  $3700\text{ cm}^{-1}$  ( $60\%$ ) and  $3641\text{ cm}^{-1}$  ( $80\%$ ) partially recovered to their original intensity. In agreement with this, after CO and  $\text{H}_2\text{O}$  treatment, stable formate species at  $1546$  and  $1360\text{ cm}^{-1}$  are formed, that were not present initially on the ceria wires. The loss of OH

## Wire

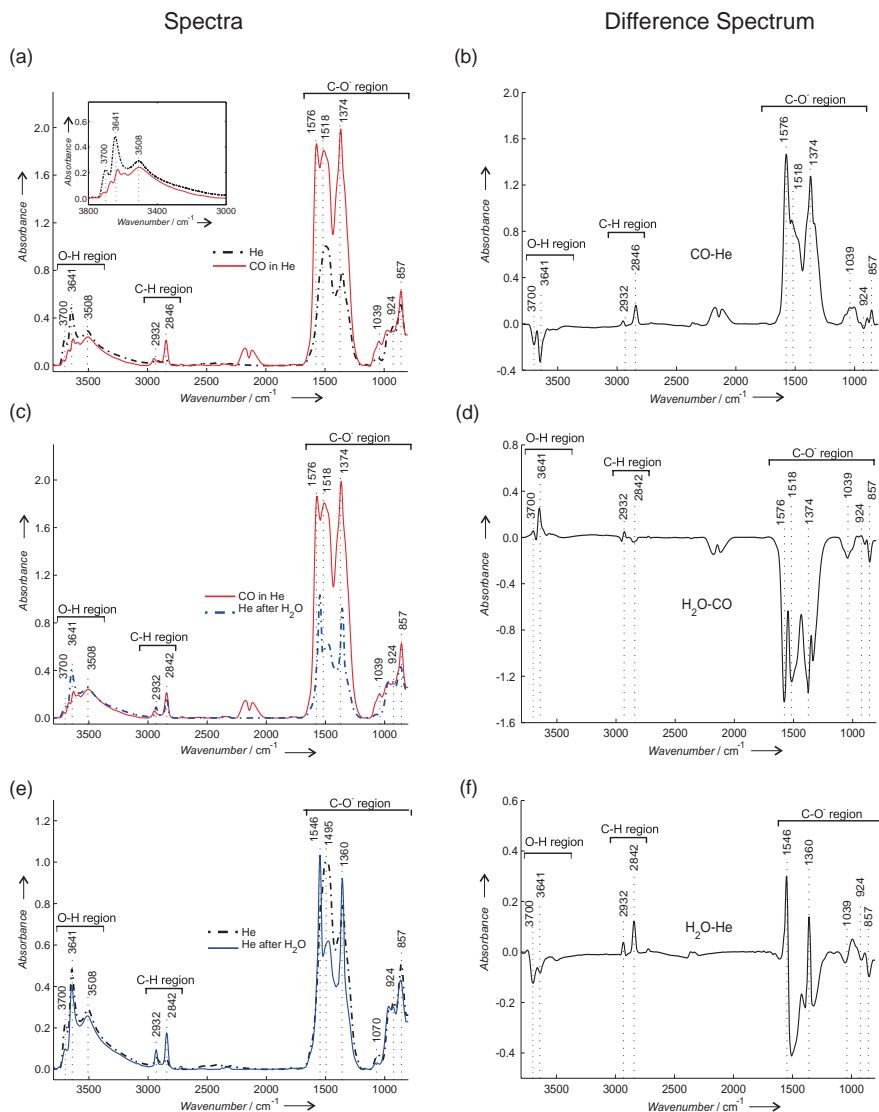


**Figure 3.6:** Baseline corrected *in situ* FTIR spectra at 200°C of ceria wire (a) in He flow (black dash-dotted spectrum), followed by 33 vol% CO/He (red solid line); (b) He-subtracted CO spectrum (black solid line); (c) in 33 vol% CO/He (red solid line) followed by He+ $\text{H}_2\text{O}$  flow (blue dash-dotted spectrum); (d) He/ $\text{H}_2\text{O}$  subtracted CO spectrum (black solid line); (e) comparison between the regenerated sample with  $\text{H}_2\text{O}/\text{He}$  (blue solid line) and fresh sample in He flow (black dash-dotted line) and (f) He/ $\text{H}_2\text{O}$  subtracted He spectrum (black solid line).

### 3.3. RESULTS AND DISCUSSION

groups may again, be related to the increase in formates. Furthermore, the band intensities of the carbonate species at  $1518 - 1400\text{cm}^{-1}$  and  $857\text{cm}^{-1}$  decreased compared to the fresh sample, indicating that carbonates can be partially decomposed on ceria wires by means of a water treatment at  $200^\circ\text{C}$ .

#### **Ceria cubes**

The FTIR spectra obtained for the fresh ceria cubes (black dash-dotted spectrum) and after CO adsorption (red-solid line) are shown in figure 3.7a, and the corresponding difference spectrum in figure 3.7b. A sharp decrease of OH intensity is observed, especially for the band at  $3641\text{cm}^{-1}$ . Similar to the wire sample, the three specific hydroxyl peaks decrease in intensity and split into five distinct O-H vibrations after CO exposure ( figure 3.7a inset). At the same time, carbonates and formates are formed, similar to the wires and octahedra but with different relative intensities, as will be discussed in the next section. The multi-coordinated carbonate peak appears in cubes at  $867\text{cm}^{-1}$  which is approximately  $10\text{cm}^{-1}$  higher than for wires and octahedra. The band at  $854\text{cm}^{-1}$  slightly decreased, suggesting the formation of a slightly altered multi-coordinated carbonate species, possibly caused by mutual interaction of these species.

On subsequent treatment with  $\text{H}_2\text{O}$ , the peaks related to adsorbed formates and carbonates largely decreased ( $1700 - 1200\text{cm}^{-1}$ ), see figure 3.7c and d, indicating their decomposition, and reproducing most of the active OH groups. The integrated intensity for the peaks at  $2932$  and  $2842\text{cm}^{-1}$  remained constant, whereas a clear decrease is observed for the  $867\text{cm}^{-1}$  peak.

The differences in the FTIR spectra of the fresh ceria cubes (black dash-dotted line) and the regenerated cubes (blue solid line) can be seen in figure 3.7e and f. The band at  $3700\text{cm}^{-1}$  re-appeared partially (50%), whereas the OH band at  $3641\text{cm}^{-1}$  gained in intensity compared to the fresh cubes. The multi-coordinated carbonate band at  $854\text{cm}^{-1}$ , as well as the bands between  $1500$  and  $1300\text{cm}^{-1}$ , decreased after CO and water treatment, indicating the partial removal of carbonates that were initially present at  $200^\circ\text{C}$ . A formate peak at  $1546\text{cm}^{-1}$  increased, which was accompanied by the increased intensity of the bands at  $2932$  and  $2842\text{cm}^{-1}$ . This suggests the formation of stable formate species under these conditions. Thus the partial loss of  $\text{OH}^{3700}$  can be connected to the formation of formates<sup>1546</sup>.

## Cube

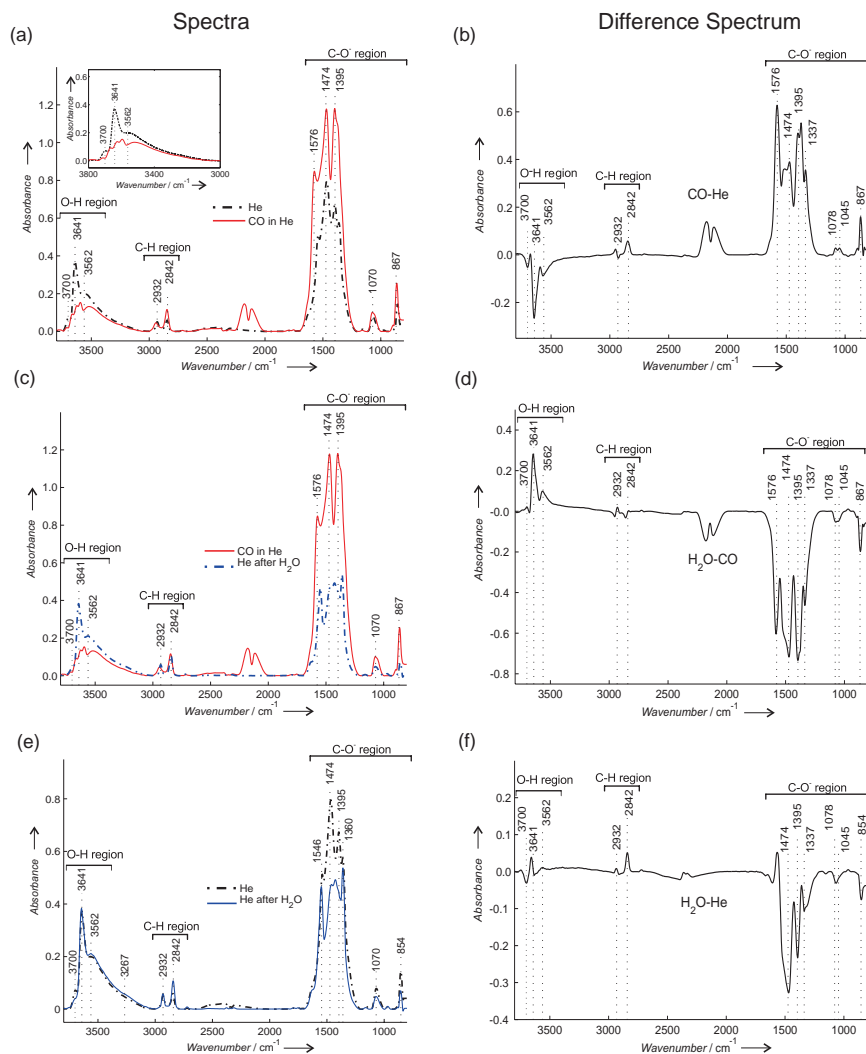


**Figure 3.7:** Baseline corrected *in situ* FTIR spectra at 200°C of ceria cube (a) in He flow (black dash-dotted spectrum), followed by 33 vol% CO/He (red solid line); (b) He-subtracted CO spectrum (black solid line); (c) in 33 vol% CO/He (red solid line) followed by He+H<sub>2</sub>O flow (blue dash-dotted spectrum); (d) He/H<sub>2</sub>O subtracted CO spectrum (black solid line); (e) comparison between the regenerated sample with H<sub>2</sub>O/He (blue solid line) and fresh sample in He flow (black dash-dotted line) and (f) He/H<sub>2</sub>O subtracted He spectrum (black solid line).

## 3.4 General discussion

XRD (figure 3.2) and Raman spectroscopy (figure 3.3) confirm the general observation that ceria nanoshapes exhibit a distorted fluorite structure, with increasing number of oxygen vacancies from octahedra to cubes to wires, in agreement with findings reported in literature.[32] The presence of vacancies in wires and cubes is supported by the FTIR spectra in helium (figure 3.4) showing that the integrated intensity ratio of carbonates to OH groups in wires and cubes is significantly higher than that of octahedra. The formation of carbonates on ceria is due to the interaction with  $\text{CO}_2$  from ambient, resulting in the reduction of ceria to  $\text{Ce}^{3+}$  and hence the creation of oxygen vacancies.[46–48]

Notably, although the nanoshapes have initially similar, but not identical, OH vibrations (figure 3.4), their reactivity towards CO at  $200^\circ\text{C}$  is remarkably different. A comparison of the difference spectra [CO-He] after CO adsorption for the three nanoshapes is shown in figure 3.8a. All samples show a clear decrease in the band caused by isolated hydroxyls at  $3700\text{cm}^{-1}$ , indicating partial reduction of ceria to  $\text{Ce}^{3+}$  by CO,[23] by means of reaction of an isolated OH group. For ceria octahedra, only a minority of the other OH groups interact with CO, and a clear band of hydrogen carbonates is observed at  $3586\text{cm}^{-1}$ . For wires and cubes it is clear that the band at  $3641\text{cm}^{-1}$  significantly decreased upon CO adsorption showing a higher reactivity compared to octahedra of the OH species at  $3641\text{cm}^{-1}$  previously assigned as bridged OH.[21, 23] This reactivity of this species is evidently determined by the specific ceria nanoshape. Furthermore, both wires and cubes do not show the formation of hydrogen carbonates, in contrast to octahedra ( $3586\text{cm}^{-1}$ ). Finally, the OH band at  $3562\text{cm}^{-1}$  interacted with CO on cubes only and was not observed on octahedra and wires.

The difference spectra [CO-He] for the three nanoshapes in the  $1800 - 800\text{cm}^{-1}$  range is shown in figure 3.8b. It is immediately apparent that, relative to the initial amount of OH present (figure 3.4), different amounts of formates and carbonates are formed, in the order cubes < wires < octahedra. On octahedra an intense broad band is observed at  $1518\text{cm}^{-1}$ , which is related to hydrogen carbonate formation in agreement with the band at  $3586\text{cm}^{-1}$ . For cubes and wires many different bands and shoulders are observed between  $1576$  and  $1337\text{cm}^{-1}$ , with different relative intensities.

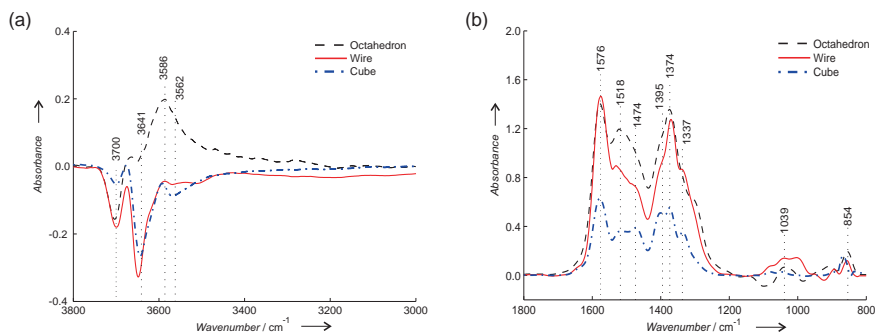


**Figure 3.8:** The He subtracted CO spectra at 200°C of ceria nanoshapes for (a) the hydroxyl region (3800 – 3000  $\text{cm}^{-1}$ ), (b) the C-O<sup>-</sup> region (1800 – 800  $\text{cm}^{-1}$ ).

General consensus is that different nanoshapes have different exposed crystal planes on their surfaces, although the exact planes exposed on these shapes are still debated.[13, 16, 49–52] <sup>†</sup> It has been proposed that wires have {110} and {100} crystal planes, whereas octahedra have mainly {111} and cubes {100} termination on their surfaces. These crystal planes differ in cerium to oxygen ratio, for instance the (111) plane has a Ce:O ratio of 7:3, as compared to 6:3 and 6:2 for the (110) and (100) planes, respectively.[53] However, it is not only the specific crystal plane that will determine reactivity. It even has been reported that undoped thin single crystal ceria films are inactive towards CO oxidation at low temperatures and show poor reducibility.[6, 54] Furthermore, the presence of defects in ceria nanoshapes has been shown to improve oxygen migration from the bulk to the surface of ceria,[32, 55, 56] thus affecting the reducibility. The surface hydroxyl groups observed on ceria in this study show similar vibrational stretch frequencies, especially for the band at 3641  $\text{cm}^{-1}$ . Based on the same stretch frequency one would expect a similar reactivity towards CO, independent of the nanoshape, but this is not observed. Clearly, there must be another explanation for the distinctly different behavior of OH<sup>3641</sup> on octahedra compared to wires and cubes. The main difference between ceria octahedra on the one hand and cubes and wires on the other, is the absence of defects in octahedra. We propose that the hydroxyl

<sup>†</sup>Note that the present work was carried out *before* Ch. 2, where we showed that the consensus in the literature of the exposed planes on rods was incorrect. This does not affect the findings in the present chapter.

### 3.4. GENERAL DISCUSSION

reactivity on ceria nanoshapes is determined by the presence of these vacancies via a concerted reaction mechanism which involves the hydroxyl group and a vacancy. Thus it is not only the surface orientation that determines the reactivity of ceria nanoshapes but also the existence of defects and enhanced oxygen transport from the bulk play a significant role in the overall behavior of ceria nanoparticles.

A recent study reported the formation energy of carbonates from CO on different surface planes of ceria, following the order (100) ( $-74\text{kcal.mol}^{-1}$ ) > (110) ( $-45\text{kcal.mol}^{-1}$ )  $\gg$  (111) ( $-6\text{kcal.mol}^{-1}$ ).[42] Consequently, carbonate formation is not favored on the (111) planes of the octahedra,[25, 26, 41, 42, 57] explaining why only a small amount of carbonates are found on octahedra (figure 3.4).

The energy for carbonate formation on specific crystal planes is related to the atomic arrangement of the exposed crystal planes and the reducibility of the ceria nanoshape.[42] Because two oxygen atoms are required from the surface, the distance between oxygen atoms, and their mobility are key parameters. On (110) and (100) oxygen displacement and accompanying reduction of ceria as a result of carbonate formation is favorable, which is in agreement with the observations in figure 3.8b. The hydrogen carbonate formation on octahedra indicates that OH groups with a relatively high reactivity are involved on (111) planes instead of, or in addition to, lattice oxygen.

Finally, formate and bi-carbonate species formed on the three nanoshapes also exhibit different reactivities towards water. The bands at  $3586$  and  $1518\text{cm}^{-1}$  on octahedra, assigned to hydrogen carbonate, disappeared upon exposure to  $\text{H}_2\text{O}$  at  $200^\circ\text{C}$ . For ceria cubes, almost all hydroxyl species recovered, whereas for wires and octahedra the recovery is incomplete (figure 3.5f, 3.6f and 3.7f). The missing hydroxyls are converted into formate species that are stable at  $200^\circ\text{C}$  in the presence of water. Cubes show almost complete regeneration of the OH groups, and only a minor amount of remaining of formate species (figure 3.7f). For wires and cubes, a portion of the carbonates originating from exposure of the sample as prepared to ambient conditions were removed upon water treatment, as evidenced by the strong negative peak at  $1474\text{cm}^{-1}$  in figure 3.6f and 3.7f. Exposure of reduced ceria surfaces to water is known to restore hydroxyl groups on the surface.[23] In the present study it is clearly shown that the ceria nanoshapes have a different reactivity towards water, resulting in removal of different relative amounts of ad-

sorbates formed on the surface from either ambient or CO. The observed reactivity for water follows a similar order as reported for CO oxidation of these materials.[16, 26, 58] In those studies, the higher oxidation rates were attributed to the increased oxygen storage capacity of ceria nanoshapes as a result of altered lattice oxygen mobility and reactivity.

The reducibility and oxygen mobility might as well affect the reactivity towards water of the ceria nanoshapes. The presented results show that the ceria nanoshapes have a distinct influence on the activation of water and the reaction of adsorbed carbonates and formates with water. This study suggests a large impact of ceria particle shape on reactions involving water, such as the water gas shift reaction.

### **3.5 Conclusions**

The present work reports on the investigation of the reactivity of hydroxyl species towards CO for different ceria nanoshapes. The interaction of specific hydroxyl groups with CO is dependent on both the shape of the ceria nanocatalysts and oxygen vacancies. Subsequent exposure to water at 200°C showed a clear shape dependent water activation and reaction with adsorbed formates and carbonates.

## Appendix 3

After exposure to CO, the cell was flushed with helium to check the stability of the adsorbed species (carbonates and formates), see figure A3.1. Approximately 10% of the formed surface species disappeared upon helium flow.

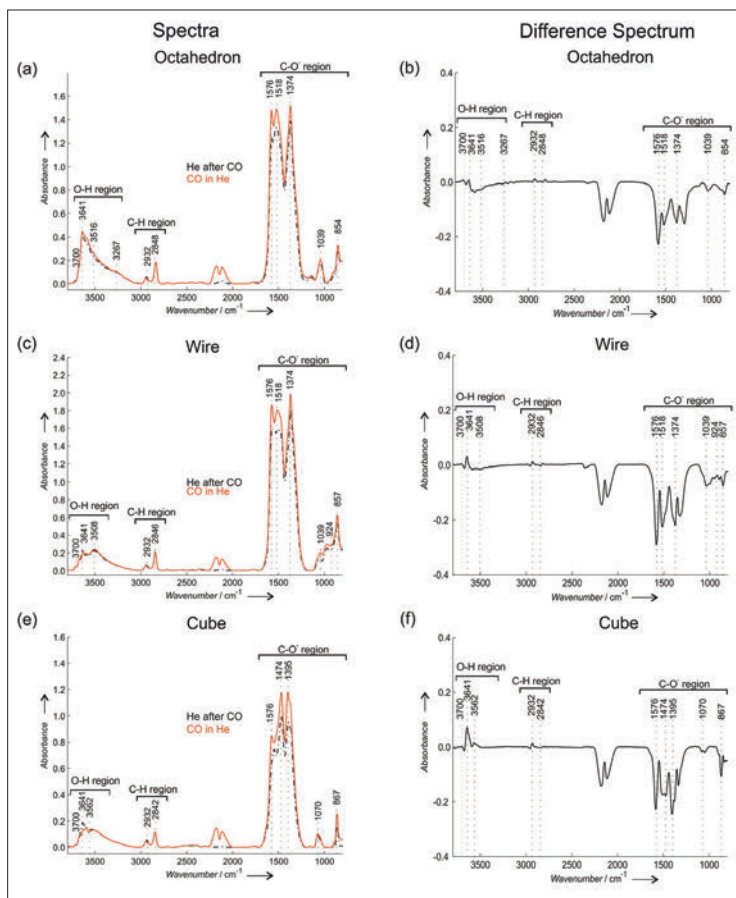


**Figure A3.1:** Baseline corrected *in situ* FTIR spectra at 200°C of ceria (a) octahedra in 33 vol% CO/He (red solid line) followed by He flow (black dash-dotted spectrum); (b) octahedra He-subtracted CO spectrum (black solid line); (c) wire in 33 vol% CO/He (red solid line) followed by He flow (black dash-dotted spectrum); (d) wire He-subtracted CO spectrum (black solid line); (e) cube in 33 vol% CO/He (red solid line) followed by He flow (black dash-dotted spectrum) and (f) cube He-subtracted CO spectrum (black solid line).

## Bibliography

- [1] Beie, H.-J. and Gnörich, A. (1991) *Sens. Actuators, B* **4(3-4)**, 393–399.
- [2] Izu, N., Shin, W., Murayama, N., and Kanzaki, S. (2002) *Sens. Actuators, B* **87(1)**, 95–98.
- [3] de Lima, J. F., Martins, R. F., Neri, C. R., and Serra, O. A. (2009) *Applied Surf. Sci.* **255(22)**, 9006–9009.
- [4] Liu, X., Zhou, K., Wang, L., Wang, B., and Li, Y. (2009) *J. Am. Chem. Soc.* **131(9)**, 3140–3141.
- [5] Steele, B. (1994) *J. Power Sources* **49(1-3)**, 1–14.
- [6] Stubenrauch, J. and Vohs, J. (1996) *J. Catal.* **159(1)**, 50–57.
- [7] Xia, C. and Liu, M. (2002) *Solid State Ionics* **152-153**, 423–430.
- [8] Zhou, K., Wang, X., Sun, X., Peng, Q., and Li, Y. (2005) *J. Catal.* **229(1)**, 206–212.
- [9] Azzam, K., Babich, I., Seshan, K., and Lefferts, L. (2008) *Appl. Catal., B* **80(1-2)**, 129–140.
- [10] Diwell, A., Rajaram, R., Shaw, H., and Truex, T. (1991) The role of ceria in three-way catalysts In A. Crucq, (ed.), *Studies in Surf. Sci. and Catalysis*, volume **71**, pp. 139–152 Elsevier.
- [11] Gorte, R. J. (2010) *AIChE Journal* **56(5)**, 1126–1135.
- [12] Mogensen, M., Sammes, N. M., and Tompsett, G. A. (2000) *Solid State Ionics* **129(1-4)**, 63–94.
- [13] Tana, Zhang, M., Li, J., Li, H., Li, Y., and Shen, W. (2009) *Catal. Today* **148(1-2)**, 179–183.
- [14] Deshpande, P. A., Hegde, M., and Madras, G. (2010) *Appl. Catal., B* **96(1-2)**, 83–93.
- [15] Han, W.-Q., Wen, W., Hanson, J. C., Teng, X., Marinkovic, N., and Rodriguez, J. A. (2009) *J. Phys. Chem. C* **113(52)**, 21949–21955.
- [16] Mai, H.-X., Sun, L.-D., Zhang, Y.-W., Si, R., Feng, W., Zhang, H.-P., Liu, H.-C., and Yan, C.-H. (2005) *J. Phys. Chem. B* **109(51)**, 24380–24385.
- [17] Natile, M. M., Boccaletti, G., and Glisenti, A. (2005) *Chem. Mater.* **17(25)**, 6272–6286.
- [18] Si, R. and Flytzani-Stephanopoulos, M. (2008) *Angew. Chem.* **120(15)**, 2926–2929.
- [19] Li, C., Sakata, Y., Arai, T., Domen, K., Maruya, K., and Onishi, T. (1989) *J. Chem. Soc., Faraday Trans. 1* **85**, 929–943.
- [20] Li, C., Sakata, Y., Arai, T., Domen, K., Maruya, K., and Onishi, T. (1989) *J. Chem. Soc., Faraday Trans. 1* **85**, 1451–1461.
- [21] Badri, A., Binet, C., and Lavalley, J.-C. (1996) *J. Chem. Soc., Faraday Trans.* **92**, 4669–4673.
- [22] Binet, C., Badri, A., Boutonnet-Kizling, M., and Lavalley, J.-C. (1994) *J. Chem.*

- Soc., Faraday Trans.* **90**, 1023–1028.
- [23] Binet, C., Daturi, M., and Lavalley, J.-C. (1999) *Catal. Today* **50(2)**, 207–225.
- [24] Binet, C., Jadi, A., and Lavalley, J.-C. (1992) *J. Chim. Phys. Phys. - Chim. Biol.* **89**, 1779–1797.
- [25] Vayssilov, G. N., Mihaylov, M., Petkov, P. S., Hadjiivanov, K. I., and Neyman, K. M. (2011) *J. Phys. Chem. C* **115(47)**, 23435–23454.
- [26] Wu, Z., Li, M., and Overbury, S. H. (2012) *J. Catal.* **285(1)**, 61–73.
- [27] Gordon, W. O., Xu, Y., Mullins, D. R., and Overbury, S. H. (2009) *Phys. Chem. Chem. Phys.* **11**, 11171–11183.
- [28] Henderson, M., Perkins, C., Engelhard, M., Thevuthasan, S., and Peden, C. (2003) *Surf. Sci.* **526(1-2)**, 1–18.
- [29] Senanayake, S. D., Gordon, W. O., Overbury, S. H., and Mullins, D. R. (2009) *J. Phys. Chem. C* **113(15)**, 6208–6214.
- [30] Senanayake, S. D., Stacchiola, D., Evans, J., Estrella, M., Barrio, L., Pérez, M., Hrbek, J., and Rodriguez, J. A. (2010) *J. Catal.* **271(2)**, 392–400.
- [31] Putna, E., Bunluesin, T., Fan, X., Gorte, R., Vohs, J., Lakis, R., and Egami, T. (1999) *Catal. Today* **50(2)**, 343–352.
- [32] Wu, Z., Li, M., Howe, J., Meyer, H. M., and Overbury, S. H. (2010) *Langmuir* **26(21)**, 16595–16606.
- [33] Balzar, D., Audebrand, N., Daymond, M. R., Fitch, A., Hewat, A., Langford, J. I., Le Bail, A., Louër, D., Masson, O., McCowan, C. N., Popa, N. C., Stephens, P. W., and Toby, B. H. (2004) *J. Appl. Crystallogr.* **37(6)**, 911–924.
- [34] Zhang, F., Jin, Q., and Chan, S.-W. (2004) *J. Appl. Phys.* **95(8)**, 4319–4326.
- [35] Keramidas, V. G. and White, W. B. (1973) *J. Chem. Phys.* **59(3)**, 1561–1562.
- [36] Kosacki, I., Suzuki, T., Anderson, H. U., and Colomban, P. (2002) *Solid State Ionics* **149(-2)**, 99–105.
- [37] Spanier, J. E., Robinson, R. D., Zhang, F., Chan, S.-W., and Herman, I. P. (2001) *Phys. Rev. B* **64**, 245407.
- [38] Taniguchi, T., Watanabe, T., Sugiyama, N., Subramani, A. K., Wagata, H., Matsushita, N., and Yoshimura, M. (2009) *J. Phys. Chem. C* **113(46)**, 19789–19793.
- [39] Reddy, B. M., Reddy, G. K., and Katta, L. (2010) *J. Mol. Catal. A: Chem.* **319(1-2)**, 52–57.
- [40] McBride, J. R., Hass, K. C., Poindexter, B. D., and Weber, W. H. (1994) *J. Appl. Phys.* **76(4)**, 2435–2441.
- [41] Sayle, T. X. T., Parker, S. C., and Catlow, C. R. A. (1992) *J. Chem. Soc., Chem. Commun.* **14**, 977–978.
- [42] Nolan, M. and Watson, G. W. (2006) *J. Phys. Chem. B* **110(33)**, 16600–16606.
- [43] Yang, P., Wei, H., Huang, H.-L., Baum, B. A., Hu, Y. X., Kattawar, G. W.,

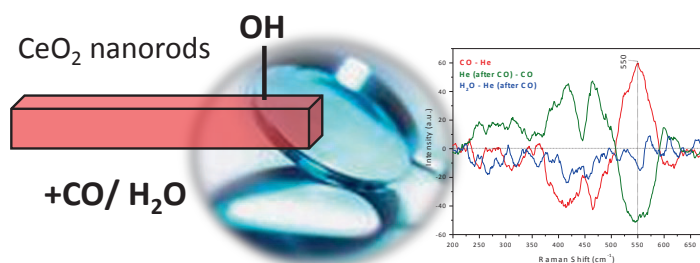
- Mishchenko, M. I., and Fu, Q. (2005) *Appl. Opt.* **44(26)**, 5512–5523.
- [44] Shido, T. and Iwasawa, Y. (1992) *J. Catal.* **136(2)**, 493–503.
- [45] Li, C., Domen, K., Maruya, K., and Onishi, T. (1990) *J. Catal.* **125(2)**, 445–455.
- [46] Appel, L. G., Eon, J. G., and Schmal, M. (1998) *Catal. Lett.* **56(4)**, 199–202.
- [47] Staudt, T., Lykhach, Y., Tsud, N., Skála, T., Prince, K. C., Matoln, V., and Libuda, J. (2011) *J. Phys. Chem. C* **115(17)**, 8716–8724.
- [48] Staudt, T., Lykhach, Y., Tsud, N., Skla, T., Prince, K., Matoln, V., and Libuda, J. (2010) *J. Catal.* **275(1)**, 181–185.
- [49] Sayle, T. X. T., Inkson, B. J., Karakoti, A., Kumar, A., Molinari, M., Mobus, G., Parker, S. C., Seal, S., and Sayle, D. C. (2011) *Nanoscale* **3**, 1823–1837.
- [50] Sun, C., Li, H., Wang, Z., Chen, L., and Huang, X. (2004) *Chem. Lett.* **33(6)**, 662–663.
- [51] Vantomme, A., Yuan, Z.-Y., Du, G., and Su, B.-L. (2005) *Langmuir* **21(3)**, 1132–1135.
- [52] Zhang, D., Fu, H., Shi, L., Pan, C., Li, Q., Chu, Y., and Yu, W. (2007) *Inorg. Chem.* **46(7)**, 2446–2451.
- [53] Ganduglia-Pirovano, M. V., Hofmann, A., and Sauer, J. (2007) *Surf. Sci. Rep.* **62(6)**, 219–270.
- [54] Cordatos, H., Bunluesin, T., Stubenrauch, J., Vohs, J. M., and Gorte, R. J. (1996) *J. Phys. Chem.* **100(2)**, 785–789.
- [55] Mamontov, E. and Egami, T. (2000) *J. Phys. Chem. Solids* **61(8)**, 1345–1356.
- [56] Chiang, Y.-M., Lavik, E. B., Kosacki, I., Tuller, H. L., and Ying, J. Y. (1996) *Appl. Phys. Lett.* **69(2)**, 185–187.
- [57] Huang, M. and Fabris, S. (2008) *J. Phys. Chem. C* **112(23)**, 8643–8648.
- [58] Sayle, T., Parker, S., and Catlow, C. (1994) *Surf. Sci.* **316(3)**, 329–336.

# 4

## Defect chemistry of ceria nanorods

### Research question:

What are the roles of defects in ceria-catalyzed reactions?



*It became clear in the previous chapter that defect chemistry plays an important role in determining the activity of ceria supports, so we investigate that here with rods as the nanoshape.*

\*Published as: S. Agarwal, X. Zhu, E. J. M. Hensen, L. Lefferts, & B.L. Mojet, "Defect chemistry of ceria nanorods," *J. Phys. Chem C* **118**, 4131–4142 (2014)

## Abstract

*Ceria rods were investigated using in situ Raman and FTIR spectroscopies for CO adsorption and subsequent reaction with water at 200°C and 350°C. The involvement of defects in ceria rods during CO adsorption and reaction with H<sub>2</sub>O is dependent on the temperature. At 200°C, most of the carbonate and formate species formed in CO do not involve the formation of defects, while at 350°C all of the carbonates and formates formed can be correlated to the formation of defects (15% by formates and 85% by mono/bi-dentate carbonates). Finally, at 350°C very stable poly-dentate carbonates are formed that do not induce defects and cannot be regenerated with water.*

## 4.1 Introduction

Cerium oxide (CeO<sub>2</sub>) is widely investigated as a catalyst or catalyst support for various applications in the field of environmental catalysis,[1] in three-way catalysts[2] and as a catalyst support in heterogeneous catalysis.[3–9] The high performance of ceria is generally attributed to the unique redox nature and high oxygen storage capacity (OSC), allowing it to quickly switch oxidation state between Ce<sup>4+</sup> and Ce<sup>3+</sup> in the stable fluorite structure.[10, 11]

Due to the recent advancement in synthesis approaches, ceria can now be synthesized into desirable nanoshapes with well-defined active exposed planes that further enhance the catalytic activity.[12, 13] CeO<sub>2</sub> rods are an example of such tailored morphologies. In our recent work, we have reported that our ceria rods expose (111) stable planes in place of the previously believed (110) and (100) planes.[14] As ceria rods provide a high surface area and have inherent defects (vacancy clusters, pits and a high degree of surface roughness),[6, 15] they are reported to have enhanced reactivity for the CO[10] and NO[16] oxidation and reduction reactions, respectively. One of the first detailed investigations of defects using UV (325 nm) Raman spectroscopy on these ceria nanoshapes, was reported by Wu *et al.*[17] The authors showed that rods contain more intrinsic defect sites in comparison to other ceria nanoshapes (cubes and octahedra). Recently, Lee *et al.* reported about CO oxidation on ceria rods (with/without Au loading) by monitoring the oxygen vacancy levels using visible (514 nm) Raman spectroscopy.[18]

## 4.2. EXPERIMENTAL SECTION

UV Raman spectroscopy is a potentially powerful tool to detect structural features, such as defect sites, oxygen vacancies and atomic scale structure disorder of ceria nanomaterials.[19] In comparison to visible laser, using UV laser enhances the detection sensitivity in the surface region of these materials due to the limited probing depth of 10 – 20 nm.[20]

Despite the intensive studies of CO adsorption and H<sub>2</sub>O reactivity on ceria supports, there is still a lack of understanding of the role of defects and active OH species on ceria catalysts.[11, 17, 21–23] In our recent work, we investigated the reactivity of OH species towards CO for different ceria nanoshapes at 200 °C.[24] We reported that the interaction of OH groups with CO depends on the shape of ceria nanoparticles, and we showed preliminary data describing the importance of intrinsic defects in the ceria structure. Furthermore, theoretical investigations have clearly indicated the formation of carbonate species induces the defects in ceria lattice upon the introduction of CO.[25, 26] In the present work, we follow up by addressing the role of defects in ceria in detail using *in situ* UV Raman spectroscopy and the results will be related to Fourier transform infrared (FTIR) measurements recorded under similar conditions. This combination of techniques has proven successful in monitoring the structural defects and adsorbates on catalysts.[8, 27, 28] We will assume that the concentration of defects at the surface is correlated with the bulk defect concentration which can be probed by Raman spectroscopy. We focus in this work on ceria rods due to their high intrinsic defect density as outlined above.

## 4.2 Experimental section

### 4.2.1 Sample preparation, TEM and BET characterization

Ceria rods were synthesized using the recipe reported by Mai *et al.*[13] For synthesis procedure details refer to the literature.[14] After drying, the sample was always calcined in air at 500 °C and subsequently analyzed using Raman and FTIR spectroscopies.

The X-ray diffraction (XRD) pattern of rods (not shown here) was similar to those reported in our previous work.[14] As reported earlier, the observed XRD diffraction peaks can be indexed as face centered cubic phase CeO<sub>2</sub>.

A Micromeritics Tristar instrument was used for determining the BET surface area. The sample was out-gassed in vacuum at 300°C for 24h prior to N<sub>2</sub> physisorption. The BET surface area of the rods after calcination was 80m<sup>2</sup>/g, which is consistent with the values reported earlier.[17]

The transmission electron microscope (TEM) image of the ceria rods was recorded on a Philips CM300ST-FEG electron microscope (operated at an acceleration voltage of 300kV). For TEM measurements, the sample was ultrasonically dispersed in ethanol and subsequently droplets of the suspension were deposited on a copper grid coated with carbon. The TEM image of ceria rods is shown in the Appendix (figure A4.1). The low magnification TEM image of ceria rods demonstrates that the particles have the desired morphologies with a length of approx. 50 – 200 nm.

## 4.2.2 UV Raman spectroscopy

UV Raman spectra (wavenumber region from 190 – 1480cm<sup>-1</sup>) were collected using a Jobin-Yvon T64000 triple-stage spectrograph with a CCD detector and a spectral resolution of 2cm<sup>-1</sup>. The laser spot size on the sample is less than 0.5 mm. The laser power at the sample was 6 mW for the 325 nm laser line of a Kinmon He-Cd laser. It was verified by recording spectra at different laser intensities that at these settings the laser did not induce any damage to the sample. The spectrum was recorded by two times 600s subsequent laser exposure (2 co-additions), hence recording per spectrum took 1200s. Teflon was used as a standard for the calibration of the Raman shift. Typically, approximately 10 mg of sample was loaded and slightly compressed to get a dense catalyst bed in a purpose-built stainless steel cell fitted with a thermocouple placed close to the sample. The cell was covered with a quartz assembly. The gas flows used in the *in situ* Raman experiments were preheated at 100°C and then flowed through the sample. For CO adsorption experiments, 33 vol% CO (Linde) in He (Linde, total flow 20 mL/min) was used. For the H<sub>2</sub>O reactivity measurements, He (20 mL/min) was flowed through a saturator filled with H<sub>2</sub>O at 5°C, resulting in a water vapor pressure of 9 mbar.

## 4.2. EXPERIMENTAL SECTION

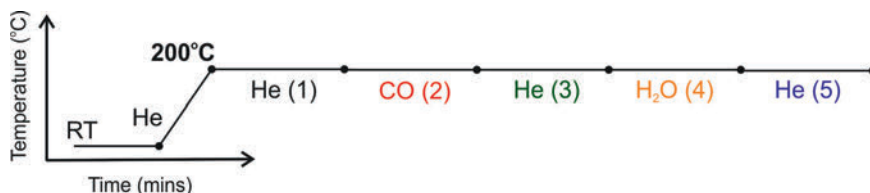


**Figure 4.1:** Experimental scheme for Raman and FTIR experiments at 200°C and 350°C.

### 4.2.3 FTIR spectroscopy

Transmission FTIR (Fourier transform infrared) measurements were recorded with a Bruker Vector 22 with MCT detector by averaging 128 scans with a spectral resolution of  $4\text{ cm}^{-1}$  and time interval of 120 s. The spectrum was collected in the wavenumber region  $800 - 4000\text{ cm}^{-1}$ . A self-supporting wafer ( $\approx 10\text{ mg}$  sample) was pressed and placed into a custom-built stainless steel cell walled by the thermocouple. For adsorption experiments, 33 vol% CO in He (Hoekloos 4.7, total flow 20 mL/min) was used. For the water reactivity measurements, He (Hoekloos 5.0, total flow 20 mL/min) was flowed through a saturator filled with  $\text{H}_2\text{O}$  at  $5^\circ\text{C}$  ( $\text{H}_2\text{O}$  vapor pressure of 9 mbar). All the tubings prior to the FTIR cell were heated to  $100^\circ\text{C}$ , to avoid condensation of  $\text{H}_2\text{O}$  in the lines. To remove traces of water in He gas during FTIR experiments, helium was dried with a Varian Chromopack CP17971 gas clean moisture filter. The background spectrum was obtained while flowing He gas through the empty cell at room temperature.

### 4.2.4 Experimental sequence

Raman and FTIR spectra were recorded after flowing gases in the sequence as shown in the experimental scheme in figure 4.1. The sample was exposed to each gas for 30 min respectively. The sample was heated to the required temperature ( $350^\circ\text{C}/200^\circ\text{C}$ ) with a ramp rate of  $5\text{ K}/\text{min}$ . The total gas flow was maintained at 20 mL/min. We labeled each separate gas flow stage of the experimental sequence with its sequential number as indicated in figure 4.1, which we use in the results and discussion sections for clarity.

## 4.2.5 Data analysis

Raman and FTIR data were analyzed using Bruker OPUS (version 7.0) software. All Raman spectra shown in the present paper were baseline corrected (concave rubberband correction, two iterations) and smoothed (using the OPUS Savitzky-Golay algorithm, 21 points) to better identify the observed changes. To verify that changes observed after smoothing are real, figures A4.2 and A4.3 (see Appendix) compare the raw and smoothed spectra. Raman spectra in figure 4.2 were normalized with respect to the F2g band at  $460\text{cm}^{-1}$ . This is in accordance with common practice, although Daniel *et al.* have also employed the 2LO band (at  $1179\text{cm}^{-1}$ ) for normalization.[29] The FTIR spectra presented in this work were baseline corrected (concave rubberband correction, two iterations). To highlight the relative differences in the Raman and FTIR spectra as a function of gas treatment, the difference spectra in figures 4.7 and 4.8 are expressed as the relative difference, defined as:

$$y = \frac{\Delta I}{\Delta(I_{CO} - I_{He})} \quad (4.1)$$

where  $\Delta I$  is defined as the difference between two consecutive treatments in the scheme shown in figure 4.1.  $\Delta(I_{CO} - I_{He})$  is the maximum peak intensity increase after dosing CO, at approximately  $550\text{cm}^{-1}$  for Raman and  $1576\text{cm}^{-1}$  for FTIR spectra, representing the total amount of species formed upon CO exposure. In addition, the relative amounts of species are calculated by integrating the specific peaks observed in normalized Raman and FTIR plots (see figure 4.7 and 4.8). By expressing both the Raman and FTIR changes in relative differences, the observed changes by the two techniques can be easily compared.

## 4.3 Results and discussion

### 4.3.1 *In situ* Raman and FTIR in helium at room temperature (RT)

*In situ* Raman and FTIR spectra of the fresh ceria rod samples in He flow at room temperature are shown in figure 4.2a and 4.2b respectively. The Raman spectra were normalized to  $460\text{cm}^{-1}$  peak. The Raman spectrum of the calcined ceria rods (figure 4.2a) consisted of sharp peaks at  $460$  and  $589\text{cm}^{-1}$ , shoulder peaks at  $404$  and  $487\text{cm}^{-1}$  and a broad intense band at  $1179\text{cm}^{-1}$ . The peak at  $460\text{cm}^{-1}$

### 4.3. RESULTS AND DISCUSSION

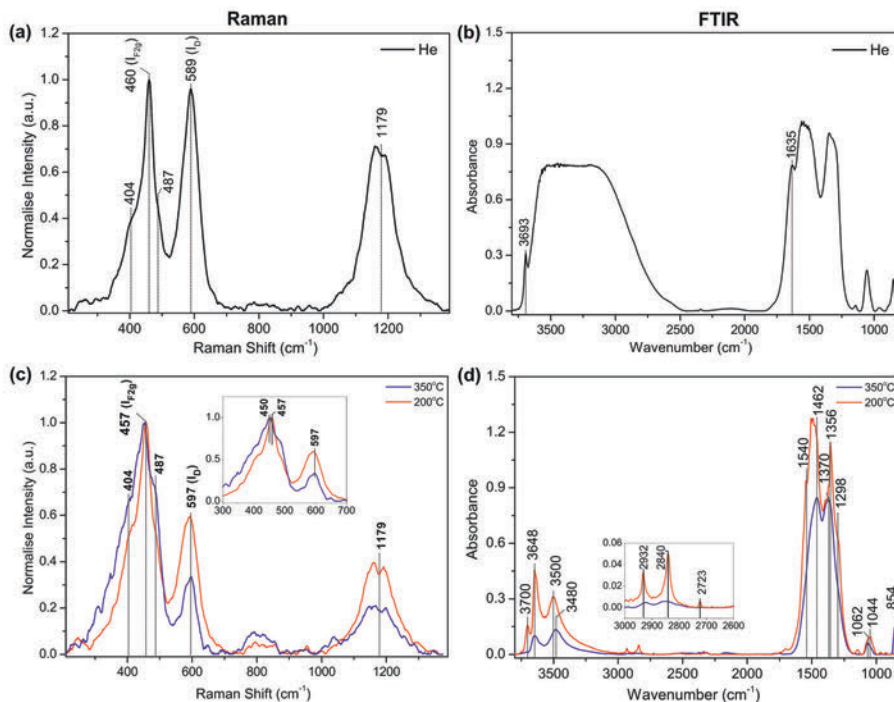


**Figure 4.2:** *In situ* (a) normalized Raman and (b) FTIR spectra of ceria rods in He flow at room temperature (black spectrum). *In situ* (c) Raman and (d) FTIR spectra of ceria rod in He flow at 200°C (red spectrum) and 350°C (blue spectrum).

(labelled as  $I_{F2g}$ ) is due to the symmetric stretch mode of Ce-O<sub>8</sub>, which is characteristic for the fluorite lattice structure.[30, 31] In addition, the peak at  $589\text{cm}^{-1}$  ( $I_D$ ) has been assigned to the defect-induced mode arising due to the presence of anion Frenkel pair defects (an oxygen ion is displaced from its lattice position to an interstitial position, creating a vacancy at its original position and a defect at the interstitial site) in the ceria lattice.[17, 20, 31, 32] Shoulder peaks at  $404$  and  $487\text{cm}^{-1}$  on both sides of the fluorite band have been earlier observed for ceria nanoparticles,[17, 33] although they were not assigned. The band centered at  $1179\text{cm}^{-1}$  corresponds to the second-overtone of the longitudinal optical (LO) band.[20, 31, 34]

In figure 4.2b, the FTIR spectrum of fresh ceria rods was dominated by the strong bands related to physisorbed water in the spectral region  $3800 - 2500\text{cm}^{-1}$  and at  $1635\text{cm}^{-1}$ .[35] Other than these physisorbed water bands, ceria hydroxyl

(O-H) stretching vibrations at  $3693\text{ cm}^{-1}$  and formate and carbonate (C-O) stretching and deformation bands between  $1700$  and  $800\text{ cm}^{-1}$  were observed.[36–38] These carbonate/formate species formed due to the interaction of lattice oxygen/hydroxyl species with atmospheric  $\text{CO}_2$  on the fresh ceria sample when exposed to air.[39, 40]

### 4.3.2 *In situ* Raman and FTIR in helium at $200^\circ\text{C}$ and $350^\circ\text{C}$

*In situ* normalized Raman spectra of calcined ceria rods in He flow at temperatures  $200^\circ\text{C}$  and  $350^\circ\text{C}$  are shown in figure 4.2c. Similar to the Raman spectrum at room temperature, the fluorite lattice vibration  $I_{F2g}$  ( $457\text{ cm}^{-1}$ ) and  $I_D$  defect band ( $597\text{ cm}^{-1}$ ) were observed at  $200^\circ\text{C}$  and  $350^\circ\text{C}$  (figure 4.2c). Two immediate observations related to the fluorite band can be made: Firstly, the peak at  $460\text{ cm}^{-1}$  (RT) shifted to  $457\text{ cm}^{-1}$  ( $200^\circ\text{C}$ ) and then to  $450\text{ cm}^{-1}$  ( $350^\circ\text{C}$ ). Secondly, the relative intensity of the shoulder fluorite peaks at  $404$  and  $487\text{ cm}^{-1}$  increased with temperature, resulting in an overall broad fluorite band centered  $450\text{ cm}^{-1}$  at  $350^\circ\text{C}$ . The relative intensities of the peaks at  $597$  and  $1179\text{ cm}^{-1}$  with respect to the  $I_{F2g}$  vibration decreased with temperature. We further observed an as yet unreported small overall shift from  $589$  to  $597\text{ cm}^{-1}$ .

As reported previously, the broad fluorite band observed in the Raman spectra (figure 4.2) and the broad XRD peaks (as compared to other ceria nanoshapes) reported earlier[17, 24] are due to the distorted fluorite structure of ceria rods. This lattice distortion occurs due to the presence of intrinsic roughness (internal voids and surface steps) in rods.[6, 15] We propose that the distortion in lattice gives rise to bands at  $404$  and  $487\text{ cm}^{-1}$  in ceria rods. At higher temperature, oxygen mobility is enhanced leading to reorganization of the ceria lattice.[41] This explains the decrease in  $I_D$  intensity with an increase in Ce-O vibration intensity ( $I_{F2g}$ ) with the increase in intensities of the side peaks at  $404$  and  $487\text{ cm}^{-1}$ , as observed in figure 4.2c. Any further shift or broadening of  $I_{F2g}$ , [18, 42] or possible shift of the  $I_D$  peak, can be attributed to thermal restructuring, i.e., the recombination of defects with vacant lattice sites.

*In situ* transmission FTIR spectra of ceria rods obtained in helium flow at  $200^\circ\text{C}$  and  $350^\circ\text{C}$  are shown in figure 4.2d. As is clearly evident, the strong bands corresponding to physisorbed water that were present at RT (figure 4.2b) disap-

### 4.3. RESULTS AND DISCUSSION

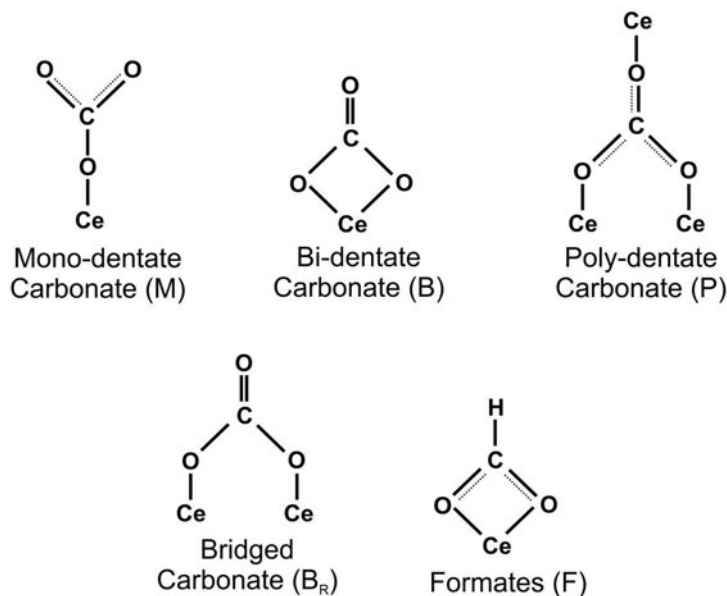


**Figure 4.3:** Schematic of the types of carbonate and formate species.

peared, leaving behind distinct peaks in the O-H stretching range between  $3800 - 3000\text{ cm}^{-1}$ .

At  $200^\circ\text{C}$  there are three clear regions, corresponding to hydroxyl, formate and carbonate species. The hydroxyl stretch regions for rods showed three strong bands at  $3700$ ,  $3648$  and approximately  $3500\text{ cm}^{-1}$ , corresponding to single-coordinated hydroxyl species, bridging hydroxyls and hydrogen bonded OH species, respectively.[5, 36, 39, 43] The peaks observed at  $2932$ ,  $2840$  and  $2723\text{ cm}^{-1}$  are assigned to C-H stretching vibrations of formate species.[43–45] Finally, between  $1800 - 800\text{ cm}^{-1}$ , intense bands were observed related to C-O stretching and bending vibrations of carbonates (visible at  $1356$  and  $854\text{ cm}^{-1}$ ) and formates (evident from peak at  $1540\text{ cm}^{-1}$ , see figure A4.10 in the Appendix).[24, 46] Based on literature, several carbonate species can be distinguished in the  $1800 - 800\text{ cm}^{-1}$  range, see figure 4.3 and table 1 for structures and the peak assignments.

As can be seen in figure 4.2d, formate ( $1540$  and  $1298\text{ cm}^{-1}$ ) and mono/bi-dentate carbonates ( $1044/1474\text{ cm}^{-1}$ ) species were no longer visible as they are unstable at  $350^\circ\text{C}$ .[45] As a result, two distinct regions related to hydroxyl and

carbonate bands were observed. In comparison to 200°C, at 350°C total hydroxyl peak intensities in the region 3800 – 3000 cm<sup>-1</sup> were lower. In addition, the 3700 cm<sup>-1</sup> band disappeared and the 3648 cm<sup>-1</sup> peak decreased in intensity relative to that at 3500 cm<sup>-1</sup>. The carbonate peaks observed in the region 1600 – 800 cm<sup>-1</sup> (see table 4.1 for peak assignments) correspond to poly-dentate species (see figure 4.3).[40]

**Table 4.1:** FTIR peak assignment of carbonate and formate species observed on fresh ceria rods at 200 and 300°C. Key: F (formates), P (poly-dentate carbonates), M (mono-dentate carbonates), B (bi-dentate carbonates) and B<sub>R</sub> (bridged carbonates).

Peaks (cm <sup>-1</sup> )	Types of species	Temperature (°C)	Reference
2932	F & 2 <sup>nd</sup> overtone of P	200	[43–46]
2922	2 <sup>nd</sup> overtone of P	350	[43]
2840	F & 2 <sup>nd</sup> overtone of P	200	[43–46]
2850	2 <sup>nd</sup> overtone of P	350	[43]
2723	F	200	[43–45]
1540	F	200	[43–46]
1494	M	200	[37, 40, 46, 47]
1474	B	200	[37, 48]
1462	P	200, 350	[37, 40, 43]
1391	B <sub>R</sub>	200	[37, 43]
1370	P	200, 350	[37, 40, 43, 46]
1356	M	200	[37, 40, 43, 46, 47]
1298	F	200	[37, 43–46]
1145	B <sub>R</sub>	200	[37, 43]
1062	P	200, 350	[40, 43, 46]
1044	M	200	[37, 46, 47]
854	M, B & P	200	[37, 40, 43, 46]
	P	350	[40, 43, 46]

At 350°C, fewer carbonate species were observed with FTIR spectroscopy compared to 200°C, accompanied by the decrease in peak ratio  $I_D/I_{F2g}$  in Raman spectra. It is reported in the literature that exposure of ceria to CO/CO<sub>2</sub> results in the formation of carbonates by interaction with lattice oxygen, which creates defects in the ceria lattice.[25, 49–51] The presence of fewer carbonate species (observed via

### 4.3. RESULTS AND DISCUSSION

FTIR spectroscopy) hence also explains the existence of fewer defects ( $I_D/I_{F2g}$ , Raman) at 350°C. More details on the relation between defects and carbonate species are discussed below.

#### 4.3.3 *In situ* Raman at 200°C: CO adsorption and H<sub>2</sub>O reactivity

To investigate the defect chemistry of ceria rods at 200°C the sample was exposed to the series of gas flows as outlined in figure 4.1, resulting in the spectra shown in figure 4.4. Running from top to bottom of figure 4.4, each plot on the left-hand side contains two spectra corresponding to ‘before’ and ‘after’ exposure to the respective gas flow. The graphs plotted in the right-hand column are the difference spectra of the spectra in the left column. The difference spectra were obtained by subtracting the spectrum obtained before exposure from the spectrum after exposure.

In figure 4.4a, the spectrum obtained in CO(2) flow at 200°C is shown together with the spectrum in He flow (He(1)). To focus on the Raman intensities of fluorite and defects bands under exposure to CO and H<sub>2</sub>O, the spectral region 200 – 680 cm<sup>-1</sup> is shown. In CO, the broad fluorite band centered at 457 cm<sup>-1</sup> decreased in intensity as is evident from the negative peaks at 413 and 464 cm<sup>-1</sup> in the difference spectrum (figure 4.4b). The overall  $I_D$  band (520 – 590 cm<sup>-1</sup>) broadened to lower wavenumber due to a new band arising at 550 cm<sup>-1</sup>, clear from the difference spectrum (2-1) in figure 4.4b. The maximum intensity of the defect peak at 593 cm<sup>-1</sup> remained unchanged. This observation indicates the formation of defects in the ceria lattice upon introduction of CO, which is in agreement with literature.[8, 18, 25] The inverse relation between the  $I_{F2g}$  lattice vibration and the defect  $I_D$  band has been suggested previously in literature.[18]

The spectrum in CO(2), the spectrum obtained in He(3) immediately after CO, and their difference are shown in figure 4.4c and 4.4d. On flowing He(3), 95 % of the changes that were observed upon CO introduction disappeared and the spectrum regained its original peak positions as for the fresh sample in He(1). This observation indicates that the CO-induced changes are reversible on the ceria rods at 200°C.

H<sub>2</sub>O/He(4) was flowed after He(3), see figure A4.4 in the Appendix for the spectrum obtained after H<sub>2</sub>O/He(4). Subsequently, He(5) was flowed to remove

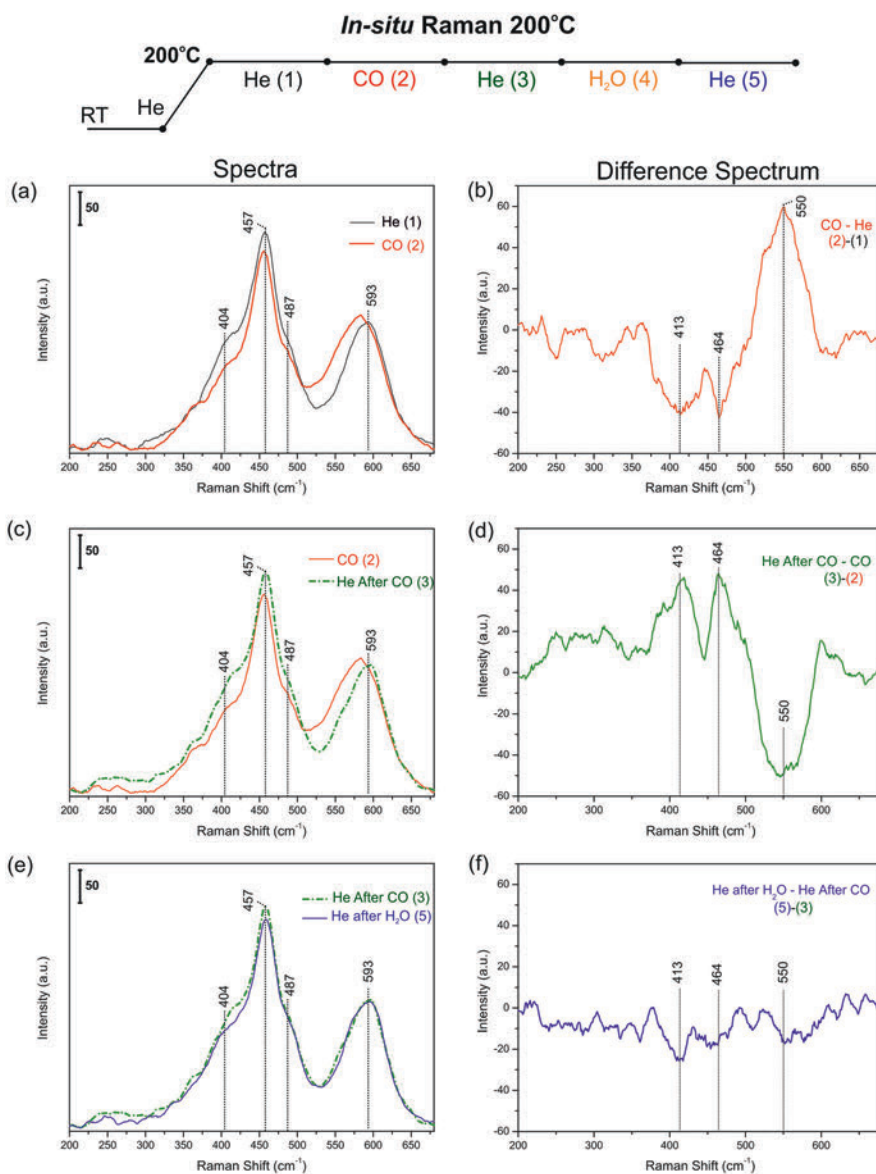


**Figure 4.4:** *In situ* Raman spectra at 200°C of ceria rods a) in He(1) (black solid spectrum), followed by CO(2) (red solid line); b) CO(2) - He(1); c) CO(2) (red solid line) followed by He(3) (green dash-dotted line); d) He(3) - CO(2); e) He(3) and He(5) after He/H<sub>2</sub>O(4) flow (blue solid spectrum); f) He(5) - He(3).

### 4.3. RESULTS AND DISCUSSION

physisorbed H<sub>2</sub>O, and the resulting spectrum is shown in figure 4.4e. Only subtle changes in intensities of the fluorite peaks at 457, 404 and the defect band at 593 cm<sup>-1</sup> were observed upon water treatment and subsequent He flow as confirmed by the difference spectrum in figure 4.4f.

#### 4.3.4 *In situ* Raman at 350°C: CO adsorption and H<sub>2</sub>O reactivity

The Raman spectra for ceria rods at 350°C after CO adsorption and rehydration with H<sub>2</sub>O can be seen in figure 4.5 (left hand column). In the difference spectra shown in figure 4.5 (right hand column), the induced changes on adsorption of CO and regeneration by H<sub>2</sub>O can be seen more specifically.

In figure 4.5a, the spectrum obtained in CO(2) flow is plotted with the spectrum in He(1). In the presence of CO, decrease in intensity of the entire fluorite band (404, 450 and 487 cm<sup>-1</sup> peaks combined) was observed. In addition, the defect peak at 597 cm<sup>-1</sup> remained unchanged. The band between 520 – 590 cm<sup>-1</sup> significantly increased due to the formation of additional new defect peaks at lower wavenumbers (see figure 4.5b). Due to the noise level of the spectrum and thus the uncertainty in peak position, individual defect peaks were not specifically assigned in figure 4.5b. The spectrum obtained on flowing He(3) after CO can be seen in figure 4.5c (green dash-dotted spectrum) together with the CO(2) spectrum. Minor changes were observed, i.e., a small increase in intensity of the 450 cm<sup>-1</sup> peak and a subtle decrease in the defect-related band, as can be better seen in the difference spectrum in figure 4.5d.

Subsequently, the sample was exposed to H<sub>2</sub>O/He(4) flow (figure A4.5 in the Appendix) followed by He(5) to remove physisorbed water (figure 4.5e). After exposure to H<sub>2</sub>O and He(5), the fluorite band centered at 450 cm<sup>-1</sup> showed an increased intensity accompanied by an overall band broadening. The CO-induced defect band centered at 550 cm<sup>-1</sup> disappeared (figure 4.5f) and thus the overall peak area of the defect band between 520 – 590 cm<sup>-1</sup> decreased. As indicated above, the observations at 350°C suggest that the I<sub>D</sub> band is inversely connected to the I<sub>F2g</sub> band.

It is clear from the Raman spectra that the interaction of CO and subsequent reaction with H<sub>2</sub>O on ceria rods is different at 200°C compared to 350°C. The differences are addressed in detail in general discussion section when compared to

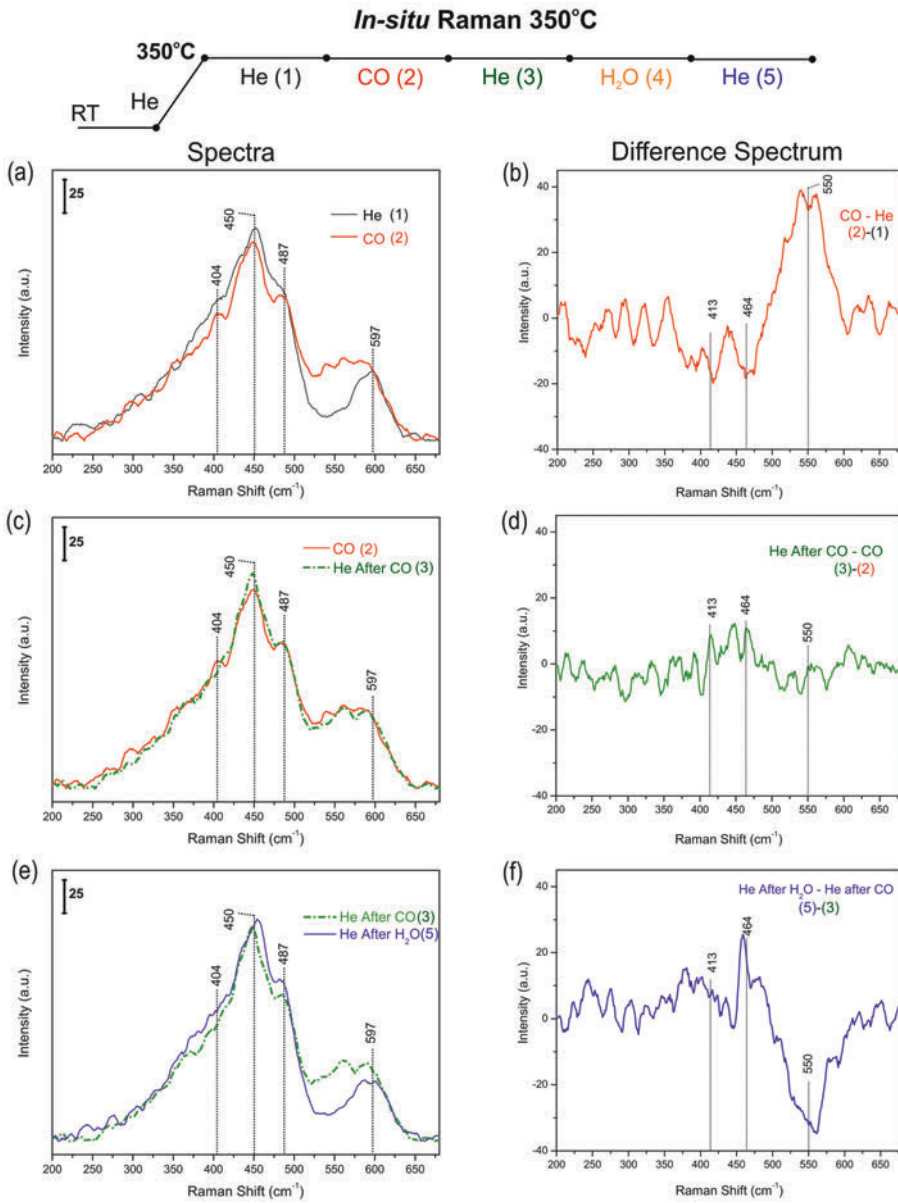


**Figure 4.5:** *In situ* Raman spectra at 350°C of ceria rods a) in He(1) (black solid spectrum), followed by CO(2) (red solid line); b) CO(2) - He(1); c) CO(2) (red solid line) followed by He(3) (green dash-dotted line); d) He(3) - CO(2); e) He(3) and He(5) after He/H<sub>2</sub>O(4) flow (blue solid spectrum); f) He(5) - He(3).

### 4.3. RESULTS AND DISCUSSION

the changes observed in the infrared spectra.

In the past years, several studies have proposed different types of defects in ceria lattices, which can be classified in four different types based on energy calculations.[52–54] The four different types are (1) anion Frenkel pairs (an oxygen atom is displaced from its lattice position to interstitial site), (2) oxygen vacancies (an oxygen atom is missing from one of the lattice positions), (3) interstitial sites (displacement of both a cerium and oxygen ion to interstitial sites) and (4) Schottky disorders (removal of cations and anions from their lattice sites creating vacancies whilst maintaining stoichiometry). In all cases, the formation of these defects introduces vacant sites (V) in the ceria lattice. Anion Frenkel pair defects (ca.  $600\text{cm}^{-1}$ ) and oxygen vacancy defects ( $550 \pm 10\text{cm}^{-1}$ ) were experimentally first assigned on doped ceria[20, 55, 56] and subsequently for uncalcined ceria nanoparticles.[42] For calcined ceria nanoshapes, Wu *et al.* suggested the presence of anion Frenkel pair defects, and showed that oxygen vacancy defects appear after  $\text{H}_2$  treatment at  $600^\circ\text{C}$ . [17]

In the present study, CO exposure to ceria rods results in the formation of a Raman band centered at  $550\text{cm}^{-1}$ , which could be assigned to oxygen vacancy defects based on previous assignments. However, the  $I_D$  band is very broad and has distinct shoulder peaks at  $525$  and  $570\text{cm}^{-1}$  (figure 4.4). In our opinion, the observation of these shoulders suggests the existence of different types of defects, such as interstitial defects and Schottky disorder, in addition to the previously proposed anion Frenkel pair defects and can also be due to the clustering of vacancy defects to form vacancy dimers and trimers.[57, 58] We believe that the present work is the first experimental evidence that shows the existence of additional types of defects. Further investigations are required for specific defect identification and corresponding peak assignment. In the remainder of this paper we will refer to vacancies (V) without differentiating between the different kinds of oxygen disorder in the ceria lattice.

#### 4.3.5 *In situ* FTIR at $200^\circ\text{C}$ : CO adsorption and $\text{H}_2\text{O}$ reactivity

Recently, we reported FTIR studies on ceria wires at  $200^\circ\text{C}$ . [24] The spectral patterns when exposed to CO and  $\text{H}_2\text{O}$  at  $200^\circ\text{C}$  for ceria rods obtained in this study are similar to those reported for ceria wires. To avoid duplication of results, the

FTIR plots for the ceria rods are shown in figure A4.6 in the Appendix. Summarizing, the following observations were made: On exposure to CO, the isolated OH species (at 3700 and 3648  $\text{cm}^{-1}$  in the Appendix, figure A4.6) decreased in intensity accompanied by significant formation of formates (3000 – 2800, 1800 – 800  $\text{cm}^{-1}$ ) and carbonates (1800 – 800  $\text{cm}^{-1}$ ). Upon subsequent exposure to He after CO flow, approximately 10% of the adsorbed carbonate and formate species desorbed with subtle regeneration of bridging hydroxyl ( $\text{OH}^{3648}$ ) species. Finally, by flowing  $\text{H}_2\text{O}/\text{He}$  for 30 min, major regeneration of hydroxyl species and decomposition of carbonate and formate species (approx. 90%) occurred; figure A4.11 in the Appendix presents a set of time-resolved spectra, showing that most of the changes take place in the first 5 min.

### 4.3.6 *In situ* FTIR at 350°C: CO adsorption and $\text{H}_2\text{O}$ reactivity

The *in situ* FTIR spectra at 350°C are shown in figure 4.6. Upon exposure to CO(2), the  $\text{OH}^{3668}$  and  $\text{OH}^{3480}$  intensities decreased, whereas the  $\text{OH}^{3648}$  peak increased and shifted to 3637  $\text{cm}^{-1}$  (figure 4.6a inset). The latter band has been previously assigned to O-H stretching in  $\text{CO}_2(\text{OH})^-$ . [43, 59] In addition, the formation of formate C-H stretch bands at 2945 and 2840  $\text{cm}^{-1}$  was observed, with a significant increase in peak intensity for C-O vibrations of formates and carbonates in the 1800 – 800  $\text{cm}^{-1}$  region (see figure 4.6a). The exact band positions of the species formed (at 1581, 1417, 1322, 1084, 1053 and 857  $\text{cm}^{-1}$ ) can be better seen in the difference spectrum (figure 4.6b). After CO, the sample was exposed to He(3) (green spectrum in figure 4.6c). The key observations were a slight rise in intensity of hydroxyl species at 3668  $\text{cm}^{-1}$ , with an increase and shift of the 3637 peak to higher wavenumber (evident from s-curve<sup>3652</sup> in difference spectrum in figure 4.6d). Furthermore, the formate peaks at 2945 and 2840  $\text{cm}^{-1}$  disappeared and the band in region 1800 – 1100  $\text{cm}^{-1}$  became narrower. These induced changes are clearly visible in figure 4.6d, where negative bands at 1581, 1294, 1084, 1033 and 847  $\text{cm}^{-1}$  were observed. [46] The disappearance of C-H and C-O vibrations of formates in difference spectrum indicates the decomposition of formate species.

On subsequent treatment with  $\text{H}_2\text{O}/\text{He}$ (4) followed by He(5) (blue spectrum in figure 4.6e), OH groups at 3668, 3637, and 3480  $\text{cm}^{-1}$  were restored (figure 4.6e inset). Furthermore, subtle changes were observed in the carbonate re-

### 4.3. RESULTS AND DISCUSSION

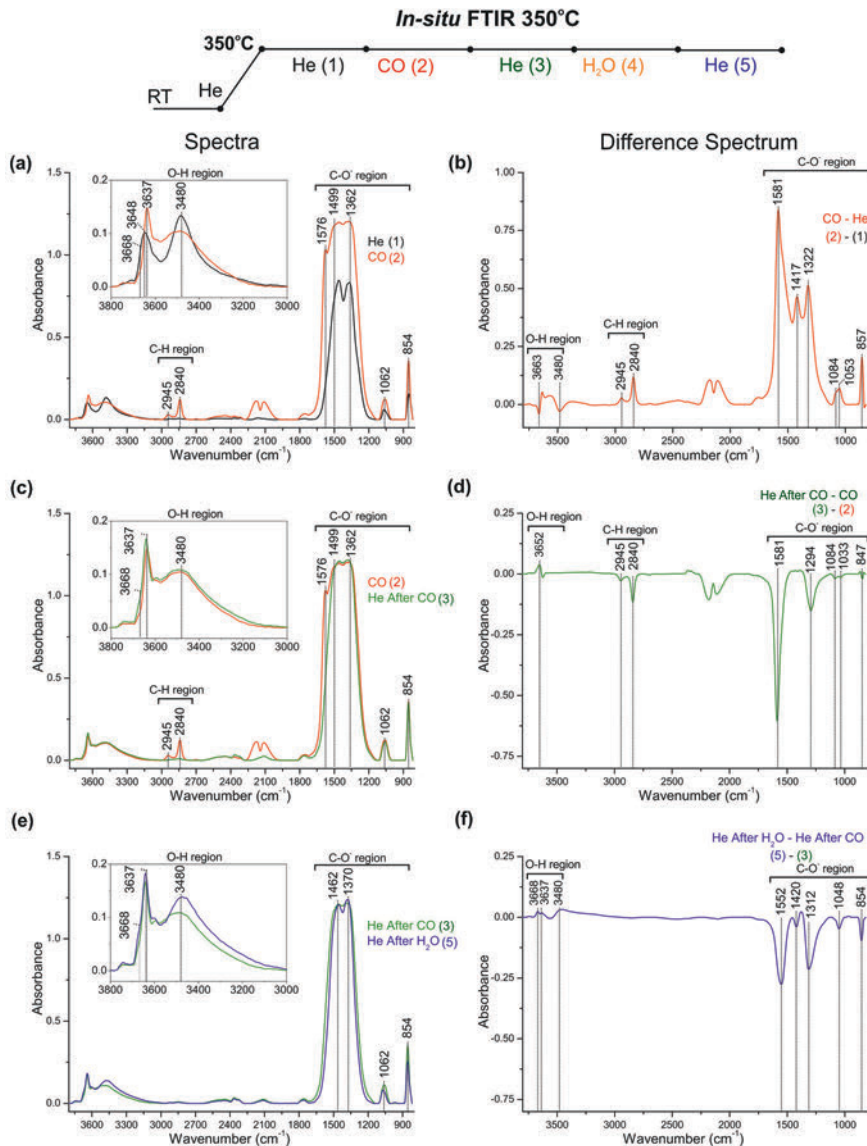


**Figure 4.6:** *In situ* FTIR spectra at 350°C of ceria rods a) in He(1) (black spectrum), followed by CO(2) (red line); b) CO(2) - He(1); c) CO(2) (red line) followed by He(3) (green line); d) He(3) - CO(2); e) He(3) and He(5) after He/H<sub>2</sub>O(4) flow (blue spectrum); f) He(5) - He(3).

gion ( $1700 - 800\text{cm}^{-1}$ ). In the difference spectrum (figure 4.6f), negative carbonate bands at  $1552$ ,  $1420$ ,  $1312$ ,  $1048$  and  $854\text{cm}^{-1}$  were observed, indicating decomposition of carbonate species. Based on the literature, these carbonate species were identified as mono/bi-dentate carbonates.[37, 39, 43] Therefore, the remaining carbonates in the spectrum (at  $1462$ ,  $1370$ ,  $1062$  and  $854\text{cm}^{-1}$ ) after treatment with  $\text{H}_2\text{O}$  correspond to poly-dentate species (see table 1).[46] These carbonates are also visible when comparing the spectra obtained at  $350^\circ\text{C}$  for the fresh and regenerated rod sample (figure A4.8). The amount of OH species (region  $3800 - 3000\text{cm}^{-1}$ ) recovered after  $\text{H}_2\text{O}$  treatment was higher in comparison to the fresh sample.

## 4.4 General discussion

### 4.4.1 Ceria rods defect chemistry at $200^\circ\text{C}$

To compare the Raman and FTIR results, the relative differences in the Raman spectra were plotted with respect to the most intense defect peak ( $\approx 550\text{cm}^{-1}$ ) formed upon introduction of CO (see section 4.2). We have assumed that the total defect concentration is semiquantitatively correlated with the relative Raman intensities. Likewise, FTIR difference spectra were normalized with respect to the most intense peak (formate peak at approximately  $1576\text{cm}^{-1}$ ). The relative changes observed on exposure to each gas type at  $200^\circ\text{C}$  in both Raman and FTIR spectra are shown in figure 4.7a and 4.7b respectively.

The red spectra in figures 4.7a and b show that with the formation of vacancies (Raman -  $550\text{cm}^{-1}$ ) significant amounts of formates and carbonates are formed (FTIR -  $1800 - 800\text{cm}^{-1}$ ). This observation is schematically represented in figure 4.7c. Upon flowing He after CO, the majority of defects disappear (figure 4.7a, green line). At the same time in the FTIR at  $200^\circ\text{C}$  (figure 4.7b green line), only approximately 10% decomposition of formates and carbonates and 10% regeneration of OH groups are observed. Thus, desorption at this stage indicates that the defects created are related to about 10% of the carbonates and formates formed on exposure to CO and that they are reversible in nature (schematically depicted in figure 4.7c top row). Separation of different types of carbonates species connected with defects is not possible for this experiment because they decompose

#### 4.4. GENERAL DISCUSSION

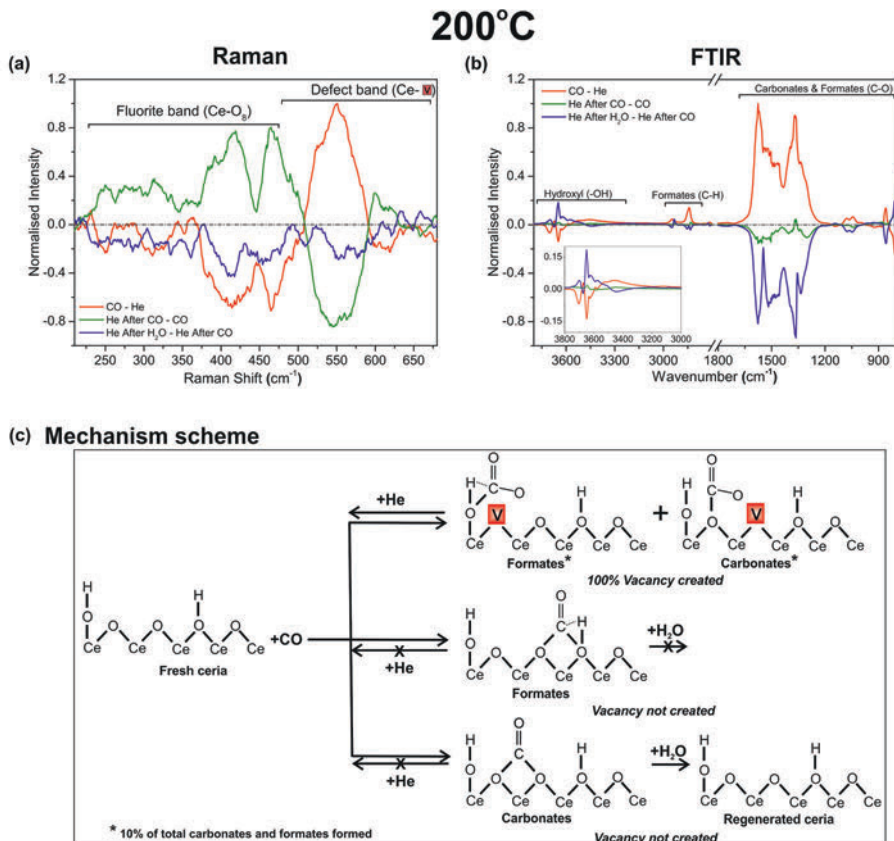


**Figure 4.7:** Relative changes introduced in different gases with respect to the species formed in CO for (a) Raman and (b) FTIR data at 200°C. c) Schematic reaction mechanism of ceria rods at 200°C (“V” represents oxygen vacancy). For simplicity only surface defects are indicated. However, oxygen diffusion will occur through the lattice to reach equilibrium between surface and bulk defects.

simultaneously.

Finally, the FTIR spectra show that major regeneration of OH species and decomposition of carbonates and formate species occurs in the presence of  $\text{H}_2\text{O}$  (figure 4.7b, blue line), without significant changes in the defects observed with Raman spectroscopy.

In conclusion, at 200°C, upon the introduction of CO, 90% of the carbonate and formate species formed do not involve the creation of defects as depicted in figure 4.7c (middle and bottom row). Most of those species decompose in the

presence of H<sub>2</sub>O while regenerating the OH groups.

#### 4.4.2 Ceria rods defect chemistry at 350°C

The normalized Raman and FTIR plots obtained at 350°C with the mechanism scheme are shown in figure 4.8. Similar to experiment at 200°C, at 350°C also formates and carbonates are formed by interaction of CO with OH species, simultaneously creating defects in the ceria lattice (figure 4.8c depicts a schematic representation).

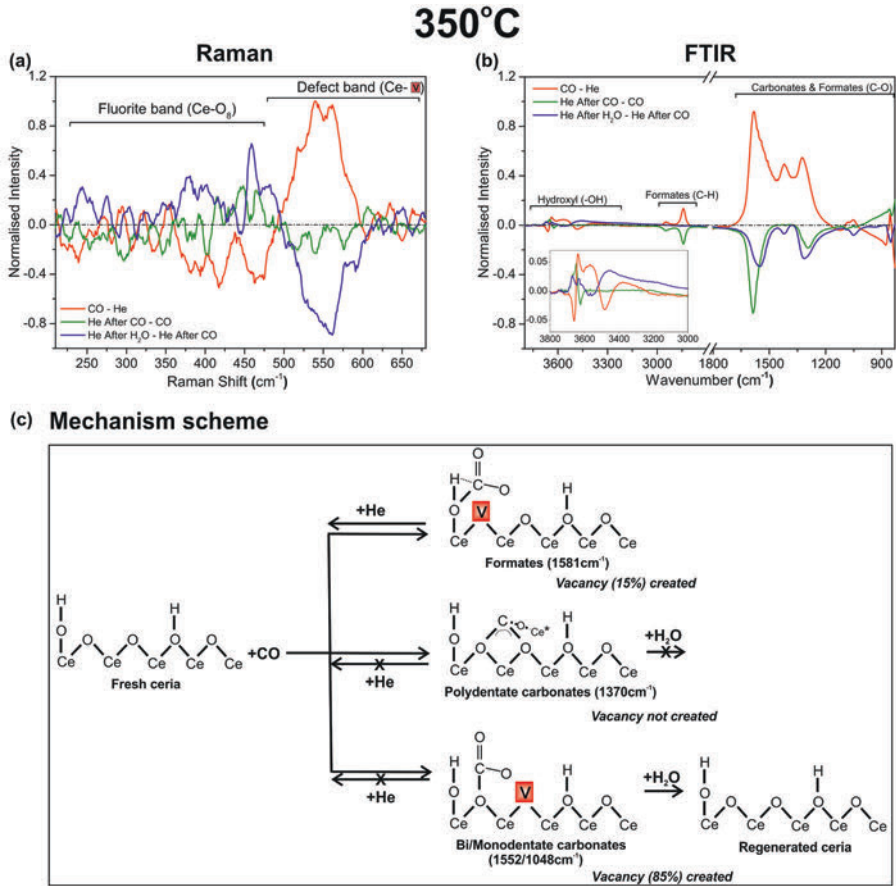
Interestingly, subsequent He flush decomposes only all formates, most clearly evidenced by the negative peak for the C-H vibrations between 3100 and 2900 cm<sup>-1</sup>. The complete formate decomposition only removes 15% of the vacancies (figure 4.8a green line), while recreating hydroxyl groups. Thus, formates are forming at the expense of part of the hydroxyl species, and creating a small amount of defects within the ceria structure (schematically shown in figure 4.8c top row).

Upon H<sub>2</sub>O flow, the remaining 85% of the defects disappeared (blue line, figure 4.8a), while 35% of the carbonates decomposed (blue line, figure 4.8b) and hydroxyl groups were formed. These carbonate bands at 1552/1048 cm<sup>-1</sup> can be specifically attributed to mono/bi-dentate carbonate species, leaving the poly-dentate carbonates as residual species on the ceria, as summarized in figure 4.8c.

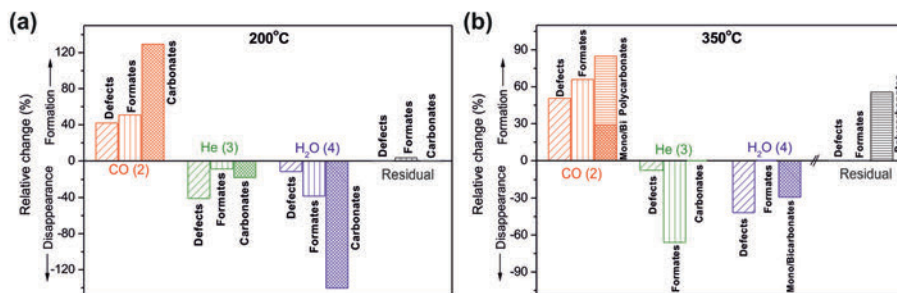
As the defects produced upon addition of CO disappeared after the series of treatments, it must be concluded that the poly-dentate carbonate species are not related to defect creation (labeled as “Vacancy not created” in figure 4.8c).

Figure 4.9 summarizes the temperature effect on the reactivity of ceria with CO and subsequently H<sub>2</sub>O. In figure 4.9 the relative amounts of species appearing and disappearing upon the different treatments are compared for the experiments at 200°C and 350°C. Clearly, after regeneration with H<sub>2</sub>O, at 350°C stable poly-dentate carbonate species were observed, while no residual carbonates were observed at 200°C (figure 4.9 (residual species)). At the same time, this study shows that the formation of vacancies in ceria rods cannot uniquely be assigned to the formation of a specific species adsorbed on ceria. Further, although the Raman signatures of the defect band arising after addition of CO are very similar (figure A4.9 of the Appendix), their chemical origin seems to be different since at 350°C the addition of H<sub>2</sub>O is needed to remove the vacancies, while at 200°C the

#### 4.4. GENERAL DISCUSSION



**Figure 4.8:** Relative changes introduced in different gases with respect to the species formed in CO for (a) Raman and (b) FTIR data at 350°C. (c) Schematic reaction mechanism of ceria rods at 350°C (“V” represents oxygen vacancy). For simplicity only surface defects are indicated. However, oxygen diffusion will occur through the lattice to reach equilibrium between surface and bulk defects.



**Figure 4.9:** Bar diagram of species formed (positive) and decomposed (negative values) on introduction different gases in ceria rods at 200°C and 350°C. The numbers represent the relative change (%) for each individual species.

majority disappeared already in He flow.

This research is an important step forward to understand the behavior of ceria rods towards the catalytic reactions involving CO and water. Furthermore, our results give scope for further theoretical and experimental work to understand the roles of different defects in ceria catalysts.

## 4.5 Conclusions

This study revealed the complex role of defects in ceria for reactions involving CO and H<sub>2</sub>O. For ceria rods, the involvement of defects during CO adsorption and consecutive reaction with H<sub>2</sub>O fundamentally changes with temperature. At 200°C, most of the carbonate and formate species that form in CO do not induce the formation of any defects in the lattice. However, at 350°C, the formation of formate and carbonate (mono/bi-dentate) species does lead to defect formation. Further, very stable poly-dentate carbonates are formed exclusively at 350°C without creating vacancies and these species are stable in water vapor. These results show that, depending on temperature, the formation of certain specific formate and carbonate surface species involves lattice oxygen from CeO<sub>2</sub> forming defects, whereas other species do not.

## Appendix 4

TEM image of the ceria sample after calcination is shown in figure A4.1. The ceria sample clearly has rod morphology.

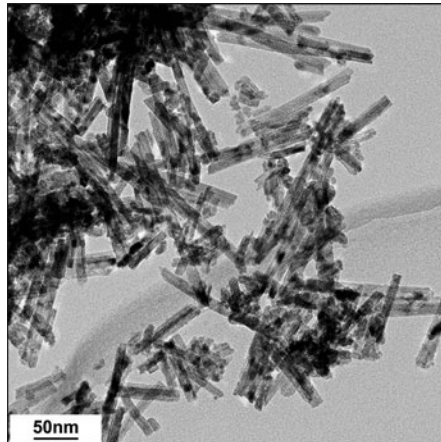


**Figure A4.1:** TEM image of ceria rods.

In figure A4.2, *in situ* Raman raw and smoothed spectra obtained in He stream at different temperatures are shown. All the Raman spectra shown in the present paper are smoothed (21 points) to better define any observed changes. As evident from figure A4.2, the peak position observed in smoothed spectrum at different temperatures is real and not an artifact of data smoothing.

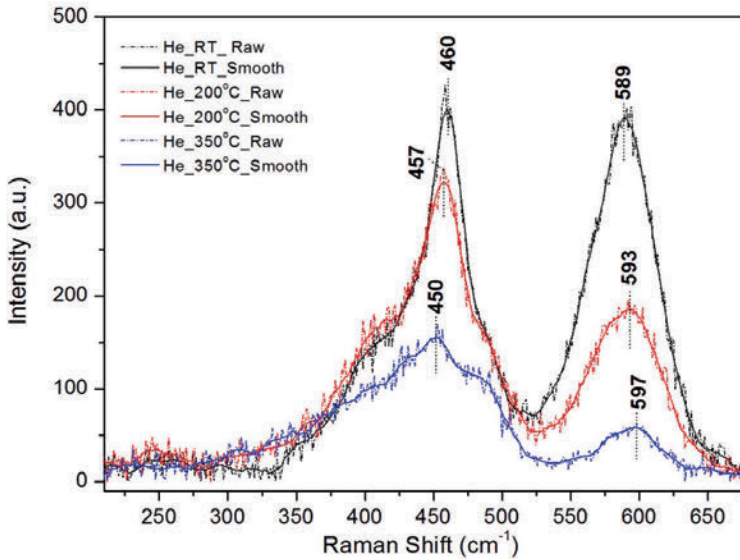


**Figure A4.2:** *In situ* Raman raw (dash-dotted) vs. smoothed (solid) spectra of ceria rods in He flow at room temperature (black spectrum), 200°C (red spectrum) and 350°C (blue spectrum).

In figure A4.3, *in situ* Raman raw and smoothed spectra obtained in CO stream at 200°C and 350°C are shown. The Raman spectra shown in the present work are smoothed (21 points) to better define any changes introduced on exposure to CO/H<sub>2</sub>O. As evident from figure A4.3, the CO-induced changes observed in smoothed spectrum at 200°C and 350°C is real and not due to the data smoothing artifact.

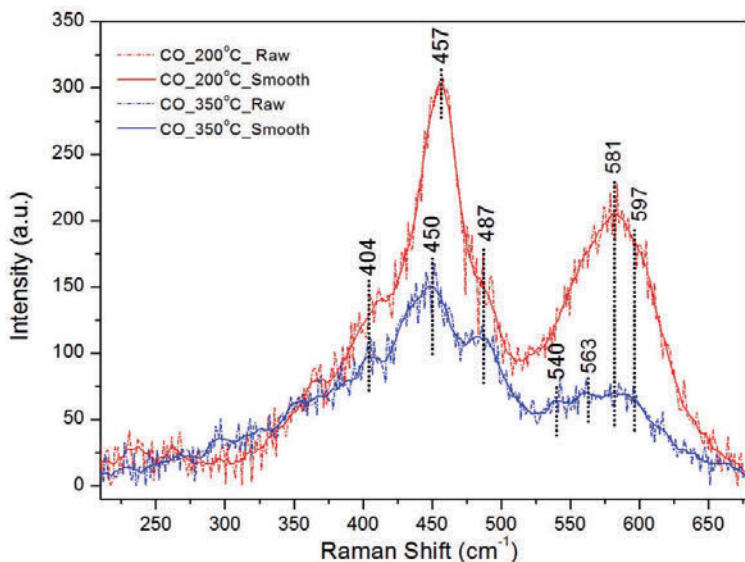


**Figure A4.3:** *In situ* Raman raw (dash-dotted) vs. smoothed (solid) spectra of ceria rods in 33 vol.% CO/He at 200°C (red spectrum) and 350°C (blue spectrum).

In figure A4.4, *in situ* Raman spectra at 200°C of ceria rods in H<sub>2</sub>O/He (4) and He after H<sub>2</sub>O (5) flow are shown. To remove the physisorbed water, He was flowed after H<sub>2</sub>O/He flow. From figure A4.4, it is evident that in He (5) flow, no major change was observed except a subtle increase in the shoulder peak at 404 and 560 cm<sup>-1</sup>. These changes are probably associated with physisorbed H<sub>2</sub>O.

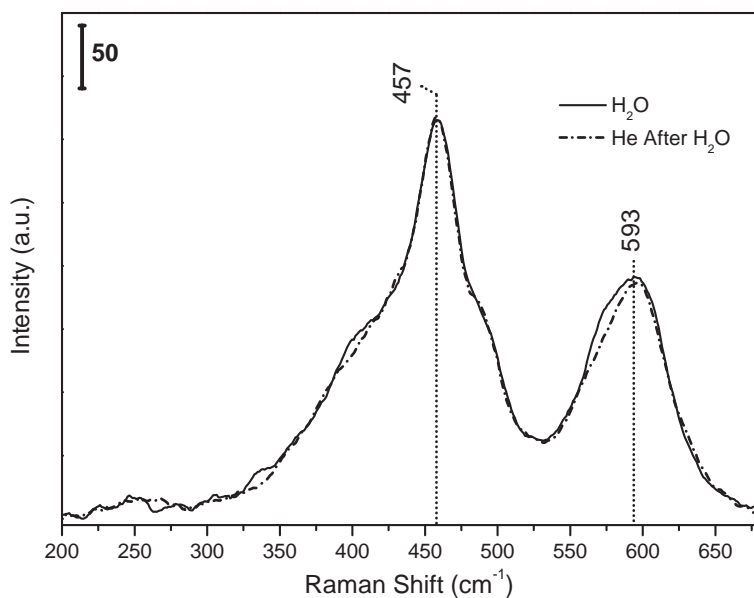


**Figure A4.4:** *In situ* Raman spectra at 200°C of ceria rods in H<sub>2</sub>O/He (4, solid spectrum) followed by He (5, dash-dotted spectrum) flow.

In figure A4.5, *in situ* Raman spectra at 350°C of ceria rod in H<sub>2</sub>O/He (4) and He after H<sub>2</sub>O (5) flow are shown. As shown in the spectrum in figure A4.5 along with the spectrum obtained in H<sub>2</sub>O/He flow, no change was observed between He (5) and the H<sub>2</sub>O (4) spectrum, apart from subtle changes at 404, 487 and 563 cm<sup>-1</sup>.

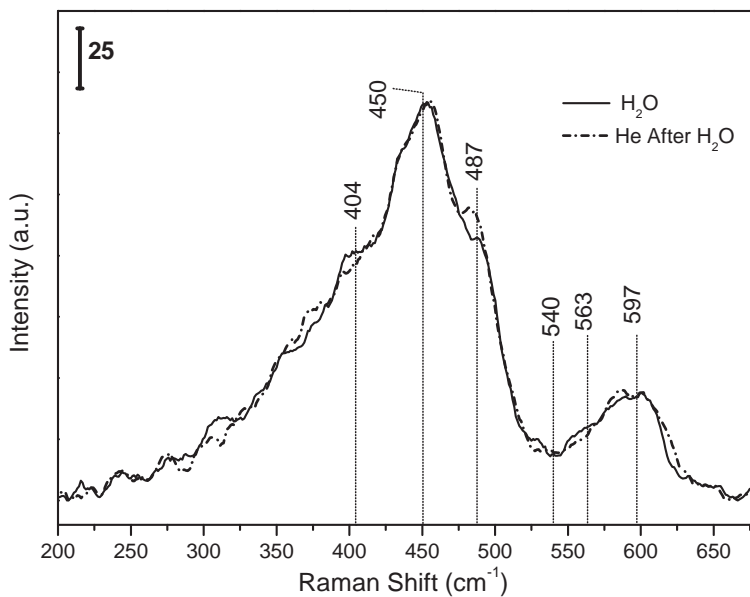
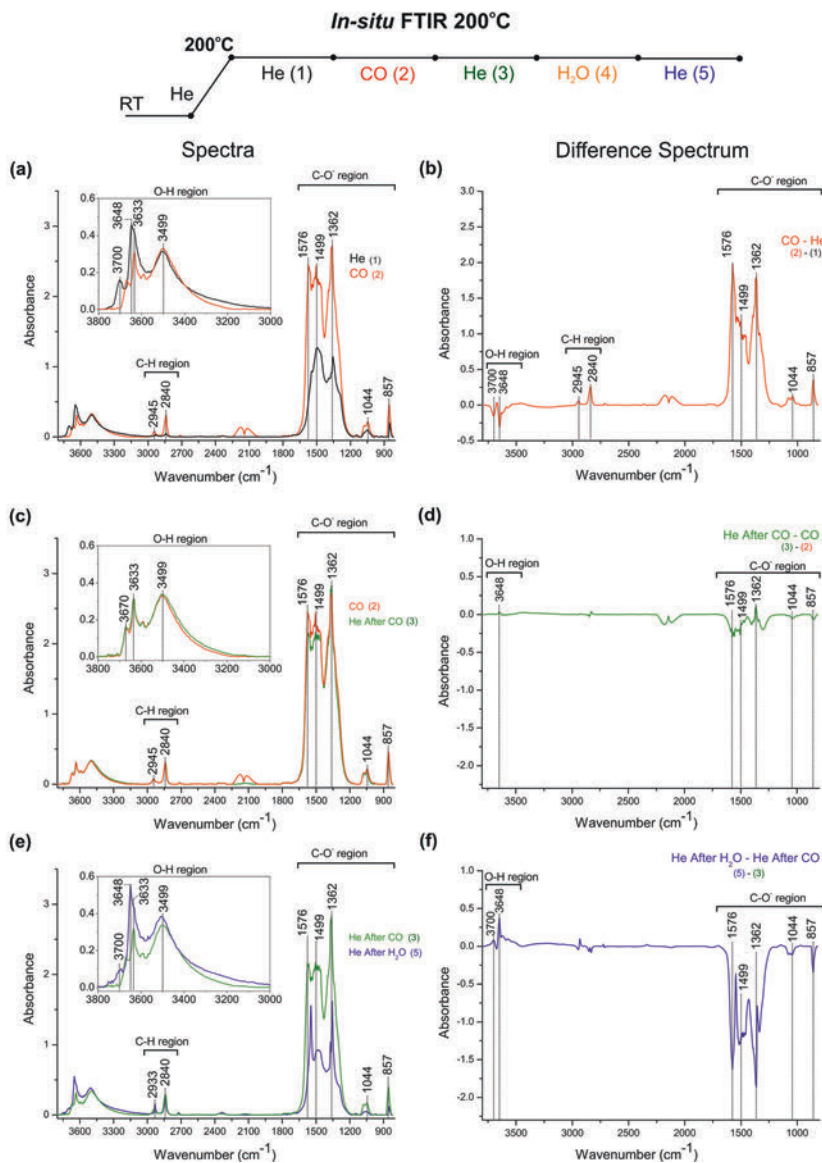


**Figure A4.5:** *In situ* Raman spectra at 350°C of ceria rods in H<sub>2</sub>O/He (4, solid spectrum) followed by He (5, dash-dotted spectrum) flow.

In figure A4.6, the spectra both with CO and He after CO, as well as He after H<sub>2</sub>O and their respective difference spectra for ceria rods at 200°C are shown. After 30 min in He flow (1, black line) at 200°C, the ceria rods were exposed to CO (2, red line) for 30 min, see FTIR spectra in figure A4.6a. On exposure to CO, the hydroxyl peaks at 3700 and 3648 cm<sup>-1</sup> decreased in intensity (see inset in figure A4.6a) with a significant increase in intensities of characteristic peaks related to formate (2840 cm<sup>-1</sup>) and carbonate (857 cm<sup>-1</sup>) species. These CO-induced changes are clearly visible in the CO-He difference spectrum shown in figure A4.6b, where the negative peaks represents the OH species that disappear with the appearance of positive formate (evident at 2945, 2840, 1576 cm<sup>-1</sup>) and carbonate (at 1362 and 857 cm<sup>-1</sup>) peaks. Note that the spikes (artifact of electronic signal) were observed in the 1800 – 1200 cm<sup>-1</sup> range for ceria rods that can be attributed to the high absorbance of the sample or sample scattering effects. Spike removal was performed on the spectra showed in figure A4.6 to better highlight the differences. To obtain the carbonate and formate peaks in wavenumber region 1600 – 1200 cm<sup>-1</sup> within detector sensitivity, the lower amount of samples is required for pressing a pellet. Therefore, ceria rod sample was diluted with inert KBr in the ratio 1:1 and FTIR experiments were performed. As can be seen in figure A4.7, fewer carbonates and formates are formed on exposure with CO. In addition the carbonate to formate pattern observed for the full and difference spectra for diluted ceria rods is similar to the pattern for pure ceria rods (figure A4.6).

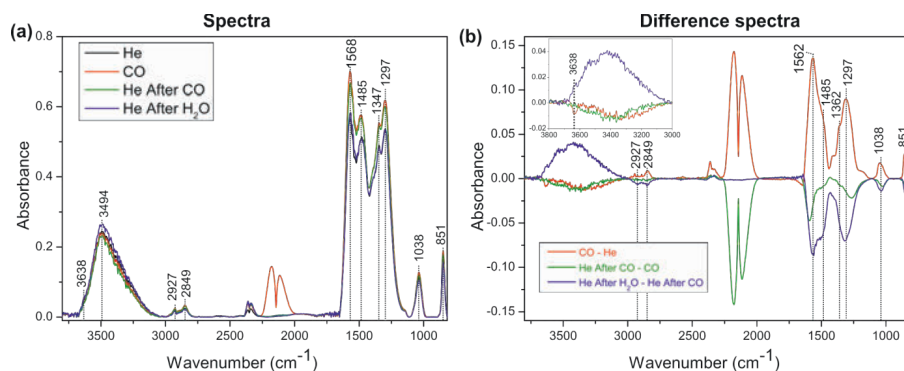
After CO, He (3) was flowed for 30 min to remove any weakly adsorbed species formed in the presence of CO (see the green spectrum in figure A4.6c and difference spectrum (3-2) in figure A4.6d). As evident in figure A4.6d, 10% desorption of adsorbed species (both carbonates and formates) occurred with the subtle regeneration of OH<sup>3648</sup> species upon flowing He after CO.

Subsequently, H<sub>2</sub>O/He (4) was flowed to regenerate the ceria support, followed by He (5) flow to remove any physisorbed H<sub>2</sub>O. The spectrum obtained in He (5, blue, after 30 min exposure) is shown in figure A4.6e with the spectrum obtained in He (3, green). As can be seen in figure A4.6e and A4.6f (difference spectrum 5-3), major regeneration of OH<sup>3700</sup> and OH<sup>3648</sup> species (inset in S6e and positive bands in S6f) and decomposition of carbonate and formate species (approx. 90%) happened upon exposure to H<sub>2</sub>O.



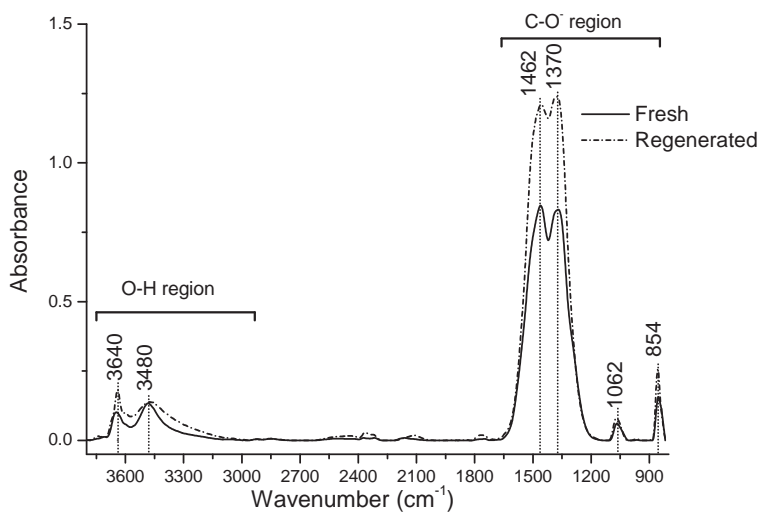
**Figure A4.6:** *In situ* FTIR spectra at 200°C of ceria rods a) in He(1) (black spectrum), followed by CO(2) (red line); b) CO (2) - He (1); c) CO(2) (red line) followed by He(3) (green line); d) He (3) - CO (2); e) He (3) and He(5) after He/H<sub>2</sub>O(4) flow (blue spectrum); f) He (5) - He (3).

Figure A4.7: To obtain the carbonate and formate bands within the sensitivity of the MCT detector, a sample pellet was prepared by diluting ceria rods with KBr (1:1). As the sample was diluted, less amount of isolated OH groups at 3700 and 3638  $\text{cm}^{-1}$  are available and the hydrogen bonded OH<sup>3494</sup> band appears prominent. As a result of less isolated OH species, fewer carbonates and formates were formed on exposure with CO. The carbonate-to-formate pattern observed for the full spectra and difference spectra was however similar to the pattern for pure ceria rods (figure A4.6).



**Figure A4.7:** *In situ* FTIR (a) spectra and (b) difference spectra at 200°C of ceria rods (with KBr) in He flow (black spectrum), followed by 33 vol.% CO/He (red line) and then by He flow (green line) and subsequently in He after H<sub>2</sub>O flow (blue spectrum).

In figure A4.8, the comparison of the spectra obtained in He flow for the fresh sample (solid line) and after regeneration with H<sub>2</sub>O (dash-dotted line) is shown. As clearly evident from the figure, an increase in intensities of hydroxyl bands is observed for the regenerated sample, indicating that more OH species were restored after water treatment. In addition, increases in intensities of poly-dentate carbonate peaks (1800 – 900 cm<sup>-1</sup>) were also observed.



**Figure A4.8:** *In situ* FTIR spectra of ceria rods at 350°C in He flow for fresh sample (solid spectrum) and after regeneration with H<sub>2</sub>O (dash-dotted spectrum).

In figure A4.9, the He subtracted CO spectrum (CO - He) of ceria rod at 200°C and 350°C are shown. As evident from figure A4.9, both spectra show peaks at similar peak position. However the relative peak intensities differ at both temperatures. This observation indicates that the similar defects with different amounts are formed on ceria rods at 200°C and 350°C.

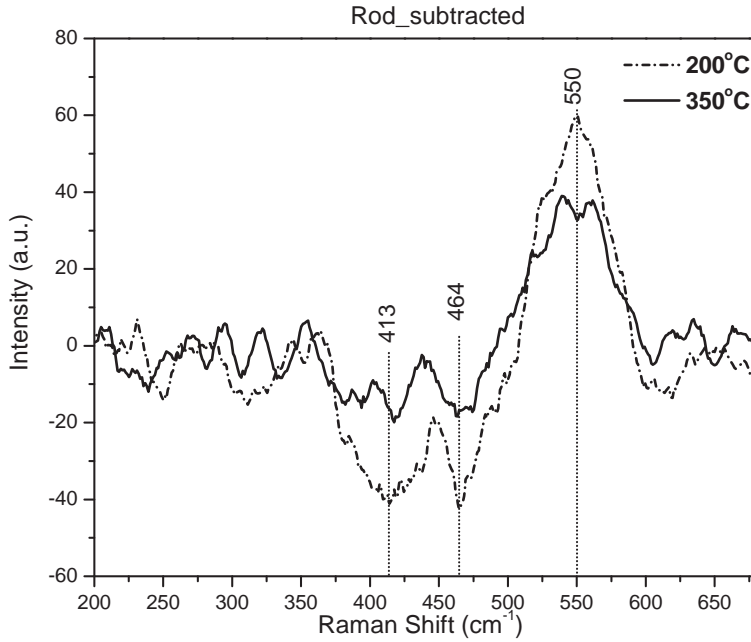


**Figure A4.9:** CO - He Raman spectra of ceria rods at 200°C (dash-dotted spectrum) and 350°C (solid spectrum).

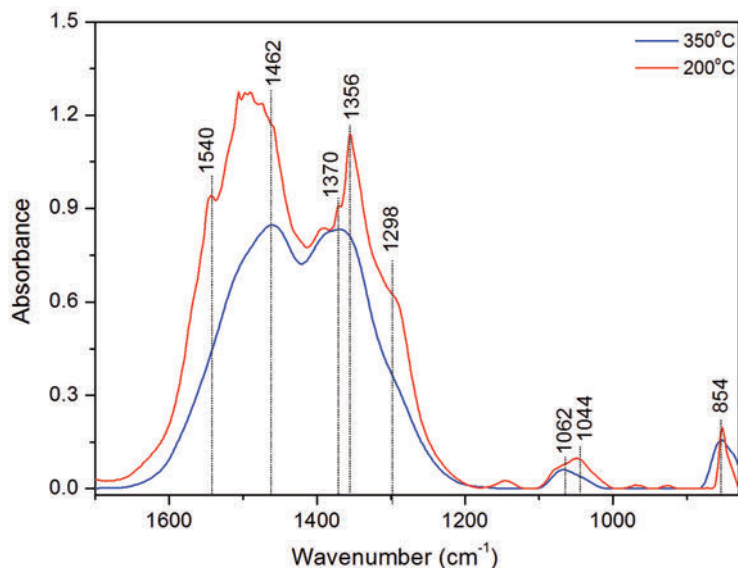


**Figure A4.10:** *In situ* FTIR spectra from 1700 – 800  $\text{cm}^{-1}$  (carbonate region) of ceria rods in He flow at 200°C (red spectrum) and 350°C (blue spectrum).

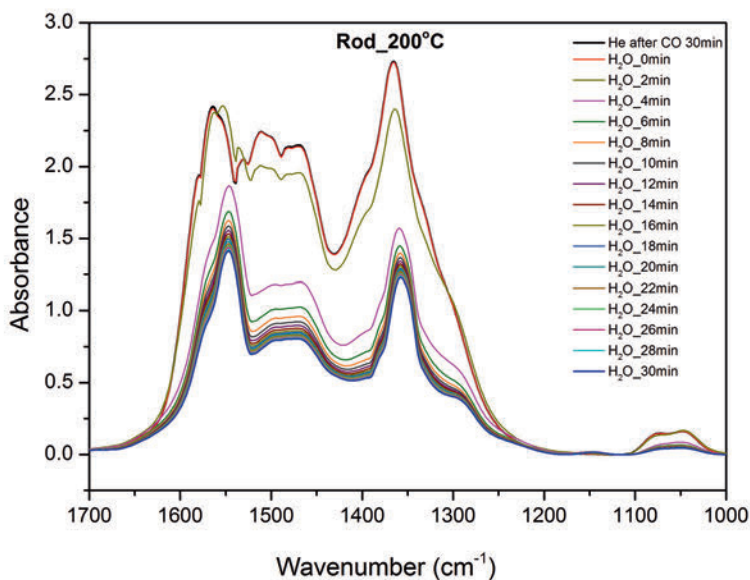


**Figure A4.11:** Time-resolved *in-situ* FTIR spectra from 1700 – 1000  $\text{cm}^{-1}$  (carbonate and formate region) of ceria rods in  $\text{H}_2\text{O}/\text{He}$  flow at 200°C.

## Bibliography

- [1] Garcia, T., Solsona, B., and Taylor, S. H. (2005)*Catal. Lett.* **105(3-4)**, 183–189.
- [2] Diwell, A., Rajaram, R., Shaw, H., and Truex, T. (1991)The role of ceria in three-way catalystsIn A. Crucq, (ed.), *Studies in Surf. Sci. and Catalysis*, volume **71**, pp. 139–152 Elsevier.
- [3] Gorte, R. J. (2010)*AIChE Journal* **56(5)**, 1126–1135.
- [4] Gorte, R. and Zhao, S. (2005)*Catal. Today* **104(1)**, 18–24.
- [5] Jacobs, G., Patterson, P. M., Williams, L., Sparks, D., and Davis, B. H. (2004)*Catal. Lett.* **96(1-2)**, 97–105.
- [6] Liu, X., Zhou, K., Wang, L., Wang, B., and Li, Y. (2009)*J. Am. Chem. Soc.* **131(9)**, 3140–3141.
- [7] Trovarelli, A., de Leitenburg, C., Boaro, M., and Dolcetti, G. (1999)*Catal. Today* **50(2)**, 353–367.
- [8] Wu, Z., Li, M., and Overbury, S. H. (2012)*J. Catal.* **285(1)**, 61–73.
- [9] Zhou, K., Wang, X., Sun, X., Peng, Q., and Li, Y. (2005)*J. Catal.* **229(1)**, 206–212.
- [10] Tana, Zhang, M., Li, J., Li, H., Li, Y., and Shen, W. (2009)*Catal. Today* **148(1-2)**, 179–183.
- [11] Trovarelli, A. (1996)*Catal. Rev.* **38(4)**, 439–520.
- [12] Zhou, K. and Li, Y. (2012)*Angew. Chem., Int. Ed.* **51(3)**, 602–613.
- [13] Mai, H.-X., Sun, L.-D., Zhang, Y.-W., Si, R., Feng, W., Zhang, H.-P., Liu, H.-C., and Yan, C.-H. (2005)*J. Phys. Chem. B* **109(51)**, 24380–24385.
- [14] Agarwal, S., Lefferts, L., Mojet, B. L., Ligthart, D. A. J. M., Hensen, E. J. M., Mitchell, D. R. G., Erasmus, W. J., Anderson, B. G., Olivier, E. J., Neethling, J. H., and Datye, A. K. (2013)*ChemSusChem* **6(10)**, 1898–1906.
- [15] Florea, I., Feral-Martin, C., Majimel, J., Ihiawakrim, D., Hirlimann, C., and Ersen, O. (2013)*Cryst. Growth Des.* **13(3)**, 1110–1121.
- [16] Liu, L., Cao, Y., Sun, W., Yao, Z., Liu, B., Gao, F., and Dong, L. (2011)*Catal. Today* **175(1)**, 48–54.
- [17] Wu, Z., Li, M., Howe, J., Meyer, H. M., and Overbury, S. H. (2010)*Langmuir* **26(21)**, 16595–16606.
- [18] Lee, Y., He, G., Akey, A. J., Si, R., Flytzani-Stephanopoulos, M., and Herman, I. P. (2011)*J. Am. Chem. Soc.* **133(33)**, 12952–12955.
- [19] Stair, P. C. and Li, C. (1997)*J. Vac. Sci. Technol., A* **15(3)**, 1679–1684.
- [20] Taniguchi, T., Watanabe, T., Sugiyama, N., Subramani, A. K., Wagata, H., Matsushita, N., and Yoshimura, M. (2009)*J. Phys. Chem. C* **113(46)**, 19789–19793.
- [21] Breyse, M., Guenin, M., Claudel, B., and Veron, J. (1973)*J. Catal.* **28(1)**, 54–62.
- [22] Han, W.-Q., Wen, W., Hanson, J. C., Teng, X., Marinkovic, N., and Rodriguez, J. A.

- (2009)*J. Phys. Chem. C* **113**(52), 21949–21955.
- [23] Shido, T. and Iwasawa, Y. (1992)*J. Catal.* **136**(2), 493–503.
- [24] Agarwal, S., Lefferts, L., and Mojet, B. L. (2013)*ChemCatChem* **5**(2), 479–489.
- [25] Nolan, M. and Watson, G. W. (2006)*J. Phys. Chem. B* **110**(33), 16600–16606.
- [26] Huang, M. and Fabris, S. (2008)*J. Phys. Chem. C* **112**(23), 8643–8648.
- [27] Dos Santos, M., Lima, R., Riccardi, C., Tranquilin, R., Bueno, P., Varela, J., and Longo, E. (2008)*Mater. Lett.* **62**(30), 4509–4511.
- [28] Filtschew, A., Stranz, D., and Hess, C. (2013)*Phys. Chem. Chem. Phys.* **15**, 9066–9069.
- [29] Daniel, M. and Loridant, S. (2012)*J. Raman Spectrosc.* **43**(9), 1312–1319.
- [30] Keramidas, V. G. and White, W. B. (1973)*J. Chem. Phys.* **59**(3), 1561–1562.
- [31] Weber, W. H., Hass, K. C., and McBride, J. R. (1993)*Phys. Rev. B* **48**, 178–185.
- [32] Mochizuki, S. (1982)*Phys. Status Solidi* **114**(1), 189–199.
- [33] Popović, Z., Dohčević-Mitrović, Z., Šćepanović, M., Grujić-Brojčin, M., and Aškračić, S. (2011)*Ann. Phys. (Berlin, Ger.)* **523**(1-2), 62–74.
- [34] Kourouklis, G. A., Jayaraman, A., and Espinosa, G. P. (1988)*Phys. Rev. B* **37**, 4250–4253.
- [35] Bertie, J. E., Ahmed, M. K., and Eysel, H. H. (1989)*J. Phys. Chem.* **93**(6), 2210–2218.
- [36] Badri, A., Binet, C., and Lavalley, J.-C. (1996)*J. Chem. Soc., Faraday Trans.* **92**, 4669–4673.
- [37] Li, C., Sakata, Y., Arai, T., Domen, K., Maruya, K., and Onishi, T. (1989)*J. Chem. Soc., Faraday Trans. I* **85**, 929–943.
- [38] Li, C., Sakata, Y., Arai, T., Domen, K., Maruya, K., and Onishi, T. (1989)*J. Chem. Soc., Faraday Trans. I* **85**, 1451–1461.
- [39] Binet, C., Badri, A., Boutonnet-Kizling, M., and Lavalley, J.-C. (1994)*J. Chem. Soc., Faraday Trans.* **90**, 1023–1028.
- [40] Bozon-Verduraz, F. and Bensalem, A. (1994)*J. Chem. Soc., Faraday Trans.* **90**, 653–657.
- [41] Binet, C., Badri, A., and Lavalley, J.-C. (1994)*J. Phys. Chem.* **98**(25), 6392–6398.
- [42] Spanier, J. E., Robinson, R. D., Zhang, F., Chan, S.-W., and Herman, I. P. (2001)*Phys. Rev. B* **64**, 245407.
- [43] Binet, C., Daturi, M., and Lavalley, J.-C. (1999)*Catal. Today* **50**(2), 207–225.
- [44] Binet, C., Jadi, A., and Lavalley, J.-C. (1992)*J. Chim. Phys. Phys. - Chim. Biol.* **89**, 1779–1797.
- [45] Li, C., Domen, K., Maruya, K., and Onishi, T. (1990)*J. Catal.* **125**(2), 445–455.
- [46] Vayssilov, G. N., Mihaylov, M., Petkov, P. S., Hadjiivanov, K. I., and Neyman, K. M. (2011)*J. Phys. Chem. C* **115**(47), 23435–23454.

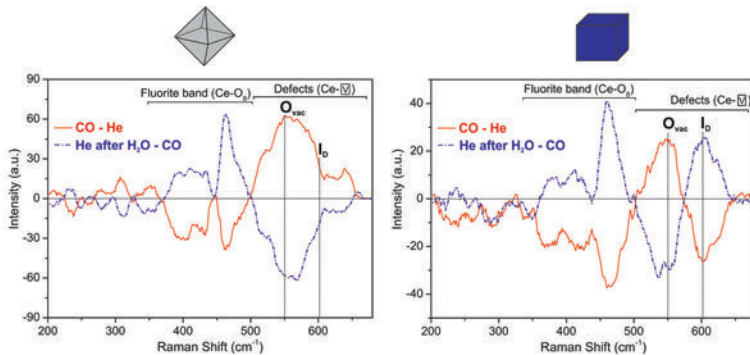
- [47] Jin, T., Zhou, Y., Mains, G. J., and White, J. M. (1987)*J. Phys. Chem.* **91(23)**, 5931–5937.
- [48] Guenin, M. (1973)*Ann. Chim. (Cachan, Fr.)* **8(2)**, 147–158.
- [49] Appel, L. G., Eon, J. G., and Schmal, M. (1998)*Catal. Lett.* **56(4)**, 199–202.
- [50] Staudt, T., Lykhach, Y., Tsud, N., Skála, T., Prince, K. C., Matoln, V., and Libuda, J. (2011)*J. Phys. Chem. C* **115(17)**, 8716–8724.
- [51] Staudt, T., Lykhach, Y., Tsud, N., Skla, T., Prince, K., Matoln, V., and Libuda, J. (2010)*J. Catal.* **275(1)**, 181–185.
- [52] Sayle, T. X. T., Molinari, M., Das, S., Bhatta, U. M., Möbus, G., Parker, S. C., Seal, S., and Sayle, D. C. (2013)*Nanoscale* **5**, 6063–6073.
- [53] Walsh, A., Woodley, S. M., Catlow, C. R. A., and Sokol, A. A. (2011)*Solid State Ionics* **184(1)**, 52–56.
- [54] Minervini, L., Zacate, M. O., and Grimes, R. W. (1999)*Solid State Ionics* **116(3-4)**, 339–349.
- [55] McBride, J. R., Hass, K. C., Poindexter, B. D., and Weber, W. H. (1994)*J. Appl. Phys.* **76(4)**, 2435–2441.
- [56] Nakajima, A., Yoshihara, A., and Ishigame, M. (1994)*Phys. Rev. B* **50**, 13297–13307.
- [57] Namai, Y., Fukui, K.-I., and Iwasawa, Y. (2003)*Catal. Today* **85(2-4)**, 79–91.
- [58] Nörenberg, H. and Briggs, G. A. D. Nov 1997*Phys. Rev. Lett.* **79**, 4222–4225.
- [59] Köck, E.-M., Kogler, M., Bielz, T., Klötzer, B., and Penner, S. (2013)*J. Phys. Chem. C* **117(34)**, 17666–17673.

# 5

## Defect chemistry of ceria nanoparticles as a function of exposed planes

### Research question:

Is the defect chemistry of ceria plane-dependent?



*In the last chapter we saw in detail the defect chemistry of ceria rods, but does this transfer to octahedra (i.e., is there plane-specificity), and, if so, what is the behavior for ceria cubes?*

\*In preparation as: S. Agarwal, X. Zhu, E. J. M. Hensen, L. Lefferts, & B.L. Mojet, "Defect chemistry of ceria nanoparticles as a function of exposed planes," *J. Phys. Chem C*

## Abstract

*The defect chemistry of reduced ceria nanoshapes was investigated using in situ Raman and FTIR spectroscopies. Octahedra and rods display similar defect patterns, principally due to the formation of anion Frenkel pairs and oxygen vacancies in CO, which is attributed to their common {111} exposed planes. Cubes, with {100} terminations, exhibit different defect patterns in CO than octahedra and rods, specifically through the formation of oxygen vacancy defects at the expense of existing anion Frenkel pairs. Furthermore, reduced octahedra and rods can be further reduced upon exposure to CO, whereas reduced cubes must undergo complex surface reconstruction to allow interaction with CO.*

## 5.1 Introduction

Ceria ( $\text{CeO}_2$ ) based materials are widely used for a range of applications such as, biomedicine[1], solid oxide fuel cells,[2] solar fuel systems,[3]  $\text{O}_2$  sensors,[4, 5] catalysis, etc. In catalysis,  $\text{CeO}_2$  is used as a promoter in three-way catalysts (TWCs) for treatment of toxic exhaust gases,[6] to remove soot from automotive engines[7] and pollutants from waste water.[8] Another significant catalytic application includes the low temperature water gas shift reaction (LT-WGS),[9–11], steam reforming of oxygenates from bio-oil[12, 13] and preferential oxidation of CO (PROX).[14, 15] In all these applications, highly mobile lattice oxygen is involved in the process that leads to facile creation of defects (e.g. oxygen vacancies) in the lattice, hence affecting the electronic and chemical properties of ceria.[16] Furthermore, defect sites in the lattice act as active sites during the catalytic reaction.[16] Therefore, the control of the density and the nature of vacant sites could provide a means for tuning the reactivity of ceria-based catalysts.

One of the widely accepted pathways to increase the activity and reducibility of ceria catalyst is through the development of robust synthesis methods to obtain ceria nanostructures with controlled crystallographic planes.[17]  $\text{CeO}_2$  nanoshapes have been successfully synthesized in various morphologies such as cubes, rods, wires, octahedra, spindle-like, etc, and examined for catalytic reactions, in which morphology-dependent performance has been reported.[18–23]

Previously, the common consensus was that ceria rods had better catalytic re-

## 5.1. INTRODUCTION

activity than ceria octahedra and cubes due to the presence of exposed  $\{110\}$  and  $\{100\}$  planes.[19, 21, 23, 24] However, we recently demonstrated that both rod and octahedra have  $\{111\}$  exposed planes; as compared to  $\{100\}$  for cubes. The exposed planes are consistent with observed WGS (water gas shift) reactivity trend: Rods  $\approx$  octahedra  $<$  cube.[25] These reports on ceria nanoshapes agree well with the experimental literature for ceria films. So far, several fundamental investigations related to the adsorption and dissociation of various probe molecules (CO,[26] methanol,[27] formic acid,[28, 29] water[30]) have been extensively studied on epitaxially grown ceria (111) and (100) surfaces. (100) surfaces are found to be more active in adsorbing and reacting with probe molecules than (111).[27] Furthermore, in order to relocate surface charge and attain stability, (100) planes undergo surface reconstruction and form defects.[31]

Based on the earlier reports, pretreatment/processing conditions that enhance the formation of clusters of oxygen vacancies result in better reducibility of ceria.[32] Generally, ceria-supported catalysts are hydrogen pretreated to reduce the metal particles on them.[33] During the reduction, ceria supports are also greatly affected. For instance,  $H_2$  dissociation on the metal particle can result in spillover of [H] species to the ceria support, generating bridging OH groups.[34]  $H_2$  exposure further results in the change of the oxidation state of the ceria from  $Ce^{4+}$  to  $Ce^{3+}$  and removal of surface oxygen atoms to generate oxygen vacancies.[16]

We recently reported that WGS activity of ceria nanoshapes, as well as the interaction with CO/ $H_2O$  as studied with FTIR, is dependent on the exposed planes.[25] We then selected rods with their exposed  $\{111\}$  planes to highlight the complex role of defects during CO adsorption and reaction with  $H_2O$ , as a function of temperature. Our motivation for the present work was thus to see whether this strong dependency on exposed planes is also true for the role of defects on these ceria nanoshapes. In the present study, we provide a detailed understanding of the roles of defects in reduced cubes (i.e., the  $\{100\}$  plane) as compared to octahedra and rods (with  $\{111\}$  planes), with focus on the local defect structure of different exposed planes of ceria and the effects on the reducibility of ceria nanoshapes. Moreover, we also investigate the effect of reducing treatment influencing the behavior of defects on these ceria nanoshapes. Our results show that reduced octahedra and rods behave similarly. Therefore, we will restrict the discussion to a comparison

between results obtained with cubes versus octahedra only; the experimental results obtained with rods are presented in the Appendix (figures A5.4, A5.7-A5.9). In the remainder of this paper we used the term ‘defect chemistry’ to refer to the dynamic behavior of defects on ceria nanoshapes as a function of gas type.

## 5.2 Experimental section

### 5.2.1 Sample preparation and initial characterization

CeO<sub>2</sub> cubes and rods were synthesized via the hydrothermal procedure, reported by Mai *et al.*[19] For details related to the synthesis procedure, refer to our earlier work.[25] CeO<sub>2</sub> octahedra (99.9% pure) with particle size smaller than 25 nm were obtained from Sigma-Aldrich. Both samples were calcined at 500°C (heating rate 5 K/min) for 4 h in synthetic air (flow rate 50 mL/min).

The initial characterization results of these ceria nanoshapes were similar to the reported data in our previous work.[25] The XRD (X-ray diffraction) data was obtained using Bruker D2 Phaser diffractometer equipped with CuK<sub>α</sub> radiation ( $\lambda = 0.1544$  nm). Refer to our earlier work for the XRD pattern and HRTEM images of ceria cubes, rods and octahedra. To summarize the XRD results of nanoshapes, the observed diffraction peaks were indexed as the face-centered cubic phase of CeO<sub>2</sub>.

The BET surface areas of samples were determined using a Micromeritics Tristar instrument. Prior to N<sub>2</sub> physisorption, the samples were out-gassed in vacuum at 300°C for 24 h. The BET values of cubes, octahedra and rods were 10, 58 and 80 m<sup>2</sup>/g, respectively.

### 5.2.2 *In situ* Raman spectroscopy

Jobin-Yvon T64000 triple-stage spectrograph equipped with CCD detector was used for the Raman measurements. The Raman spectra with resolution of 2 cm<sup>-1</sup> were obtained using Kinmon He-Cd 325 nm (UV) laser. The output power of the laser was 30 mW. However, the power on the sample was maintained at 6 mW. The laser was exposed for 10 min on the sample 2 times (2 co-additions), hence recording each spectrum took 20 min. Powdered samples (approximately 10 mg) were loaded in the homemade stainless steel cell and then compressed to obtain a

## 5.2. EXPERIMENTAL SECTION

dense catalyst bed. For calibration of Raman spectra, Teflon was used as a standard material. All the gas lines before the Raman cell were heated to 100°C to avoid condensation.

All the samples are pretreated in H<sub>2</sub> (Linde 5.0) at 450°C for 60 min. For CO reactivity studies, 33 vol% CO (Supplier: Linde 4.7) in He (Linde 5.0) was used. For H<sub>2</sub>O adsorption experiments, He (20 mL/min) was flowed through the saturator filled with H<sub>2</sub>O. To obtain the H<sub>2</sub>O vapor pressure of 9 mbar, the saturator temperature was kept at 5°C. The total flow of gases used during the experiments was maintained to 20 mL/min.

### 5.2.3 *In situ* FTIR spectroscopy

A Bruker Vector 22 was used for the transmission FTIR (Fourier transform infrared) measurements. The spectra were recorded using MCT detector by averaging 128 scans with a spectral resolution and time interval of 4 cm<sup>-1</sup> and 120 s respectively. The empty cell was used to collect the background spectrum. Self-supporting pellets of typically 13 to 15 mg of samples were pressed and put into a purpose-built stainless steel cell.

Varian Chromopack CP17971 Gas Clean Moisture Filter was used to trap any moisture from the He (Linde 5.0) gas. Prior to CO/H<sub>2</sub>O studies, pressed ceria samples were pretreated in H<sub>2</sub> (Linde 5.0) for 60 min at 450°C. For CO adsorption experiments, 33 vol% CO (Linde 4.7) in He (total flow 20 mL/min) was used. For obtaining the H<sub>2</sub>O flow with vapor pressure 9 mbar, He (20 mL/min) was bubbled through the saturator (temperature maintained at 5°C) filled with H<sub>2</sub>O. All the tubing from the gas panel to the cell was preheated to 200°C in order to avoid condensation in lines and temperature drop in FTIR cell.

### 5.2.4 Experimental procedure

Raman and FTIR spectra were recorded after flowing gases in the sequence as shown in the experimental scheme in figure 5.1. The samples were heated in H<sub>2</sub> flow (20 mL/min) to 450°C (heating rate 5 K/min) followed by an isothermal period of 60 min. After pretreatment, ceria shapes were cooled to 150°C in He flow and then heated to the reaction temperature (350°C) at the rate of 5 K/min in He flow (20 mL/min). The samples were exposed to He, CO and H<sub>2</sub>O for 30 min in

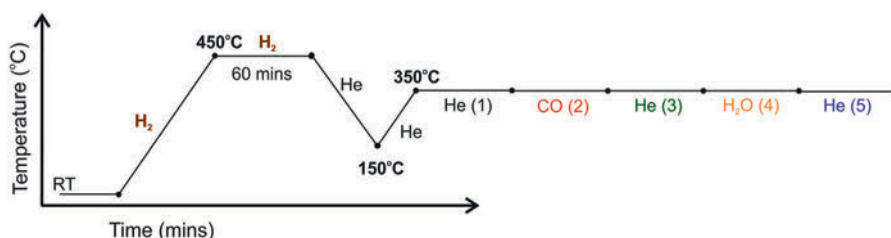


**Figure 5.1:** Experimental scheme for Raman and FTIR experiments at 350°C.

the order as presented in figure 5.1. For simplicity, all the gas flows are labeled with a sequential number that will be used as a reference for each gas in result and discussion section.

### 5.2.5 Data analysis

Raman and FTIR spectra were analysed using Bruker OPUS (version 7.0) spectroscopy software. All the Raman spectra presented in this work were baseline corrected (concave rubberband correction, 1 iteration) and smoothed (using Savitzky-Golay algorithm, 25 points). In a similar way, FTIR spectra (baseline correction-2 points, smoothed-21 points) were processed.

## 5.3 Results and discussion

*In situ* Raman and FTIR spectra of H<sub>2</sub>-reduced ceria octahedra and cubes in He flow at 350°C are shown in figure 5.2. The Raman spectra were normalized to the 455 cm<sup>-1</sup> peak. The Raman spectra of both nanoshapes consisted of two broad peaks centered at 455 (I<sub>F2g</sub>) and 594 (I<sub>D</sub>) cm<sup>-1</sup>. Based on the literature, the peaks at 455 and 594 cm<sup>-1</sup> have been assigned to the symmetric stretch mode of Ce-O<sub>8</sub>[35, 36] and anion Frenkel pair defects in the ceria lattice,[37, 38] respectively. As suggested in our earlier work for unreduced ceria rods, the shoulder bands at 404 and 487 cm<sup>-1</sup> on both sides of fluorite peak are due to distortion in the fluorite structure.[39] This distortion is the result of an imperfect fluorite lattice with Ce-O<sub>x</sub>, where x = 5, 6, 7. The shoulder peaks in 540 – 560 cm<sup>-1</sup> region previously has been assigned to the oxygen vacancy defects.[38, 40, 41]

### 5.3. RESULTS AND DISCUSSION

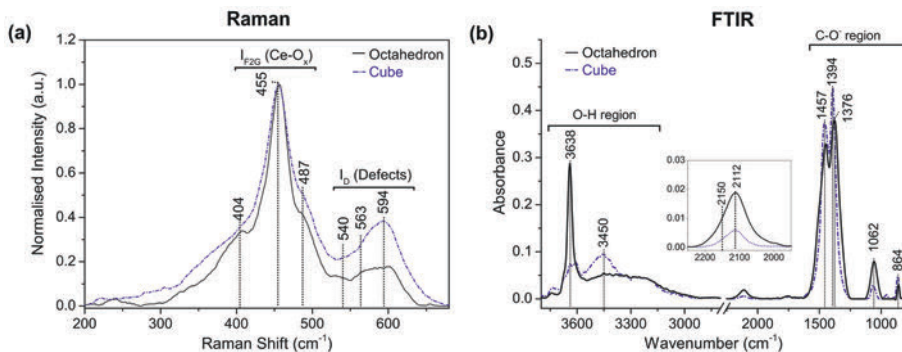


**Figure 5.2:** *In situ* normalized Raman (a) and FTIR (b) spectra of H<sub>2</sub> reduced ceria octahedra (solid black spectrum) and cubes (dash-dotted blue spectrum) in He flow at 350°C.

On comparing the Raman spectra of the two reduced nanoshapes in figure 5.2a, we observed that the  $I_{F2g}$  peak for octahedra (solid black spectrum) was less broad in comparison to the cubes (dash-dotted blue spectrum). The broadening of this peak at 350°C for cubes is due to the increase in intensity of the side features at 404 and 487 cm<sup>-1</sup>. Similar features were previously reported for the unreduced ceria nanoshapes.[39] These features are further supported by the XRD and Raman data, where cubes were found to have more strain and distortion in the lattice in comparison to octahedra.[25, 42]

The relative intensities of  $I_D$  to  $I_{F2g}$  in the present work follows the trend cubes > octahedra. This observation is again consistent with the previous studies and indicates that cubes have a higher fraction of defects.[38, 42] In addition, the ratio of the peak maxima  $I_D/I_{F2g}$  for reduced ceria samples (figure 5.2a) was higher in comparison to the unreduced nanoshapes (figure A5.1a). This observation was more evident in case of cubes, pointing out that cubes are more easily reduced. Furthermore, the shoulder bands at 404 and 487 cm<sup>-1</sup> next to the fluorite peak (455 cm<sup>-1</sup>) are more prominent for the unreduced ceria nanoshapes (figure A5.1a).

*In situ* transmission FTIR spectra of the reduced ceria octahedra (solid black) and cubes (dash-dotted blue spectrum) are shown in figure 5.2b. It must be noted that the peak intensity in FTIR cannot be directly correlated with the amount of sample as the light scattering properties are not only affected by the amount of sample, but also by the shape and size of particles.[43]

Three distinct sets of peaks can be observed: O-H stretching vibrations between 3800 and 3000  $\text{cm}^{-1}$ , [44, 45] stretching linear vibration of CO adsorbed on  $\text{Ce}^{4+}$  and  $\text{Ce}^{3+}$  (2200 – 2000  $\text{cm}^{-1}$ ) [45] and  $\text{C-O}_x^-$  ( $x = 2, 3$ ) stretching and deformation between 1700 and 800  $\text{cm}^{-1}$ . [46–49]

The peaks in the OH and  $\text{C-O}_x^-$  region for reduced ceria nanoshapes have been extensively discussed in our previous work. The reader is referred to chapter 2 for further details. Summarizing, the following observations were made: The main hydroxyl (OH) peak for the cubes and octahedra was observed at 3638  $\text{cm}^{-1}$ , assigned to bridging hydroxyl species. [44, 45] Broad bands (at approx. 3450 and 3173  $\text{cm}^{-1}$ ) related to multi-bonded and hydrogen bonded hydroxyl species were observed in the spectral region 3500 – 3000  $\text{cm}^{-1}$ . [45] Both of the ceria nanoshapes exhibit these distinct OH peaks, however with different relative intensities. For instance, the ratio of the peak maximum  $I_{3638}/I_{3450}$  was lower for cubes in comparison to octahedra. Furthermore, on comparing the reduced (figure 5.2b) and unreduced ceria cubes (figure A5.1b in the Appendix), it is clear that during hydrogen pretreatment the isolated hydroxyl species at 3710  $\text{cm}^{-1}$  [44, 45] completely disappear along with major decrease in  $\text{OH}^{3638}$  species, again indicating cubes are highly reducible.

The carbonate peak positions in  $\text{C-O}_x^-$  region for the cubes and octahedra varied, and in fact these peaks were sharper for cubes. This difference can be attributed to the different exposed planes on cubes ( $\{100\}$ ) versus octahedra ( $\{111\}$ ). Furthermore, the relative ratio of carbonates (1700 – 1200  $\text{cm}^{-1}$ ) with respect to hydroxyl (3800 – 3000  $\text{cm}^{-1}$ ) region for cubes was higher in comparison to octahedra due to the favorable formation of carbonates on the (100) plane in comparison to the (111) plane. [42, 50] Note that the peak position of carbonate species on the reduced and unreduced (figure A5.1) ceria nanoshapes varies.

*CO on  $\text{Ce}^{3+}$  and  $\text{Ce}^{4+}$*  – For the reduced samples, a small peak at 2112 and a shoulder band at 2150  $\text{cm}^{-1}$  were observed (figure 5.2b inset). These features have been attributed to the CO adsorption on the  $\text{Ce}^{3+}$  and  $\text{Ce}^{4+}$  sites. [45, 51] The CO adsorbed on the cerium cations is possibly formed during the  $\text{H}_2$  pretreatment, where the carbonates (formed on exposure to atmospheric  $\text{CO}_2$ ) species partially decompose into CO and  $\text{CO}_2$  giving rise to cleaner samples. [45, 52]

To summarize our Raman and FTIR data for reduced ceria nanoshapes, more

### 5.3. RESULTS AND DISCUSSION

defects, as well as higher amount of carbonates with respect to hydroxyl, were observed for ceria cubes than for octahedra.

#### 5.3.1 *In situ* Raman: CO adsorption and reactivity with water

To investigate the defect chemistry of the ceria nanoshapes at 350°C, the H<sub>2</sub>-reduced sample was exposed to the series of gas flows as outlined in the figure 5.1 (section 5.2), resulting in the spectra shown in figure 5.3. The left and right hand side plots are related to the octahedra and cubes, respectively, with each plot containing spectra from ‘before’ and ‘after’ each stage of the gas treatments.

Raman spectra of the reduced octahedra and cubes obtained in He(1) and CO(2) flow are shown together in figure 5.3a and b. After 30 min in He(1) flow, CO was adsorbed on the sample (red dash-dotted spectrum). In CO, for both nanoshapes, the fingerprint fluorite peak at 455 cm<sup>-1</sup> and the side peaks at 404 and 487 cm<sup>-1</sup> decreased in intensity. In the case of octahedra, the intensities of the defect bands, including the peaks in region 540 – 560 cm<sup>-1</sup> (oxygen vacancy, O<sub>vac</sub>)[38, 40, 41] and 594 cm<sup>-1</sup> (anion Frenkel pair, I<sub>D</sub>)[37, 38] increased indicating the creation of new defects. For cubes, new CO-induced defect bands were observed in 540 – 560 cm<sup>-1</sup>. Unlike for octahedra, in cubes the anion Frenkel defect peak at 594 cm<sup>-1</sup> decreased in intensity on introduction of CO. This observation for the cubes hints towards the formation of oxygen vacancy at the expense of anion Frenkel pair defects in CO. Comparing the CO-induced defects for reduced (figure 5.3) and unreduced (figure A5.2 in the Appendix) nanoshapes, it is immediately apparent that the reduced samples form relatively higher amount of defects, especially for cubes. We believe that the present work is the first experimental evidence clearly showing that the CO induced defects are formed differently on ceria shapes with different exposed planes. In the past few years, Wu *et al.* have extensively studied similar ceria nanoshapes for the reactivity towards CO, methanol, and ethanol.[24, 38, 53, 54] Unfortunately, direct comparison of their results with our data cannot be made as the experimental conditions are very different.

After CO exposure, the cell was exposed to He(3) to remove weakly adsorbed CO (solid green spectrum in figure 5.3c and 5.3d). Subtle changes were observed for both nanoshapes. Firstly, the peak at 455 cm<sup>-1</sup> increased in intensity, whilst peaks at 404 and 487 cm<sup>-1</sup> showed almost no change. Secondly, the overall defect

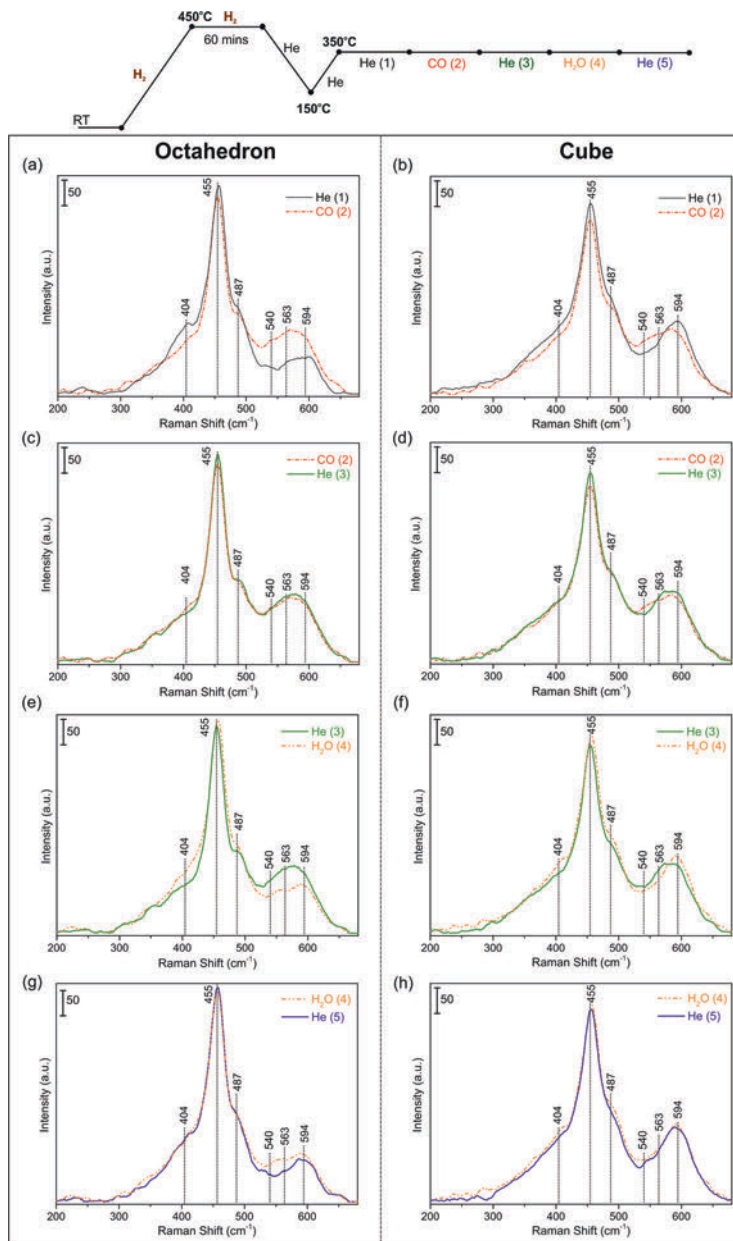


**Figure 5.3:** *In situ* Raman spectra at 350°C of reduced ceria octahedra (left plots) and cubes (right plots) in; (a) & (b) He (1, solid black), followed by CO (2, red dash-dotted); (c) & (d) CO(2) followed by He (3, solid green); (e) & (f) He(3) followed by H<sub>2</sub>O/He (4, dash-dotted orange); (g) & (h) H<sub>2</sub>O/He followed by He (5, solid blue) flow.

### 5.3. RESULTS AND DISCUSSION

band showed subtle increase in intensity for the octahedra, whereas for cubes  $O_{vac}$  ( $540 - 560\text{cm}^{-1}$ ) decreased with an increase in intensity of  $I_D$  ( $594\text{cm}^{-1}$ ).

After He(3),  $\text{H}_2\text{O}/\text{He}(4)$  flow was introduced in the Raman cell (dash-dotted orange spectrum in figure 5.3e and 5.3f). In the presence of  $\text{H}_2\text{O}/\text{He}$ , the fluorite peaks at  $404$ ,  $455$  and  $487\text{cm}^{-1}$  showed increased intensities accompanied by partial disappearance of peaks assigned to defects that were induced by CO treatment, for both ceria octahedra and cubes. Specifically, the  $I_D$  peak in cubes increases in intensity accompanied by a decreasing  $O_{vac}$  peak, whereas for octahedra both peak intensities were reduced in  $\text{H}_2\text{O}/\text{He}$  flow (4).

Subsequently, He(5) was flowed after  $\text{H}_2\text{O}/\text{He}(4)$  to remove physisorbed water from the sample. The spectra obtained for ceria octahedra and cubes in He (5, solid blue spectrum) and  $\text{H}_2\text{O}/\text{He}(4)$  are shown in figure 5.3g and h respectively. In octahedra, the  $455\text{cm}^{-1}$  peak showed a subtle increase in intensity with the further disappearance of CO-induced defects, whereas for cubes very minor decreases in intensities of the fluorite and defect peaks were observed. Note that for both shapes, in particular for octahedra, the disappearance of defects occurred in two stages: First in  $\text{H}_2\text{O}/\text{He}(4)$  and the remaining in He(5) after  $\text{H}_2\text{O}$  flow.

#### 5.3.2 *In situ* FTIR: CO and $\text{H}_2\text{O}$ adsorption

To investigate the types of species involved/formed during defect creation on reduced ceria nanoshapes, *in situ* FTIR spectroscopy was performed under identical conditions to the *in situ* Raman experiments. The plots obtained by subtracting spectra obtained after two consecutive gas treatments are plotted in figure 5.4. The positive peaks in the difference spectra correspond to the species formed, whilst negative peaks indicate that species have disappeared on introduction of CO. (The original un-subtracted spectra are shown in figure A5.3-A5.5 of the Appendix).

In CO, the peaks corresponding to formate and carbonate species increased in intensity significantly (solid red spectrum in figure 5.4a and b, respectively) along with decreasing intensity of OH peaks (bridging, multi and hydrogen bonded) for octahedra and cubes. On comparing the CO-He FTIR spectrum of cubes with octahedra, the C-O vibration of formed formate species was observed at the same peak position ( $1580\text{cm}^{-1}$ ), whereas the C-H vibration was observed at  $2843\text{cm}^{-1}$  ( $2838\text{cm}^{-1}$  for octahedra). Unlike octahedra, carbonate-related positive peaks

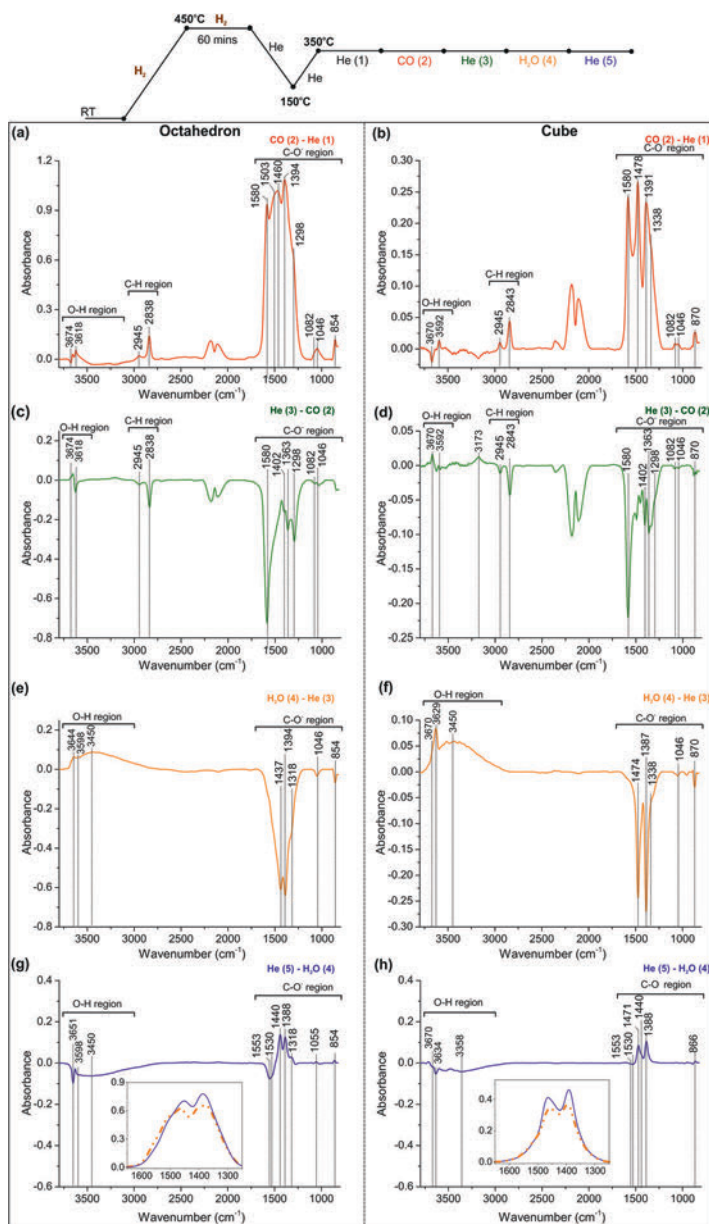


**Figure 5.4:** *In situ* FTIR subtracted spectrum at 350°C of reduced ceria octahedra (left plots) and cube (right plots) obtained by subtracting (a) and (b) He (1, solid black) from CO (2, solid red); (c) and (d) CO(2) from He (3, solid green); (e) and (f) He(3) from H<sub>2</sub>O (4, solid orange); (g) and (h) H<sub>2</sub>O(4) from He (5, solid blue). Insets in figure 5.4g and 5.4h are expanded spectra of carbonate regions obtained in H<sub>2</sub>O (dash-dotted orange) and He (5, solid blue) flow.

### 5.3. RESULTS AND DISCUSSION

were observed for ceria cubes at 1491 and 870 $\text{cm}^{-1}$  (1494 and 854 $\text{cm}^{-1}$  for octahedra) and a positive OH peak related to bi-carbonates species ( $\text{CO}_2(\text{OH})^-$ ) was observed at 3592 $\text{cm}^{-1}$  (for octahedra at 3618 $\text{cm}^{-1}$ ). [25, 39] In addition, the pronounced negative  $\text{OH}^{3173}$  peak was also observed for cubes.

As can be seen in figure 5.4c and d, on subsequent treatment with He (3, solid green spectrum), the peaks related to formate species (2945 and 1580 $\text{cm}^{-1}$ ) disappeared with a shift and partial re-appearance of the  $\text{OH}^{3674}$  peak ( $\text{OH}^{3670}$  for cubes). The disappearance of formate peaks is clearly evident in figures A5.3b and A5.5b (in the Appendix). This observation indicates a backward reaction of formates to CO. Furthermore, partial decomposition of bi-carbonate species, evident from negative peaks at 1402 $\text{cm}^{-1}$  and 3592 $\text{cm}^{-1}$  for cubes (3618 $\text{cm}^{-1}$  for octahedra) was observed for the reduced ceria nanoshapes.

Similar to our previous findings, on exposing octahedra to  $\text{H}_2\text{O}$  vapor (solid orange spectrum, figure 5.4e), mono and bi-dentate carbonate species decomposed (evident from negative peaks at 1394, 854 $\text{cm}^{-1}$ ) leaving behind stable poly-dentate carbonates (1388 $\text{cm}^{-1}$ ; figure A5.3c). [39] In addition, an increase in intensity of OH peaks was observed, pointing towards hydroxyl group regeneration. On subsequent exposure of the cubes to  $\text{H}_2\text{O}$  vapor (figure 5.4f), decomposition of carbonates (evident from 1387, 870 $\text{cm}^{-1}$ ) together with regeneration of hydroxyl species (3670, 3629 and 3450 $\text{cm}^{-1}$ ) was observed.

The FTIR difference spectra He(5)- $\text{H}_2\text{O}$ (4) for the octahedra and cubes are shown in figure 5.4g and h, respectively. The spectra (carbonate region 1700 – 1200 $\text{cm}^{-1}$ ) obtained in  $\text{H}_2\text{O}$  (4, dash-dotted orange spectrum) and He (5, solid blue spectrum) flow are plotted in the insets of figure 5.4g and h. Negative OH peaks were observed for octahedra and cubes due to the removal of weakly adsorbed H-bonded water (figure 5.4g and h). Interestingly, for octahedra, the band in the 1700 – 1200 $\text{cm}^{-1}$  region becomes narrower along with an increase in the peak maxima (figure 5.4g inset). These induced changes are better reflected in the difference spectrum (figure 5.4g) where negative peaks at 1553 and 1530 $\text{cm}^{-1}$  and positive peaks at 1440, 1388, 1318 $\text{cm}^{-1}$  are observed. These peaks are clearly associated with carbonates and not with formate species, since no CH peaks were observed in the 3000 – 2800 $\text{cm}^{-1}$  region. Based on the peak positions we assign negative and positive peaks to bi-dentate and poly-dentate carbonate species

respectively.[55] From this observation, it seems that rearrangements of carbonate species on ceria octahedra occurred, which resulted in the formation of stable poly-carbonates at the expense of bi-dentate carbonates. This agrees well with the theoretical prediction of Vayssilov *et al.*, whom have reported the transition of bi-dentate carbonates in the vicinity of oxygen vacancies to stable poly-carbonates due to the enhanced structural flexibility next to the oxygen vacancy defects.[56] In addition, a change in the dipole moment of the carbonate C-O bond upon desorption of water may also affect the peak position and intensity of carbonates. For cubes, an increase in intensity of poly-dentate carbonate peaks ( $1471, 1388\text{ cm}^{-1}$ ) was observed with a subtle decrease in bi-dentate species ( $1553$  and  $1530\text{ cm}^{-1}$ , figure 5.4h). Notably, the overall carbonate band in the region ( $1700 - 1200\text{ cm}^{-1}$ ) did not become narrower on introduction of He(5), see figure 5.4h inset.

Finally, on comparing the FTIR subtracted spectra for reduced (figure 5.4) and unreduced ceria (figure A5.6) nanoshapes, the global trend with respect to the different gas types was similar especially for the ceria cubes. However with careful inspection, the following observations were made: Firstly, the actual peak position of hydroxyl, carbonates and formates species and carbonate/formate peak ratio varied based on whether the samples were pretreated or not. These observations are much more pronounced for the ceria octahedra. Secondly, unlike reduced ceria cubes (figure 5.4b), no OH species related to bi-carbonates species ( $\text{CO}_2(\text{OH})^-$ ) at  $3592\text{ cm}^{-1}$  were observed in CO for the unreduced ceria cubes (figure A5.6b).

### 5.3.3 *In situ* FTIR: CO adsorption on $\text{Ce}^{4+}$ and $\text{Ce}^{3+}$

To investigate the reducibility of ceria nanoshapes (pretreated in  $\text{H}_2$ ) after exposure to CO and  $\text{H}_2\text{O}$ , we plotted the FTIR spectra in the range  $2250 - 2000\text{ cm}^{-1}$  (figure 5.5). As indicated earlier, the observed peaks at  $2150$  and  $2112\text{ cm}^{-1}$  for both ceria nanoshapes in He (1, solid black line) flow are due to CO adsorbed on accessible  $\text{Ce}^{4+}$  and  $\text{Ce}^{3+}$  respectively. See figure 5.1 for the gas flow labels. In the presence of CO in the gas phase, these peaks are usually hidden within the very intense vibration peak of  $\text{CO}_{(g)}$ .

On flowing He after CO (3, dashed green line in figure 5.5), peaks related to  $\text{CO}_{(g)}$  disappeared and peaks due to CO adsorbed on cerium ions can now be observed. In the case of octahedra, increases in intensities of the  $2112$  and  $2150\text{ cm}^{-1}$

### 5.3. RESULTS AND DISCUSSION

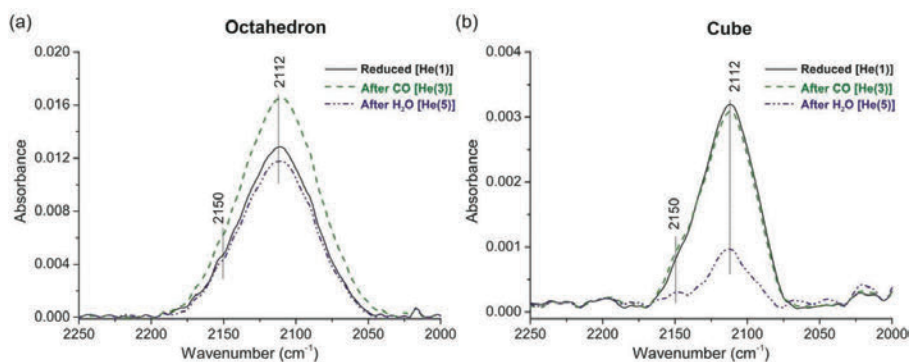


**Figure 5.5:** *In situ* FTIR of reduced ceria (a) octahedra and (b) cubes at 350°C obtained in He(1), He(3) and He(5) flow. Key: He(1) black solid line is obtained for the freshly reduced samples in He flow, He(3) dashed green line is obtained in He flowed after exposure to CO gas and He(5) dash-dotted blue line is recorded in He flow after exposure to H<sub>2</sub>O vapor.

peaks were observed. The increase in intensity of these peaks is due to the interaction of CO with the accessible cerium ions formed either during H<sub>2</sub> pretreatment or on exposure to CO(2) flow. For the cubes a subtle increase in intensity of 2150cm<sup>-1</sup> with slight decrease in intensity of 2112cm<sup>-1</sup> peak was observed, indicating the absence of accessible cerium ions for interaction with CO. On comparing the results of both nanoshapes and keeping in mind the possibility that CO exposure can further form more bare cerium ions, we suggest that in the presence of CO octahedra further reduce, whereas cubes are not further reduced in CO.

Finally, decreasing intensities at 2112 and 2150cm<sup>-1</sup> were observed as a result of the exposure to H<sub>2</sub>O, followed by flushing with He (5, dash-dotted blue line in figure 5.5). The intensity of the Ce<sup>3+</sup> and Ce<sup>4+</sup> peaks were lower after H<sub>2</sub>O exposure (dash-dotted blue spectra) than the intensities of the respective peaks obtained for the freshly reduced ceria samples (solid black spectra). In addition, the decrease was much more pronounced for the cube sample, indicating towards their higher extent of re-oxidation in H<sub>2</sub>O in comparison to other ceria nanoshapes, which agrees well with our previous work.[42]

## 5.4 General discussion

Raman and FTIR spectroscopy results (figure 5.2) confirm that the reduced ceria cubes have a higher amount of intrinsic defects and a higher relative ratio of carbonates to hydroxyl species than octahedra. This is in agreement with the literature and is attributed to the difference in surface termination on these ceria nanoshapes. Octahedra, with  $\{111\}$  planes, have accessible Ce and O in the top layer (see figure A5.10 in the Appendix). In the case of cubes, with  $\{100\}$  exposed planes, the surface layer is O terminated. Due to the difference in geometry and coordination number, the interaction of different exposed planes with gases varies. The differences on interaction with CO and H<sub>2</sub>O as observed on these ceria nanoshapes are illustrated in figure 5.6. The structure of both nanoshapes has been simplified to 2-D representations for clarity reasons, implying that the surface, i.e. the top layer is presented in 2-D.

*Octahedra* – The presence of intrinsic defects ( $I_D$  and  $O_{vac}$ ) for reduced ceria octahedra (figure 5.2a) is shown in figure 5.6a. When the surface is exposed to CO, more oxygen vacancy ( $O_{vac}$ ) and anion Frenkel pair ( $I_D$ ) defects are created (dash-dotted red spectrum in figure 5.3a) along with a significant increase in amounts of formates, carbonates (mono (I) and bi (II)-dentate) and bi-carbonates (solid red spectrum in figure 5.4a). These observations are correlated and illustrated in figure 5.6b, where we observe that oxygen moves from the lattice position to interact with CO to form carbonates (I and II) while creating a vacant site  $\boxed{V}$  at its lattice position ( $O_{vac}$  defect). At the same time, an oxygen leaves its lattice position  $\boxed{F}$  and moves to an interstitial site in the lattice, giving rise to more  $I_D$  defects. In addition to defect-related carbonates, bi-dentate (II) carbonates (bonded to two oxygen of the ceria lattice), bi-carbonates and formates are also formed in CO.

Interestingly, on flushing He(3) after CO, a subtle increase in the  $I_D$  defect band is observed (solid green spectrum in figure 5.3c), as illustrated in figure 5.6c (highlighted region). At the same time, the disappearance of formate species with partial re-appearance of the hydroxyl peak is observed (figure 5.4c). In addition, the partial decomposition of bi-carbonate species is also observed. The disappearance of formates and bi-carbonates with re-appearance of OH groups is shown in figure 5.6c. Based on the above findings, it is clear that the formation of formates and bicarbonates by the interaction of OH species with CO does not involve the

## 5.4. GENERAL DISCUSSION

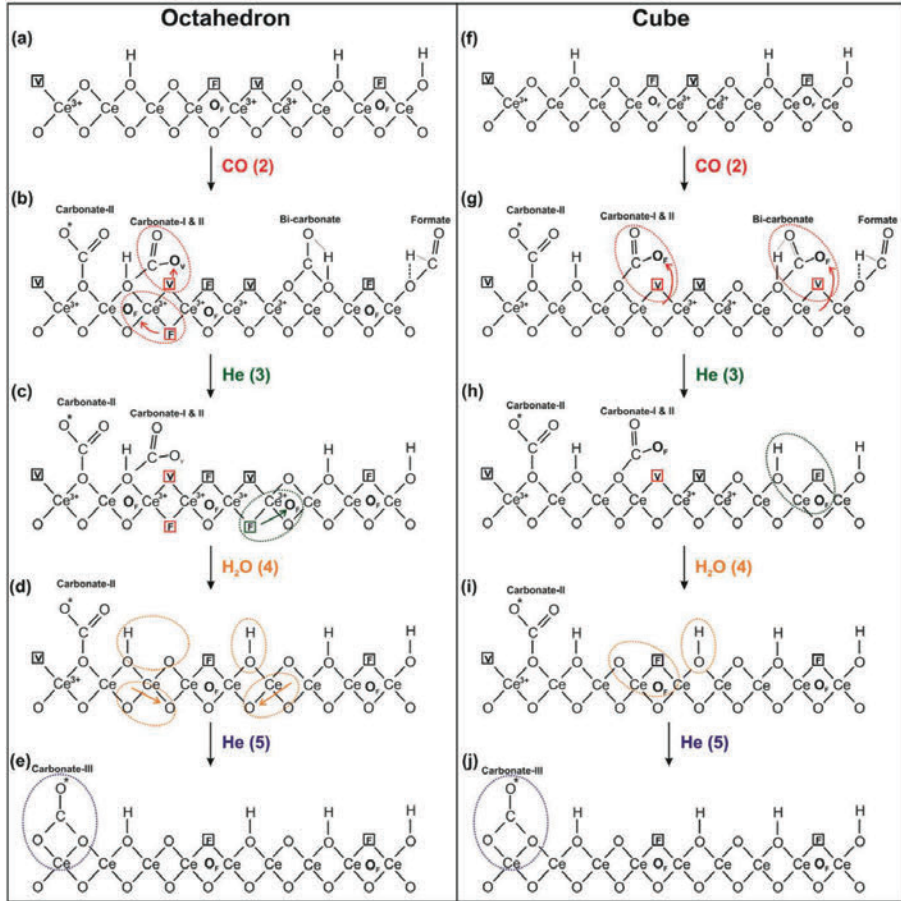


**Figure 5.6:** Schematic representation of the interaction of ceria octahedra (left plots) and cubes (right plots) as a function of different gas flows at 350°C. Key:  $O_F$  represents oxygen that moves from the lattice position to interstitial site forming anion Frenkel pair defects.  $O_V$  denotes oxygen in ceria lattice interacting with CO to form carbonate species while creating vacant site at its original lattice position (oxygen vacancy defects).  $F$  and  $V$  symbolize vacant lattice sites created due to the formation of anion Frenkel pair and oxygen vacancy defects, respectively. For recognizing the defects created with respect to each gas type, the square boxes are colored accordingly. Lastly, \* denotes oxygen bonded with other cerium atom which cannot be presented in the 2-D model.

creation of defects in the octahedra lattice.

In the presence of H<sub>2</sub>O/He(4), the I<sub>D</sub> and O<sub>vac</sub> defects partly disappear (figure 5.3e) with the decomposition of mono (I) and bi-dentate (II) carbonates (figure 5.4e) accompanied by the regeneration of hydroxyl species. As illustrated in figure 5.6d, the carbonate (I and II) species related to the defects disappear and the vacant sites  $\boxed{\text{F}}$  and  $\boxed{\text{V}}$  are refilled with oxygen accompanied by the regeneration of OH species on exposure to H<sub>2</sub>O/He.

Finally, in He after H<sub>2</sub>O(5) further disappearance of CO-induced defects is observed (figure 5.3g) along with the formation of stable poly-carbonates at the expense of bi-dentate carbonates (figure 5.4g). Based on the above, we propose that the bi-dentate (II) carbonate species remaining after H<sub>2</sub>O treatment further interacts with the neighboring vacant  $\boxed{\text{V}}$  sites in the lattice to form stable poly-dentate (III) carbonates while successively refilling the oxygen vacancy site (highlighted in figure 5.6e).

*Cubes* – The lattice sketch of the reduced cube is shown in figure 5.6f. Similar to octahedra, on exposure to CO, formation of formates, carbonates and bi-carbonates (figure 5.4b) are observed in cubes. However, unlike octahedra, the new CO-induced defects, specifically O<sub>vac</sub> are created at the expense of existing I<sub>D</sub> defects (figure 5.3b). It must be noted that the formates cannot be associated with defects as they are formed by the interaction of CO with only one oxygen of the ceria lattice. On linking the Raman and FTIR findings, it is apparent that the formation of mono/bi-dentate carbonates and bi-carbonates induces the formation of oxygen vacancy sites  $\boxed{\text{V}}$  by interacting with the interstitial oxygen (O<sub>F</sub>) associated with the existing anion Frenkel pair defects (see figure 5.6g for a schematic). Furthermore, formates and bi-dentate carbonates (II) that do not create defects are also formed in CO.

The key difference in the interaction of ceria nanoshapes with CO is that the (111)-terminated octahedra forms both anion Frenkel pair and oxygen vacancy defects, whereas the (100)-terminated cubes form oxygen vacancy defects at the expense of anion Frenkel pairs, i.e., octahedra can be further reduced in CO, whereas cubes cannot accumulate any more oxygen so must undergo vacancy reorganization. This observation is further supported by FTIR data (figure 5.5). Even after pretreatment with H<sub>2</sub>, octahedra can be further reduced exposing bare cerium ions,

## 5.4. GENERAL DISCUSSION

see figure 5.5a (dashed green spectra) while forming more defects ( $O_{vac}$  and  $I_D$ ). On the other hand, cubes seem not to be further reduced in CO (dash green spectrum in figure 5.5b) and hence undergo lattice rearrangement to interact with CO.

In He after CO (figure 5.3d), the decrease in the  $O_{vac}$  with an increase in intensity of  $I_D$  is observed. Similar to octahedra, the disappearance of formate species with partial re-appearance of the OH groups and the partial decomposition of bi-carbonate species are observed (figure 5.4d). Based on the above findings, it is clear that with the disappearance of bi-carbonate species, the  $O_{vac}$  defects also partly disappear while restoring part of  $I_D$  defects in the cube lattice (the proposed scheme shown in figure 5.6h). On comparing the results with octahedra (figure 5.6c), it is evident that the bi-carbonate species do not create defects in the octahedra lattice.

On subsequent exposure to  $H_2O(4)$  vapor, the  $I_D$  band further increases in intensity with a decrease in the  $O_{vac}$  peak (figure 5.3f) followed by the decomposition of carbonates (figure 5.4f) with the regeneration of hydroxyl species. This observation indicates that the carbonates (I and II) related to defects decompose and disappear in  $H_2O$  while refilling the vacant site  $\boxed{V}$  with oxygen (or OH group) and subsequently regenerate the anion Frenkel pair defects in the cube lattice (illustrated in figure 5.6i). On the other hand, in case of octahedra (figure 5.6d), regeneration of both defects ( $O_{vac}$  and  $I_D$ ) is observed in  $H_2O(4)$  vapor. The re-oxidation of ceria nanoshapes after exposure to  $H_2O$  vapor is further reflected by the decrease in intensity of peaks associated with CO adsorbed on bare cerium ions (dash-dotted blue spectrum in figure 5.5).

Finally, in He after  $H_2O(5)$  a minor decrease in the  $O_{vac}$  peak is noted (figure 5.3h) along with rearrangements of bi-dentate to stable poly-dentate carbonate species (figure 5.4h). Similar to octahedra (figure 5.6e), we suggest that the oxygen vacancies are further filled during the interaction of bi-dentate (II) carbonates with the neighboring vacant  $\boxed{V}$  sites to form poly-carbonates (III) in the cube lattice (schematically shown in figure 5.6j).

Lastly, the defect behaviors for octahedra and rods are the same (figure 5.3 left plots and figure A5.7), which reinforces the fact that they share the same exposed (111) planes. This is despite the fact that rods and octahedra exhibit different structural features, which has been demonstrated through the existence of dark

pits (“intrinsic” defects) in TEM images of rods but not in octahedra.[25, 32]

The present work is relevant to understand the defect chemistry of ceria nanoshapes applicable for catalytic reactions, such as WGS, steam reforming of hydrocarbons, CO oxidation etc. According to the literature, for these reactions the important role of defects has been greatly emphasized and the current work gives clear insight on the effect of exposed planes of ceria nanoshapes as a function of reductive pretreatment.

## 5.5 Conclusions

A detailed understanding of the defects chemistries of ceria nanoshapes during the interaction with CO/H<sub>2</sub>O in cubes (i.e., the {100} plane) as compared to octahedra and rods (with {111} plane) is presented. The CO-induced defects for rods and octahedra were found to be the same, while the defects formation in CO for cubes were fundamentally different. For instance, in cubes oxygen vacancy ( $O_{vac}$ ) defects were formed at the expense of existing anion Frenkel pair ( $I_D$ ) defects, whereas in case of other two nanoshapes both defect types ( $O_{vac}$  and  $I_D$ ) were formed irrespective of existing  $I_D$  defects. The Raman results are further supported by FTIR findings that clearly confirm that H<sub>2</sub>-reduced ceria rods and octahedra can be further reduced in CO, simultaneously creating bare cerium ions and new defects ( $O_{vac}$  and  $I_D$ ). However, in the case of H<sub>2</sub>-reduced cubes, interaction with CO occurs by lattice/vacancy reorganization as the H<sub>2</sub>-pretreated cubes are not further reducible in CO. These observations affirm that the defect chemistry of ceria nanoshapes is directly dependent on the surface terminations. This knowledge is essential for optimizing ceria nanoshapes for reactions involving CO and H<sub>2</sub>O.

## Appendix 5

The normalized Raman and FTIR plots of ceria nanoshapes at 350°C are shown in figure A5.1. These spectra are obtained for ceria nanoshapes that were not pretreated with H<sub>2</sub>.

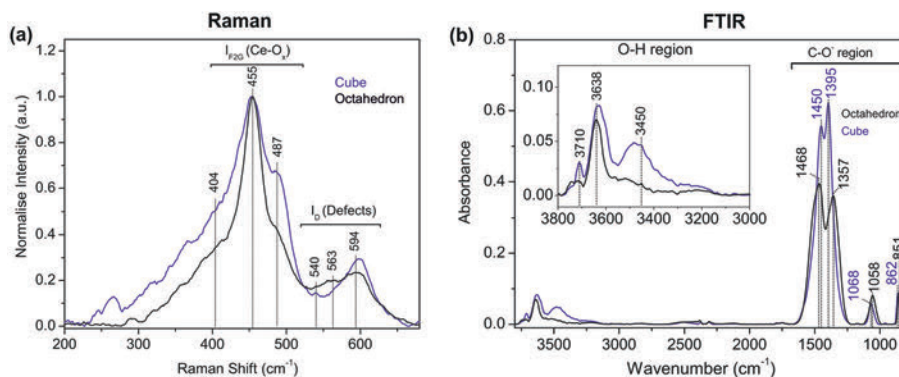


**Figure A5.1:** *In situ* normalized Raman (a) and FTIR (b) spectra of unreduced ceria octahedra (black) and cubes (blue) in He flow at 350°C.

The Raman spectra of unreduced ceria nanoshapes obtained on exposure to CO are shown in figure A5.2. The ceria samples used for investigation did not undergo any prior H<sub>2</sub> pretreatment

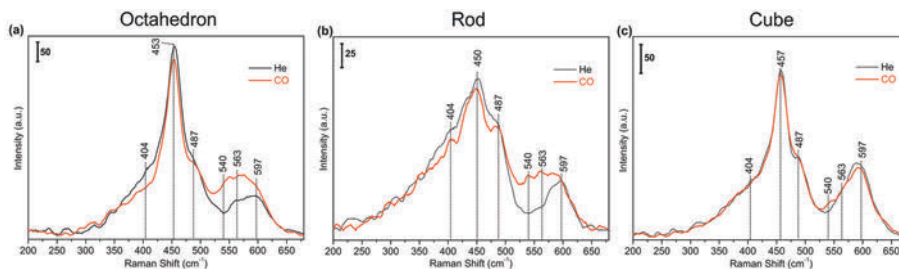


**Figure A5.2:** *In situ* Raman spectra of unreduced ceria (a) octahedra, (b) rods and (c) cubes at 350°C obtained in He (black) flow followed by CO (red) flow.

FTIR spectra of H<sub>2</sub>-reduced ceria octahedra at 350°C are shown in figure A5.3. On introduction of CO, OH<sup>3640</sup> slightly increase in intensity with decrease in intensity of OH<sup>3668</sup> and the broad OH band in region 3500 – 3000 cm<sup>-1</sup> (figure A5.3a). Peaks related to C-H stretch of formate species at 2945 and 2838 cm<sup>-1</sup> were observed. In addition, peaks at 1580, 1457, 1388, 1298, 1055 and 854 cm<sup>-1</sup> were also observed. These peaks are related to C-O stretching and bending vibration of carbonate and formate species. In He after CO, subtle increase in intensity of OH<sup>3668</sup> peak was observed (figure A5.3b). Formate species (evident from 2945 and 2838 cm<sup>-1</sup> peaks) disappeared. The bands in the region 1800 – 1200 cm<sup>-1</sup> were less broad due to the disappearance of peak at 1580 cm<sup>-1</sup>. Peaks at 1055 and 854 cm<sup>-1</sup> slightly decreased in intensities. Subsequently in H<sub>2</sub>O, an increase in intensity of OH peaks were observed. The broad OH band in the region 3500 – 3000 cm<sup>-1</sup> increased in intensity. For further details see the subtracted section (figure A5.4). Bands related to carbonate species partly decomposed in the presence of H<sub>2</sub>O. Please note that all the carbonates formed in the presence of CO did not disappear, indicating the formation of stable carbonates. Finally in He after H<sub>2</sub>O, the decrease in intensity of OH peaks was observed (figure A5.3d). The broad OH band in the region 3500 – 3000 cm<sup>-1</sup> decreased in intensity due to desorption of physisorbed water. Bands related to carbonate species showed an increase in intensity at 1457 and 1388 cm<sup>-1</sup> with a decrease in the 1553 and 1530 cm<sup>-1</sup> bands. This is suggested to be due to the restructuring of carbonates on octahedra, as well as the change in dipole moment of the C-O bond due to the removal of weakly adsorbed water.

# Octahedron

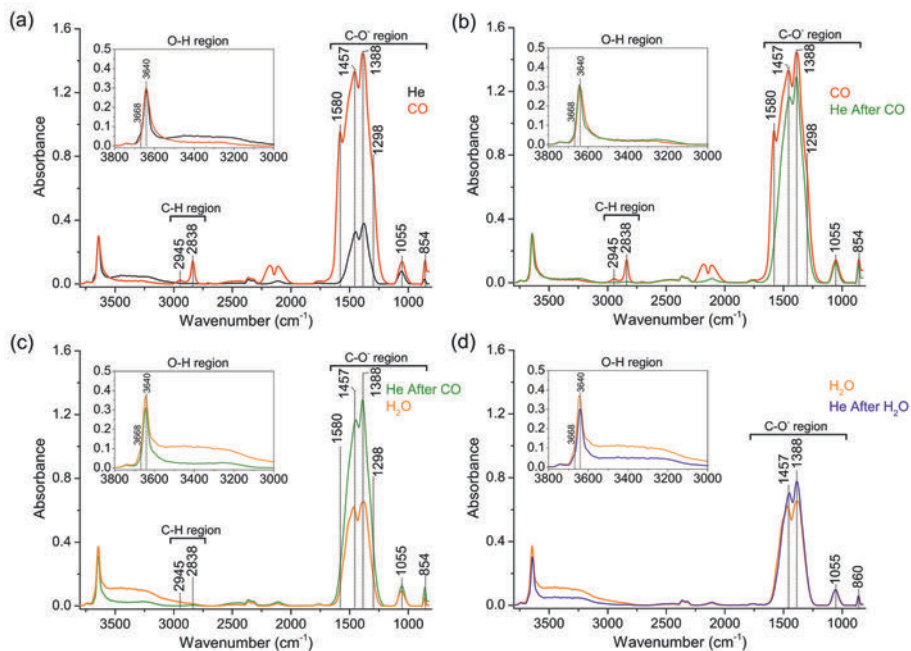


**Figure A5.3:** *In situ* FTIR spectra at 350°C of reduced ceria octahedra in a) He(1, black spectrum), followed by CO(2, red line); b) CO(2) followed by He(3, green spectrum); c) He(3) followed by  $\text{H}_2\text{O}$ /He(4, orange line); d) in  $\text{H}_2\text{O}$ (4) followed by He(5, blue spectrum).

In figure A5.4 the FTIR spectra of ceria rods obtained in different gas treatments are shown. As the observation for rods are similar to octahedra, refer to the description of the previous figure A5.3 for details.

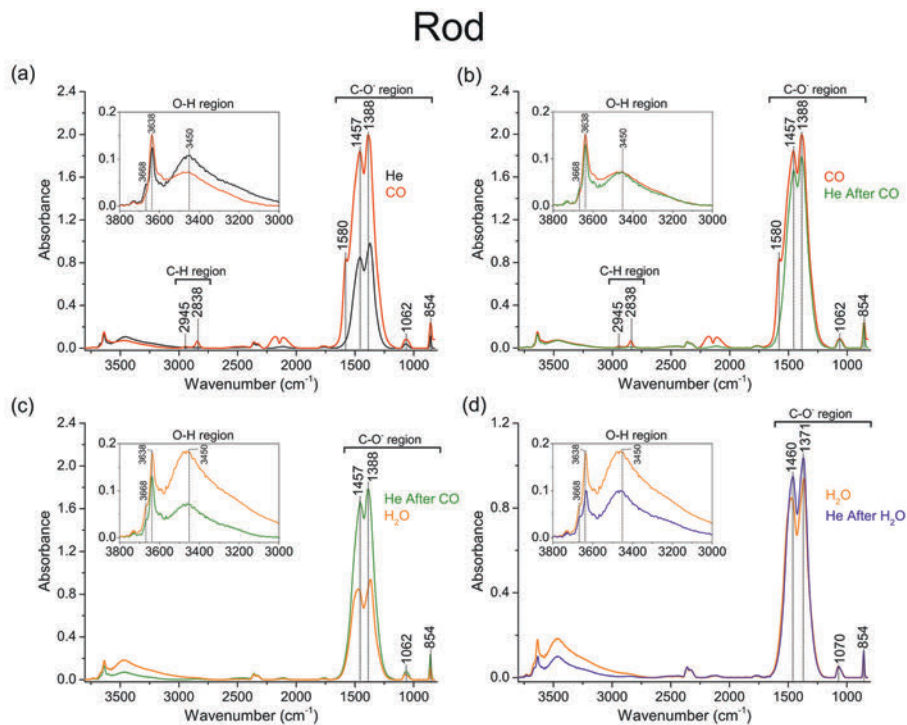


**Figure A5.4:** *In situ* FTIR spectra at 350°C of reduced ceria rods in a) He(1, black spectrum), followed by CO(2, red line); b) CO(2) followed by He(3, green spectrum); c) He(3) followed by  $\text{H}_2\text{O}$ /He(4, orange line); d) in  $\text{H}_2\text{O}$ (4) followed by He(5, blue spectrum).

The resulting FTIR spectra of cubes obtained on exposure to CO and H<sub>2</sub>O are shown in figure A5.5. In CO, significant amounts of carbonates and formates were formed (figure A5.5a). Formate formation was evident from the peaks at 2845 and 1580 cm<sup>-1</sup>, whereas C-O stretch of carbonates were observed at 1391 and 866 cm<sup>-1</sup>. Furthermore, OH<sup>3602</sup> increased in intensity with decrease in intensity of OH<sup>3670</sup> and a broad OH band in the region 3500 – 3000 cm<sup>-1</sup>.

Upon exposure to He, a subtle increase in intensity of the OH<sup>3670</sup> peak was observed (figure A5.5b). For further details see subtracted section (figure 5.4). Similar to octahedra and rods, 2945 and 2845 cm<sup>-1</sup> peaks related to C-H stretch of formates disappeared. Bands in the region 1800 – 1200 cm<sup>-1</sup> were less broad due to the disappearance of the peak at 1580 cm<sup>-1</sup>. Peaks at 1069 and 866 cm<sup>-1</sup> decreased in intensities.

On introduction of H<sub>2</sub>O vapor, increases in intensity of OH peaks were observed along with an increase in the broad OH band in the region 3500 – 3000 cm<sup>-1</sup>. Bands related to carbonate species decomposed in the presence of H<sub>2</sub>O.

Finally in He after H<sub>2</sub>O, an overall decrease in intensity of OH peaks was observed (figure A5.5d). Due to desorption of physisorbed water, the broad OH band in the region 3500 – 3000 cm<sup>-1</sup> further decreased in intensity. Bands related to carbonate species showed an increase in intensity at 1470 and 1391 cm<sup>-1</sup> with a subtle decrease in 1553 and 1530 cm<sup>-1</sup> peaks.

## Cube

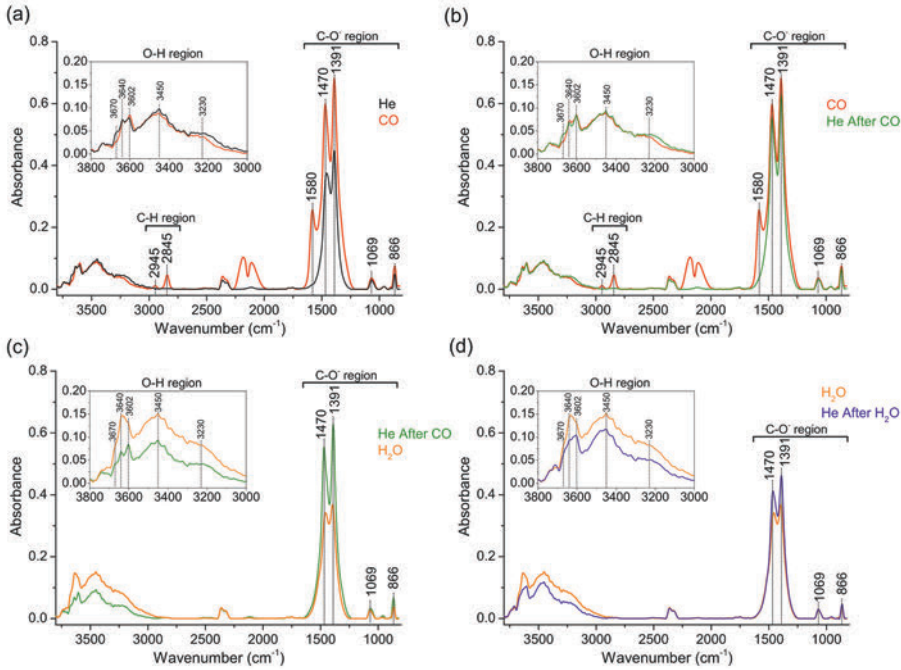


**Figure A5.5:** *In situ* FTIR spectra at 350°C of reduced ceria cubes in a) He(1, black spectrum), followed by CO(2, red line); b) CO(2) followed by He(3, green spectrum); c) He(3) followed by H<sub>2</sub>O/He(4, orange line); d) in H<sub>2</sub>O(4) followed by He(5, blue spectrum).

In figure A5.6 the subtracted FTIR spectra of unreduced ceria octahedra (left plots) and cubes (right plots) are shown. As the observation for reduced ceria nanoshapes are similar to unreduced, refer to the section 5.3.2 for further details.

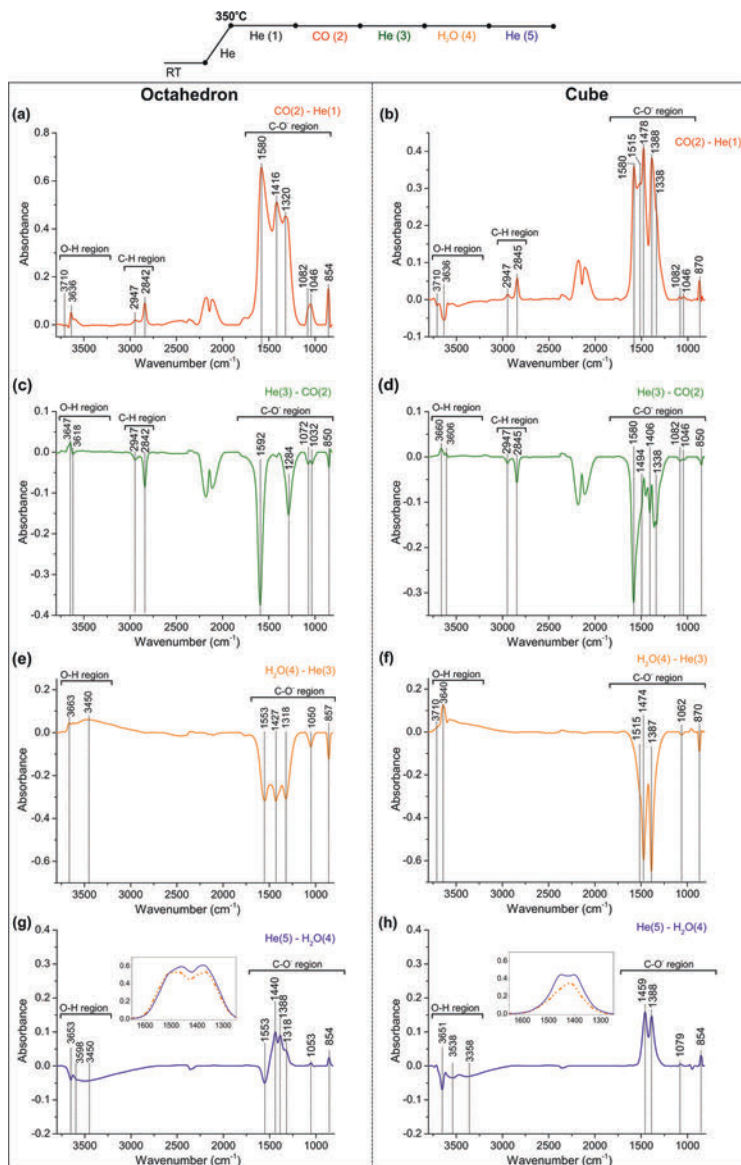


**Figure A5.6:** *In situ* FTIR subtracted spectrum at 350°C of unreduced ceria octahedra (left plots) and cubes (right plots) obtained by subtracting (a) and (b) He(1) from CO(2); (c) and (d) CO(2) from He(3); (e) and (f) He(3) from H<sub>2</sub>O(4); (g) and (h) H<sub>2</sub>O(4) from He(5). Insets in figure 5.4g and 5.4h are expanded spectra of carbonate regions obtained in H<sub>2</sub>O (dash-dotted orange) and He (5, blue) flow.

In figure A5.7, Raman spectra of ceria rods obtained in consecutive gas treatments are shown. As can be seen in figure A5.7a, the fluorite peaks ( $404$ ,  $455$  and  $487\text{ cm}^{-1}$ ) decrease in intensities and new defects ( $540$ ,  $563$ ,  $594\text{ cm}^{-1}$ ) are created on introduction of CO. Subsequently, on flowing He after CO, subtle changes in the fluorite ( $350 - 500\text{ cm}^{-1}$ ) and defect ( $500 - 600\text{ cm}^{-1}$ ) regions were observed. On exposure to  $\text{H}_2\text{O}/\text{He}$ , fluorite peaks further increased in intensity with major disappearance of defect bands. Finally in He after  $\text{H}_2\text{O}$ , further increase in fluorite peaks observed and the remaining CO-induced defects disappeared. The Raman behavior for rods is similar to the octahedra, indicating that defect chemistry is dependent on the exposed planes.

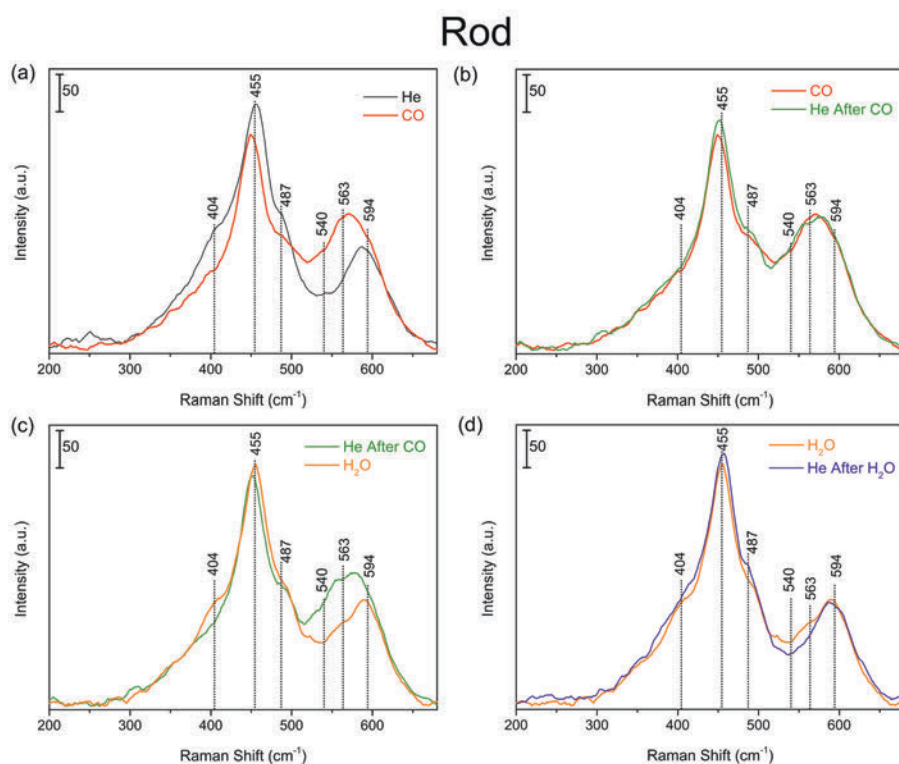


**Figure A5.7:** *In situ* Raman spectra at  $350^\circ\text{C}$  of reduced ceria rods in; (a) He(1, black spectrum), followed by CO(2, red line); (b) CO(2) followed by He(3, green spectrum); (c) He(3) followed by  $\text{H}_2\text{O}/\text{He}$ (4, orange line); (d)  $\text{H}_2\text{O}/\text{He}$  followed by He(5, blue spectrum) flow.

In figure A5.8, the subtracted FTIR spectra of ceria rods obtained by subtracting the spectrum in ‘before’ and ‘after’ stage can be seen. The observations for rods are similar to octahedra.

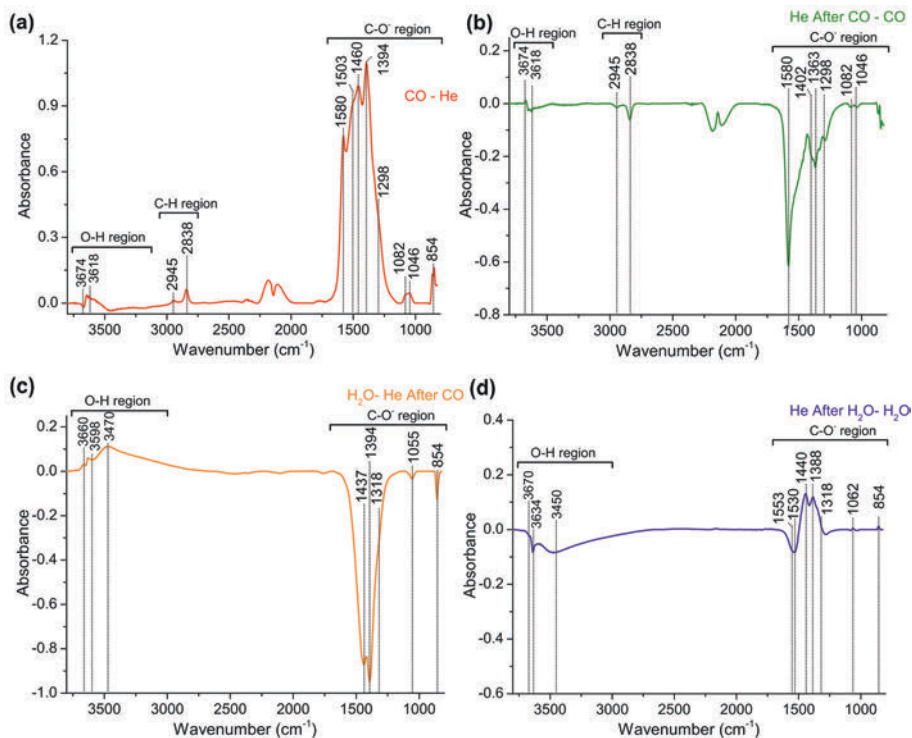


**Figure A5.8:** *In situ* FTIR spectrum of reduced ceria rods at 350°C obtained by subtracting (a) He(1) from CO(2); (b) CO(2) from He(3); (c) He(3) from H<sub>2</sub>O(4); (d) H<sub>2</sub>O(4) from He(5) spectrum.

In figure A5.9, the FTIR spectra for ceria rods obtained after exposure to CO and H<sub>2</sub>O can be seen. The observations for rods are similar to octahedra (figure 5.5a). For details refer to section 5.3.3.

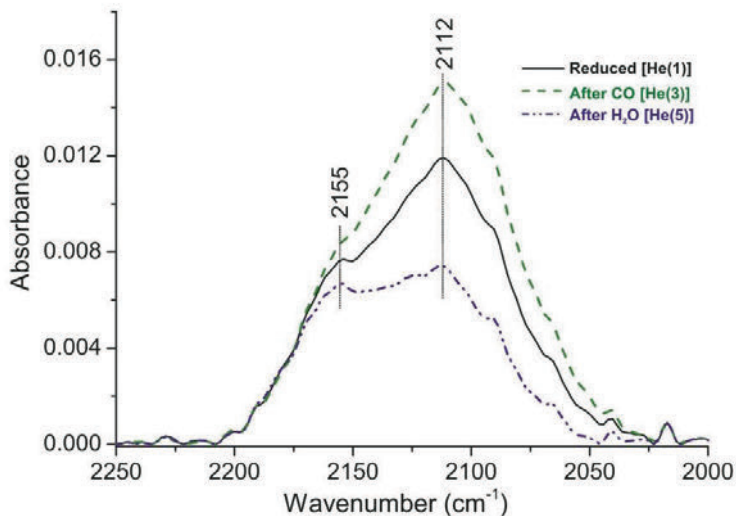


**Figure A5.9:** *In situ* FTIR of reduced ceria rods at 350°C obtained in He(1), He(3) and He(5) flow. Key: He(1) black solid line, He(3) dashed green line and He(5) dash-dotted blue line.

The lattice representations (side view) of the (111) and (100) ceria surfaces are shown in figure A5.10. The CeO<sub>2</sub> (111) surface has both Ce and O accessible in the top layer, whereas CeO<sub>2</sub> (100) has either O or Ce accessible in top layer.

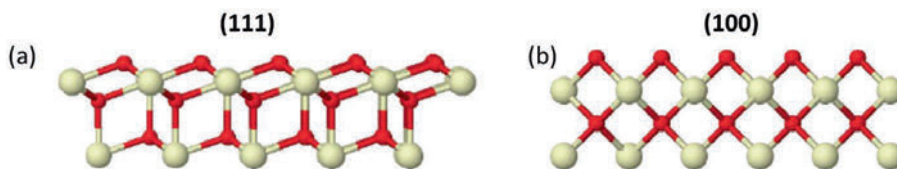


**Figure A5.10:** The ball and stick model of the (111) and (100) surfaces. Key: Ce (Light yellow) and O (red) atoms. These structures were drawn using Jmol (an open-source Java viewer for chemical structures in 3D; <http://www.jmol.org/>).

## Bibliography

- [1] Karakoti, A., Monteiro-Riviere, N., Aggarwal, R., Davis, J., Narayan, R., Self, W., McGinnis, J., and Seal, S. (2008) *JOM* **60(3)**, 33–37.
- [2] Xia, C. and Liu, M. (2002) *Solid State Ionics* **152-153**, 423–430.
- [3] Furler, P., Scheffe, J., Gorbar, M., Moes, L., Vogt, U., and Steinfeld, A. (2012) *Energy Fuels* **26(11)**, 7051–7059.
- [4] Jasinski, P., Suzuki, T., and Anderson, H. U. (2003) *Sens. Actuators, B* **95(1-3)**, 73–77.
- [5] Beie, H.-J. and Gnörich, A. (1991) *Sens. Actuators, B* **4(3-4)**, 393–399.
- [6] Diwell, A., Rajaram, R., Shaw, H., and Truex, T. (1991) The role of ceria in three-way catalysts In A. Crucq, (ed.), *Studies in Surf. Sci. and Catalysis*, volume **71**, pp. 139–152 Elsevier.
- [7] Bueno-López, A. (2014) *Appl. Catal., B* **146**, 1–11.
- [8] Li, J., Kalam, A., Al-Shihri, A. S., Su, Q., Zhong, G., and Du, G. (2011) *Mater. Chem. Phys.* **130(3)**, 1066–1071.
- [9] Han, W.-Q., Wen, W., Hanson, J. C., Teng, X., Marinkovic, N., and Rodriguez, J. A. (2009) *J. Phys. Chem. C* **113(52)**, 21949–21955.
- [10] Jacobs, G., Patterson, P. M., Williams, L., Sparks, D., and Davis, B. H. (2004) *Catal. Lett.* **96(1-2)**, 97–105.
- [11] Polychronopoulou, K., Kalamaras, C. M., and Efstathiou, A. M. (2011) *Recent Patents on Materials Science* **4(2)**, 122–145.
- [12] Rioche, C., Kulkarni, S., Meunier, F. C., Breen, J. P., and Burch, R. (2005) *Appl. Catal., B* **61(1-2)**, 130–139.
- [13] Snell, R. W., Hakim, S. H., Dumesic, J. A., and Shanks, B. H. (2013) *Appl. Catal., A* **464-465**, 288–295.
- [14] Han, J., Kim, H. J., Yoon, S., and Lee, H. (2011) *J. Mol. Catal. A: Chem.* **335(1-2)**, 82–88.
- [15] Yi, G., Xu, Z., Guo, G., Tanaka, K., and Yuan, Y. (2009) *Chem. Phys. Lett.* **479(1-3)**, 128–132.
- [16] Esch, F., Fabris, S., Zhou, L., Montini, T., Africh, C., Fornasiero, P., Comelli, G., and Rosei, R. (2005) *Science* **309(5735)**, 752–755.
- [17] Zhou, K. and Li, Y. (2012) *Angew. Chem., Int. Ed.* **51(3)**, 602–613.
- [18] Lin, K.-S. and Chowdhury, S. (2010) *Int. J. Mol. Sci.* **11(9)**, 3226–3251.
- [19] Mai, H.-X., Sun, L.-D., Zhang, Y.-W., Si, R., Feng, W., Zhang, H.-P., Liu, H.-C., and Yan, C.-H. (2005) *J. Phys. Chem. B* **109(51)**, 24380–24385.
- [20] Sun, C., Li, H., and Chen, L. (2012) *Energy Environ. Sci.* **5**, 8475–8505.
- [21] Tana, Zhang, M., Li, J., Li, H., Li, Y., and Shen, W. (2009) *Catal. Today* **148(1-2)**,

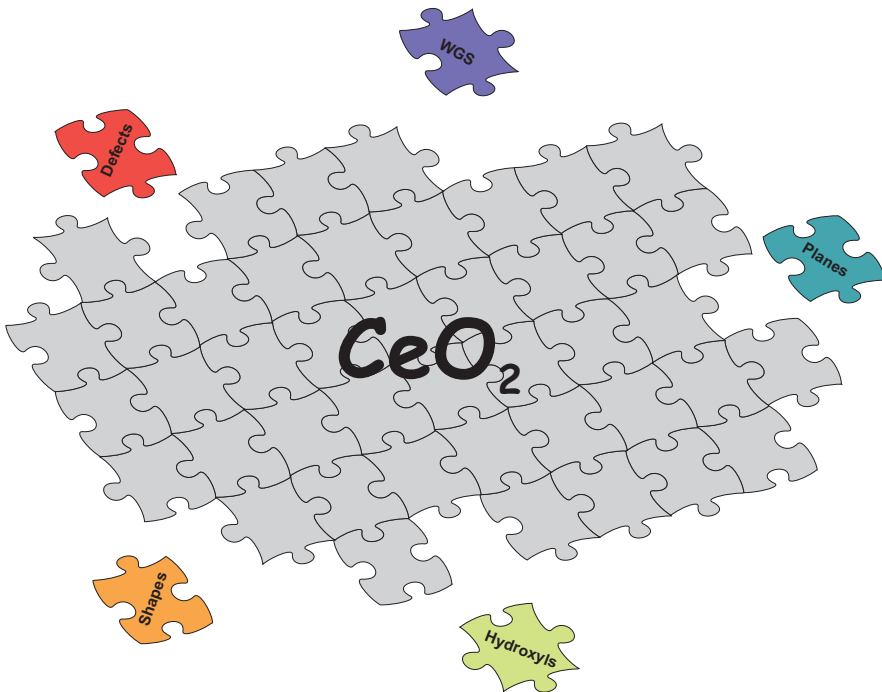
- 179–183.
- [22] Wang, S., Zhao, L., Wang, W., Zhao, Y., Zhang, G., Ma, X., and Gong, J. (2013) *Nanoscale* **5**, 5582–5588.
- [23] Zhou, K., Wang, X., Sun, X., Peng, Q., and Li, Y. (2005) *J. Catal.* **229(1)**, 206–212.
- [24] Wu, Z., Li, M., and Overbury, S. H. (2012) *J. Catal.* **285(1)**, 61–73.
- [25] Agarwal, S., Lefferts, L., Mojet, B. L., Ligthart, D. A. J. M., Hensen, E. J. M., Mitchell, D. R. G., Erasmus, W. J., Anderson, B. G., Olivier, E. J., Neethling, J. H., and Datye, A. K. (2013) *ChemSusChem* **6(10)**, 1898–1906.
- [26] Mullins, D. and Overbury, S. (1999) *J. Catal.* **188(2)**, 340–345.
- [27] Albrecht, P. M. and Mullins, D. R. (2013) *Langmuir* **29(14)**, 4559–4567.
- [28] Senanayake, S. D. and Mullins, D. R. (2008) *J. Phys. Chem. C* **112(26)**, 9744–9752.
- [29] Stubenrauch, J., Brosha, E., and Vohs, J. (1996) *Catal. Today* **28(4)**, 431–441.
- [30] Mullins, D. R., Albrecht, P. M., and Calaza, F. (2013) *Top. Catal.* **56(15-17)**, 1345–1362.
- [31] Nörenberg, H. and Harding, J. H. (2001) *Surf. Sci.* **477(1)**, 17–24.
- [32] Liu, X., Zhou, K., Wang, L., Wang, B., and Li, Y. (2009) *J. Am. Chem. Soc.* **131(9)**, 3140–3141.
- [33] Padeste, C., Cant, N. W., and Trimm, D. L. (1994) *Catal. Lett.* **28(2-4)**, 301–311.
- [34] Kalamaras, C. M., Americanou, S., and Efstathiou, A. M. (2011) *J. Catal.* **279(2)**, 287–300.
- [35] Mochizuki, S. (1982) *Phys. Status Solidi* **114(1)**, 189–199.
- [36] Weber, W. H., Hass, K. C., and McBride, J. R. (1993) *Phys. Rev. B* **48**, 178–185.
- [37] Mamontov, E. and Egami, T. (2000) *J. Phys. Chem. Solids* **61(8)**, 1345–1356.
- [38] Wu, Z., Li, M., Howe, J., Meyer, H. M., and Overbury, S. H. (2010) *Langmuir* **26(21)**, 16595–16606.
- [39] Agarwal, S., Zhu, X., Hensen, E. J. M., Lefferts, L., and Mojet, B. L. (2014) *J. Phys. Chem. C* submitted.
- [40] Nakajima, A., Yoshihara, A., and Ishigame, M. (1994) *Phys. Rev. B* **50**, 13297–13307.
- [41] Taniguchi, T., Watanabe, T., Sugiyama, N., Subramani, A. K., Wagata, H., Matsushita, N., and Yoshimura, M. (2009) *J. Phys. Chem. C* **113(46)**, 19789–19793.
- [42] Agarwal, S., Lefferts, L., and Mojet, B. L. (2013) *ChemCatChem* **5(2)**, 479–489.
- [43] Yang, P., Wei, H., Huang, H.-L., Baum, B. A., Hu, Y. X., Kattawar, G. W., Mishchenko, M. I., and Fu, Q. (2005) *Appl. Opt.* **44(26)**, 5512–5523.
- [44] Badri, A., Binet, C., and Lavalley, J.-C. (1996) *J. Chem. Soc., Faraday Trans.* **92**, 4669–4673.
- [45] Binet, C., Daturi, M., and Lavalley, J.-C. (1999) *Catal. Today* **50(2)**, 207–225.
- [46] Binet, C., Badri, A., Boutonnet-Kizling, M., and Lavalley, J.-C. (1994) *J. Chem.*

- Soc., Faraday Trans.* **90**, 1023–1028.
- [47] Binet, C., Jadi, A., and Lavalley, J.-C. (1992) *J. Chim. Phys. Phys. - Chim. Biol.* **89**, 1779–1797.
- [48] Li, C., Sakata, Y., Arai, T., Domen, K., Maruya, K., and Onishi, T. (1989) *J. Chem. Soc., Faraday Trans. 1* **85**, 929–943.
- [49] Li, C., Sakata, Y., Arai, T., Domen, K., Maruya, K., and Onishi, T. (1989) *J. Chem. Soc., Faraday Trans. 1* **85**, 1451–1461.
- [50] Nolan, M. and Watson, G. W. (2006) *J. Phys. Chem. B* **110(33)**, 16600–16606.
- [51] Happel, M., Mysliveček, J., Johánek, V., Dvořák, F., Stetsovykh, O., Lykhach, Y., Matolín, V., and Libuda, J. (2012) *J. Catal.* **289**, 118–126.
- [52] Bozon-Verduraz, F. and Bensalem, A. (1994) *J. Chem. Soc., Faraday Trans.* **90**, 653–657.
- [53] Li, M., Wu, Z., and Overbury, S. (2013) *J. Catal.* **306**, 164–176.
- [54] Wu, Z., Li, M., Mullins, D. R., and Overbury, S. H. (2012) *ACS Catal.* **2(11)**, 2224–2234.
- [55] Li, C., Domen, K., Maruya, K., and Onishi, T. (1990) *J. Catal.* **125(2)**, 445–455.
- [56] Vayssilov, G. N., Mihaylov, M., Petkov, P. S., Hadjiivanov, K. I., and Neyman, K. M. (2011) *J. Phys. Chem. C* **115(47)**, 23435–23454.



# 6

## Conclusions and outlook



## Abstract

*The work presented in this thesis highlights the fundamental aspects of ceria nanoshapes and the effect of exposed planes on their performance as a catalyst support. The main objectives were to investigate the true exposed facets, as well as to understand the reactivity of hydroxyl species and the role of defects on the ceria nanoshapes. In this chapter, the main conclusions of this work are summarized, followed by recommendations for future research.*

## 6.1 Conclusions

CeO<sub>2</sub> particles tailored into nanoshapes are desirable for enhanced activity and selectivity for catalytic applications. However, at the start of this work a coherent understanding of the surface species actually responsible for the enhanced activity was lacking. This thesis thus aimed to provide a coherent, systematic and consistent picture of fundamental aspects of ceria nanoshapes, with emphasis on the effects of exposed planes on overall performance.

The first part of this thesis is dedicated to the identification of the true exposed facets on ceria nanoshapes using aberration-corrected transmission electron microscopy (AC-TEM) and high-angle annular dark field imaging (HAADF) (**chapter 2**). Prior to the present work, it was the common belief in the literature that rods expose {110} and {100} planes, and this was used to explain their enhanced activity. However, data in the previous literature were recorded prior to the recent advancements in TEM (of AC and HAADF), and the results were unclear. Our WGS and FTIR results hinted that rods must have the same exposed planes as octahedra, which spurred us to re-examine rods with up-to-date equipment. From our new AC-TEM results it is evident that ceria octahedra and rods both expose {111} surfaces, whereas ceria cubes principally expose {100} surfaces. In addition, H<sub>2</sub>-reduced ceria nanoshapes were tested for the water gas shift reaction to evaluate the catalytic behavior as a function of surface plane. WGS activity normalized with surface area (m<sup>2</sup>) was identical for ceria octahedra and rods, whereas ceria cubes were found to be much more active. Furthermore, to gain mechanistic insight related to the interaction of CeO<sub>2</sub> with CO/H<sub>2</sub>O molecules during the WGS catalytic reaction, H<sub>2</sub>-reduced ceria nanoshapes were analyzed using FTIR

## 6.1. CONCLUSIONS

spectroscopy at 350°C. FTIR data further proves that rods and octahedra resemble each other in surface termination, as evidenced by the hydroxyl (O-H) vibration bands, whereas cubes clearly have a different relative amount of the surface OH species. Moreover, the interaction of OH species with CO results in similar spectral features for rods and octahedra, whereas clear differences were observed for cubes. By combining WGS reactivity, FTIR and TEM measurements it is clear that the surface termination affects the overall performance of ceria nanoshapes. Due to the presence of the same {111} exposed planes, ceria rods and octahedra show similar WGS activity, as well as similar interaction of OH species with CO as observed with FTIR spectroscopy. Interestingly, cubes with more reactive {100} surface planes have different OH bands and interactions with CO, resulting in a higher WGS activity per m<sup>2</sup>.

In the second part of this thesis (**chapter 3**), focus is on the role of different types of active hydroxyl (OH) species on the different exposed planes (from wires, cubes and octahedra) and their reactivities towards CO and the extent of regeneration in water at 200°C. It is known that hydroxyl species are the active sites in ceria-supported catalytic reactions such as WGS, and it is also known that steric constraint can lead to different amounts of hydroxyl species on different exposed planes. To what extent is the activity of hydroxyl groups affected by the exposed planes? At 200°C, all three ceria nanoshapes showed similar O-H stretching bands although with different relative intensities. In the case of wires and cubes, the bridged hydroxyl species (OH<sup>3641</sup>) was found to be reactive towards CO, whilst only limited interaction with CO was observed for octahedra (schematically shown in figure 6.1). Moreover, octahedra showed the formation of hydrogen carbonates in CO, which was not the case for other two shapes. Furthermore, the relative amount of defects observed follows the trend: Octahedra < cubes < wires. Based on all these observations, it is proposed that the interaction of specific hydroxyl

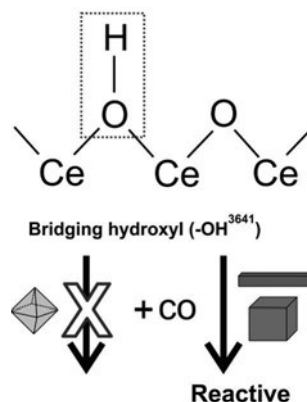


**Figure 6.1:** Schematics presenting the interaction of bridging hydroxyl on ceria nanoshapes with CO.

groups with CO is influenced by the presence of defects as well as shape of the ceria nanoforms. In addition, subsequent exposure to water vapor at 200 °C showed a clear shape-dependent water activation, resulting in removal of different relative amounts of formates and carbonates formed in either ambient or CO.

Finally, in the last part of the thesis, the defect chemistry of unreduced and reduced ceria nanoshapes is extensively discussed based on the Raman and FTIR results by varying the temperature (**chapter 4**) and gas environment (**chapter 5**). It is well known in the literature that the presence of intrinsic defects, as well as the ease of formation of defects during the reaction, strongly influences the ceria-catalyzed reactions. This gives rise to several questions: Is defect chemistry affected by different exposed planes? Are all of the defect types known/accounted for? Are the formation/healing of defects during the interaction with CO/H<sub>2</sub>O dependent on the surface terminations of the ceria nanoshapes?

In **chapter 4**, the complex role of defects was explored during CO adsorption and consecutive reaction with H<sub>2</sub>O in ceria rods using a combination of *in situ* Raman and FTIR spectroscopies. It is proposed that apart from the reported defects, such as anion Frenkel pair and oxygen vacancies, the ceria lattice might also form other defect types, e.g., vacancy clusters, interstitial and Schottky disorder, on exposure to CO. In addition, the involvement of defects in ceria rods for the formation of specific formate and carbonate surface species was found to be dependent on temperature. For instance, the majority of formates and carbonates formed in CO at 200 °C do not induce vacancies in the ceria lattice, whilst at 350 °C formation of both formates and carbonates (mono/bi-dentate) result in the creation of vacancies. Furthermore, stable poly-dentate carbonates are formed at 350 °C that neither decompose in water vapor nor create vacancies in the ceria lattice. It must be noted that the Raman signatures of the defect peaks arising in CO are very similar. However, their chemical origin seems to be different since at 350 °C the addition of H<sub>2</sub>O is needed to remove the vacancies, while at 200 °C the majority disappeared already in He flow. Further theoretical studies are highly recommended for specific defect identification and corresponding peak assignment in the Raman spectra.

In **chapter 5**, a detailed synopsis of the roles of defects in cubes (i.e., the {100} plane) as compared to octahedra and rods (with {111} plane) is presented. The

## 6.2. GENERAL RECOMMENDATIONS

defect chemistries of both rods and octahedra as functions of gas environment was found to be the same. Interestingly, the CO-induced defects on cubes were intrinsically different to the defects on octahedra and rods. For instance, in cubes oxygen vacancies ( $O_{vac}$ ) were formed in CO at the expense of existing anion Frenkel pair defects ( $I_D$ ), whereas for the other two nanoshapes both  $O_{vac}$  and  $I_D$  defects were formed irrespective of existing  $I_D$  defects. These findings are further supported by FTIR data which shows that  $H_2$ -pretreated rods and octahedra can be further reduced in CO, whereas  $H_2$ -pretreated cubes are not further reducible in CO and hence undergo structural rearrangement to further react with CO. These observations confirm that the defect chemistry on ceria nanoshapes is directly dependent on the surface terminations.

From this work it is clear that the ceria cubes show higher catalytic activity (per  $m^2$ ) than rods or octahedra. This is due to the different exposed planes, which give rise to different defect-creation mechanisms and different relative amount of hydroxyl species (and their interaction with CO and  $H_2O$ ).

## 6.2 General recommendations

In light of the present work new questions have arisen. These general recommendations begin with the validation of some of the assumptions made in this thesis followed by the recommendations for the future research.

### 6.2.1 Wire vs. rod

When the work in this thesis was initiated the three ceria nanoshapes were octahedra, cubes, and wire (chapter 3), but later the wire was replaced with rods (chapter 2, 4, 5). In chapter 3 (not shown) rods were also used but omitted due to their similar spectroscopic signatures to wire (see figure A6.1 in Appendix). The main reason for changing to rods was to allow better comparison with the literature (where rods are by far used most often). Bearing in mind the similar FTIR spectra and geometries, the assumption that both wires and rods have similar terminations  $\{111\}$  was straightforward. However, this does require validation using AC-TEM.

## 6.2.2 Bridged hydroxyls on ceria nanoshapes at 200°C

One of the principle conclusions of this thesis is that the catalytic behavior of ceria nanoshapes is dependent on their exposed planes, and extensive experimental evidence has been provided to support this. However, there is still a puzzle when comparing the FTIR data for ceria nanoshapes at 200°C (chapter 3). To be precise, bridged hydroxyl group reactivity with CO on wires (or rods with the {111} plane) and octahedra {111} is different (figure 3.8a, chapter 3). It appears that the reactivity of bridged OH may not be dependent on the surface plane. How can this discrepancy be understood?

The defects introduced on exposure to CO at 200°C are similar for both octahedra and rods. Therefore, the different reactivities of bridged OH cannot be explained due to the presence of CO-induced defects. However, it must be noted that the relative amount of intrinsic defects observed using Raman followed the trend: Wires (similar to rods, see above)  $\gg$  octahedra (figure 3.3b, chapter 3). Therefore, it seems that at 200°C, the bridged OH reactivity is most probably determined by the presence of intrinsic defects and not CO-induced defects in the vicinity of OH groups.

## 6.2.3 Cubes with high surface area

Based on this work, cubes are the most promising ceria shape due to their high WGS activity per m<sup>2</sup>. In reality, cubes have very low surface area in comparison to other ceria nanoshapes. To make them attractive as an active support for industrial catalytic applications such as the water gas shift (WGS) reaction, CO oxidation, and steam reforming of hydrocarbons, it is recommended to synthesize cubes with higher surface area, i.e., with much smaller dimensions and less polydispersity. In fact, some recent literature has shown that the hydrothermal-microwave assisted synthesis approach result in ceria shapes with high surface area.[1]

## 6.2.4 Role of vacancy clusters in ceria nanoshape catalysis

In this thesis focus has been made on point defects. However, the presence of vacancy clusters, such as dimers and trimers, and their influence in determining the oxidation-reduction properties of ceria nanoshapes cannot be fully ignored. There

## 6.2. GENERAL RECOMMENDATIONS

have been reports in the literature related to these vacancy clusters using AFM and STM on ceria oriented ceria films.[2–5] With the recent advancements in experimental physical chemistry, the integration of spectroscopic techniques (e.g., Raman) with interfacial techniques (e.g., scanning probe microscopy) allows the understanding of surface chemistry of materials on a truly atomic scale.[6–8] It is highly recommended to investigate the defect chemistry of ceria nanoshapes using the *in situ* Raman technique coupled with scanning force techniques to enable direct identification of defect types as a function of temperature and gas environment. Furthermore, theoretical studies are required for identifying and assigning different types of point defects and vacancy clusters in the Raman spectrum.

### 6.2.5 Ceria nanoshapes with metal loading

Now that the fundamental behavior of ceria nanoshapes is better understood, the more industrially relevant catalytic reactions (such as WGS, CO oxidation, steam reforming of hydrocarbons/bio-oil) involving ceria loaded with metal particles can be addressed. As mentioned in the introduction, all of the studies to date on metal-loaded ceria nanoshapes emphasize the underlying (110) and (100) exposed planes of ceria rods as giving rise to the enhanced reactivity. The presence of these active planes increases the bonding strength between the metal particles with the ceria support, as well as an increase in the presence and transfer of lattice oxygen from the ceria support to metal particles. However, it is now known from the present work that ceria rods preferentially expose {111} facets, which completely reopens the field in terms of interpretation and understanding of the interaction of metal particles with ceria nanoshapes, as well as what drives the overall performance of these catalysts. Key questions include how the metal dispersion is influenced by the surface plane of ceria; how the metal/particle interaction is affected by the different surface terminations of ceria; can the synthesis of *stable* ceria nanoshapes be up-scaled for industrial applications; is the presence of active surface planes, i.e., (100), really desirable, bearing in mind that these planes can actively interact with the reactants/intermediates and, if the bonding is too strong, can lead to support poisoning?

## Appendix 6

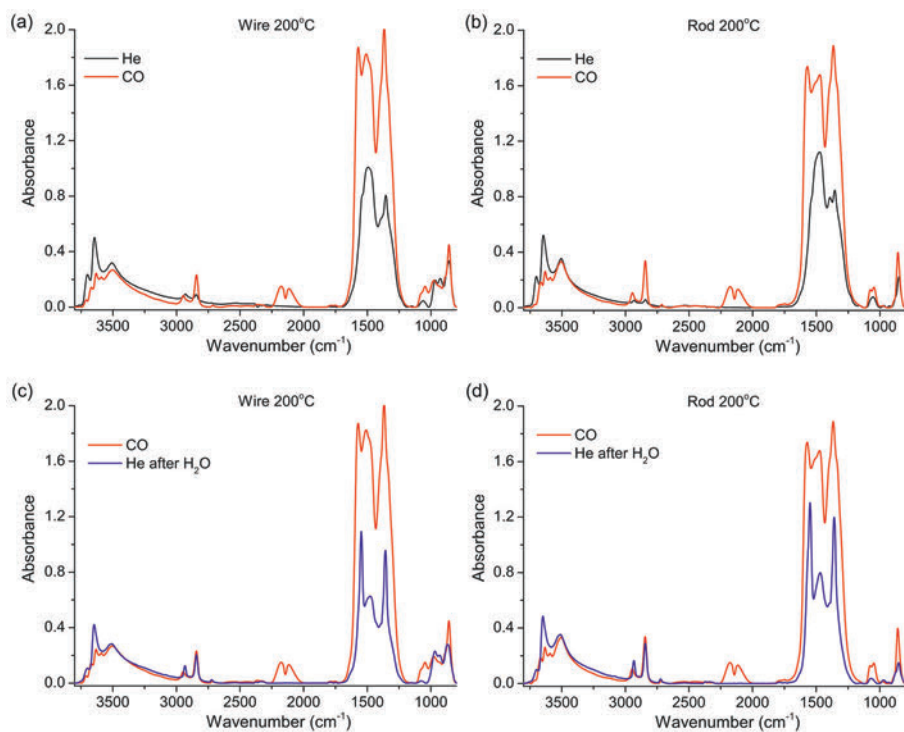


**Figure A6.1:** *In situ* FTIR spectra at 200°C of ceria wire (a, c) and rod (b, d) in He flow (black spectrum), followed by CO (red) and finally in He after regeneration in H<sub>2</sub>O vapor (blue spectrum).

## Bibliography

- [1] Gao, F., Lu, Q., and Komarneni, S. (2006) *J. Nanosci. Nanotechnol.* **6(12)**, 3812–3819.
- [2] Esch, F., Fabris, S., Zhou, L., Montini, T., Africh, C., Fornasiero, P., Comelli, G., and Rosei, R. (2005) *Science* **309(5735)**, 752–755.
- [3] Namai, Y., Fukui, K.-I., and Iwasawa, Y. (2003) *Catal. Today* **85(2-4)**, 79–91.
- [4] Nörenberg, H. and Briggs, G. A. D. Nov 1997 *Phys. Rev. Lett.* **79**, 4222–4225.
- [5] Nörenberg, H. and Harding, J. H. (2001) *Surf. Sci.* **477(1)**, 17–24.
- [6] Araujo, P. T., Barbosa Neto, N. M., Chacham, H., Carara, S. S., Soares, J. S., Souza, A. D., Canado, L. G., deOliveira, A. B., Batista, R. J. C., Joselevich, E., Dresselhaus, M. S., and Jorio, A. (2012) *Nano Lett.* **12(8)**, 4110–4116.
- [7] Harvey, C. E., vanSchrojenstein Lantman, E. M., Mank, A. J. G., and Weckhuysen, B. M. (2012) *Chem. Commun.* **48**, 1742–1744.
- [8] Lucas, M., Wang, Z. L., and Riedo, E. (2009) *Appl. Phys. Lett.* **95(5)**, 1–3.



# Scientific contributions

## Publications

1. Ceria Nanocatalysts: Shape Dependent Reactivity and Formation of OH  
**S. Agarwal**, L. Lefferts, & B. L. Mojet  
*ChemCatChem* **5**, 479–489 (2013)
2. Exposed surfaces on shape controlled ceria nanoparticles revealed via ACTEM and water gas shift reactivity  
**S. Agarwal**, L. Lefferts, B. L. Mojet, D. A. J. M. Ligthart, E. J. M. Hensen, D. R. G. Mitchell, W. J. Erasmus, B. G. Anderson, E. J. Olivier, J. H. Neethling, & A. K. Datye  
*ChemSusChem* **6**, 1898–1906 (2013)
3. Defect chemistry of ceria nanorods  
**S. Agarwal**, X. Zhu, E. J. M. Hensen, L. Lefferts, & B. L. Mojet  
*J. Phys. Chem C* **118**, 4131–4142 (2014)
4. Defect chemistry of ceria nanoparticles as a function of exposed planes  
**S. Agarwal**, X. Zhu, E. J. M. Hensen, L. Lefferts, & B. L. Mojet  
(*in preparation*)
5. Ceria nano-shapes – structural and catalytic properties  
**S. Agarwal**, L. Lefferts, A. K. Datye, & B. L. Mojet  
(*Invited review for book chapter, in preparation*)

## Oral presentations

1. Morphological mysteries of ceria catalysts: Water activation  
2<sup>nd</sup> ADEM conference, NL (25-26<sup>th</sup> April 2013)  
*Invited*
2. Morphological mysteries of ceria catalysts  
NCCC-XIII, NL (5-7<sup>th</sup> March 2012)  
*Contributed*
3. Catalytic water activation  
1<sup>st</sup> ADEM conference, NL (26-27<sup>th</sup> May 2011)  
*Invited*

**Poster presentations**

1. Nano-catalysis with cerium oxide: Water activation  
Mesa+ Day, NL (18<sup>th</sup> September 2012)
2. Nano-catalysis with cerium oxide: Water activation  
15<sup>th</sup> ICC, DE (1-6<sup>th</sup> July 2012)
3. A spectroscopic study of cerium oxide nano-catalyst: Water activation  
4<sup>th</sup> Operando congress, USA (29<sup>th</sup> April-3<sup>rd</sup> May 2012)  
→ ***Received poster prize***
4. Tailored ceria nanoparticles for highly active OH species-Green future  
NCCC-XII, NL (28<sup>th</sup> February-2<sup>nd</sup> March 2011)
5. How to enhance activation of water on inorganic oxides  
6<sup>th</sup> EFCATS summer school - Catalysis and surface science for renewables  
& energy, TUR (13-19<sup>th</sup> September 2010)
6. How to enhance activation of water  
NCCC-XI, NL (1-3<sup>rd</sup> March 2010)
7. In-situ ATR-FTIR spectroscopy of structured zeolite H-ZSM-5 catalysts  
16<sup>th</sup> IZA, IT (4-9<sup>th</sup> July 2010)

# Acknowledgements

Finally the moment arrived! Last 4 years has been incredible and taught me so much about life and people. Of-course like every Ph.D., it was a roller coaster ride: Exciting, scary, full of insecurities and crazy. End of this journey is incomplete without acknowledging and appreciating people who whole-heartedly supported and believed in me.

Leon, many thanks for offering me the opportunity to do PhD in your group. Your inputs and suggestions related to this project and scientific chapters of this thesis were always highly appreciated. Thank you for all your help and inputs regarding the finalization of this thesis. I would also like to thank Barbara for accepting to be my daily supervisor. Thanks for teaching me to be very critical while analyzing data.

I also want to express my gratitude to Emiel for the fruitful collaboration that resulted in good quality publications. Special thanks to Michel for your help with WGS testing and Xiaochun for your assistance with Raman experiments. My gratitude also goes to Abhaya. Many thanks for all the Skype meetings and your availability to discuss results that led to a publication in ChemSusChem.

Many thanks Seshan and Arie for the scientific/non-scientific discussions. Your advices and suggestions were greatly appreciated!

Sabine, Lidy and Maaïke thanks for all the administrative support. Maaïke you are simply wonderful to everyone in CPM. Thanks for arranging social events that brought life to CPM.

Bert, whenever I knocked on your door with questions related to FTIR setup, software installments and advice about my project/people/life, you were always available and supportive. Thank you for everything:)

Karin, many thanks for helping me with my setup, ordering chemicals, chemisorption and BET analysis, for all the encouragement and lastly for the warm hugs. I always enjoyed talking about food and recipes with you. Finally, whenever you came to see me in the lab you always remembered to bring your sphere of positivity with you. Without this I surely would have struggled.

Many thanks Tom and Ruben for the technical support in laboratory. Louise, thank you for all the XRF and BET measurements. I would like to also thank

## ACKNOWLEDGEMENTS

Mark Smithers for performing TEM and SEM measurements.

During my project, I supervised Darren for his master thesis. Many thanks Darren for your contributions to my project. I wish you all the best in your career.

Special thanks to my office mates Joline, Yinni and Arturo. Joline, I will miss you a lot, the wonderful game nights (with Arnout), our long chats. Thanks for being my Dutch translator for last four years :) and now for accepting to be my paranimph! Yinni, while writing this I have strong craving for the tasty dumplings. I will miss seeing you and your happy face on daily basis. I wish you and Yin a happy and healthy life together. Arturo will miss the tasty Mexican food and our long chit chats. I wish you all the success in your life.

Furthermore, I would like to thank my recent and former colleagues Son, Masoud, Jose, Songbo, Cristina, Raman, Inga, Sergio, Davide, Roger, Kamilla, Chau, Kaisa, Rao, Hrudyia in CPM for the pleasant time. Every year trip to NCCC was so much fun. Still the reactor story makes me smile. Thanks Roger for that:)

Marijana, during my PhD and especially in the last few months you were extremely supportive. Thanks for beautiful and amazing moments, for many nights out for a glass of wine, for a cup of macchiato at Bagels, IKEA trips and many more. I wish from my heart that all your dreams come true:))

Enschede felt like home as soon as I moved in with Julian and Lisa. Usselerweg 116 became my home. Miss you both and the time we spent together. Organizing dinner/ dance parties, playing squash and going to Rico Latino was always fun. I miss Julian's deadly salsa sauce and Lisa's Thai curry soup. I miss dancing salsa with Julian and going for horse-riding lesson with Lisa. You both gave me wonderful moments to look back and simply smile. Thank you both!

During the last 4 years I came to know beautiful people from around the world. Chieh-chao, Gonzalo, Vicky, Bilge, David, Flavia, Julia and many more who made my stay in Enschede memorable.

Daniela, thank you for being a wonderful teacher. Painting lessons at your place were always relaxing. I learned a lot from you and this thesis cover may never have been completed without your guidance. Nandprasad thank you for teaching me a life skill. Thank you for your positivity and the driving lessons you gave in Hindi:) Masha you were extremely supportive and nice to me. I will miss our regular meets once you move to Essen.

Mishra Sir, thank you for making chemistry lessons so much fun and exciting. It's because of you I can proudly say, "I am a chemist". Savita our trip to Niagara Falls and New York is really close to my heart. I miss you buddy. I wish you all the best with your PhD. Thanks Eve and Richard for making sure James and I have relaxing long weekends whenever we were looking for an escape from Netherlands.

Reaching this stage wouldn't have been possible without the support and love of my family. Chinu and Siddhu, I am so lucky to have you both. You both were extremely supportive all my life. I love you both! Mum and Papa thanks for your unconditional love, understanding and coping with my mood swings. Mamma without you I'm nothing!

James, without you, I would have never made it this far! Thanks for all the support and energy you gave me. Thanks for your patience and love when I was in my worst of moods. Thanks for bringing beautiful little beings (Kiiki and Baaghera) in my life. Thanks for making home a place where I can forget all my worries. Thanks for making me and my Ph.D. the top-most priority. Thanks for making me feel so loved. Thank you so much, for everything my wonderful man. I am looking forward to spend and enjoy all my life with you. Love you:))



Kiiki and Baaghera helping me in their own little ways!

Shilpa Agarwal was born in Delhi (India) in 1985. She received her bachelor degree in Industrial Chemistry from AMU, India in June 2007. After her bachelor degree, she was awarded an Erasmus mundus scholarship for the dual master program in Advanced Material Science & Engineering (AMASE) in September 2007. She received her master degrees from Luleå University of Technology, LTU (Sweden) as well as from the Institut National Polytechnique de Lorraine, INPL (France) in October 2009. During this period, she also received a second bachelor degree in Chemistry from LTU (Sweden) in December 2009. She was awarded an LTU scholarship during this bachelor degree. In January 2010, she started her Ph.D. degree at the University of Twente (The Netherlands) in the Catalytic Processes & Materials group (CPM). The current thesis presents the outcome of her Ph.D. research.



ISBN 978-90-365-3641-7



9 789036 536417 >